INSTITUT FÜR
ENERGIETECHNIK
UND THERMODYNAMIK
Institute of Energy Systems and Thermodynamics

DISSERTATION

Numerical investigation and optimisation of a new Pelton turbine distributor system

Authored by

Dipl.-Ing. Franz Josef Johann Hahn, BSc
Matr.Nr. 01225338

Supervised by

Univ.Prof. Dipl.-Ing. Dr.-Ing. Christian Bauer
Institute of Energy Systems and Thermodynamics, E302
Research Unit of Fluid Flow Machinery

Submitted to

Faculty of Mechanical and Industrial Engineering,
Technische Universität Wien
for the degree of *Doktor der Technischen Wissenschaften (Dr.techn.)*

Reviewed by

Ao.Univ.Prof. Dipl.-Ing.
Dr.techn. Reinhard Willinger
Institute of Energy Systems
and Thermodynamics
Technische Universität Wien

Associate Prof. doc. Ing.
Pavel Rudolf, Ph.D.
Victor Kaplan Department
of Fluid Engineering
Brno University of Technology

Freundorf, September 2024

Statutory Declaration

I declare in lieu of oath that I have carried out this thesis and the associated research activities on my initiative and without recourse to third parties. It is not substantially the same as any that I have submitted or is being concurrently submitted for a degree, diploma, or other qualification at Technische Universität Wien or any other university or similar institution.

I acknowledge that the submitted thesis will be checked electronically and technically using suitable and state-of-the-art means (e.g. plagiarism detection software). This procedure ensures that the submitted thesis was prepared according to high-quality standards and within the applicable rules of good scientific practice (Code of Conduct) at Technische Universität Wien. Printing and reproduction of this thesis require the consent of the examination committee.

Freundorf, September 2024 ....

(Dipl.-Ing. Franz Josef Johann Hahn, BSc)

Preface

Parts of this thesis have been published in the following peer-reviewed journal article:

- *Numerical Investigation of Pelton Turbine Distributors Systems with Axial Inflow*
  Energies 16, 2023, DOI: 10.3390/en16062737
  This article is an extended version of my contribution of the same name to Viennahydro 2022.

Parts of this thesis have been presented at the following peer-reviewed scientific conferences:

- 31st Symposium on Hydraulic Machinery and Systems (IAHR 2022):
  On the numerical assessment of flow losses and secondary flows in Pelton turbine manifolds
  26.06. - 01.07.2022, Norwegian University of Science and Technology (NTNU), Trondheim, Norway. DOI: 10.1088/1755-1315/1079/1/012082

- 21st International Seminar on Hydropower Plants (Viennahydro 2022):
  Numerical Investigation of Pelton Turbine Distributors Systems with Axial Inflow
  09.11. - 11.11.2022, Laxenburg, Austria
  An extended version of this contribution was published under the same name in the journal Energies (see above).

- 3rd IAHR Young Professionals Congress:
  Numerical investigation of the secondary flow pattern in a Pelton turbine jet
  28.11. - 02.12.2022, Online. DOI: 10.34726/3545

This thesis was partly supported by Österreichische Forschungsförderungsgesellschaft (FFG) within the framework of the project *AxFeeder* (FFG project number: FO999888084).

Footprints in the Sand

One night I dreamed a dream.
As I was walking along the beach with my Lord.
Across the dark sky flashed scenes from my life.
For each scene, I noticed two sets of footprints
in the sand,
One belonging to me and one to my Lord.

After the last scene of my life flashed before me
I looked back at the footprints in the sand.
I noticed that at many times along the path of
my life,
especially at the very lowest and saddest times,
there was only one set of footprints.
"I don't understand why, when I need You most,
You would leave me."

He whispered, "My precious child, I love you
and will never leave you,
Never, ever, during your trials and testings.
When you saw only one set of footprints,
It was then that I carried you."

Margaret Fishback Powers, 1964

Acknowledgements

Writing a dissertation is a monumental task and can seem like an eternal journey. Looking back at all the planned and unplanned detours on this journey, when it comes down to the wire, it is not the publications and citations that matter but the people who have accompanied one on this journey. Thus, this chapter is dedicated to those who showed me the right direction when I took the wrong path, those who picked me up when I fell and those who encouraged me to keep going when I could not go any further.

First and foremost, my sincere gratitude goes to my doctoral advisor, Univ.Prof. Dipl.-Ing. Dr.-Ing. Christian Bauer, Dean of the Faculty of Mechanical and Industrial Engineering at TU Wien, for his guidance during the execution of this research. He has supported me since the beginning of my scientific career and has always provided meaningful help on any of my professional and personal concerns.

I would like to express my extraordinary thanks to Ao.Univ.Prof. Dipl.-Ing. Dr.techn. Reinhard Willinger and Associate Prof. doc. Ing. Pavel Rudolf, Ph.D. for reviewing this thesis and for their valuable comments and remarks on my research.

I extend a special thank you to the co-author of my publications and office mate, Associate Prof. Dipl.-Ing. Bernhard Semlitsch, PhD. His willingness to help, endless patience, and personal support were highly appreciated.

A heartfelt thanks goes to Senior Scientist Dipl.-Ing. Dr.techn. Anton Maly, BSc, co-author of two of my publications and in charge of the project *AxFeeder*. He provided a confined environment in which I regularly worked on my thesis in isolation and pushed my motivation by jogging with me during some of our lunch breaks.

From the bottom of my heart, I thank my partner, Steffi, for her patience and understanding, particularly during the last few months in the final throes of completing this dissertation. She endured my unavailability when times were stressful and comforted me when I needed it. God bless her.

Most of all, I would like to express my deepest gratitude to my beloved parents, Veronika and RgR Ing. Franz Hahn. They have mastered their fate with modesty and humility, endured all my ups and downs, my joys and fears during my studies, and always supported me in every way. That is why I dedicate this thesis to them. God bless them.

Abstract

Pelton turbines rely on a distributor system and injectors to feed high-quality water jets to the runner to operate efficiently. The jet formation is highly influenced by the upstream flow history, where secondary flows are mainly created in the distributor system. A good distributor system allows for low energy losses and limited secondary flow. Previously, it was proven that for conventional distributor systems of six-jet Pelton turbines, the secondary flows upstream of the injectors, and thus, the jet qualities differ significantly, leading to notable variations in turbine efficiencies. Following these observations, this thesis explores how Pelton turbine distributor systems must be designed to allow for similar flow conditions in all branches and injectors and maintain a high-quality water jet at all relevant operating conditions. A yet unexplored solution could be distributor systems with axial inflow. Hence, this thesis describes the flow phenomena in such distributor systems with axial inflow (= *AxFeeder*) and derives designs favourable for high-quality flow.

Four core designs of the *AxFeeder*, the diffuser manifold (basic model), the diffuser manifold with conical frustum, the spherical manifold and the cylindrical manifold, differing mainly in the shape of the manifold and the positioning of the branch lines, were drafted. Operating parameters representative of future potential applications of the *AxFeeder* in small hydropower plants were derived, the operating regime was simulated, and a realistic design point for the parametric investigation was selected. The parametric investigation analysed the effects of changes in the manifold and branch line geometries on the flow quality criteria, namely the power losses, the dissipation power coefficient and the secondary velocity ratio.

In particular, the parametric investigation detected areas of the *AxFeeder* where the flow reacted most sensitively to a change. These included the size of the manifold, the transition zone from the manifold head to the branch line and the injector bend. A conical frustum connecting the manifold and the branch line, combined with a steep deviation angle of the branch line, results in low losses in the distributor system and limited secondary flow upstream of the injector position. The secondary flow at this station showed a distinct reverse S-shape pattern, which appeared to be characteristic of many *AxFeeder* configurations. All concepts were compared by a compound quality coefficient that equally weighs losses and secondary velocities. Only a few combinations of geometrical parameters allowed for minimal losses and secondary flows simultaneously. With a reduction of the compound quality coefficient of 44 %, the best results were achieved by the diffuser-shaped manifold with a conical frustum and a converging branch line of a deviation angle of 90°.

Kurzfassung

Um hohe Wirkungsgrade zu erzielen, muss das Laufrad der Peltonturbine mit qualitativ hochwertigen Freistrahlen beaufschlagt werden. Die Strahlformation wird dabei von in der Verteilleitung generierter Sekundärströmung beeinflusst. Eine gute Verteilleitung ermöglicht geringe Energieverluste und begrenzte Sekundärströmung. Aktueller Stand der Forschung ist, dass bei konventionellen Verteilleitungen die Sekundärströmungen vor den Düsen, die Strahlqualität und die Turbinenwirkungsgrade deutlich variieren. Hiervon ausgehend wird in dieser Arbeit die Frage gestellt, wie Verteilleitungen von Peltonturbinen gestaltet sein müssen, um ähnliche Strömungsverhältnisse in allen Verzweigungen und Düsen zu ermöglichen und einen hochwertigen Freistrahl unter allen relevanten Betriebsbedingungen zu erzielen. Eine wenig erforschte Lösung könnten Verteilleitungen mit axialer Zuströmung sein. Daher werden in dieser Arbeit die Strömungsphänomene in solchen Verteilleitungen mit axialer Zuströmung (= *AxFeeder*) mithilfe numerischer Strömungssimulationen beschrieben und hohe Strömungsqualität ermöglichende Konstruktionen abgeleitet.

Es wurden vier Basis-Varianten des *AxFeeders* entworfen, welche sich vor allem durch die Form des Mehrfach-Abzweigeelements und der Abzweigeleitungen unterscheiden. Aus einer potentiellen zukünftigen Anwendung des *AxFeeders* in Kleinwasserkraftwerken wurden typische Auslegungsdaten abgeleitet, danach die Kennlinien simuliert und ein Betriebspunkt für die Parameterstudie festgelegt. In dieser wurden die Auswirkungen geometrischer Änderungen an Mehrfach-Abzweigeelement und Abzweigeleitungen auf die Qualitätskriterien zur Beurteilung der Strömung, nämlich Verluste und Sekundärströmungsanteil analysiert.

Das Volumen des Mehrfach-Abzweigeelements, der Übergang von diesem zu den Abzweigeleitungen und der Düsenkrümmer waren besonders sensible Bereiche hinsichtlich geometrischer Änderungen. Geringe Verluste und niedrige Sekundärströmungsanteile konnten bei Verwendung eines Kegelstumpfes als Verbindung von Mehrfach-Abzweigeelement und Abzweigeleitung erzielt werden, insbesondere, wenn die letztere unter einem steilen Winkel abzweigte. Dabei zeigte sich in der Auswerteebene stromauf der Düsenposition eine charakteristische, umgekehrte S-Form der Sekundärströmung. Ein Vergleich aller Varianten erfolgte mittels eines Verbund-Qualitätskoeffizienten, bei dem die Verluste und die Sekundärströmungsanteile gleichermaßen gewichtet wurden. Mit einer Reduzierung des Verbund-Qualitätskoeffizienten von 44 % wurden die besten Ergebnisse durch das Mehrfach-Abzweigeelement mit Diffusor und Kegelstumpf in Verbindung mit einer 90°-Abzweigeleitung mit konvergentem Düsenkrümmer erzielt.

Contents

Nomenclature

Core manifold designs

a	Diffuser manifold (basic model)
b	Diffuser manifold with conical frustum
c	Spherical manifold
d	Cylindrical manifold

Abbreviations

CFD	Computational fluid dynamics
CFX	CFD solver of ANSYS, Inc.
EARSM	Baseline-Explicit Algebraic Reynolds Stress turbulence model
FFG	Österreichische Forschungsförderungsgesellschaft
GCI	Grid convergence index/method
HPP	Hydropower plant
kE	k-ε turbulence model
LES	Large Eddy Simulation
RANS	Reynolds-averaged Navier-Stokes equations
SLA	Second law analysis
SST	k-ω Shear Stress Transport turbulence model
SSTCC	k-ω SST turbulence model with curvature correction

Latin Symbols

A_i	Surface area of station i	m^2
AR	Area ratio of a diffuser or nozzle	1
$a_{0/1}/b/k$	Coefficients of fit/regression curves	1
C_p	Pressure coefficient	1
$C_{p,max}$	Maximum pressure recovery coefficient	1
c_i	Sensitivity coefficient of a parameter	misc.
$c_{s,ref}$	Reference velocity in streamwise direction	m/s
D_1	Penstock diameter	m
D_{hc}	Deviation hole circle diameter in the manifold head	m
D_i	Diameter of pipe segment at station i	m
D_p	Pitch cycle diameter of the runner	m
d	Diameter of a cylindrical pipe	m
$e_{a/ext}$	Approximated/Extrapolated error	%
GCI^{21}_{fine}	Fine-grid convergence index	1
g	Gravitational acceleration	$\mathrm{m/s}^2$
H	Geodetic head	m

h	Average cell size	m
h_{sep}	Height of a separation zone	%
I_s	Intensity of secondary flow	1
I_t	Turbulence intensity	1
$I_{t,est}$	Estimated turbulence intensity	1
i	Branch line index	1
$K_{ana/PmTE/\Phi}$	Rate of change for analytical pressure correlation/ power losses/dissipation power	1
k	Turbulent kinetic energy	m^2/s^2
k_a	Alternative definition of the turbulence intensity	1
L_i	Length of pipe segment starting from station i	m
L_{ij}	Length of pipe segment between stations i and j	m
L_{out}	Length of the outlet body	m
$L_{up/down}$	Length of upstream/downstream tangent	m
l	General length	m
l_{sep}	Length of a separation zone	%
$\dot{m}_i$	Mass flow rate (at station i)	kg/s
$N_{m/p}$	Number of mesh cells /data points	1
n	Number of branch lines	1
$P_{mTE/KE}$	Power of mechanical total energy/kinetic energy	W
$P_{Turb/Vis}$	Power of turbulent/viscous dissipation	W
P_Φ	Dissipation power	W
p	(Static) Pressure	Pa
$p_{dyn/mod/ref/t}$	Dynamic/Modified/Reference/Total pressure	Pa
p_{oa}	Apparent order of the method	1
Q	Volumetric flow rate	m^3/s
q	Auxiliary variable in the GCI method	1
R^2	Coefficient of determination of a fit/regression curve	1
R_i	(Curvature) radius at station i	m
R_{oc}	Ratio of oscillatory convergence	1
Re	Reynolds number	1
r	Refinement factor in the grid studies	1
$r_{\zeta\phi}$	Compound quality coefficient	1
SR_i	Spherical radius related to position i	m
s	Streamwise coordinate; Auxiliary variable in the GCI method	m, 1
T_i	Axial position (of the manifold head) at station i	m
$U_{R,95}$	Expanded uncertainty of a result	misc.
$U_{RSS/RMS}$	Root-sum-square/Root-mean-square of the individual uncertainties/errors	misc.
u_R	Combined standard uncertainty of a result	misc.
$u_{RMS}(x)$	Root-mean-square residual of a quantity x	misc.
u_b	Bulk velocity	m/s
u_τ	Shear velocity	m/s
u^+	Non-dimensional velocity	1
$u(x)$	Standard deviation/Uncertainty of a quantity x	misc.

V	Integration volume; Domain volume	m^3
x	Value on the x-axis; Wildcard variable name	misc.
y^+	Non-dimensional wall distance	1

Greek Symbols

α	Deviation angle of first segment of the branch line of core manifold design a; Swirl angle	$^\circ$
α_{sep}	Bend angle, at which the flow starts to separate	$^\circ$
β	Diffuser angle	$^\circ$
β^*	Coefficient of k-ω SST turbulence model	
Γ	Circulation	m^2/s
γ	Pivot angle of the injector bend	$^\circ$
Δ	Difference between quantities	misc.
δ	Deviation angle of the branch line	$^\circ$
ε	Turbulent eddy dissipation	m^2/s^3
ζ_{PmTE}	Power loss coefficient	1
ζ_{fr}	Loss coefficient due to pipe friction	1
$\zeta_{p,t}$	Total pressure loss coefficient (total resistance coeff.)	1
$\zeta_{p,ts}$	Total pressure loss coefficient including the exit losses	1
ζ_{Φ}	Dissipation power coefficient	1
$\zeta^{(\prime)}$	General resistance coefficient	1
η_{pipe}	Efficiency of a pipe (system)	1
λ	Pipe friction factor	1
μ	Dynamic viscosity of water	Pa s
μ_t	Turbulent (eddy) viscosity	Pa s
ν	Kinematic viscosity of water	m^2/s
ρ	Density of water	kg/m^3
τ_{wall}	Wall shear stress	Pa
Φ	Dissipation	W/m^3
$\Phi_{Turb/Vis}$	Turbulent/Viscous dissipation	W/m^3
Φ_{cd}	Dissipation from change of direction	W/m^3
Φ_{fr}	Background dissipation (from wall friction)	W/m^3
ϕ	Wildcard variable name in the GCI method	1
ϕ_{II}	Secondary velocity ratio	1
$\phi_{II,i}$	Integral value of the secondary velocity ratio at station i	1
φ	Pivot angle of the branch line; Angular position in the 90° bends	$^\circ$
ω	Turbulent eddy frequency	1/s

Vectors and Tensors

$\vec{c} = (c_r, c_\theta, c_s)^T$	Flow velocity in a cylindrical coordinate system	m/s
$\vec{n}$	Normal vector of surface $\vec{A} = A \cdot \vec{n}$	1
$\vec{r} = (r, \theta, z(z'))$	Cylindrical coordinate system in Sudo's experiment	m, 1, m
$\vec{s}$	Unit normal vector in streamwise direction	1
$\vec{u} = (u, v, w)^T$	Flow velocity in a Cartesian coordinate system	m/s

$\vec{u}_{I/II}$	Primary/Secondary flow velocity	m/s
$\vec{u}_{ref}$	Reference flow velocity	m/s
$\vec{x} = (x, y, z)^T$	Cartesian coordinate system	m
Π_{ij}	Stress tensor in index notation	Pa
τ_{ij}	Viscous stress tensor in index notation	Pa
$\vec{\omega}$	Vorticity	1/s

Subscripts

0	Station 0, begin of domain of interest
101	Station 101, end of domain of interest
1011	Difference between stations 1 and 101
$1, 2, 3$	Indices for mesh refinement: fine, medium, coarse
95	95 % confidence interval
I, II	Primary; Secondary
a	Approximated
ana	Analytical
b	Bulk
cd	Change of flow direction
dyn	Dynamic
est	Estimated
Exp	Experimental
ext	Extrapolated
fine	Indicates relation to fine grid
fr	Friction
hc	hole circle
i	Station index; General sum index
in/inlet	Inlet
j	Sum index for mesh cells
KE	Kinetic energy
max	Maximum
min	Minimum
$\dot{m}$	Quantity related to a mass flow rate
norm	Normalised quantity
oa	Apparent order of the numerical method
oc	Oscillatory convergence
out/outlet	Outlet
(P)mTE	(Power) of mechanical total energy
p	Data point
R	Result $R = f(X_i)$
ref	Reference
s	Static; Streamwise
sep	Separation
t	Total
Turb	Turbulent
Vis	Viscous
Φ	Dissipation

Superscripts

A	Area average value of a field variable
L	Lumped
M	Mass average value of a field variable

Further mathematical symbols

δ_{ij}	Kronecker delta, 1 if $i = j$, 0 if $i \neq j$
$\overline{(.)}$	Mean value = arithmetic average; time-averaged quantity
$\hat{(.)}$	Area (cross-section) integrated value of a field variable
$(.)'$	Fluctuating variable

Some conventions

In agreement with Greitzer et al. [26], the nomenclature should be easy to read, and follow industry conventions. Therefore, whenever convenient, widespread symbols were used, even if it was necessary to employ the same symbol for more than one quantity, e.g. the letter x, a linear coordinate and a wildcard variable used in several equations. Naturally, the context should clarify what the symbol stands for in a particular use case.

For the definition of coefficients, e.g. the loss coefficients in Section 3.3 or the secondary velocity ratio in Section 3.4, the more convenient cartesian velocity notation $\vec{u} = (u, v, w)^T$ was used. For describing the flow in a pipe system such as the *AxFeeder*, where the mean streamline of the pipe is not always aligned with cartesian coordinates, the velocity formulated in cylindrical coordinates $\vec{c} = (c_r, c_\theta, c_s)^T$ was employed.

Stations were often numbered from 0, 1, 2, and so on or are labelled by capital letters A, B, C, ... In other cases, designations such as Roman numerals or position specifications, e.g. $z/d = 2.0$, were also used.

Software

All simulations presented in this thesis were computed with the computational fluid dynamics solver ANSYS CFX 19.2. The geometries were created in Solidworks 2020 and ANSYS DesignModeler, for spatial discretisation ANSYS Meshing was used, and post-processing of the simulation results used the ANSYS post-processing utilities CFD-Post 19.2 and CFD-Post 2022 R1. Data curation and visualisation were done in Matlab R2019b, Microsoft Excel 2016, and LaTeX (mainly using the PGFPLOTS and TikZ packages). For sketching and figure preparation, Inkscape 1.1 was used.

CHAPTER 1

Introduction

Pelton turbines are impulse-type water turbines used for heads up to 2000 m and low to moderate volumetric flow rates. Within the turbine itself, a distributor system guides the flow to the injectors, where the potential energy of the water is converted into kinetic energy of the free-surface water jets. These jets push on the buckets of the runner and thus create the turning motion of the turbine shaft. Typically, for low flow rates, Pelton turbines with one or two injectors are used; with higher flow rates, Pelton turbines fed with up to six injectors are built. Often, Pelton turbines with one or two injectors have a horizontal turbine shaft, while Pelton turbines with three to six injectors have a vertical turbine shaft. The significant advantages of Pelton turbines are their simple concept, fast controllability and excellent part-load efficiencies. These advantages make Pelton turbines highly suitable for storage power plants to fulfil peak load demands. Conversely, some of the challenges Pelton turbines face are the dependence of the formation of high-quality water jets on the upstream flow conditions in the penstock, the distributor system and injectors; the susceptibility of the injectors and the runner to erosion and cavitation wear; the intermittent, pulsating loads on the buckets and the runner due to the finite number of jets acting only for a specific period of a complete runner revolution; and the two-phase flow phenomena in the casing of multi-injector Pelton turbines.

From an operational point of view, at the cost of the increased complexity of the distributor system, a higher number of injectors leads to better load distribution and utilisation of the runner, as well as smaller buckets and runners. A lighter runner allows for higher runner speeds, simpler generators and a more compact turbine unit with the same power output at significantly reduced costs. Overall, it is also economically favourable to have a design with a horizontal shaft instead of a vertical shaft, as a horizontal shaft allows for a more straightforward turbine shaft arrangement, less complex bearings and generator supports, especially at lower heads. These design and economic advantages would make a six-jet Pelton turbine with a horizontal shaft a highly favourable combination of Pelton turbines. The benefits above are outweighed by the difficulties of feeding a high-quality flow to the turbine through a simple and reliable distributor system and by discharging the flow from the casing of such a six-jet horizontal shaft Pelton turbine.

Over the years, various ideas and concepts were researched to overcome the difficulties of a six-jet Pelton turbine with a horizontal shaft. The most extensive studies on this configuration were published by Erlach [18–20]. In his studies, Erlach and his collaborators conducted model tests to investigate the efficiency potential of two possible designs of six-jet Pelton turbines with horizontal shafts. One design had a conventional spiral-like distributor system, where one branch line parts at a time. This design was turned by 90° towards the vertical direction to allow for a horizontal turbine shaft. The other design used a novel type of distributor system with axial inflow, where all branch lines part simultaneously. Both designs were also equipped with a new type of casing, allowing for a better flow discharge. Two main findings were that the novel type of distributor with axial inflow had very low deviation in the turbine efficiencies when single-jet operation was tested and that both turbine designs profited significantly from the new type of casing. Despite the successful model test, Erlach's ideas were not acted upon. A prototype of a six-jet Pelton turbine using a horizontal shaft was not built before 2022[1].

Elaborating on the challenges of the six-jet Pelton turbine with a horizontal shaft, this thesis focuses on the distributor system feeding the flow to such a turbine configuration. Distinctly, each Pelton turbine distributor system has the task of distributing the flow evenly to all injectors. Thereby, the energy losses must not exceed 2 % to 3 % of the available energy computed from the geodetic head and a good flow quality shall be maintained over a wide range of operating conditions [89]. Due to this, a conventional Pelton turbine distributor system is constructed from welded steel sheets with gradually tapering cross-sections and special branch segments. Usually, each conventional distributor system is a unique prototype made to fit one particular power plant precisely. Also, within the distributor system, each of the branches is unique. Therefore, effort is required to provide the same flow rate to every injector over a wide range of operating scenarios, also dramatically increasing manufacturing complexity and costs.

It was shown by Peron et al. [70] and Staubli et al. [101, 103] that a bad quality flow upstream of the injectors in the distributor system leads to ill-formed jets. These, in turn, cause an unfavourable momentum transfer from the jets to the buckets, leading to excessive splash water in the casing and, ultimately, a reduction in the turbine efficiency. Poor flow quality in Pelton turbine distributor systems is commonly associated with secondary flows and high turbulence. Semlitsch proved that disturbances upstream [89] or in [90] a conventional distributor system[2] propagate through the distributor system and the injectors and deform the jets unevenly. Thus, the efficiencies of a Pelton turbine fed by a conventional distributor system vary significantly as systematic tests of single-jet operation unfolded. Typically, the last jet produces the highest efficiency, see e.g. Erlach [19].

[1] In this year, in two refurbishment projects, Gerlos I [57, 58] and Vermuntwerk [77], six-jet Pelton turbines with horizontal shaft were installed for the first time. In both projects, a conventional Pelton turbine distributor system, turned by 90° towards the vertical direction to allow for the horizontal shaft, was employed together with a novel type of casing.

[2] E.g. during part-load operation when multiple injectors are out of operation or by baffle blades that are primarily aligned for full-load conditions.

The central question in the research of Pelton turbine distributor systems, therefore, is: *"How do Pelton turbine distributor systems need to be designed to allow for similar flow conditions in all branches and injectors and maintain a high-quality water jet at all relevant operating conditions?"*

One possible solution to allow for similar flow conditions in all branches and injectors and overcome the issue of varying jet quality was proposed by Erlach and Staubli [21] in 2007 and included the study series mentioned above [18–20]. This novel type of distributor with axial inflow, where all branch lines part at the same time, appeared to be promising[3], but a detailed, isolated analysis of the flow in such a system with axial inflow was never conducted before.

Consequently, this thesis investigates the flow in Pelton turbine distributor systems, which allow axial inflow and outflow tangential to the runner. First, criteria are developed to unbiasedly compare different types of Pelton turbine distributor systems with axial inflow. Then, alternative designs are elaborated on, and the effect of geometric changes of the main design parameters on the flow is studied. A further objective is understanding the flow phenomena in these distributor systems and finding a combination of geometric parameters favourable for high-quality flow. The method chosen for this thesis is numerical flow simulations, which allow for testing a wide variety of possible designs and parameter combinations before even starting with expensive laboratory testing. Furthermore, the distributor system is seen as an isolated component because any integration into the whole turbine system would increase the number of variables and the complexity of the studies to a point where such a study could not be conducted with rational effort. Therefore, the results of this thesis do not account for the flow in the injectors or the free-surface jets.

[3]Another aspect that makes this type of distributor system interesting is the potential to reduce manufacturing costs as all branch lines are made from identical components.

CHAPTER 2

Literature review

In considering the key aspects of investigating and optimising the flow of a new Pelton turbine distributor system, one has to understand the effects impacting the high efficiency of Pelton turbines. Therefore, using a top-down approach of reviewing Pelton turbine literature, this chapter addresses how the flow phenomena in a Pelton turbine distributor system affect the turbine efficiency and what to pay attention to when studying a new type of distributor system.

2.1 On the efficiency of a Pelton turbine

When studying, building, and deploying a Pelton turbine, the ultimate goal is to maximise its efficiency. Several contributions have proven that the efficiency of a Pelton turbine is highly dependent on the jet quality, necessitating not only numerical and experimental work but also research on past efforts. Their most relevant findings are discussed in this section.

Within the *Jet Improvement for Swiss Pelton Plants* project led by Staubli and Bissel [102], several refurbishment projects of Swiss Pelton turbine power plants were analysed. In this report, the potential to improve the efficiency of a Pelton turbine by modifying the injectors is estimated in the range of 0.4 % to 0.8 %. By the example of hydropower plant (HPP) Fionnay, Peron et al. [70] reported a measured efficiency increase of around 0.4 % in the whole power range. This increase was attributed to the improved jet quality, e.g. less dispersion[1], as a result of modifying the injectors. For the refurbishment project of HPP Rothenbrunnen, Staubli et al. [103] were able to improve the efficiency of the Pelton turbines by 1.4 % by replacing the injectors and modifying the casing. The authors conclude that the efficiency increase correlates with fewer disturbances on the jet surface, less jet dispersion, and a smaller amount of splashing water [103].

[1]In cases with highly dispersed jets, the pressure field is distributed over a wider area, which deviates from the hydraulic optimum and thus hurts the runner efficiency [70].

Further understanding of the correlation of jet quality and turbine efficiency was gained by computational fluid dynamics (CFD) simulations.
Santolin et al. [81] compared the performance of a runner admitted with an ideal, circular jet to that of a runner admitted with a perturbed real jet. In the real jet configuration, the jet was perturbed by the needle wake and secondary flows induced by upstream parts, e.g. penstock and distributor system [81]. Consequently, the simulated differences in efficiency between the runner subject to the ideal jet and real jet amount to 1.9 %.
Gupta et al. [27] investigated the effects of several jet shapes on the performance of the runner and the flow patterns during jet-bucket interaction. One main finding of this research was that a circular-shaped jet exhibits the highest force on the buckets, and thus, the runner admitted by this jet has the highest torque and efficiency.
Jošt et al. [40, 41] obtained a negative correlation between secondary velocity in the jets and turbine efficiency for 1-nozzle operation. They simulated the entire flow path comprised of the final part of the penstock, the conventional distributor system, the injectors and the runner of a six-jet Pelton turbine with a vertical axis. Their simulation strategy was such that the penstock, distributor system, injectors and free-surface jets were simulated in the first step. In the second step, the velocity fields from the jets and the air-water distribution were prescribed as boundary conditions for the runner simulations. The results for single jet operation show that the losses in the distributor system were the highest when the last jet was active. However, in this case, the secondary velocities in the jet were the lowest, and the acquired efficiency was the highest. The monitored spread in turbine efficiency between the best and the worst active jet was almost 0.4 %.
Petley et al. [71] aimed at improving the performance of a Pelton turbine by changing the geometry of the needle and the nozzle in the injector[2]. Their computations estimated the difference in turbine efficiency between a case where the buckets were admitted with an ideal jet and a case with a real jet from their standard injector with 1.7 %. With their optimised injector geometry, this difference shrunk to remarkably low 0.2 %, implying an efficiency increase of 1.5 %. The experimental tests resulted in a similar efficiency increase of around 1.4 % in efficiency between their standard and their optimised injector. Petley et al. [71] attributed the efficiency increase to a more uniform jet velocity profile with their optimised injector[3].

Generally, an ill-formed jet not only lowers the efficiency of the Pelton turbine but also affects the flow pattern in the buckets and the time the jet enters the buckets. It further causes uneven forces on the buckets, the relative amplitudes of pressure pulsations of the turbine increase significantly, the axial forces on and axial oscillations of the runner increase, and the buckets become more susceptible to vibration, cavitation and fatigue damage. The latter three raise maintenance costs and lower the lifetime of the runner. A high overall noise level of the turbine can also be associated with ill-formed jets [70]. Deng et al. [14] showed that the jet

[2]Within this thesis, the entire assembly of injector pipe, nozzle, needle, needle body (= torpedo), torpedo support, ribs is called the injector. The term nozzle denotes the contracting part of the injector. The zone of the nozzle with the smallest diameter is called the throat.

[3]The optimised injector has steeper needle and nozzle angles. The authors emphasise that the steeper angles might cause more secondary velocity in the flow.

position also massively impacts the jet-bucket interaction. The authors found that even a slight radial deviation of the jet, which corresponds to a different effective pitch cycle diameter, increased the axial force on the runner by a factor of two and decreased the tangential force on the runner, which is directly associated with the turbine efficiency, by roughly 0.25 %. An axial deviation of the jet axis towards either side of the bucket would eventually increase the axial forces by a factor of four and decrease the tangential force and thus the turbine efficiency by around 0.40 %.

Following the examples presented above, this section closes with the statement:

"Bad jet quality = low turbine efficiency"

2.2 On the quality of a Pelton turbine jet

This section aims to understand a good jet and what phenomena might lead to a bad jet. Thereby, this section presents quantities commonly used to describe the quality of a jet.

Among the most relevant parameters to describe the quality of a jet are:

- The jet dispersion - how much does the jet diameter increase along its path?
- The jet deviation - how much does the jet centreline differ from the injector axis?
- The jet surface deformation - how much does the jet surface differ from an axisymmetric shape?

The jet dispersion is typically expressed by a dispersion angle α. Zhang and Casey [117, 118] reported typical dispersion angles of 0.2° to 0.5°. Unterberger et al. [110] measured dispersion angles between 0.25° for small nozzle openings and thus low volumetric flow rates and 1.20° for the maximum nozzle opening and high volumetric flow rates. Jet dispersion is mainly caused by secondary flows upstream of the nozzle [101, 102]. It is thus influenced by bends, bifurcations, and any other object in the flow, such as the mechanism for adjusting the needles. It is further influenced by the nozzle and needle geometry and the head. For example, Unterberger et al. [110] observed that steeper nozzle angles lead to higher dispersion angles but decreased energy losses in the injector. Two effects should be considered when discussing jet dispersion. One effect is the jet expansion of the jet cross-sectional area due to decreased jet velocity. The other effect is the entrainment of air bubbles on the surface of the jet. Zhang and Casey [117, 118] demonstrated by analytical considerations that the first effect contributes only slightly to the energy loss according to dispersion. Peron et al. [70] deducted from snapshots of jets operating at different heads that the second effect heavily depends on the head. Jets operated at high heads show an increased thickness of the mixed air-water flow zone, which forms a dispersed phase directly impacting and decreasing the turbine efficiency.

Many publications, e.g. [70, 101, 117], identify the upstream flow structures in the distributor system and the injectors as the root cause for jet deviation. Semlitsch [89] proved that the mass flow rate imbalance across the nozzle sides and the total pressure distribution upstream of the nozzle also play an essential role. The mass flow rates and, thus, the flow velocities on the outside of the injector (with respect to the last bend) are higher than those on the inside. This is called mass flow rate imbalance. Also, the static pressure on the outside of the injector (with respect to the last bend) is higher than that on the inside. Thus, the total pressure in the injector is as well higher on the outside than on the inside. When the balance of momentum is applied to the jet, the only forces acting on the jet are those at the nozzle exit and at the tip of the needle[4]. Because the total pressure in the nozzle is not uniform, the flow momentum over the jet axis is not balanced, deviating the centreline of the water jet of the injector axis towards the inside of the last bend. At the same time, secondary flows induced by upstream bends or the ribs holding the needle are present. These secondary velocities induce a radial flow momentum, which can counteract the effect of the mass flow rate imbalance. Depending on the strength of the mass flow rate imbalance and the strength of the secondary flow, either effect can dominate. Experience shows that the jet is typically deviated towards the inner side of the upstream bend, indicating that the effect originating from the mass flow rate imbalance is more pronounced than the effect of the secondary flows[5]. Semlitsch [89] reported numbers for the deviation angle between 0.17° to 0.32°, a seemingly low figure. However, referring to Deng et al. [14] as discussed in Section 2.1, even such minor deviations significantly impact the performance of the turbine.

In a systematic comparison of the jet envelopes produced by an injector with a straight inlet to those produced by an injector with a 90° elbow bend upstream, Fiereder et al. [24] found that secondary flows due to the inlet elbow generated an asymmetry in the jet profile which developed to a distinct bulge (nose). Riemann [75] explained that this bulge is always located at the inside of the injector with respect to the last bend and increases as the jet travels away from the nozzle opening. This type of deformation, which was also observed in [12, 70, 89, 90, 117] is a primary example of jet surface deformation exemplifying the difference between jet dispersion (which also deforms the jet surface to some extent) and jet surface deformation, which means deformations on a larger scale. Similar to any other large-scale jet surface deformation, such a nose in the jet envelope alters the jet profile from the ideal circular form. This alteration of how much the jet cross-section differs from a circle can be described by a circularity or out-of-roundness coefficient. Staubli and Bissel [102] defined this out-of-roundness coefficient as the difference between the maximum and the minimum diameter of the water jet at a given cross-section over the mean diameter at this cross-section.

[4]Hereby, it is assumed that the jet expands into free ambient conditions.

[5]The effect of mass flow rate imbalance is highly dependent on the interior geometry of the injector, the number of ribs that support the needle adjusting mechanism and the upstream flow from the branch lines and the bends. These features also affect the production of secondary flows, though, and it has to be analysed for each combination of distributor system and injector individually, which effect dominates.

Semlitsch [89] suggested accounting for general, non-elliptic or axisymmetric jet shapes by using the difference between the maximum and the minimum radius of the water jet over the theoretical radius. Staubli and Bissel [102] reported out-of-roundness coefficients for a straight pipe and an injector with internal servomotor around 4 % to 5 %, depending on the head. When a 90° pipe bend or a rod in the inlet pipe upstream of the injector was considered, the values mentioned above more than doubled as a direct result of the secondary flow induced by the upstream components. For a conventional distributor system, Semlitsch [89] computed out-of-roundness coefficients of around 15 % to 20 %, depending on the position of the injector. Those injectors subjected to the highest secondary velocity magnitudes showed the highest values of the out-of-roundness coefficient. Chongji et al. [12] simulated the flow in a Pelton turbine injector attached to a 120° elbow pipe and calculated out-of-roundness coefficients of around 5 % for a medium nozzle opening and around 10 % for a large nozzle opening[6]. The authors also plotted patterns of the secondary velocity in the jet, from which a correlation between the jet shape deformation and the secondary flow structures was identified. Further, the secondary flow structures were associated with the upstream elbow and the ribs supporting the needle. All values of the out-of-roundness coefficient presented here were given for a position four throat diameters downstream of the nozzle opening.

Other criteria mentioned by Zhang and Casey [117, 118] are the jet core shift and the jet instability. Zhang and Casey describe the jet core shift as the shift of the centre of the jet, which is identified by the wake of the needle, from the original axis of the needle [117]. The jet core shift appears due to transversal flow in the jet, which again results from secondary flow induced by the upstream internals of the injector and by bends and branches. The jet instability corresponds to fluctuations in the highly dynamic jet surface.

The quality of the jet is further affected by the axial velocity distribution in the jet, as was suggested by Petley et al. [71] and discussed in Section 2.1. Khan and Kumar [43] express the velocity distribution in the jet by a jet flow uniformity index.

The overall deformation of a jet is a superposition of the effects discussed in this section. Thus, a jet with a highly-disturbed surface has most likely a significant jet deviation and might be unstable. However, one common cause could be identified for all of these effects: strong secondary flows. Therefore, from the criteria to quantify the jet quality, it is possible to conclude:

$$\boxed{\text{"High secondary flow = Bad jet quality"}}$$

[6] Chongji et al. [12] did not calculate the out-of-roundness coefficients explicitly but gave data for the maximum and minimum diameters in two perpendicular coordinate directions from which the out-of-roundness coefficients stated in this section were derived.

2.3 On the flow in a Pelton turbine distributor system

The quality of a jet is highly influenced by secondary flow induced upstream of the injectors by the distributor system, bends and branches, bifurcations, and in the injectors by the needle regulating parts such as the torpedo, the rod or the ribs. Therefore, this section focuses on these parts and describes the mechanisms creating losses and secondary flow structures, especially in the distributor system.

Sick et al. [93] investigated the flow in the distributor system and the injectors of a six-jet vertical Pelton turbine at high Reynolds numbers, $\mathcal{O}(10^6)$. This uncovered that there are two types of losses in a distributor system. First, there are the energy losses in the distributor itself related to pipe friction, change of direction, and parting of the flow. Second, losses occur during the jet-bucket interaction as a direct result of the secondary flow structures in the distributor and the injectors that adversely influence jet formation. Parkinson et al. [68] concluded that energy losses in the junction pipe (branch line) and injectors are three times higher than in the main pipe of a distributor system. The research emphasised that flow patterns present at the inlet of the injectors were convected through the injectors into the jet and directly influenced the behaviour of the runner, even if the ratio of secondary flow kinetic energy related to axial kinetic energy was very low.

Different definitions are used in the literature to elaborate on the energy losses in the distributor system; thus, the individual results are hard to compare unbiasedly. However, some general trends still emerge. For example, plausible numbers for the energy losses in the distributor system and the injector are around 2 % to 3 % [80, 89]. The majority of these energy losses can be attributed to the injector. Fan et al. [22] reported that more than 90 % of the head losses came from the injector. Zeng et al. [116] estimated the head losses in the distributor system between an upstream reference station and a probe position upstream of the injectors to 0.2 %. Yilin et al. [115] achieved a similar result. Lei et al. [55] computed the head losses in the injectors (including the contraction in the nozzle) to be two orders of magnitude higher than the losses attributed to the bifurcations. While the losses in the injector, especially in the contracting nozzle section, are substantial, Patel et al. [69], Mack et al. [56] or Sandmaier et al. [80] proved the potential of careful changes in the distributor geometry to reduce distributor losses significantly.

The following observations are notable regarding the losses due to secondary flows. Peron et al. [70] witnessed in a refurbishment project of HPP Bordogna that the vortices induced by several upstream bends and by the servomotor shaft were convected with the flow and resulted in severe deformation of the jet surfaces. Staubli et al. [101] computed the ratio of secondary velocity to jet axial velocity of a two-jet horizontal Pelton turbine to around 3 %, Zeng et al. [116] found the magnitude of secondary velocity in the jet of a four-jet distributor configuration to be about 2 % of the main flow and Patel et al. [69] estimated the kinetic energy of the secondary flow at the injector inlets of a six-jet vertical Pelton turbine to be between

10 % to 100 % of the turbulent kinetic energy of the flow, where the lower values accounted for an improved distributor design. For comparison, Hahn et al. [28] analysed the secondary flow patterns in a jet of a single injector with straight, undisturbed inflow and acquired secondary velocity magnitudes of around 2.5 % of the theoretical jet velocity in the wake region of the ribs and less than 1.0 % of the theoretical jet velocity in those areas of the jet less affected by the wake. Han et al. [32], with their simulations of a distributor system for a six-jet vertical Pelton turbine, were able to correlate the jet surface deformation observed at the sixth injector to the Dean vortices created in the last bend of the distributor main line upstream of the injector. In this case, as indicated by Parkinson et al. [68], the vortices were convected with the flow and deformed the jet in multiple directions.

To gain a deeper understanding of the effect of secondary flows on the jet formation, instead of the complex case of a distributor system, many researchers resorted to the generic case of a 90° pipe bend upstream the injector, e.g. [24, 75, 102, 117]. This approach allowed for an isolated analysis of the effects such bends have on the jet formation and served as the artificial case closest to a real-world distributor system. In 90° pipe bends, there is an inward pressure gradient due to the centrifugal forces induced by the turning of the flow. In the boundary layers at the wall, where the centrifugal forces are less due to the lower velocity, the inward pressure gradient forces the flow along the wall towards the inner part of the bend. For continuity to be fulfilled, the flow has to move towards the outside of the bend in the centre of the pipe. Thus, a pair of counter-rotating Dean vortices is induced. These vortices are convected through the injector and, while being superimposed by the vortices generated due to the ribs in the injector, stay visible as secondary velocities in the jet, e.g. [12, 101, 117].

Practically, the same mechanism was reported for the flow in distributor systems. Zeng et al. [116] related the deformations in the jet surface to the Dean vortices and other secondary flow induced by the elbow upstream of the injectors and by the support ribs in injectors. Han et al. [32] observed secondary flow created in the distributor and transiting into the bifurcations, injectors and then the jet, which caused deviation from the ideal jet shape. Especially in the bifurcations of a six-jet distributor system, the secondary flow phenomena (Dean vortices) in and downstream of the bifurcations appeared identical to those in a 90° pipe bend. They explicitly said the flow pattern was similar to classical bend pipe flow. Fan et al. [22] showed that Dean vortices appear already in the only slightly curved main pipe of a six-jet Pelton turbine distributor system. Investigating the transient flow in a Pelton turbine during startup, Sun et al. [106] found that strong vortices were induced in the bifurcation pipe of the conventional distributor system. These vortices, influenced by upstream inflow and downstream reverse flow during the startup process, occupied a significant area of the flow passage.

From the analysis of the literature most relevant for understanding the flow in a Pelton turbine distributor system, it can be concluded that:

$\boxed{\text{"Good distributor system = Limited secondary flow and low energy losses"}}$

2.4 On the different distributor system concepts

While a distributor system with large curvature radius and pipe diameters would allow for limited secondary flows and low energy losses, the cost of manufacturing the distributor and the construction of the powerhouse might be untenable. Hence, a compact distributor with small curvature radius and pipe diameters would be less heavy and expensive but might not match the guaranteed performance. The aforementioned is one general compromise for any distributor system, but apart from that, unfortunately, next to no information is published or publicly available about how a good Pelton turbine distributor has to be designed in order to accomplish the goals of low energy losses and low secondary flows at the same time. However, the literature provides some examples of flow-calming devices primarily applied in refurbishment projects and some remarkable concepts of distributor systems themselves.

In hydropower plant refurbishment projects, due to constraints in the power plant layout, it is often not possible to alter the geometry of the distributor system as a whole. Therefore, the most common solution to address problems with secondary flow is to install guide vanes or a flow straightener directly upstream of the injector or as an integral part of the injector. Peron et al. [70] showed for HPP Bordogna that guide vanes placed as a form of extension to the ribs holding the needle rod reduced the secondary flows significantly, improving the jet shape. A similar approach was presented by Mack et al. [56] for modernising HPP Lünersee in Austria. At this power plant, a flow straightener was installed in the first part of the injector. The reduction of secondary flows was so effective that efficiency gains of up to 0.60 % could be achieved for small and medium flow rates. Only at high flow rates do the increased friction losses due to the flow straightener outweigh the reduced secondary flow improvements.

Concerning Pelton turbine distributor systems, the most common concept for multi-jet turbines with four to six injectors is sketched in part a) of Figure 2.1. This conventional Pelton turbine distributor system consists of the distributor main line and the bifurcation parts, where at each bifurcation, one branch line deviates from the main line, leading to the injector. As mentioned in Chapter 1, the conventional distributor system is constructed from welded steel sheets with gradually tapering cross-sections and unique branch segments. It is thus complex and costly to manufacture and often requires precautionary measures when transported from the manufacturer to the power plant site. An exciting alternative with likely similar flow behaviour to a conventional distributor was employed in HPP Silz in Austria, where the turbine is fed by two semi-distributor systems as shown in part b) of Figure 2.1.

From a fluidic point of view, several authors reported that the energy losses and the amount of secondary velocity upstream of the injectors in a conventional distributor vary significantly for the different injectors [68, 69, 80, 93]. Semlitsch [89, 90] also found that the mass flow rate imbalance between the two sides of the injectors varies for every injector up to 2 %. The same author pointed out that under oper-

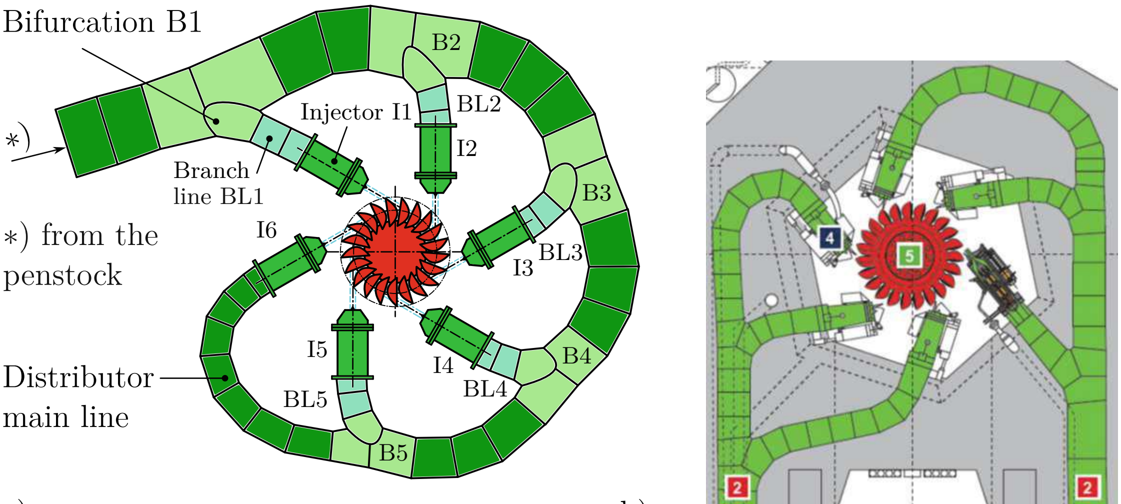

a) b)

Figure 2.1: Two concepts of a Pelton turbine distributor system for a six-jet Pelton turbine with vertical shaft. Part a) recreated and modified from [30], part b) modified from [109].

ating conditions where one or more injectors were shut off entirely, the secondary velocities upstream of the injector lay between 7 % of the primary flow velocity for the best injector, which was the first injector, and 18 % for the worst injector. In model tests of a conventional distributor system, Erlach [20] found that, as a consequence of the flow characteristics of a conventional distributor, the turbine efficiencies varied up to about 2 % when the turbine was operated in single-jet mode.

This characteristic behaviour of Pelton turbines fed by conventional Pelton turbine distributor systems underlines significant room for improvement. Therefore, the central question regarding Pelton distributor systems remains[7] as stated in Chapter 1. The most far-reaching attempt to overcome the known issues of conventional Pelton turbine distributor systems was made by Erlach and his research partners. Erlach and Staubli patented a novel type of Pelton turbine distributor system [21] that, in theory, should allow for the same inflow conditions to every injector, thus the same jets and a more uniform energy transfer from the individual jets to the buckets. This system was envisioned such that all six branch lines separate from the central distributor pipe[8] at the same time. The central distributor pipe was aligned in the axial direction with the runner shaft instead of perpendicular to the shaft, as known from conventional distributor systems. Further, all six branch lines were claimed to be identical, allowing for possible standardisation in the manufacturing process. This standardisation could reduce costs and make such a system especially suitable for small hydropower plants, where investment costs are a decisive factor in project planning. Extensive model

[7] *"How do Pelton turbine distributor systems need to be designed to allow for similar flow conditions in all branches and injectors and maintain a high-quality water jet at all relevant operating conditions?"*

[8] In this section, when citing from the patent of Erlach and Staubli [21], the terms of the patent are translated as close to their German meaning as possible. Further in the thesis, especially in Chapter 6, a terminology defined within this thesis will be used.

tests were conducted [18–20], which showed that the turbine efficiencies varied much less in single-jet operating conditions when the turbine was fed by such a novel type of Pelton turbine distributor system. Notably, in these model tests, a novel casing approach was also investigated at the same time, so the effects of the distributor system could not be isolated entirely. Apart from these model tests, detailed studies of this novel type of distributor system were never conducted. Therefore, at this stage of the research, the exact effects occurring in the novel type of distributor system remain uninvestigated, and it has not been explored yet if the designs published by Erlach et al. [18–21] are the most promising when it comes to distributor systems with axial inflow and branch lines departing at the same time.

Consequently, this section cannot close with definite statements as in the previous sections, as the question remains:

$$\boxed{\text{"New concept} \overset{?}{=} \text{Good distributor system"}}$$

2.5 Research questions

In the next steps of investigating such a new concept of Pelton turbine distributor system, in order to allow for an orderly, well-projected and unbiased analysis, the following main questions guide the research of this thesis:

1. What potential Pelton turbine distributor system designs allow axial inflow and outflow tangential to the runner?
2. Is a steady-state simulation approach feasible to accurately predict the flow in such a Pelton turbine distributor system?
3. How does the operating regime of such a Pelton turbine distributor system in the context of small hydropower plants look like, and what is a realistic design case?
4. How does the flow behave in a Pelton turbine distributor system with axial inflow, and what components significantly influence the flow quality?
5. Which combination of geometric parameters is favourable?

The answers to these questions will be outlined in Chapter 7.

CHAPTER 3

Flow quality criteria

The first step in answering the proposed research questions is to assess whether the flow in a given Pelton turbine distributor system behaves favourably or not. Therefore, this chapter is dedicated to specifying criteria to rate the quality of a flow in such a Pelton turbine distributor system. These flow quality criteria concentrate on quantifying the losses and the secondary flow in the distributor system and were either taken from reference books and papers or derived from basic fluid mechanics equations. The total pressure drop, Section 3.2.2, the losses, Section 3.3, and the secondary velocity ratio, Section 3.4.1, were applied similarly in prior publications of mine, including *On the numerical assessment of flow losses and secondary flows in Pelton turbine manifolds* [31] and *Numerical Investigation of Pelton Turbine Distributors Systems with Axial Inflow* [30].

3.1 Averaging of field variables

Instead of interpreting the local flow fields in non-uniform flows, it is often desired to compute an average value over a station of interest to quantify the state of a variable. This section, therefore, addresses how to define an appropriate average value for a flow property in a non-uniform incompressible flow with constant density.

The two most common definitions of an average value[1] are:

- The area average, where a quantity is integrated over the surface area A_i of a station of interest. No weighting is applied. It can be derived from the conservation of mass, where, e.g. the area averaged velocity u^A is defined as

$$u^A = \frac{\int_{A_i} \vec{u} \cdot \mathrm{d}\vec{A}}{\int_{A_i} \mathrm{d}\vec{A}} = \frac{1}{A_i} \cdot \int\limits_{A_i} \vec{u} \cdot \mathrm{d}\vec{A}\,. \tag{3.1}$$

[1]For a comprehensive derivation and discussion, it shall be referred to Greitzer et al. [26]. There, another form of average is introduced, namely the mixed out average. For example, a mixed out average stagnation pressure is defined as the stagnation pressure that would exist after full mixing at constant area [26].

- The mass average, where in the integration over the surface area A_i of a station of interest, each area element is weighted by its associated mass flow per unit area. It can be derived from the balance of momentum and, in the case of the mass averaged velocity u^M, is defined as

$$u^M = \frac{\int_{A_i} (\rho\vec{u})\,\vec{u}\cdot \mathrm{d}\vec{A}}{\int_{A_i} \rho\vec{u}\cdot \mathrm{d}\vec{A}} = \frac{1}{\dot{m}_i} \cdot \int\limits_{A_i} (\rho\vec{u})\,\vec{u}\cdot \mathrm{d}\vec{A}\,. \tag{3.2}$$

Usually, the two average values are different. In mass averaging, the parts in the stream with high velocities are more heavily weighted than those parts with low velocities [26, 111]. In area averaging, all parts are weighted the same. Therefore, the mass average value is generally higher than the area average value[2], $u^M > u^A$. Assuming inviscid, constant density flow in a straight pipe of constant area with no external forces acting, the balance of momentum between the 'inlet' and the 'outlet' (positioned such that all flow quantities have become uniform) of a control volume denotes as

$$\int\limits_{A_i} (\rho\vec{u})\,\vec{u}\cdot \mathrm{d}\vec{A} + \int\limits_{A_i} p\mathrm{d}\vec{A} = \dot{m}u^? + p^? A\,. \tag{3.3}$$

Comparing the momentum terms on both sides of Equation (3.3), gives the definition of the mass average as presented in Equation (3.2) and comparing the pressure terms closely resembles the definition of the area average as presented in Equation (3.1)

$$\dot{m}u^M = \int\limits_{A_i} (\rho\vec{u})\,\vec{u}\cdot \mathrm{d}\vec{A} \qquad \text{and} \qquad p^A A = \int\limits_{A_i} p\mathrm{d}\vec{A} \tag{3.4}$$

Therefore, within this thesis, if not specified otherwise, all velocity-related quantities (primary and secondary flow velocity, total pressure and dynamic pressure, turbulent kinetic energy) were mass averaged, and the static pressure was area averaged. The only exceptions to these rules were the intensity of secondary flow, described in Section 3.4.2, and the turbulence intensity, described in Section 3.5.2. Both quantities were area averaged to allow for a direct comparison to the experimental data from Sudo et al. [104]. For the sake of easier to read symbols, the superscripts 'A' and 'M' are dropped again.

3.2 Pressure

3.2.1 Pressure coefficient

The pressure coefficient C_p is one standard method to express the pressure in a flow domain in non-dimensional form, e.g. the pressure distribution along the walls in a pipe bend [104], or the pressure distribution at the surface of an aerofoil [87]. Thereby, the pressure at the location of interest is related to the pressure at a reference location and divided by the dynamic pressure at this reference location

[2] Greitzer proves this statement by the example of averaging the stagnation pressure [26].

$$C_p = \frac{p - p_{ref}}{p_{dyn,ref}} = \frac{2\,(p - p_{ref})}{\rho \vec{u}_{ref}^2}\,. \tag{3.5}$$

In conditions with an adverse pressure gradient in streamwise direction, $\frac{\mathrm{d}p}{\mathrm{d}s} > 0$, e.g. at the outer wall of the first segment of a 90° bend, the flow is decelerated and C_p increases, whereas in conditions with a favourable pressure gradient, $\frac{\mathrm{d}p}{\mathrm{d}s} < 0$, e.g. at the inner wall of the first segment of such a bend, the flow is accelerated and C_p decreases (see also Figure 5.2).
One can show that under the assumption of steady-state, incompressible flow [2], for a stagnation point, where the flow velocity becomes zero, the pressure coefficient equals 1. Following a streamline from the reference station to a stagnation point (index 0), Bernoulli's equation gives

$$p_{ref} + \frac{\rho \vec{u}_{ref}^2}{2} = p_0 \tag{3.6}$$

which, inserted into Equation (3.5), results in

$$C_{p,0} = \frac{2\,(p_0 - p_{ref})}{\rho \vec{u}_{ref}^2} = \frac{\frac{\rho \vec{u}_{ref}^2}{2}}{\frac{\rho \vec{u}_{ref}^2}{2}} = 1\,. \tag{3.7}$$

3.2.2 Total pressure drop

In many industries, e.g. hydraulic machinery and piping systems, a commonly used quantity to rate the losses and the 'quality' of the flow is the total pressure drop[3] between two stations of interest, e.g. the inlet and the outlet, $\Delta p_t = p_{t,inlet} - p_{t,outlet}$. To allow for a better comparison of different situations, in hydraulic machinery applications, the geodetic head H, or a pressure $p = \rho g H$ or a velocity $u = \sqrt{2gH}$ derived from the head H are often used as reference values. If, under the assumption of $p_{t,inlet} \sim \rho g H$, the total pressure drop is normalised by the reference value acquired from the geodetic head, the following relationship can be derived

$$\frac{\Delta p_t}{p_{t,inlet}} = \frac{p_{t,inlet} - p_{t,outlet}}{p_{t,inlet}} = 1 - \frac{p_{t,outlet}}{p_{t,inlet}} = 1 - \frac{Q \cdot p_{t,outlet}}{Q \cdot p_{t,inlet}} = 1 - \frac{P_{outlet}}{P_{inlet}} = 1 - \eta\,. \tag{3.8}$$

where, if the fraction is expanded by the volumetric flow rate Q, one ends up with the ratio of the hydraulic powers at the inlet, P_{inlet} and the outlet, P_{outlet}, which equals the definition of an efficiency η. So, in the case of a pipe system, when using the assumption $p_{t,inlet} \sim \rho g H$, the efficiency can be expressed as

$$\eta_{\text{pipe}} = \frac{p_{t,outlet}}{p_{t,inlet}} = \frac{p_{t,outlet}}{\rho g H}\,. \tag{3.9}$$

This way of defining a non-dimensionalised loss quantity has a major disadvantage, namely, that in pipe systems[4], the losses and thus the pressure at the outlet, in general, scale with the square of the flow velocity and not with the pressure level at

[3]The terms total pressure drop and total pressure loss are largely used synonymously.
[4]Here and during the rest of this thesis, the flow is always assumed to be incompressible.

the inlet (e.g. the geodetic head). The flow velocity in such a situation is typically in the low single-digit range[5] and also independent of the pressure level at the inlet. However, a situation might occur where two pipe systems have the same efficiency η_{pipe} but at a different pressure level. Then, the pipe system with the lower pressure level would have a lower pressure drop and should be rated as the pipe system with the better flow quality. Unfortunately, if the efficiency were used, this result would be hidden. Therefore, the presented approach is unsuitable for an unbiased method to assess the flow quality in a Pelton turbine distributor system.

3.3 Losses

3.3.1 Power loss coefficient - Classical approach

Following the conclusions from the previous chapter, choosing a reference velocity representative of the flow in the pipe system is a more suitable approach for calculating and comparing total pressure losses in a non-dimensionalised form. Then, analogously to Equation (3.5), the total pressure loss coefficient[6] $\zeta_{p,t}$ can be defined as

$$\zeta_{p,t} = 2 \cdot \frac{p_{t,inlet} - p_{t,outlet}}{\rho \vec{u}_{ref}^2}, \tag{3.10}$$

where the difference in total pressure $p_t = p + 0.5\,\rho\vec{u}^2$ between two stations of interest, most often inlet and outlet of a domain of interest, is non-dimensionalised by the dynamic pressure $p_{dyn} = p_t - p = 0.5\,\rho\vec{u}^2$ computed from the average velocity magnitude at one of these stations or a suitable reference station.
Alternatively, a total pressure loss coefficient $\zeta_{p,ts}$ is employed by Shiraishi et al. [92]

$$\zeta_{p,ts} = 2 \cdot \frac{p_{t,inlet} - p_{outlet}}{\rho \vec{u}_{ref}^2}, \tag{3.11}$$

by subtracting the static pressure at a station of interest, e.g. the outlet, from the total pressure of an upstream station of interest, e.g. the inlet, and dividing it by the dynamic pressure computed from a reference velocity. This definition follows the experimental configuration for determining loss coefficients in pipe bends presented in Idelchik [38], which was set up such that the pressure losses at the exit of the bend into the atmosphere were included. An equivalent statement regarding the accounting of pressure losses at the exit of pipes is made by Bohl and Elmendorf [6].

Both definitions, Equations (3.10) and (3.11), are commonly used for loss accounting in pipe systems. However, for a Pelton turbine distributor system with one inlet and n outlets, a more convenient way to calculate a loss coefficient is to compute the fluxes of total pressure and dynamic pressure and account for them in the same way as in Equation (3.10).

[5] A list of typical flow velocities for common hydropower applications is presented in Table 6.5.

[6] An alternative name for the total pressure loss coefficient, found primarily in the literature related to piping systems, e.g. [37, 38], is (total) resistance coefficient. For further reference on the definition of the total pressure loss coefficient, refer to [6, 16, 38].

When the total pressure at station i is integrated over the area A_i of that station, the flux of total pressure through this station is defined as

$$P_{mTE,i} = \int\limits_{A_i} \left(p + \frac{\rho}{2}\vec{u}^2\right) \vec{u} \cdot \mathrm{d}\vec{A}\,. \tag{3.12}$$

The flux of total pressure can be interpreted as the power of mechanical total energy[7], where $\vec{u} = (u, v, w)^T$ is the flow velocity vector written in a Cartesian (x, y, z)-coordinate system. The magnitude of $\vec{u}$ becomes $||\vec{u}|| = \sqrt{(u^2 + v^2 + w^2)}$.

Analogously, the dynamic pressure at station i can be integrated over the area A_i of that station to compute the corresponding flux

$$P_{KE,i} = \int\limits_{A_i} \left(\frac{\rho}{2}\vec{u}^2\right) \vec{u} \cdot \mathrm{d}\vec{A}\,, \tag{3.13}$$

which can be interpreted as the power of kinetic energy[8].

Combining Equations (3.12) and (3.13) according to the concept of Equation (3.10), one arrives at the definition of the power loss coefficient between a reference station ref and station i for an arbitrary pipe system[9]

$$\zeta_{PmTE}\big|_{ref}^{i} = \frac{P_{mTE,ref} - P_{mTE,i}}{P_{KE,ref}} = \frac{\int_{A_{ref}} \left(p + \frac{\rho}{2}\vec{u}^2\right) \vec{u} \cdot \mathrm{d}\vec{A} - \int_{A_i} \left(p + \frac{\rho}{2}\vec{u}^2\right) \vec{u} \cdot \mathrm{d}\vec{A}}{\int_{A_{ref}} \left(\frac{\rho}{2}\vec{u}^2\right) \vec{u} \cdot \mathrm{d}\vec{A}}\,. \tag{3.14}$$

This definition is independent of the pressure level (head) and allows for an unbiased comparison of any pipe system. Therefore, different Pelton turbine distributor systems can be compared, even if projected for different heads.

When applied to evaluate the loss coefficient of a simple pipe (without partitions of the stream), Equation (3.14) can be traced back to the basic definition of Equation (3.10). Assuming a pipe with a 90° bend similar to that of Shiraishi et al. [92] (see Section 5.2), where the losses shall be computed between two stations A (far upstream the bend) and Z (far downstream the bend), the power loss coefficient becomes

$$\zeta_{PmTE}\big|_{A}^{Z} = \frac{P_{mTE,A} - P_{mTE,Z}}{P_{KE,A}} \overset{(1)}{=} \frac{\int_A \left(p + \frac{\rho}{2}\vec{u}^2\right) \vec{u} \cdot \rho\mathrm{d}\vec{A} - \int_Z \left(p + \frac{\rho}{2}\vec{u}^2\right) \vec{u} \cdot \rho\mathrm{d}\vec{A}}{\int_A \left(\frac{\rho}{2}\vec{u}^2\right) \vec{u} \cdot \rho\mathrm{d}\vec{A}} \overset{(2)}{=}$$

$$= \frac{\frac{\int_A \left(p+\frac{\rho}{2}\vec{u}^2\right)\vec{u}\cdot\rho\mathrm{d}\vec{A}}{\int_A \rho\vec{u}\cdot\mathrm{d}\vec{A}} - \frac{\int_Z \left(p+\frac{\rho}{2}\vec{u}^2\right)\vec{u}\cdot\rho\mathrm{d}\vec{A}}{\int_A \rho\vec{u}\cdot\mathrm{d}\vec{A}}}{\frac{\int_A \left(\frac{\rho}{2}\vec{u}^2\right)\vec{u}\cdot\rho\mathrm{d}\vec{A}}{\int_A \rho\vec{u}\cdot\mathrm{d}\vec{A}}} \overset{(3)}{=} \frac{p_{t,A} - \frac{\int_Z \left(p+\frac{\rho}{2}\vec{u}^2\right)\vec{u}\cdot\rho\mathrm{d}\vec{A}}{\int_Z \rho\vec{u}\cdot\mathrm{d}\vec{A}}}{p_{dyn,A}} \overset{(4)}{=}$$

[7] Hence the symbol P_{mTE}.

[8] Hence the symbol P_{KE}.

[9] For convenience, instead of, e.g. $\zeta_{PmTE}\big|_{1}^{101}$, the more straightforward form $\zeta_{PmTE,1011}$ is used within this thesis, especially in Chapter 6.

$$= \frac{p_{t,A} - p_{t,Z}}{p_{dyn,A}} = \zeta_{pt,AZ}\,. \tag{3.15}$$

In step (1), the fraction is expanded by the constant density ρ. In a single pipe configuration with constant diameter and stations A and Z far upstream and downstream of the bend, the conservation of mass states

$$\int_A \rho\vec{u}\cdot \mathrm{d}\vec{A} = \int_Z \rho\vec{u}\cdot \mathrm{d}\vec{A}\,. \tag{3.16}$$

Therefore expanding the fraction by $1/\dot{m} = 1/\left(\int_A \rho\vec{u}\cdot \mathrm{d}\vec{A}\right)$ in step (2) is justified. Step (3) follows with

$$p_{t,A} = \frac{\int_A \left(p + \frac{\rho}{2}\vec{u}^2\right)\vec{u}\cdot\rho\mathrm{d}\vec{A}}{\int_A \rho\vec{u}\cdot\mathrm{d}\vec{A}} \qquad \text{and} \qquad p_{dyn,A} = \frac{\int_A \left(\frac{\rho}{2}\vec{u}^2\right)\vec{u}\cdot\rho\mathrm{d}\vec{A}}{\int_A \rho\vec{u}\cdot\mathrm{d}\vec{A}}\,, \tag{3.17}$$

where $p_{t,A}$ is the mass average total pressure and $p_{dyn,A}$ is the mass average dynamic pressure in station A. With these intermediate steps, in step (4), the equation is simplified to

$$\frac{p_{t,A} - p_{t,Z}}{p_{dyn,A}}\,, \tag{3.18}$$

which is equivalent to $\zeta_{pt,AZ}$. This derivation proves that in a case without partitions in the stream, both definitions of loss coefficients, $\zeta_{PmTE}|_A^Z$ and $\zeta_{pt,AZ}$ are identical[10].

In [31], a lumped power loss coefficient, denoted by the superscript L, was employed for a conventional Pelton turbine distributor system. Within this example, the lumped power loss coefficient was computed by weighing the individual contributions of every branch line by their respective mass flow rate. It can be demonstrated that such a lumped power loss coefficient is also a dedicated form of the general definition. Starting from this general definition as presented in Equation (3.14), and performing the same steps (1) and (2) that were explained in Equation (3.15), the power loss coefficient for a Pelton turbine distributor system to be evaluated between stations 1 (before the flow is parted) and 100[11] (upstream the injectors of the Pelton turbine distributor system) denotes as

$$\begin{aligned}
\zeta^L_{PmTE}\Big|_1^{100} &= \frac{p_{t,1} - \frac{\int_{A_{100}}\left(p+\frac{\rho}{2}\vec{u}^2\right)\vec{u}\cdot\rho\mathrm{d}\vec{A}}{\int_{A_1}\rho\vec{u}\cdot\mathrm{d}\vec{A}}}{p_{dyn,1}} = \frac{p_{t,1} - \frac{\int_{A_{100}}\left(p+\frac{\rho}{2}\vec{u}^2\right)\vec{u}\cdot\rho\mathrm{d}\vec{A}}{\dot{m}_1}}{p_{dyn,1}} \overset{(1)}{=} \\
&= \frac{p_{t,1} - \frac{\sum_{i=1}^n \int_{A_{10i}}\left(p+\frac{\rho}{2}\vec{u}^2\right)\vec{u}\cdot\rho\mathrm{d}\vec{A}}{\dot{m}_1}}{p_{dyn,1}} \overset{(2)}{=} \frac{p_{t,1} - \frac{\sum_{i=1}^n \dot{m}_{10i}\cdot p_{t,10i}}{\dot{m}_1}}{p_{dyn,1}} = \\
&= \frac{p_{t,1} - \sum_{i=1}^n \frac{\dot{m}_{10i}}{\dot{m}_1}\cdot p_{t,10i}}{p_{dyn,1}}\,.
\end{aligned} \tag{3.19}$$

[10] For the cases of Shiraishi et al. [92], see Section 5.2, the relative differences between the two forms were $\left|1 - \frac{\zeta_{PmTE}|_A^Z}{\zeta_{pt,AZ}}\right| < 2\cdot 10^{-3}$.

[11] The $n = 6$ individual station $101, 102\ldots 106$, one station number $10i$ for every branch line i, together form station 100. Each station $10i$ has its surface area A_{10i}. The total surface area of station 100 thus becomes $A_{100} = \sum_{i=1}^n A_{10i}$.

Here, in step (1), the integration over station 100 is replaced by the sum of the integrals over the $n = 6$ individual stations $101, 102 \ldots 106$

$$\int_{A_{100}} \left(p + \frac{\rho}{2}\vec{u}^2\right) \vec{u} \cdot \rho \mathrm{d}\vec{A} = \sum_{i=1}^{n} \int_{A_{10i}} \left(p + \frac{\rho}{2}\vec{u}^2\right) \vec{u} \cdot \rho \mathrm{d}\vec{A} \,. \tag{3.20}$$

In step (2), the integrals in the sum were exchanged by the corresponding mass average total pressures and the mass flow rates

$$\sum_{i=1}^{n} \int_{A_{10i}} \left(p + \frac{\rho}{2}\vec{u}^2\right) \vec{u} \cdot \rho \mathrm{d}\vec{A} \quad \rightarrow \quad \sum_{i=1}^{n} \dot{m}_{10i} \cdot p_{t,10i} \,. \tag{3.21}$$

In Chapter 6 , the power loss coefficient is evaluated between stations 1 and 100 as

$$\zeta_{PmTE}\big|_1^{100} = \frac{\int_{A_1} \left(p + \frac{\rho}{2}\vec{u}^2\right) \vec{u} \cdot \rho \mathrm{d}\vec{A} - \sum_{i=1}^{n} \int_{A_{10i}} \left(p + \frac{\rho}{2}\vec{u}^2\right) \vec{u} \cdot \rho \mathrm{d}\vec{A}}{\int_{A_1} \left(\frac{\rho}{2}\vec{u}^2\right) \vec{u} \cdot \rho \mathrm{d}\vec{A}} \,. \tag{3.22}$$

In this form, the only term that changes in cases where the number of branch lines would change is the upper limit of the sum.

3.3.2 Dissipation power coefficient - Second law analysis

Instead of computing the losses by balancing the power of mechanical total energy between two stations of interest, the irreversible entropy produced within the system's borders can be integrated over the entire domain of interest to achieve a different loss coefficient. This approach is based on the second law of thermodynamics. It thus trades under the name second law analysis (SLA)[12]. The second law analysis method in its present form was derived rigorously by Kock [50] in 2003 and since then was continuously adapted and improved, e.g. by Kock and Herwig [48, 49] or Herwig et al. [34]. Prominent applications of Kock's form of the SLA method were shown for analysing and optimising conduit components such as bends [84, 85], diffusers and nozzles [83], and external flows [35]. Compact introductions to the most critical aspects of employing the SLA method in the CFD simulation process when analysing hydraulic machinery were presented in [7, 33] for pumps and in [30, 31] for Pelton turbine distributor systems. An extensive review of recent applications of the SLA method in pumps and turbines is given by Zhou et al. [119]. The following paragraph gives an overview of the implementation of the SLA concept in the present study and largely follows Hahn et al. [30].

Analogously to Equation (3.14), a dissipation power coefficient ζ_Φ can be defined as

$$\zeta_\Phi = \frac{P_\Phi}{P_{KE,ref}} = \frac{P_{Turb} + P_{Vis}}{P_{KE,ref}} \tag{3.23}$$

with P_{Turb} and P_{Vis} being the power of turbulent (Turb) and viscous (Vis) dissipation and $P_\Phi = P_{Turb} + P_{Vis}$ the dissipation power. These two terms are computed by the

[12]Another widespread name is entropy production method, e.g. [119].

volume integrals of the corresponding dissipation terms over the domain of interest

$$P_{Turb} = \int\limits_V \Phi_{Turb}\,\mathrm{d}V \qquad \text{and} \qquad P_{Vis} = \int\limits_V \Phi_{Vis}\,\mathrm{d}V\,. \tag{3.24}$$

With Reynolds averaging Section 4.1.2, the viscous (direct) dissipation Φ_{Vis} follows from inserting the time-averaged velocity components $\bar{u}$, $\bar{v}$, $\bar{w}$ into the product of the viscous stress tensor τ_{ij} and velocity gradients $\partial u_i/\partial x_j$

$$\Phi_{Vis} = \bar{\tau}_{ij}\cdot\frac{\partial \bar{u}_i}{\partial x_j} = \mu\cdot\left(\begin{array}{c} 2\cdot\left[\left(\frac{\partial\bar{u}}{\partial x}\right)^2+\left(\frac{\partial\bar{v}}{\partial y}\right)^2+\left(\frac{\partial\bar{w}}{\partial z}\right)^2\right]+ \\ +\left(\frac{\partial\bar{u}}{\partial y}+\frac{\partial\bar{v}}{\partial x}\right)^2+\left(\frac{\partial\bar{v}}{\partial z}+\frac{\partial\bar{w}}{\partial y}\right)^2+\left(\frac{\partial\bar{u}}{\partial z}+\frac{\partial\bar{w}}{\partial x}\right)^2\end{array}\right). \tag{3.25}$$

The turbulent (indirect) dissipation is either computed directly from the turbulent eddy dissipation ε, e.g. when using a variant of the k-ε model (kE) of Launder and Spalding [53], or the turbulent dissipation is computed from the turbulent kinetic energy k, the turbulent eddy frequency ω and the turbulence model coefficient $\beta^* = 0.09$, when using ω-based turbulence models, e.g. the k-ω Shear Stress Transport (SST) model of Menter [61]

$$\Phi_{Turb} = \rho\cdot\varepsilon \overset{(1)}{=} \beta^*\rho\omega k\,. \tag{3.26}$$

Here, in step (1), the relation $\varepsilon = \beta^*\omega k$ is used [23, 83, 113]. Because all of the turbulence variables mentioned above rely on some modelling assumptions of the turbulence model and the specified boundary conditions, this approach induces an additional uncertainty to the method[13].

Alternatively, instead of integrating over a volume V, the integration can be split such that, at first, the direct dissipation Φ_{Vis} and the indirect dissipation Φ_{Turb} are computed for every cross-section

$$\hat{\Phi}_{Turb} = \int\limits_A \Phi_{Turb}\,\mathrm{d}A \qquad \text{and} \qquad \hat{\Phi}_{Vis} = \int\limits_A \Phi_{Vis}\,\mathrm{d}A\,. \tag{3.27}$$

Then, at second, these cross-section integral values (indicated by the ˆ symbol), which equate to a dissipation per unit length, can be integrated along the streamwise direction,

$$P_{Turb} = \int\limits_s \hat{\Phi}_{Turb}\,\mathrm{d}s \qquad \text{and} \qquad P_{Vis} = \int\limits_s \hat{\Phi}_{Vis}\,\mathrm{d}s\,, \tag{3.28}$$

to again give the powers of turbulent and viscous dissipation.

3.4 Secondary flow

Secondary flows created in the upstream distributor system and the injectors are the primary source of disturbances in Pelton turbine jets. Secondary flows in piping systems such as a Pelton turbine distributor system are mainly caused by changes in the flow direction and flow divisions, e.g., in the manifold or branches, and the interior parts, e.g., baffles or guides needed in the injector.

[13] This issue will be discussed by the example of the 90° pipe bend of Shiraishi et al. [92] in Section 5.2.3.

3.4.1 Secondary velocity ratio

In order to quantify the amount of secondary flow in a pipe, the magnitude of the secondary velocity needs to be compared to the magnitude of the primary velocity. Therefore, at first, the flow velocity $\vec{u} = (u, v, w)^T$ has to be split into a primary flow velocity $\vec{u}_I$ and a secondary flow velocity $\vec{u}_{II}$, such that $\vec{u} = \vec{u}_I + \vec{u}_{II}$. The primary flow velocity[14] is the velocity component in principal flow direction $\vec{n}$,

$$\vec{u}_I = (\vec{u} \cdot \vec{n})\, \vec{n}\,, \tag{3.29}$$

and the secondary flow velocity is the velocity component orthogonal to the principal flow direction,

$$\vec{u}_{II} = \vec{u} - \vec{u}_I = \vec{u} - (\vec{u} \cdot \vec{n})\, \vec{n} \quad \text{with} \quad \vec{u}_{II} \cdot \vec{n} = 0\,. \tag{3.30}$$

Typically, a Cartesian coordinate system would be oriented so that one coordinate axis coincides with the principal flow and the other two directions span the plane in which the secondary flow is described. When using a velocity formulation in cylindrical coordinates, e.g. $\vec{c} = (c_r, c_\theta, c_s)^T$, the streamwise direction $\vec{s}$ would represent the principal flow direction and thus the streamwise component c_s would correspond to the primary flow velocity.
Implementing the equations necessary to compute the secondary velocities in a post-processing utility is explained in Appendix B.1 and published in [30].

After these preparatory steps, the secondary velocity ratio at any location within the area of an arbitrary station i of an internal flow system is defined as

$$\phi_{II} = \frac{||\vec{u}_{II}||}{||\vec{u}_I||} = \sqrt{\frac{u_{II}^2 + v_{II}^2 + w_{II}^2}{u_I^2 + v_I^2 + w_I^2}}\,, \tag{3.31}$$

with

$$||\vec{u}_I|| = \vec{u} \cdot \vec{n} = \sqrt{u_I^2 + v_I^2 + w_I^2} \tag{3.32}$$

being the magnitude of the primary flow velocity and

$$||\vec{u}_{II}|| = \sqrt{u_{II}^2 + v_{II}^2 + w_{II}^2} \tag{3.33}$$

being the magnitude of the secondary flow velocity.
To achieve a single value for the secondary velocity ratio at a given station i, the magnitudes of the primary and the secondary velocity are mass averaged

$$\phi_{II,i} = \frac{\frac{\int_{A_i} (\rho||\vec{u}_{II}||)\vec{u} \cdot \mathrm{d}\vec{A}}{\int_{A_i} \rho\vec{u} \cdot \mathrm{d}\vec{A}}}{\frac{\int_{A_i} (\rho||\vec{u}_I||)\vec{u} \cdot \mathrm{d}\vec{A}}{\int_{A_i} \rho\vec{u} \cdot \mathrm{d}\vec{A}}} \overset{(1)}{=} \frac{\int_{A_i} ||\vec{u}_{II}||\, (\vec{u} \cdot \vec{n})\, \mathrm{d}A}{\int_{A_i} ||\vec{u}_I||\, (\vec{u} \cdot \vec{n})\, \mathrm{d}A} \overset{(2)}{=} \frac{\int_{A_i} ||\vec{u}_{II}|| \cdot ||\vec{u}_I|| \mathrm{d}A}{\int_{A_i} ||\vec{u}_I|| \cdot ||\vec{u}_I|| \mathrm{d}A}\,. \tag{3.34}$$

Here, in step (1), the constant density and the mass flow rate $\int_{A_i} \rho\vec{u} \cdot \mathrm{d}\vec{A}$ are cancelled out. In step (2), the term $(\vec{u} \cdot \vec{n})$ is replaced by the magnitude of the primary

[14] Sometimes also referred to as transport velocity.

velocity $||\vec{u}_I||$ as defined in Equation (3.32). This way, the denominator $||\vec{u}_I||$ and the enumerator $||\vec{u}_{II}||$ are both weighted by the primary velocity magnitude. If not stated otherwise, this definition of the secondary velocity ratio $\phi_{II,i}$ in station i was used in all subsequent chapters of the thesis.

In a similar way to Equation (3.19), a lumped form of the secondary velocity ratio

$$\phi^L_{II,100} = \frac{\int_{A_{100}} \rho ||\vec{u}_{II}|| \,(\vec{u}\cdot\vec{n})\,\mathrm{d}A}{\int_{A_{100}} \rho ||\vec{u}_{I}|| \,(\vec{u}\cdot\vec{n})\,\mathrm{d}A} \overset{(1)}{=} \frac{\Sigma_{i=1}^n \int_{A_{10i}} \rho ||\vec{u}_{II}|| \,(\vec{u}\cdot\vec{n})\,\mathrm{d}A}{\Sigma_{i=1}^n \int_{A_{10i}} \rho ||\vec{u}_{I}|| \,(\vec{u}\cdot\vec{n})\,\mathrm{d}A} \overset{(2)}{=} \\ = \frac{\Sigma_{i=1}^n \dot{m}_{10i}\cdot ||\vec{u}_{II}||_{10i}}{\Sigma_{i=1}^n \dot{m}_{10i}\cdot ||\vec{u}_{I}||_{10i}} \tag{3.35}$$

denoted by the superscript L, can be derived exemplary for station 100 of a Pelton turbine distributor system. Station 100 is located just upstream of the injectors and thus is composed of multiple surfaces. Starting from Equation (3.34), in step (1), again, the integration over station 100 is replaced by the sum of the integrals over the $n = 6$ individual stations $101, 102 \ldots 106$ of a typical Pelton turbine distributor systems with six branch lines. In step (2), the integrals in the sum were exchanged by the corresponding mass average velocities ($* = I$ or II) and the mass flow rates

$$\sum_{i=1}^{n} \int_{A_{10i}} \rho ||\vec{u}_*|| \,(\vec{u}\cdot\vec{n})\,\mathrm{d}A \quad \rightarrow \quad \sum_{i=1}^{n} \dot{m}_{10i}\cdot ||\vec{u}_*||_{10i}\,. \tag{3.36}$$

This lumped form of $\phi^L_{II,100}$ is equivalent to the secondary velocity ratio employed in [31].

Alternatively, the secondary velocity ratio itself can be mass averaged

$$\phi^M_{II,i} = \frac{\int_{A_i} (\rho\phi_{II})\,\vec{u}\cdot\mathrm{d}\vec{A}}{\int_{A_i} \rho\vec{u}\cdot\mathrm{d}\vec{A}} \overset{(1)}{=} \frac{\int_{A_i} \frac{||\vec{u}_{II}||}{||\vec{u}_I||}\,(\vec{u}\cdot\vec{n})\,\mathrm{d}A}{\int_{A_i} (\vec{u}\cdot\vec{n})\,\mathrm{d}A} \overset{(2)}{=} \frac{\int_{A_i} ||\vec{u}_{II}||\mathrm{d}A}{\int_{A_i} ||\vec{u}_{I}||\mathrm{d}A}\,. \tag{3.37}$$

Here, in step (1), the constant density is cancelled out, and in step (2), the definition of the magnitude of the primary flow velocity, $||\vec{u}_I|| = \vec{u}\cdot\vec{n}$, is employed.

3.4.2 Intensity of secondary flow

Instead of taking the ratio of the secondary flow velocity magnitude $||\vec{u}_{II}||$ to the primary flow velocity magnitude $||\vec{u}_I||$, the intensity of secondary flow

$$I_s = \phi^2_{II} = \left(\frac{||\vec{u}_{II}||}{||\vec{u}_I||}\right)^2 = \frac{u^2_{II} + v^2_{II} + w^2_{II}}{u^2_I + v^2_I + w^2_I} \tag{3.38}$$

can be introduced as the square of the secondary velocity ratio ϕ_{II}. This definition is motivated by comparing the kinetic energies of the primary and secondary flows rather than the velocities.

Analogously to Equation (3.34), a single value for the intensity of the secondary flow at a given station i is computed by using the mass average values of $||\vec{u}_I||^2$ and $||\vec{u}_{II}||^2$

$$I_{s,i} = \frac{\frac{\int_{A_i} \left(\rho ||\vec{u}_{II}||^2\right) \vec{u} \cdot \mathrm{d}\vec{A}}{\int_{A_i} \rho \vec{u} \cdot \mathrm{d}\vec{A}}}{\frac{\int_{A_i} \left(\rho ||\vec{u}_{I}||^2\right) \vec{u} \cdot \mathrm{d}\vec{A}}{\int_{A_i} \rho \vec{u} \cdot \mathrm{d}\vec{A}}} \overset{(1)}{=} \frac{\int_{A_i} ||\vec{u}_{II}||^2 \left(\vec{u} \cdot \vec{n}\right) \mathrm{d}A}{\int_{A_i} ||\vec{u}_{I}||^2 \left(\vec{u} \cdot \vec{n}\right) \mathrm{d}A} \overset{(2)}{=} \frac{\int_{A_i} ||\vec{u}_{II}||^2 \cdot ||\vec{u}_I|| \mathrm{d}A}{\int_{A_i} ||\vec{u}_I||^3 \mathrm{d}A} \,. \tag{3.39}$$

Steps (1) and (2) are the same as for Equation (3.34). To allow for an exact comparison of the simulation results against the experimental data of Sudo et al. [104] in Section 5.1, the form presented in Equation (3.39) is not used in this thesis. Instead, a version with area average values of $||\vec{u}_I||^2$ and $||\vec{u}_{II}||^2$ is introduced

$$\begin{aligned} I_{s,i} &= \frac{\frac{\int_{A_i} ||\vec{u}_{II}||^2 \mathrm{d}\vec{A}}{\int_{A_i} \mathrm{d}\vec{A}}}{\frac{\int_{A_i} ||\vec{u}_{I}||^2 \mathrm{d}\vec{A}}{\int_{A_i} \mathrm{d}\vec{A}}} = \frac{\int_{A_i} ||\vec{u}_{II}||^2 \mathrm{d}\vec{A}}{\int_{A_i} ||\vec{u}_{I}||^2 \mathrm{d}\vec{A}} \overset{(1)}{=} \\ &= \frac{\int_{A_i} \left\|\vec{u}_{II}\right\|^2 \mathrm{d}\vec{A}}{\int_{A_{ref}} \left\|\vec{u}_{ref}\right\|^2 \mathrm{d}\vec{A}} \overset{(2)}{=} \frac{4}{\pi d^2 u_b^2} \cdot \int\limits_{A_i} \left\|\vec{u}_{II}\right\|^2 \mathrm{d}\vec{A} \,. \end{aligned} \tag{3.40}$$

The primary flow velocity $\vec{u}_I$ at station i in the denominator can be substituted by a reference velocity $\vec{u}_{ref}$ taken at any station, which is done in step (1). If, as done by Sudo et al. [104], $\vec{u}_{ref}$ is set to be the constant bulk velocity u_b of the flow in a cylindrical pipe with diameter d, the integral in the denominator can be replaced by multiplication in step (2). The advantage of relating the secondary velocity to the bulk velocity is that for many cases, the bulk velocity can be computed explicitly from the Reynolds number[15] or from given operating conditions. For configurations where a change of the primary (transport) velocity occurs, e.g. by a change of the pipe diameter, it seems to be advisable to follow the definitions of Equations (3.34) and (3.39), where both the primary (transport) velocity and the secondary velocity are evaluated at the same station.

3.4.3 Secondary velocity ratio in pipes with changing cross-section

In Pelton turbine distributor systems, the cross-section of the pipe usually becomes smaller along the flow path, raising the question: How is the secondary velocity ratio ϕ_{II} affected if the diameter of a pipe changes[16]?

[15] Within this thesis, if not stated otherwise, the Reynolds number in its standard definition for pipe flow, $\mathrm{Re} = \frac{u_b \cdot d}{\nu}$, with a bulk velocity u_b, the diameter d of a cylindrical pipe, and the kinematic viscosity $\nu = \mu/\rho$, is used.

[16] Such a situation occurs in the *AxFeeder* when the influence of converging branch lines is studied in Section 6.5.1.

Assuming uniform density, incompressible, inviscid flow with conservative body forces[17], Kelvin's theorem

$$\frac{\mathrm{D}\Gamma}{\mathrm{D}t} = 0 \tag{3.41}$$

states that the circulation Γ is constant for a vortex tube of fixed identity[18] [26]. The circulation is defined as the line integral of the velocity $\vec{u}$ along a curve C [51]

$$\Gamma = \oint_C \vec{u} \cdot \mathrm{d}\vec{x} \overset{(1)}{=} \int_A (\boldsymbol{\nabla} \times \vec{u}) \cdot \vec{n} \mathrm{d}A \overset{(2)}{=} \int_A \vec{\omega} \cdot \vec{n} \mathrm{d}A \,. \tag{3.42}$$

With Stokes' theorem applied in step (1), the line integral can be rewritten as a surface integral of the curl of the velocity $\boldsymbol{\nabla} \times \vec{u}$, which, in step (2), is substituted by the vorticity $\vec{\omega} := \boldsymbol{\nabla} \times \vec{u}$. Eventually, the circulation becomes equivalent to the net flux of vorticity through a closed surface $\vec{A}$.

For a vortex tube with radius r small enough for the vorticity ω to be considered uniform over the area [26], the combination of Kelvin's theorem, Equation (3.41), with the definition of the circulation, Equation (3.42), yields

$$\omega \cdot \mathrm{d}A = const. \quad \text{or} \quad \Gamma = \omega \pi r^2 = const. \tag{3.43}$$

If the vortex tube is stretched (e.g. because the pipe diameter becomes smaller), the vorticity must increase to keep the circulation constant. In this scenario, the secondary velocity u_{II} corresponds to the swirl velocity ωr, whereas the primary velocity u_I is computed from a constant mass flow rate as $u_I = \dot{m}/(\rho \pi r^2)$. The secondary velocity ratio then becomes a function of the radius r only

$$\phi_{II} = \frac{u_{II}}{u_I} = \frac{(\omega r) \cdot (\rho \pi r^2)}{\dot{m}} \overset{(1)}{=} \frac{\Gamma r \rho}{\dot{m}} = const. \cdot r \,, \tag{3.44}$$

where in step (1), the relation $\omega = \Gamma / (\pi r^2)$ was inserted. The conclusion from Equation (3.44) is that in a pipe with decreasing diameter (e.g. a nozzle or converging branch line), the space for the vortex tubes becomes smaller, and the secondary velocity ratio is reduced. An equivalent statement is made by Greitzer et al. [26], who approximates the vortex tube equivalent to a streamtube and relates the swirl velocity ωr to the axial velocity u (computed from the continuity equation in the streamtube) in terms of a swirl angle $\tan(\alpha) \sim \alpha \sim (\omega r)/u$.

3.5 Turbulence

3.5.1 Turbulent kinetic energy

A detailed explanation of the turbulent kinetic energy k can be found in Section 4.1.2. For the sake of completeness, only the basic definition of k is given as

$$k = \frac{\overline{u_i' u_i'}}{2} = \frac{\overline{u'u'} + \overline{v'v'} + \overline{w'w'}}{2} = \frac{\overline{u'u' + v'v' + w'w'}}{2} \,. \tag{3.45}$$

[17] The integral of a conservative (body) force along a closed curve C is zero, regardless of the path of C. This is equivalent to the force being the gradient of a potential.

[18] This corresponds to Helmholtz's first theorem [100].

3.5.2 Turbulence intensity

For the simulation of engineering flows, especially when prescribing inlet boundary conditions, the turbulent kinetic energy k is often unknown. Instead, the turbulence intensity I_t, typically a value between 1 % to 10 %, is specified. Motivated by the assumptions of one-dimensional mean flow with flow velocity $\bar{u}$ (which is frequently encountered in engineering problems, e.g. at the inlet of a pipe) and isotropic turbulence, $\overline{u'u'} = \overline{v'v'} = \overline{w'w'}$, a commonly presented definition for the turbulence intensity is

$$I_t = \sqrt{\frac{\overline{u'u'}}{\bar{u}^2}} = \sqrt{\frac{\overline{u'u'} + \overline{v'v'} + \overline{w'w'}}{3\bar{u}^2}} = \sqrt{\frac{2k}{3\bar{u}^2}} \tag{3.46}$$

Here, the turbulence intensity I_t describes the fraction of the fluctuating portion of the flow to the mean flow [23].

For a fully developed flow in a straight pipe, an average value over the cross-section area can be estimated by the correlation found from Russo and Basse [79]

$$I_{t,est} = 0.140 \cdot \mathrm{Re}^{-0.0790}\,, \tag{3.47}$$

which, for a Reynolds number of $1 \cdot 10^6$, results in a turbulence intensity of 4.7 %. This value coincides with the engineers' rule of thumb value of 5 %.

A different definition of the turbulence intensity was introduced by Sudo et al. [104], where the turbulent kinetic energy is related to the square of a constant bulk velocity u_b. This definition denotes as

$$k_a = \frac{k}{u_b^2} = \frac{3}{2} \cdot I_t^2\,, \tag{3.48}$$

and can easily be linked to Equation (3.46), if the bulk velocity is interpreted as the mean flow velocity $\bar{u}$.

When estimating boundary conditions for the turbulent kinetic energy in CFD simulations, I_t is much more commonly used than k_a. Thus, within this thesis, the turbulence intensity will be expressed by I_t, and values for k_a retrieved from the literature will be converted following Equation (3.48).

Computations of the turbulent kinetic energy k and the turbulence intensity I_t rely heavily on modelling assumptions. Any resulting value of k and I_t must be seen concerning these assumptions, especially to the specified inlet turbulence level. It was demonstrated by Hahn et al. [31] that the choices of turbulence model and inlet turbulence intensity significantly impact the loss coefficient and flow structures. Therefore, to avoid over-interpretation, in this thesis, the turbulence intensity is used to validate the modelling approach against experimental data from Sudo et al. [104], but not taken as a criterion for assessing the flow quality in a Pelton turbine distributor system.

CHAPTER 4

Simulation methods

This chapter will introduce the most relevant theoretical considerations for understanding and simulating incompressible, isothermal turbulent flow. To start, the Navier-Stokes equations are presented, and the idea of Reynolds averaging is outlined in the context of this research. Second, the turbulence models applied in this thesis are explored. Third, the importance of choosing the correct boundary conditions is highlighted. Finally, the Grid Convergence Method of Celik et al. [11] as the standard method for error estimation and reporting in CFD simulations is summarised.

For detailed derivations of the Finite Volume Method, interpolation and differentiation practices, as well as solution strategies for the discretised equations, please refer to the relevant literature, in particular, the reference books of Ferziger et al. [23], Laurien and Oertel [54], and Schwarze [86].

4.1 Basic equations for turbulent flows

4.1.1 Navier-Stokes equations

Under the assumptions of incompressible and isothermal flow, the governing equations in index notation[1] for the motion of a Newtonian fluid with constant density ρ and constant dynamic viscosity μ are:

- Conservation of mass

$$\frac{\partial u_i}{\partial x_i} = 0 \tag{4.1}$$

- Conservation of momentum

$$\rho \left(\frac{\partial u_i}{\partial t} + u_j \frac{\partial u_i}{\partial x_j} \right) = -\frac{\partial p}{\partial x_i} + \mu \frac{\partial^2 u_i}{\partial x_i \partial x_j} + F_i \tag{4.2}$$

[1]The convention of the index notation states that a repeated subscript implies summation over the appropriate indices [26].

Together, the conservation of mass (= continuity equation) and the conservation of momentum form the Navier-Stokes equations[2], which represent a set of partial differential equations with the velocity vector $u_i(x_i,t)$, in Cartesian notation $\vec{u}(x,y,z,t) = (u(x,y,z,t), v(x,y,z,t), w(x,y,z,t))^T$, and the pressure $p = p(x_i,t)$ being unknown.
The terms on the left-hand side of Equation (4.2) correspond to the material derivative

$$\frac{\mathrm{D}}{\mathrm{D}t} = \frac{\partial}{\partial t} + u_j \frac{\partial}{\partial x_j}\,. \tag{4.3}$$

The first two terms on the right-hand side of Equation (4.2) represent the divergence $\frac{\partial}{\partial x_j}(\Pi_{ij})$ of the stress tensor

$$\Pi_{ij} = -p\delta_{ij} + \tau_{ij} = -p\delta_{ij} + \mu\left(\frac{\partial u_i}{\partial x_j} + \frac{\partial u_j}{\partial x_i}\right) \tag{4.4}$$

of an incompressible Newtonian fluid, with τ_{ij} being the viscous stress tensor and δ_{ij} being the Kronecker delta. The body forces acting on the fluid element, e.g. gravity, buoyancy or rotational forces[3], are represented by the vector $F_i(x_i,t)$, in Cartesian notation $\vec{F}(x,y,z,t) = (F_x(x,y,z,t), F_y(x,y,z,t), F_z(x,y,z,t))^T$.

4.1.2 Reynolds decomposition

The complexity of the Navier-Stokes equations requires some modelling assumptions when working on engineering flow problems. The most common approach is to model the flow as statistically steady[4] and write every variable, e.g. the velocity u, as the sum of a time-averaged value $\bar{u}_i$ and a fluctuation in time u_i' about that value [23]

$$u_i(x_i,t) = \bar{u}_i(x_i) + u_i'(x_i,t) \quad \text{and} \quad p(x_i,t) = \bar{p}(x_i) + p'(x_i,t)\,. \tag{4.5}$$

This type of averaging is called Reynolds-averaging, and when applied to the Navier-Stokes equations (body forces will not be considered further in this thesis), the resulting equations for the mean flow are called Reynolds-averaged Navier-Stokes (RANS) equations:

- Conservation of mass

$$\frac{\partial \bar{u}_i}{\partial x_i} = 0 \tag{4.6}$$

[2]A detailed derivation of the Navier-Stokes equations can be found in many textbooks, e.g. [26, 36, 51, 82, 100]. This thesis largely follows the derivations of Greitzer et al. [26], Schlichting and Gersten [82] and Ferziger et al. [23].

[3]Within the modelling assumptions taken in this thesis for the validation cases in Chapter 5 and the studies of the distributor systems with axial inflow in Chapter 6, neither of these forces is significant. They are therefore dropped in the following.

[4]Averaging is conducted over a time scale Δt that is large relative to the turbulent fluctuations, but small relative to the time scale to which the equations are solved [3]. For unsteady flows, the equations are averaged over ensembles, and the resulting mean flow equations may be unsteady too; hence, they are called unsteady RANS (URANS) equations [3, 23]. Durbin [17] states that in this URANS modelling approach, the mean flow can also be a function of time, and eventual time-averaging is a mere post-processing step. Concerning these aspects, the presence of the temporal derivative $\frac{\partial \bar{u}_i}{\partial t}$ is justified in Equation (4.7).

- Conservation of momentum

$$\rho\left(\frac{\partial \bar{u}_i}{\partial t}+\bar{u}_j\frac{\partial \bar{u}_i}{\partial x_j}\right)=-\frac{\partial \bar{p}}{\partial x_i}+\mu\frac{\partial^2\bar{u}_i}{\partial x_i\partial x_j}-\rho\frac{\partial \overline{u_i^{'}u_j^{'}}}{\partial x_j} \tag{4.7}$$

By comparison, Equations (4.2) and (4.7) are formally the same, except for the term $-\rho\frac{\partial \overline{u_i^{'}u_j^{'}}}{\partial x_j}$. This term arises from the non-linear advection term $u_j\frac{\partial u_i}{\partial x_j}$ of the Navier-Stokes equations, from which the mean of the product of the turbulent fluctuations $\overline{u_i^{'}u_j^{'}}$ cannot be eliminated. This additional term, though, can be rewritten as

$$-\rho\frac{\partial \overline{u_i^{'}u_j^{'}}}{\partial x_j}=\frac{\partial}{\partial x_j}\left(-\rho\overline{u_i^{'}u_j^{'}}\right)=\frac{\partial}{\partial x_j}\tau_{ij}^{'}\,, \tag{4.8}$$

where, in analogy to the viscous stress tensor τ_{ij}, the tensor of the turbulent stresses $\tau_{ij}^{'}$ is defined as

$$\tau_{ij}^{'}\coloneqq-\rho\overline{u_i^{'}u_j^{'}}\,. \tag{4.9}$$

The six components of the turbulent stress tensor[5] $\tau_{ij}^{'}$ are additional unknowns and cannot be computed directly. A turbulence closure is required to solve the system of the RANS Equations (4.6) and (4.7).

4.1.3 Eddy viscosity hypothesis

Following the idea of Boussinesq [8] to model the turbulent stresses in analogy to the viscous stresses as proportional to the mean velocity gradients by introducing a turbulent (eddy) viscosity μ_t, the eddy viscosity hypothesis states

$$\tau_{ij}^{'}=-\rho\overline{u_i^{'}u_j^{'}}=-\frac{2}{3}\rho k\delta_{ij}+\mu_t\left(\frac{\partial \bar{u}_i}{\partial x_j}+\frac{\partial \bar{u}_j}{\partial x_i}\right)\,. \tag{4.10}$$

To close the RANS equations, the turbulent viscosity $\mu_t=\mu_t(x,y,z)=\rho\cdot\nu_t(x,y,z)$ needs to be modelled. Here, the turbulent kinetic energy is defined as

$$k=\frac{\overline{u_i^{'}u_i^{'}}}{2}=\frac{\overline{u^{'}u^{'}+v^{'}v^{'}+w^{'}w^{'}}}{2}\,. \tag{4.11}$$

The right-hand side of Equation (4.7) can be rewritten as

$$\begin{aligned}-\frac{\partial \bar{p}}{\partial x_i}+\mu\frac{\partial^2\bar{u}_i}{\partial x_i\partial x_j}-\rho\frac{\partial \overline{u_i^{'}u_j^{'}}}{\partial x_j}&=\frac{\partial}{\partial x_j}\left[-p\delta_{ij}+\mu\left(\frac{\partial \bar{u}_i}{\partial x_j}+\frac{\partial \bar{u}_j}{\partial x_i}\right)-\rho\overline{u_i^{'}u_j^{'}}\right]\overset{(1)}{=}\\&=\frac{\partial}{\partial x_j}\left[-p\delta_{ij}+\mu\left(\frac{\partial \bar{u}_i}{\partial x_j}+\frac{\partial \bar{u}_j}{\partial x_i}\right)-\frac{2}{3}\rho k\delta_{ij}+\mu_t\left(\frac{\partial \bar{u}_i}{\partial x_j}+\frac{\partial \bar{u}_j}{\partial x_i}\right)\right]=\\&=\frac{\partial}{\partial x_j}\left[-p\delta_{ij}-\frac{2}{3}\rho k\delta_{ij}\right]+\frac{\partial}{\partial x_j}\left[(\mu+\mu_t)\left(\frac{\partial \bar{u}_i}{\partial x_j}+\frac{\partial \bar{u}_j}{\partial x_i}\right)\right]\,,\end{aligned} \tag{4.12}$$

[5]The turbulent stress tensor is also known as the Reynolds stress tensor.

wherein step (1), the eddy viscosity hypothesis, Equation (4.10), was inserted. Launder and Sandham [52] suggest assimilating the isotropic part of the closure model into the pressure term

$$p_{mod} = p + \frac{2}{3}\rho k \tag{4.13}$$

to achieve a modified pressure.
The Reynolds-averaged momentum equation[6] subjected to the eddy viscosity hypothesis becomes

$$\rho \left(\frac{\partial \bar{u}_i}{\partial t} + \bar{u}_j \frac{\partial \bar{u}_i}{\partial x_j} \right) = \frac{\partial p_{mod}}{\partial x_i} + \frac{\partial}{\partial x_j} \left[(\mu + \mu_t) \left(\frac{\partial \bar{u}_i}{\partial x_j} + \frac{\partial \bar{u}_j}{\partial x_i} \right) \right] . \tag{4.14}$$

The six unknown components of the turbulent stress tensor $\tau_{ij}^{'}$ could be reduced to two new unknowns, the turbulent kinetic energy k and the turbulent viscosity μ_t. Both must be modelled.

4.2 Turbulence models

This section briefly introduces the turbulence models applied in Chapters 5 and 6. First, two-equation models based on the eddy viscosity hypothesis are outlined. These are the k-ε model (kE) of Launder and Spalding [53], and the k-ω Shear Stress Transport model (SST) of Menter [61]. Both are often applied for computing flows where the assumption of isotropic turbulence[7] is justified [86]. Second, a Reynolds-stress model, the Baseline-Explicit Algebraic Reynolds Stress Model (EARSM) of Menter, Garbaruk, and Egorov [62], is presented.

4.2.1 k-ε model

The eddy viscosity hypothesis reduced the six unknown components of the turbulent stress tensor to two independent parameters, the turbulent viscosity μ_t, and the turbulent kinetic energy k. In the k-ε model, these parameters are linked by

$$\mu_t = \rho \cdot C_\mu \frac{k^2}{\varepsilon} , \tag{4.15}$$

where ε is the turbulent eddy dissipation (or turbulent energy dissipation rate) and $C_\mu = 0.09$ a model constant. The turbulent kinetic energy k is associated with the intensity or "strength" of the turbulence [54]. Based on the observation that dissipation is needed in the energy equation to balance the rates of production and

[6] Launder and Sandham [52] point out that in this equation, the turbulence field is coupled to the mean field only through the turbulent viscosity. In general, $\mu_t > \mu$ and thus, an additional diffusivity is induced in the RANS equations, possibly distorting the behaviour of the flow.

[7] To speak of isotropic turbulence in a strict sense, the turbulence quantities must be independent of the orientation of the coordinate system [36]. From this, $\overline{u'u'} = \overline{v'v'} = \overline{w'w'}$ and $\overline{u'v'} = \overline{v'w'} = \overline{w'u'} = 0$ follows. For practical applications, it is sufficient if the turbulent fluctuations in the three principal directions of the Reynolds stress tensor, $\overline{u'u'}$, $\overline{v'v'}$, and $\overline{w'w'}$, are of the same order of magnitude [54].

destruction of turbulence in equilibrium turbulent flows [23], the turbulent eddy dissipation is associated with the dissipation of small-scale turbulent structures [54]. Both scalar quantities need to be modelled in the form of a transport equation. For the turbulent kinetic energy k, the modelled equation[8] denotes

$$\rho\frac{\partial k}{\partial t} + \underbrace{\rho\bar{u}_j\frac{\partial k}{\partial x_j}}_{Convection} = \underbrace{\mu_t\frac{\partial \bar{u}_i}{\partial x_j}\left(\frac{\partial \bar{u}_i}{\partial x_j} + \frac{\partial \bar{u}_j}{\partial x_i}\right)}_{Production} + \underbrace{\frac{\partial}{\partial x_j}\left[\left(\mu + \frac{\mu_t}{\sigma_k}\right)\frac{\partial k}{\partial x_j}\right]}_{Diffusion} - \underbrace{\rho\varepsilon}_{Dissipation}, \quad (4.16)$$

and for the turbulent eddy dissipation ε, the modelled equation[9] denotes

$$\rho\frac{\partial \varepsilon}{\partial t} + \underbrace{\rho\bar{u}_j\frac{\partial \varepsilon}{\partial x_j}}_{Convection} = \underbrace{C_{\varepsilon 1}\frac{\varepsilon}{k}\mu_t\frac{\partial \bar{u}_i}{\partial x_j}\left(\frac{\partial \bar{u}_i}{\partial x_j} + \frac{\partial \bar{u}_j}{\partial x_i}\right)}_{Production} + \underbrace{\frac{\partial}{\partial x_j}\left[\left(\mu + \frac{\mu_t}{\sigma_\varepsilon}\right)\frac{\partial \varepsilon}{\partial x_j}\right]}_{Diffusion} - \underbrace{C_{\varepsilon 2}\rho\frac{\varepsilon^2}{k}}_{Dissipation}. \quad (4.17)$$

The five empirical model constants are $C_\mu = 0.09$, $\sigma_k = 1.0$, $\sigma_\varepsilon = 1.3$, $C_{\varepsilon 1} = 1.44$ and $C_{\varepsilon 2} = 1.92$ [3, 23, 54].

The k-ε model is known for its stability and robustness to the choice of inflow boundary conditions and is therefore widely used in engineering simulations of fully turbulent flows [54]. When used in a high-Re formulation with wall-functions[10], the grid towards the walls can be coarse[11]. Hence, the simulation needs fewer computational resources than a simulation with a grid for low-Re models with full wall resolution (see also Tables C.2 and C.7). The k-ε model is less suited for the computation of complex flows with stagnation points, swirling flows or in the accurate prediction of flow separation[12] [86]. Several sub-variants of the k-ε model were derived to overcome its deficiencies, e.g. the Renormalization-Group-k-ε model of Yakhot et al. [114] or the Realizable-k-ε model of Shih et al. [91].

4.2.2 k-ω Shear Stress Transport model

A different approach is to use the turbulent eddy frequency

$$\omega = \frac{\varepsilon}{\beta^* k} \quad (4.18)$$

as a substitute for the turbulent eddy dissipation ε. Here, $\beta^* = 0.09$ is a model coefficient [113]. Wilcox [113] derived the k-ω model, which uses a modified form of the k-equation and another differential equation for ω to describe the

[8] A detailed derivation for both equations is given in Laurien and Oertel [54]. There, the k-equation is derived from the momentum equation, and modelling assumptions are introduced for all terms, including fluctuating quantities, e.g. the triple velocity correlation $\overline{u_i'u_i'u_j'}$.

[9] Ferziger et al. [23] point out that the modelling applied to it is so severe that it is best to regard the entire equation as a model, although it is possible to derive an exact equation for ε from the momentum equations as well.

[10] In ANSYS CFX, the k-ε model is combined with scalable wall functions to model the flow near the wall [3].

[11] Sample grid points for a high-Re model with wall functions are included in Figure 4.1.

[12] See also Figure 5.6 and the related discussion.

turbulence. This model proved superior near solid walls but was sensitive to free-stream conditions for ω and thus susceptible to ill-prediction of free-shear flows. Consequently, several improved versions of the Wilcox k-ω model have been implemented. However, of these, the k-ω Shear Stress Transport model (SST) of Menter [61], due to its effective combination of both the k-ω model close to walls and the k-ε model in free-stream situations, has become the most widely used model for simulating engineering flows.
In the SST model of Menter, slightly different forms of the k-equation

$$\frac{\mathrm{D}\rho k}{\mathrm{D}t} = \underbrace{\mu_t \frac{\partial \bar{u}_i}{\partial x_j}\left(\frac{\partial \bar{u}_i}{\partial x_j} + \frac{\partial \bar{u}_j}{\partial x_i}\right)}_{Production} + \underbrace{\frac{\partial}{\partial x_j}\left[(\mu + \sigma_k \mu_t)\frac{\partial k}{\partial x_j}\right]}_{Diffusion} - \underbrace{\beta^* \rho \omega k}_{Dissipation} \tag{4.19}$$

and the ω-equation

$$\frac{\mathrm{D}\rho\omega}{\mathrm{D}t} = \underbrace{\frac{\gamma}{\nu_t}\tau_{ij}\frac{\partial \bar{u}_i}{\partial x_j}}_{Production} + \underbrace{\frac{\partial}{\partial x_j}\left[(\mu + \sigma_\omega \mu_t)\frac{\partial \omega}{\partial x_j}\right]}_{Diffusion} + \underbrace{2\rho(1-F_1)\sigma_{\omega 2}\frac{1}{\omega}\frac{\partial k}{\partial x_j}\frac{\partial \omega}{\partial x_j}}_{Cross-Diffusion} - \underbrace{\beta \rho \omega^2}_{Dissipation} \tag{4.20}$$

with the definition

$$\tau_{ij} = \mu_t \left(\frac{\partial \bar{u}_i}{\partial x_j} + \frac{\partial \bar{u}_j}{\partial x_i}\right) \tag{4.21}$$

are used[13].
These equations were derived by inserting $\varepsilon = \omega k$ into the ε-equation[14] and combining the equations of the k-ω model and the thus transformed equations of the k-ε model through a blending function F_1. This blending function guarantees a smooth transition of the ω-equation between the near wall formulation according to the k-ω model and the free-stream formulation according to the k-ε model. The new model constants σ_k, σ_ω, β, β^*, γ are calculated from the constants of the k-ω model[15] (index 1) and the the transformed k-ε model[16] (index 2) by $\phi = F_1\phi_1 + (1 - F_1)\phi_2$. Menter [61] introduces an additional blending function F_2 to enforce a limit to the turbulent viscosity

$$\mu_t = \rho \frac{a_1 k}{max(a_1\omega; SF_2)}\,, \tag{4.22}$$

where $a_1 = 0.31$ is a constant and S is an invariant measure of the strain rate [3]. This method improves the prediction of boundary layer separations.

In the ANSYS CFX implementation of the SST model, automatic near-wall treatment is performed [3]. In this approach, the turbulent eddy frequency ω is blended between the near wall formulation in the viscous sub-layer and the formulation in the logarithmic section of the boundary layer [3]. This blending effectively automatically switches between the low-Re near wall formulations and the scalable

[13] Menter et al. [63] use a formulation of the SST model, where the coefficients were chosen slightly different. Smirnov and Menter [95] use a different factor for the turbulent viscosity.
[14] Thereby, a new cross-diffusion term emerges.
[15] $\sigma_{k1} = 0.5$, $\sigma_{\omega 1} = 0.5$, $\beta_1 = 0.0750$, $\beta^* = 0.09$, $\kappa = 0.41$, $\gamma_1 = \beta_1/\beta^* - \sigma_{\omega 1}\kappa^2/\sqrt{\beta^*}$
[16] $\sigma_{k2} = 1.0$, $\sigma_{\omega 2} = 0.856$, $\beta_2 = 0.0828$, $\beta^* = 0.09$, $\kappa = 0.41$, $\gamma_2 = \beta_2/\beta^* - \sigma_{\omega 2}\kappa^2/\sqrt{\beta^*}$

wall functions [3]. The experience of Hahn et al. [31], the simulations in Chapter 5, as well as the suggestions by Menter et al. [63], show, however, that the most trustworthy simulations and the best agreements between the simulation results and experimental data are achieved if the computational mesh is refined close to the walls such that a non-dimensional wall distance y^+ close to or less than one is guaranteed.
If this requisite is met, the SST model shows significant improvements over the k-ε and the k-ω models, especially in flows with strong adverse pressure gradients and in predicting pressure-induced flow separations. Further, the stability and numerical effort are comparable to the previous models.

Curvature correction

Eddy viscosity turbulence models cannot capture the effects of streamline curvature and system rotation in full detail [63]. Spalart and Shur [97] attempted to overcome these deficiencies by multiplying a rotation function

$$f_{rotation} = (1 + c_{r1}) \frac{2r^*}{1 + r^*} \left[1 - c_{r3} \arctan(c_{r2}\tilde{r})\right] - c_{r1} \tag{4.23}$$

to the production term in the eddy viscosity transport equation of the Spalart-Allmaras model [98]. Here, c_{r1}, c_{r2} and c_{r3} are empirically found constants and r^* and $\tilde{r}$ are functions depending on the strain and vorticity tensors. Smirnov and Menter [95] apply a slightly altered rotation function

$$f_{r1} = max\left[min(f_{rotation}, 1.25), 0.0\right] \tag{4.24}$$

as a multiplication factor to the production terms of the k- and ω-equation of the SST model.
Smirnov and Menter [95] benchmarked their implementation of the curvature correction terms in the SST model against the SST model without curvature correction and a Reynolds-stress model for several cases. The cases most relevant to this thesis were the two-dimensional flow in a duct with a U-turn and the developed flow in a curved channel. For both cases, the SST model with activated curvature correction (SSTCC) matched the given experimental data more closely than the SST model without curvature correction. Therefore, turbulence models with curvature correction were also tested in the validation cases presented in Chapter 5.

4.2.3 Baseline-Explicit Algebraic Reynolds Stress model

In complex three-dimensional flows, the eddy viscosity hypothesis does not hold. In particular, the assumption of isotropic turbulence cannot be fulfilled. Thus, the Reynolds stresses, and the strain rates are related by a tensor-type formulation of the eddy viscosity instead of a simple scalar quantity as presented in Equation (4.10). In Reynolds stress models, a partial differential equation is derived from the Navier-Stokes equations for each of the six components of the Reynolds stress tensor $\tau_{ij}^{'}$ [23, 36]. These equations include several new terms, such as the pressure-strain relation, the dissipation tensor and the turbulent diffusion, that must be modelled to achieve a closed system of equations. The benefits of Reynolds stress models lie in their improved performance for swirling flows, flows with strong curvature and separation from curved surfaces [23]. Unfortunately, six additional transport equations to be solved, one for each component of $\tau_{ij}^{'}$, drastically raises the computational costs of Reynolds stress models.

Menter, Garbaruk, and Egorov [62] came up with the idea to combine the stress-strain relationship proposed in the Explicit Algebraic Reynolds Stress model of Wallin and Johansson [112] with the ω-equation baseline model underlying the SST model. In this approach, the anisotropy of the Reynolds stress tensor is taken into account by modifying the production terms $\widetilde{P}_k$ of the k- and ω-equations by using the stress-strain relationship [62]

$$\tau_{ij}^{'} = \overline{u_i^{'} u_j^{'}} = k \left(a_{ij} + \frac{2}{3}\delta_{ij} \right) \tag{4.25}$$

with the anisotropy tensor $a_{ij} = f\left(S_{ij}, \Omega_{ij}\right)$ being a function of the non-dimensional strain tensor

$$S_{ij} = \frac{\tau}{2} \left(\frac{\partial \bar{u}_i}{\partial x_j} + \frac{\partial \bar{u}_j}{\partial x_i} \right) , \tag{4.26}$$

and the non-dimensional vorticity tensor

$$\Omega_{ij} = \frac{\tau}{2} \left(\frac{\partial \bar{u}_i}{\partial x_j} - \frac{\partial \bar{u}_j}{\partial x_i} \right) , \tag{4.27}$$

where τ represents a turbulent time scale. The Baseline-Explicit Algebraic Reynolds Stress Model reads for the k-equation

$$\frac{\mathrm{D}k}{\mathrm{D}t} = \underbrace{\widetilde{P}_k}_{Production} + \underbrace{\frac{\partial}{\partial x_j}\left[\left(\nu + \delta_k \nu_t\right) \frac{\partial k}{\partial x_j} \right]}_{Diffusion} - \underbrace{\beta^* \omega k}_{Dissipation} , \tag{4.28}$$

and for the ω-equation

$$\frac{\mathrm{D}\omega}{\mathrm{D}t} = \underbrace{\frac{\gamma\omega}{k}\widetilde{P}_k}_{Production} + \underbrace{\frac{\partial}{\partial x_j}\left[\left(\nu + \delta_\omega \nu_t\right) \frac{\partial \omega}{\partial x_j} \right]}_{Diffusion} + \underbrace{\frac{\delta_d}{\omega}\frac{\partial k}{\partial x_j}\frac{\partial \omega}{\partial x_j}}_{Cross-Diffusion} - \underbrace{\beta\omega^2}_{Dissipation} . \tag{4.29}$$

The production term[17] is defined as

$$\widetilde{P}_k = min\left(\tau_{ij}^{'} \frac{\partial \bar{u}_i}{\partial x_j}, 10\beta^* \omega k \right) , \tag{4.30}$$

including a production limiter as customary in the SST model [3, 62]. Also, the model constants are defined as in the SST model Section 4.2.2.

The significant advantage of the presented approach is that the anisotropy tensor is calculated from a set of linear equations. Thus, the computational costs of a

[17] Menter et al. [62] put a minus sign in front of $\tau_{ij}^{'}$. However, this minus sign does not appear in any of the EARSM models presented in [65] and is therefore omitted in Equation (4.30).

simulation with the EARSM model are only moderately higher than with eddy viscosity models (see also Tables C.2 and C.7) but reasonably less than for other Reynolds stress models. The performance of the EARSM approach was investigated in a series of test cases by Menter et al. [62]. For a rectangular diffuser as an example of an internal flow problem, Menter et al. [62] proved that the flow field and the pressure coefficient predicted by the EARSM model matched the experimental data better than the results of the SST model. This performance qualifies the EARSM model as a notable alternative for the validation cases in Chapter 5.

4.3 Boundary conditions and wall treatment

A complete description of the flow problem requires boundary conditions for each of the unknowns. In the case of a turbulent flow to be computed by solving the Reynolds averaged Navier-Stokes equation with one of the turbulence models introduced in Section 4.2, these unknowns are the three velocity components u, v and w, the pressure p, the turbulent kinetic energy k and either the turbulent eddy dissipation ε or the turbulent eddy frequency ω. When modelling an internal flow problem, like a Pelton turbine distributor system, the most relevant types of boundaries are the inlet and outlet(s), walls and symmetry planes.

4.3.1 Inlet, outlet and symmetry

The combination of specifying the values of the velocity components at the inlet and the pressure at the outlet (Dirichlet type boundary condition) has proven favourable. At the outlet, a zero-gradient boundary condition (von Neumann type), $\frac{\partial \vec{u}}{\partial \vec{n}} = 0$, is then imposed for the velocity. Conversely, the zero-gradient boundary condition for the pressure, $\frac{\partial p}{\partial \vec{n}} = 0$, is imposed at the inlet.

Hahn et al. [31] emphasised the importance of carefully selecting appropriate inlet boundary conditions for the turbulence quantities. Typically, the turbulent kinetic energy at the inlet

$$k_{inlet} = \frac{3}{2} \left(\bar{u}_{inlet} I_{t,inlet} \right)^2 \tag{4.31}$$

is computed from the turbulence intensity[18] $I_{t,inlet}$ and a mean flow velocity $\bar{u}$ (calculated from a mass flow rate or the Reynolds number).

The turbulent viscosity at the inlet can be approximated by a velocity scale and a length scale. With $\sqrt{k_{inlet}}$ for the velocity scale and $l_{t,inlet} = x \cdot D_h$ as the length scale[19], the turbulent viscosity becomes $\nu_{t,inlet} = \sqrt{k_{inlet}} \cdot l_{t,inlet} = \sqrt{k_{inlet}} \cdot (xD_h)$. From Equation (4.15), the equation for the turbulent eddy dissipation at the inlet[20]

$$\varepsilon_{inlet} = C_\mu \frac{k_{inlet}^2}{\nu_{t,inlet}} = C_\mu \frac{k_{inlet}^{\frac{3}{2}}}{l_{t,inlet}} = C_\mu \frac{k_{inlet}^{\frac{3}{2}}}{xD_h} \tag{4.32}$$

[18] The rule of the thumb for engineering flows is $I_{t,inlet} = 5\,\%$.

[19] The length scale is a measure of the size of the largest turbulent eddies.

[20] A different version of this equation with $C_\mu^{3/4}$ is commonly used as well.

was derived, where x is a fraction of the hydraulic diameter D_h at the inlet. An often-used assumption for developed flow is $x = 0.1$.
The turbulent eddy frequency at the inlet follows with

$$\omega_{inlet} = \frac{\varepsilon_{inlet}}{\beta^* k} = \frac{\sqrt{k_{inlet}}}{l_{t,inlet}} = \sqrt{\frac{3}{2}} \cdot \frac{\bar{u}_{inlet} I_{t,inlet}}{x D_h} , \tag{4.33}$$

where the constants C_μ and β^* were cancelled out.

At the outlet, the flow should have developed sufficiently, such that for all three turbulence quantities, k, ε and ω, a von Neumann type zero-gradient boundary condition, $\frac{\partial k}{\partial \vec{n}} = \frac{\partial \varepsilon}{\partial \vec{n}} = \frac{\partial \omega}{\partial \vec{n}} = 0$, should be specified.

The velocity perpendicular to the symmetry plane is zero, $\vec{u} \cdot \vec{n} = 0$. For all other quantities $\phi = (p, k, \varepsilon, \omega)$, the gradient perpendicular to the symmetry plane is zero, $\frac{\partial \phi}{\partial \vec{n}} = 0$.

4.3.2 Wall

At the wall of the domain, the no-slip and no-penetration conditions state that the flow tangential to the wall, $\vec{u} \cdot \vec{t}$, and perpendicular to the wall, $\vec{u} \cdot \vec{n}$, is zero.

In many internal flow problems, turbulence is generated in the turbulent boundary layers. The flow in turbulent boundary layers is either modelled by wall functions (high-Re models) or resolved down to the viscous sublayer (low-Re models).
The wall function approach is based on the velocity distribution in the boundary layer of turbulent Couette flow [86]. This boundary layer can be divided into three regions: the viscous sublayer ($y^+ < 5$), the buffer layer ($5 < y^+ < 30$) and the log-law region ($y^+ > 30$). The velocity profile and the three regions are displayed in Figure 4.1 in non-dimensional coordinates

$$y^+ = \frac{y \cdot u_\tau}{\nu} \qquad \text{and} \qquad u^+ = \frac{\bar{u}}{u_\tau} , \tag{4.34}$$

with the shear velocity $u_\tau = \sqrt{\tau_{wall}/\rho}$ [23].

Under the assumption of constant shear stress in the turbulent Couette flow and that turbulence production and dissipation are balanced in the buffer layer, with

$$k^+ = \frac{k}{u_\tau^2} = \frac{1}{C_\mu^{1/2}} \approx 3.3 \qquad \text{and} \qquad \varepsilon^+ = \frac{\varepsilon \nu}{u_\tau^4} = \frac{\nu}{u_\tau \kappa y} = \frac{1}{\kappa y^+} , \tag{4.35}$$

non-dimensional forms of the turbulence quantities are derived [86].

Most wall functions for high-Re turbulence models offered in CFD codes are based on the standard wall functions of Launder and Spalding [53]

$$y^* < 11.06 : \quad u^* = y^* \tag{4.36a}$$

$$y^* > 11.06 : \quad u^* = \frac{1}{\kappa} \ln(E y^*) \quad \text{with} \quad E = 9.793 \tag{4.36b}$$

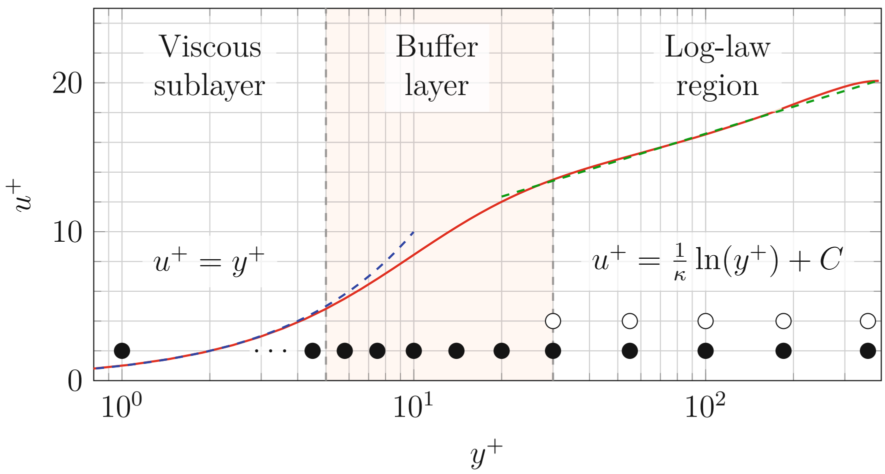

Figure 4.1: Universal law of the wall with the Karman-constant $\kappa = 0.41$, and a constant for smooth surfaces $C \cong 5.5$ [51, 86]. Sample grid points for high-Re models with wall functions are indicated by $\circ$, for low-Re models and models with full wall resolution by $\bullet$.

For improved numerical stability[21], y^+ and u^+ were replaced by y^* and u^*. The latter are computed with the turbulent kinetic energy k instead of the shear velocity u_τ [86]. Unfortunately, the standard wall functions lack precision in predicting flows with adverse pressure gradients, swirling flows or flows in small gaps. Therefore, scalable wall functions are employed in ANSYS CFX [3]. In the scalable wall function method, y^* is limited such that only mesh points outside the viscous sublayer are considered. The turbulent kinetic energy is computed in the entire domain, and the boundary condition for the turbulent eddy dissipation becomes [3]

$$\varepsilon = \frac{\rho u^*}{\mu y^*} \cdot \frac{C_\mu^{3/4}}{\kappa} \cdot k^{3/2} \,. \tag{4.37}$$

The wall functions for low-Re turbulence models are often modified versions of the standard wall functions. Because the boundary layer is resolved down to $y^+ < 1$, setting $k_{wall} = 0$ and $\varepsilon_{wall} = 0$ at the walls is justified.

For a correct application of wall functions in high-Re turbulence models, the wall-nearest grid point must lie in the log-law region, $30 < y^+ < 300$. To achieve the most accurate results with low-Re turbulence models, the wall-nearest grid point must lie in the viscous sublayer, ideally $y^+ < 1$. Further, the viscous sublayer and the buffer layer must be resolved with at least ten to twenty grid points [3, 86].

4.4 Estimation of discretisation uncertainty

One important measure of quality control in CFD simulations projects is to estimate the potential error induced by discretisation. Several guidelines on that matter were published over the last decades, e.g. [1, 10, 76]. Among these issues, the

[21] At separation points, u_τ approaches zero and u^+ becomes singular.

Grid Convergence Method (GCI) of Celik et al. [11] has established itself as the quasi-standard for every carefully executed CFD study.

The underlying idea of this method is to run simulations for at least three different grids and observe the impact of a change of the number of mesh cells N_m on variables ϕ critical to the flow problem. The number of mesh cells in these three grids has to vary such, that, ideally, the refinement factors

$$r_{21} = \frac{h_2}{h_1} \quad \text{and} \quad r_{32} = \frac{h_3}{h_2}\,, \quad \text{with} \quad h_1 < h_2 < h_3\,, \tag{4.38}$$

which are computed from the average cell sizes

$$h = \left[\frac{1}{N_m}\sum_{j=1}^{N_m}(\Delta V_j)\right]^{1/3} \tag{4.39}$$

are greater than 1.3.
For each of the selected quantities ϕ, the apparent order p_{oa} of the method is computed iteratively by

$$p_{oa} = \frac{1}{\ln(r_{21})} \cdot \left| \ln\left|\frac{\phi_3 - \phi_2}{\phi_2 - \phi_1}\right| + q(p_{oa})\right| \tag{4.40a}$$

$$q(p_{oa}) = \ln\left(\frac{r_{21}^{p_{oa}} - s}{r_{32}^{p_{oa}} - s}\right) \qquad \text{with} \qquad s = 1 \cdot \operatorname{sgn}\left(\frac{\phi_3 - \phi_2}{\phi_2 - \phi_1}\right) \tag{4.40b}$$

A negative value of s is an indication of oscillatory convergence. The ratio of data points with oscillatory convergence

$$R_{oc} = \frac{1}{N_p} \cdot \sum_{i=1}^{N_p} \text{if}\,(s_i < 0) \tag{4.41}$$

counts how many data points i of a quantity ϕ result in a value of $s < 0$.
The extrapolated values of each variable ϕ are obtained by

$$\phi_{ext}^{21} = \frac{r_{21}^p\phi_1 - \phi_2}{r_{21}^p - 1} \quad \text{and} \quad \phi_{ext}^{32} = \frac{r_{32}^p\phi_2 - \phi_3}{r_{32}^p - 1}\,. \tag{4.42}$$

Then, the approximate relative error e_a^{21}, the extrapolated relative error e_{ext}^{21} ,

$$e_a^{21} = \left|\frac{\phi_1 - \phi_2}{\phi_1}\right| \quad \text{and} \quad e_{ext}^{21} = \left|\frac{\phi_{ext}^{21} - \phi_1}{\phi_{ext}^{21}}\right|, \tag{4.43}$$

and the fine-grid convergence index

$$GCI_{fine}^{21} = \frac{1.25 \cdot e_a^{21}}{r_{21}^p - 1} \tag{4.44}$$

are calculated for each variable ϕ.
Finally, for each quantity of interest, the mean value $GCI_{fine,mean}^{21}$ and the maximum value $GCI_{fine,max}^{21}$ of the fine-grid convergence index as well as the mean value of the apparent order p_{oa} of the method together the ratio of data points with oscillatory convergence R_{oc} are reported. Celik et al. [11] recommend to indicate the numerical uncertainty for computed profiles by adding error bars (e.g. Figure C.2).

CHAPTER 5

Comparison to experimental data

This chapter tests the applicability of the flow quality criteria and numerical methods introduced in Chapters 3 and 4 on two 90° pipe bends. These were chosen as the references because the examples discussed in Section 2.3 showed an excellent analogy of the flow phenomena in a 90° pipe bend and a Pelton turbine distributor system. Also, the branch lines of the *AxFeeder* combine straight and bent pipe sections. Thus, if the flow quality criteria and numerical methods match the experimental results for the cases of the 90° pipe bends, the numerical results for the parametric simulations of the *AxFeeder* are also trustworthy.

Numerical studies were conducted for two configurations of 90° pipe bends:

A) $R/D = 2$ and $\mathrm{Re} = 6.0 \cdot 10^4$, experimental data from Sudo et al. [104]

B) $R/D \cong 1$ and $\mathrm{Re} = 3.2 \cdot 10^5,\ 1.2 \cdot 10^6,\ 2.8 \cdot 10^6$ and $3.7 \cdot 10^6$, experimental data from Shiraishi et al. [92]

These studies investigated the impact of different meshes and turbulence models on loss generation, velocity contours, secondary flows and turbulence intensity.

5.1 Configuration A - Sudo

In 1998, Sudo et al. [104] conducted experiments on the steady, turbulent flow in a 90° pipe bend with smooth walls ($R/D = 2$, $\mathrm{Re} = 6.0 \cdot 10^4$).

5.1.1 Test configuration - A

The experimental apparatus is sketched in Figure 5.1. By a fan (1), the airflow is pushed into a settling chamber (2) and forced through a contraction (3) before it goes through a straight pipe section with $l/d = 100$, the upstream tangent (4). This guarantees fully developed turbulent flow conditions upstream of the bend (5). It is followed by the downstream tangent (6), a straight pipe with $l/d = 40$. Velocity measurements were made by rotating a single inclined hot wire [104]. Due to symmetric flow, these measurements were executed only in the bottom half of the

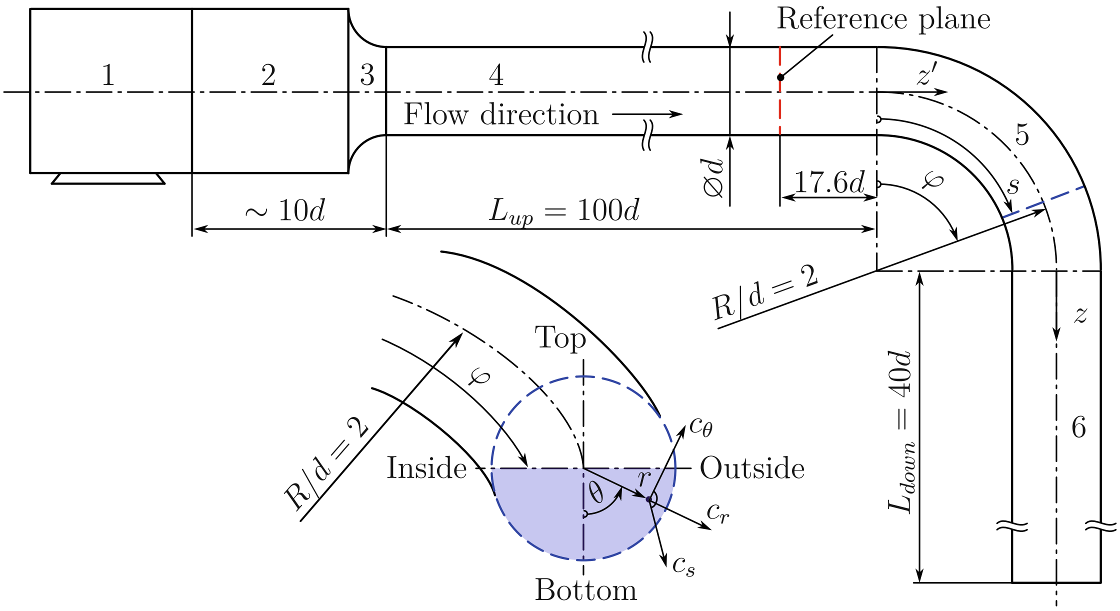

Figure 5.1: Test configuration of Sudo's experiment, recreated and modified from [104]. 1 Fan, 2 Settling chamber, 3 Contraction, 4 Upstream tangent, 5 90° bend, 6 Downstream tangent

pipe (shaded in blue in Figure 5.1). The static pressure was measured on the pipe wall between the upstream and the downstream tangents including the bend [104].

5.1.2 Investigated cases - A

In the first series of simulations, four meshes, differing in grid spacing from coarse to fine, were tested. Three of those meshes were made from hexahedral cells (Coarse H, Medium H and Fine H) and in one mesh, hexahedral cells were used in the straight pipe sections, and tetrahedrons were employed in the bend (Medium rM). All of these simulations were run with the k-ω Shear Stress Transport (SST) turbulence model.

In a second series of simulations, four turbulence models were investigated. These were: the k-ε model (kE) of Launder and Spalding [53] with the scalable wall function approach [3]; the k-ω Shear Stress Transport model of Menter [61] with automatic wall treatment for ω-based models [3]; further, the SST model with activated curvature correction (SSTCC) and the Baseline-Explicit Algebraic Reynolds Stress model (EARSM) of Menter, Garbaruk and Egorov [62]. All of these simulations were run with the Medium H mesh[1].

A detailed description of all cases and the relevant numerical settings for simulating the steady, incompressible and isothermal internal flow problem is presented in Appendix C.1.1.

[1]For the kE model cases, the boundary layer resolution was adjusted to meet the requirements of the wall function approach.

5.1.3 Station averaged quantities

Pressure coefficient

The distribution of the pressure coefficient C_p along the inside, bottom and outside wall of the pipe is shown in Figure 5.2 for different mesh sizes and turbulence models and compared against experimental values[2]. An explanation for the pressure coefficient at the outside wall being greater than at the inside wall can be derived from the radial equilibrium [16]

$$\frac{1}{\rho}\frac{\mathrm{d}p}{\mathrm{d}r} = \frac{c_s^2}{r} \, . \tag{5.1}$$

With the centripetal acceleration c_s^2/r always being positive, the radial direction pressure gradient is also positive. Thus, the pressure coefficient at the outside wall must be higher than at the inside wall of the 90° bend. The general decline of C_p along the streamwise coordinate can be attributed to the pressure losses due to the deflection of the flow and wall friction.

The differences between the C_p curves for the hexahedral meshes are almost negligible. This observation is supported by the results of the grid independence study in subsection Appendix C.1.2. Also, the resulting curves for the mixed-element mesh Fine rM are practically identical to the curves of the hexahedral meshes. Thus, for evaluating wall pressures, a discretisation with purely hexahedral cells or mixed hexahedral and tetrahedral cells gives plausible and reproducible results as long as the spatial resolution is sufficient.

The analysis of the C_p curves for cases with different turbulence modelling approaches in part b) of Figure 5.2 reveals general agreement between simulation results and experimental data. It is also notable that the kE model delivers its best results if the wall-adjacent mesh node lies within the region of validity of the logarithmic law of the wall. In contrast, the SST model delivers its best results if the wall-adjacent mesh node lies well within the viscous sublayer region of the boundary layer. Consequently, using a sufficiently refined grid near the walls is necessary for the SST model to predict the velocity profiles close to the walls as accurately as the modelling assumptions allow. The EARSM model delivers results indistinguishable from the two-equation eddy viscosity models but at slightly higher computational costs (Table C.2).

Intensity of secondary flow

Regardless of the meshing and turbulence modelling approach, all cases shown Figure 5.3 underestimate the intensity of secondary flow caused by the change of direction in the bend between $\varphi = 0°$ and $\varphi = 90°$. At the entrance to the bend at $\varphi = 0°$, simulation and experiments lie in good agreement. The gap between the simulated values of I_s and their respective experimental values increases through the bend. The biggest difference occurs at the bend exit at $\varphi = 90°$, where the

[2]Sudo et al. [104] did not specify measurement uncertainties for C_p.

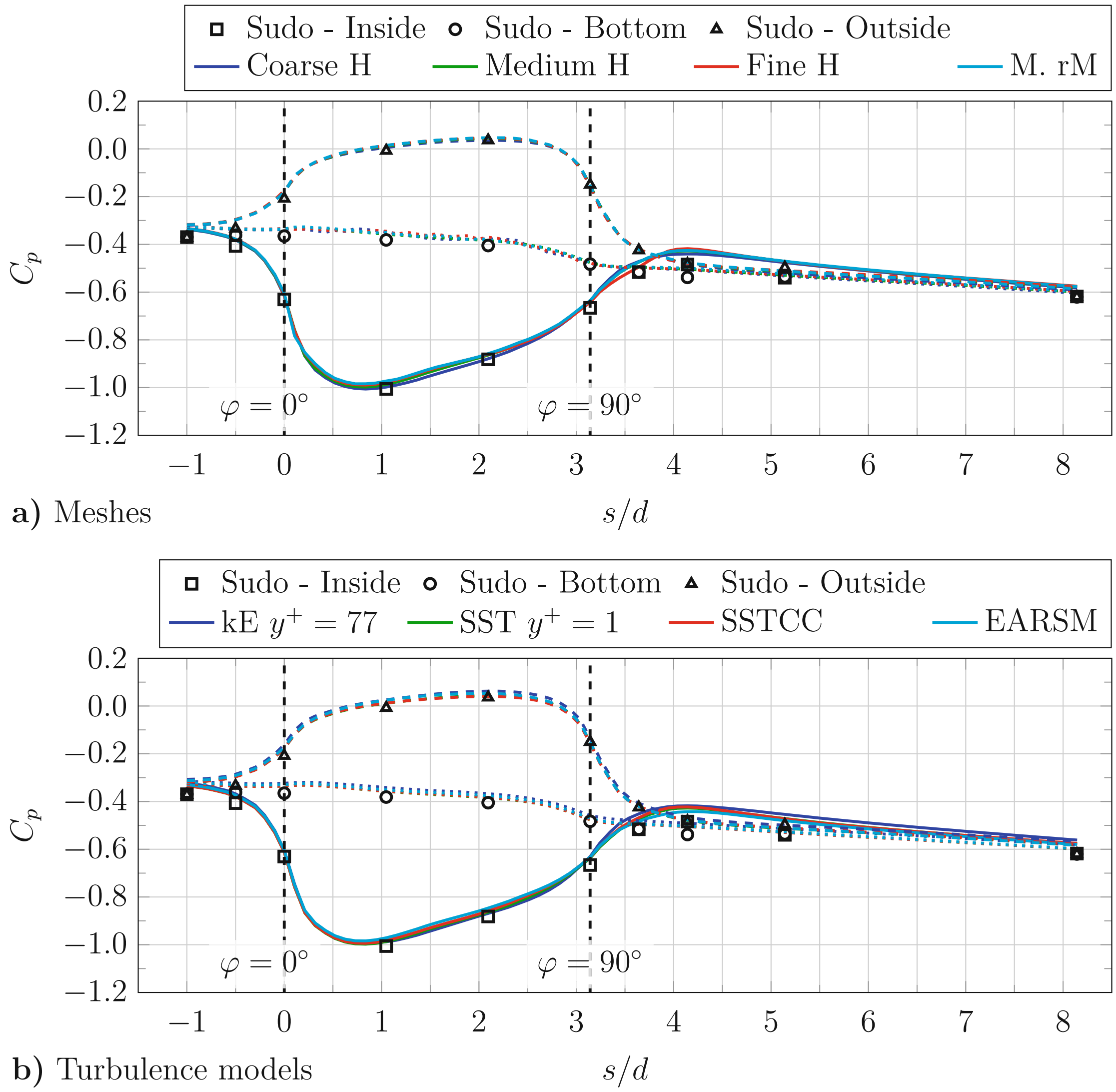

Figure 5.2: Longitudinal distributions of the pressure coefficient C_p at the inside (full stroke), bottom (dotted) and outside wall (dashed lines). Comparison of experimental data (measurement uncertainties not specified) of Sudo et al. [104] against CFD results for different meshes and turbulence models. M. = Medium.

secondary flow has the strongest intensity. This difference stays roughly the same until approximately 6 to 8 diameters downstream of the bend when most of the secondary flow has dissipated.

The differences in the I_s curves are again negligible for the investigated meshes. The cases with the SST turbulence model most closely match the experimental data. In the bend, the SST model without curvature correction is evidently slightly better, while in the downstream leg, the SSTCC model with curvature correction lies marginally closer to the experiments. The kE and EARSM models under-predict the secondary flow in the bend and the downstream leg.

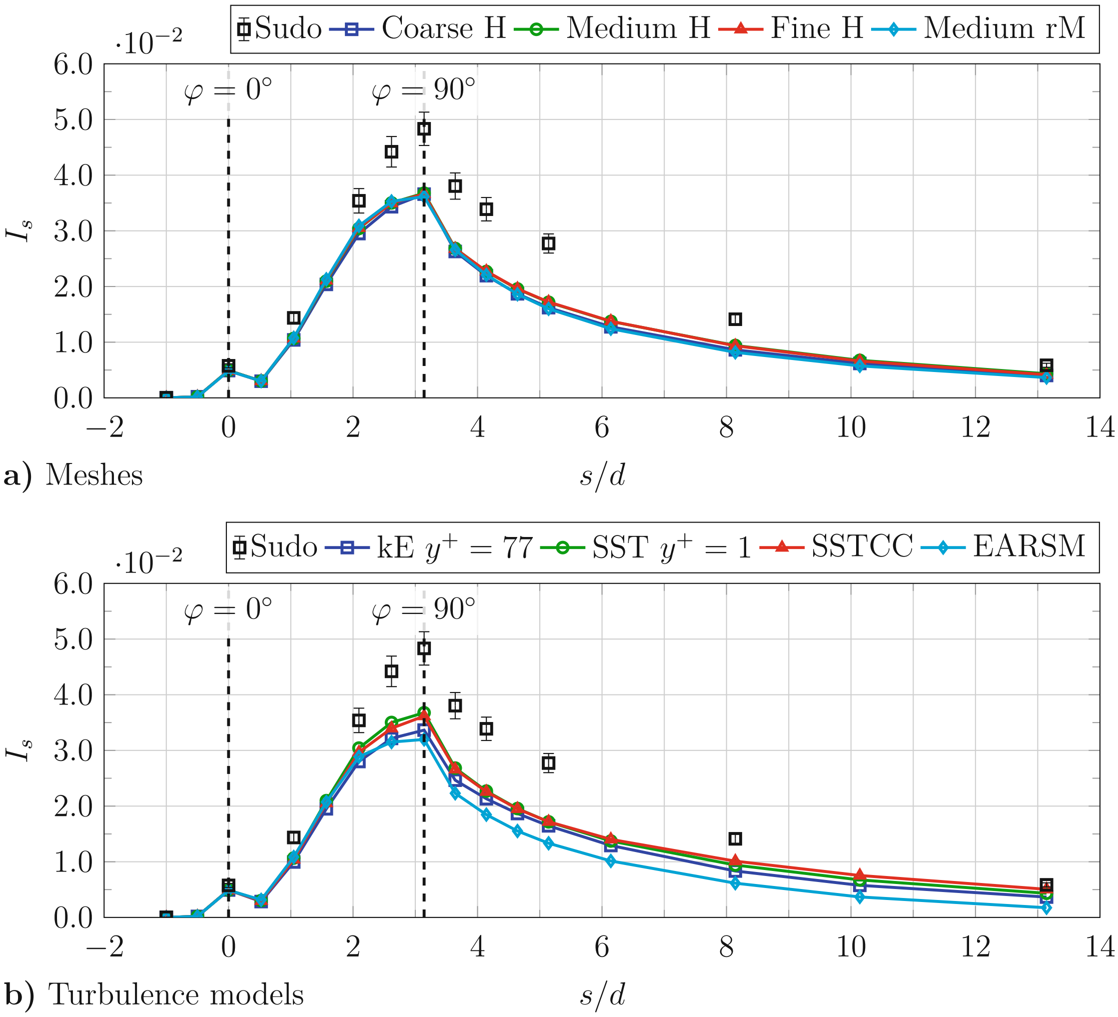

Figure 5.3: Longitudinal distributions of the area average intensity of secondary flow I_s. Comparison of experimental data (including measurement uncertainties) of Sudo et al. [104] against CFD results for different meshes and turbulence models.

Turbulence intensity

The distribution of the turbulence intensity[3] along the mean streamline is displayed in Figure 5.4. All simulated cases start from an approximate $I_t \sim 6 \cdot 10^{-2}$. This value is slightly larger than that of the experiments. However, it coincides pretty well with the correlation of Russo and Basse, Equation (3.47), which gives an estimated turbulence intensity of $5.87 \cdot 10^{-2}$ for the Reynolds number of $6 \cdot 10^4$. After the flow enters the bend, the turbulence intensity increases towards its maximum values, which are reached just downstream the exit of the bend. In the downstream leg, there is a good agreement between the simulated data and the experimental data for all cases, regardless of the grid resolution. All tested meshes predict values of I_t within the measurement uncertainty range for most parts of the region of interest.

[3] Sudo et al. [104] specify the uncertainty for the turbulence intensity k_a as defined in Equation (3.48). A conversion of the measurement uncertainty to I_t is explained in Appendix A.3.2.

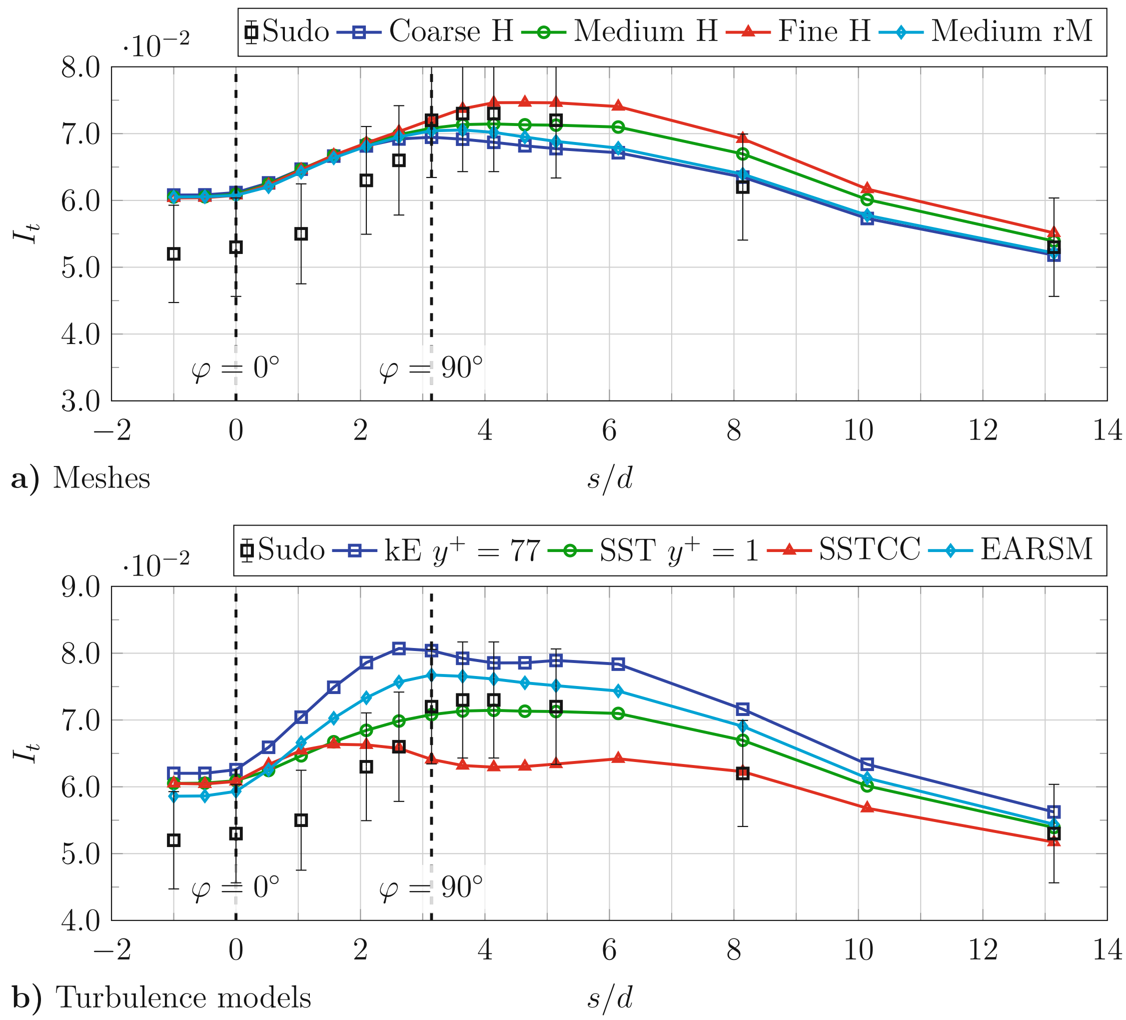

Figure 5.4: Longitudinal distributions of the area average turbulence intensity I_t. Comparison of experimental data (including measurement uncertainties) of Sudo et al. [104] against CFD results for different meshes and turbulence models.

Typically, the tetrahedral cells in the Medium rM mesh lead to higher numerical dissipation and, thus, a lower level of turbulent kinetic energy in the pipe than the Medium H mesh with purely hexahedral cells. The observed differences lie in the same margin as those between the Coarse H and the Medium H meshes.

In part b) of Figure 5.4, the effect of different turbulence models on the area average turbulence intensity along the mean streamline is compared against the experimental results. The kE model case shows the sharpest increase of the turbulence intensity in the bend and the highest levels of I_t in the downstream leg. This behaviour is attributed to the issue of standard two-equation turbulence models producing excessive turbulent kinetic energy upstream of areas with stagnating flow [42]. In the case of the pipe bend, the area of stagnating flow is located on the outside of the bend, which causes I_t to rise to higher values reached at lower s/d.

In the cases using the SST and the EARSM model, the turbulence intensity rises moderately in the bend, thus resembling the experimental data quite well, especially in and after the bend. With the EARSM model case, I_t climbs steeply in the bend and reaches peak levels approximately in the middle of the kE model and the SST model cases. The effect of curvature correction leads to an early decline of I_t in the SSTCC case. Moreover, in this case, I_t never reaches the same maximum values as for the SST and EARSM model cases. A likely explanation is that the rotation function (Equation (4.23)) and especially the included production limiter (Equation (4.24)) of the SSTCC model hinder the production of turbulent kinetic energy and thus I_t a bit too much for such a type of flow problem [95, 97]. Overall, the SST model with $y^+ = 1$ matches the experimental data best.

5.1.4 Local flow quantities

The local flow velocities were evaluated at eleven stations, starting one diameter upstream of the bend and ending ten diameters downstream of the bend. For all these stations, the streamwise velocity c_s was evaluated in a horizontal plane from the inside to the outside wall of the pipe and in a vertical half-plane from the bottom of the pipe to its centre. Also, the circumferential velocity c_θ was evaluated in the vertical half-plane from bottom to centre. All velocities were normalised by the mass averaged streamwise velocity $c_{s,ref}$ at the reference plane. The normalised flow velocities are plotted in Figure 5.5 for the cases with different meshes and in Figure 5.6 for the cases with different turbulence models. In these figures, the top plot depicts the streamwise velocity in the horizontal plane, and the mid and bottom plots depict the streamwise and the circumferential velocity in the vertical half-plane.

The velocity curves for the different meshes almost overlap at most stations. Differences appear towards the inside wall of the bend starting at station $\varphi = 60°$. Here, the pressure increases near the inside wall; simultaneously, the flow is decelerated, which causes a deficit in the streamwise velocity. This deficit is also visible in the contour plots of Figure 5.7. Nevertheless, the velocity curves reveal that neither mesh can fully capture this phenomenon. This difference between CFD results and experiments has its most considerable extent at the bend exit ($\varphi = 90°$) and becomes less as the flow is mixed out when moving downstream. The mid plot of Figure 5.5 shows a better agreement between simulated and measured streamwise velocities in the vertical half-plane for all mesh cases. The lower plot in this figure gives an even better agreement of simulation data and experiments for the circumferential velocity in this vertical half-plane. Also, the case with the mixed element mesh can replicate the circumferential velocity curves with satisfactory precision.

The velocity curves predicted in the different turbulence model cases match the experimental data satisfactorily, except for the distortion of the velocity profiles at the inside of the bend. Notably, in the cases with turbulence models that integrate the velocity profile to the wall (SST, SSTCC and EARSM; all with $y^+_{max} < 1$), this distortion of the velocity profiles is predicted too early. Here, the wall function approach of the kE model proves superior. As the flow moves along the bend, the streamwise velocity deficit becomes more and more pronounced at the inside of

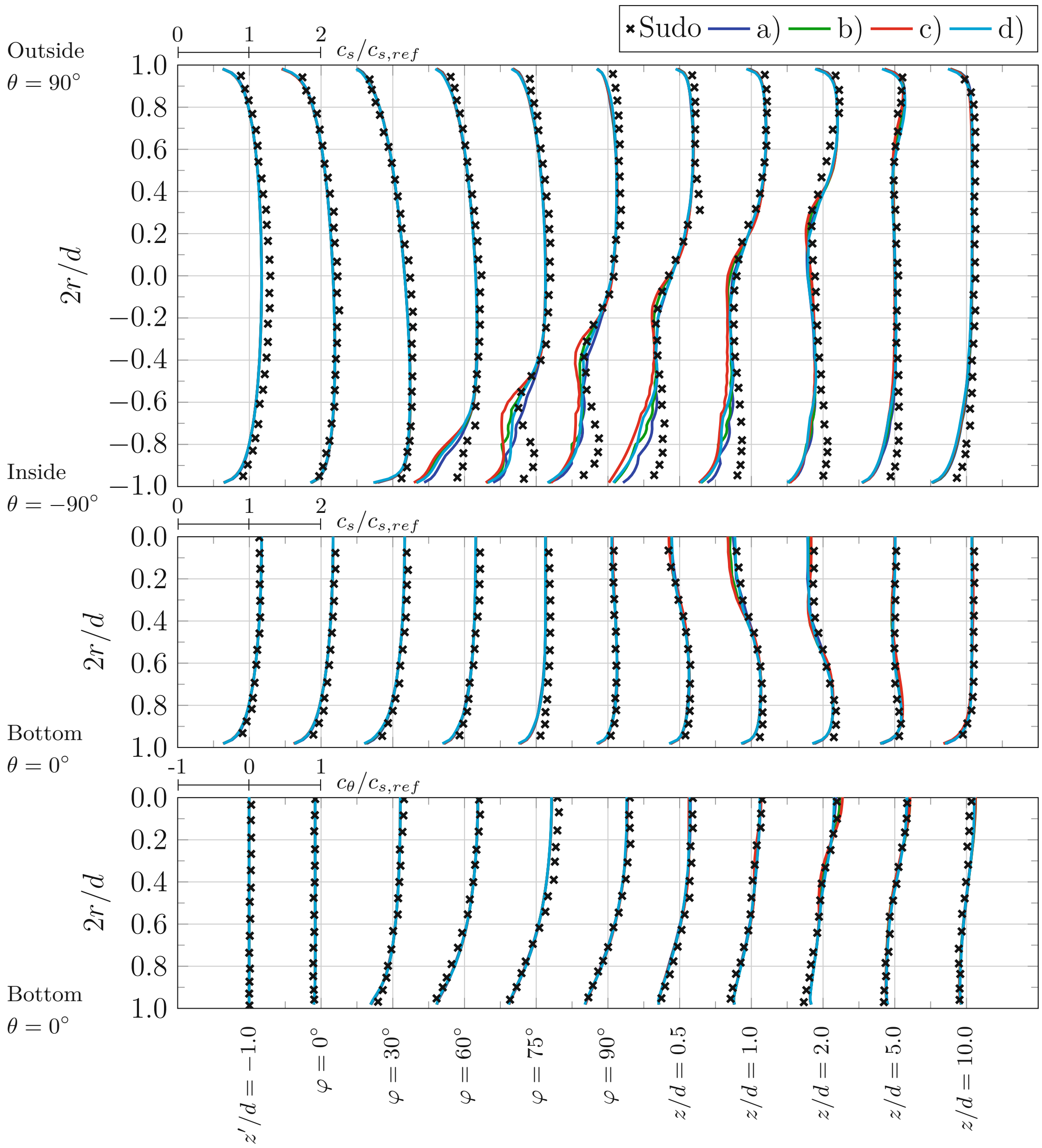

Figure 5.5: Velocity distributions at several stations for different meshes. a) = Coarse H, b) = Medium H, c) = Fine H, d) = Medium rM

the wall. The ω-based turbulence models (SST, SSTCC and EARSM) can capture this deficit to an observable extent. In contrast, the velocity curves predicted by the kE model deviate noticeably more from the experimental data. Overall, the kE turbulence model cannot accurately compute the velocity deficit associated with the deceleration of the flow at the inside of the bend[4]. This is especially seen at stations $\varphi = 75°$ and $\varphi = 90°$.

In contrast, the two cases using the SST model in combination with a finely resolved wall layer mesh, SST $y^+ = 1$ and SSTCC, can partially reproduce the velocity deficits in the curves of the streamwise velocity. The EARSM model performs

[4]For further discussion on the features of the kE model see Section 4.2.1.

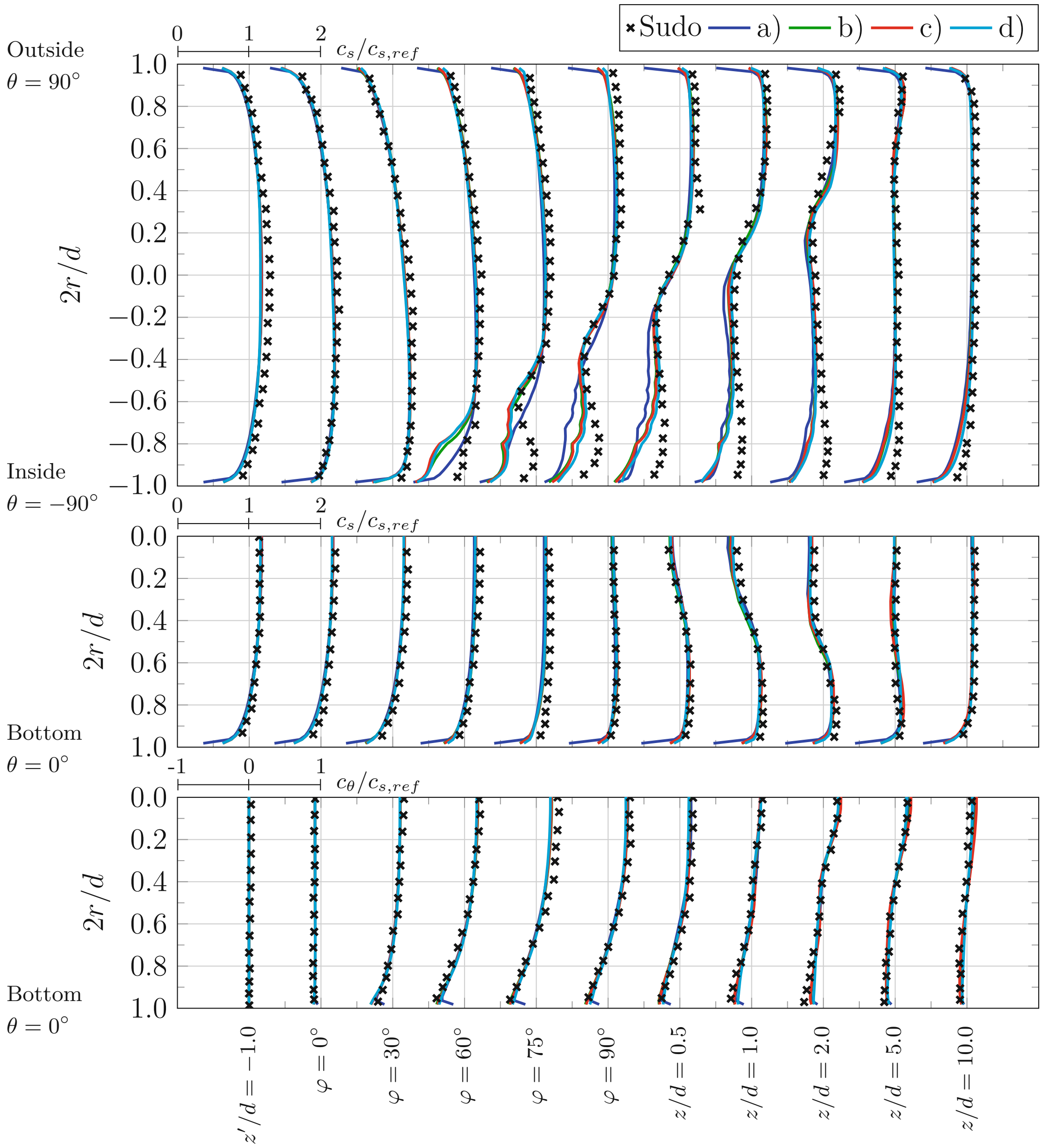

Figure 5.6: Velocity distributions at several stations for four turbulence models. a) = kE $y^+ = 77$, b) = SST $y^+ = 1$, c) = SSTCC, d) = EARSM

similarly to the SST model with $y^+ = 1$. The simulated curves deviate from the experimental data towards smaller values of $2r/d$, i.e., closer to the inside wall. Just as in the SST model cases, the velocity deficit at the inside wall is predicted too early (top plot of Figure 5.6). Apart from that, the simulated profiles follow the experimental curves of the streamwise velocity very well.

Except for the weaknesses in predicting the distortion of the velocity profiles at the inside of the bend, the agreement between the simulated velocity curves and the experimental ones in the horizontal plane is satisfactory. The simulation results for the streamwise and circumferential velocities in the vertical half-plane meet the experimental data, as in the cases with different meshing approaches.

5.1.5 Contour plots

In order to better assess flow structure downstream the pipe bend, contours of the normalised streamwise velocity $c_s/c_{s,ref}$ and the turbulence intensity I_t are plotted in Figure 5.7 for the cases with different meshes and in Figure 5.8 for the cases with different turbulence models. Each of these figures is structured such that the upper half of the figure shows the velocity contours and the lower half shows the contours of turbulence intensity. In every line, for one station, four cases are shown. For every case, the simulation data is depicted in the upper half of the plot, and the experimental contours are depicted in the lower half. The contour bands of the simulation data are adjusted to meet the values of the contour bands from the experiments. Therefore, the minimum and maximum values of the legends are determined by the respective values of the experimental contours. The plot view is oriented towards the upstream direction. Thus, the left of the circular plots corresponds to the inside of the bend, and the right corresponds to the outside.

Cases Medium H and Fine H can emulate the contours of the experimental streamwise velocities with reasonable accuracy. The plots from the Coarse H case differ slightly from the other two meshes. This mesh is too coarse to precisely capture the distortion of the velocity contours on the inside of station $\varphi = 90°$. While mesh Medium rM delivers a result similar to meshes Coarse H and Medium H, mesh Fine H exaggerates the size and shape of the distortion zone, forming a blue, mushroom-shaped contour at the centre of the pipe at station $z/d = 1$. Some discrepancies between simulation results and experiments are noticeable downstream of the bend at station $z/d = 5$ for all cases, where the remains of the mushroom-shaped distortion zone are still recognisable.

All cases shown in Figure 5.7, for which the mesh was varied, have difficulties recreating the turbulence intensity contours. At the exit of the bend at $\varphi = 90°$, the CFD results of cases Medium H, Fine H and Medium rM show a noticeably better similarity to the experimental contours than the results of case Coarse H. A mushroom-like structure extending from the inside wall to the centre of the pipe appears downstream. This structure is prominent in cases Medium H and Fine H and less in case Medium rM. It is invisible in case Coarse H. The most recognisable difference between experiments and simulation is a red ring close to the wall at station $z/d = 5$ in the simulation results. This red ring contour only appears in a thin annulus beside the wall. It comes from the correctly predicted high values of the turbulence intensity in the turbulent boundary layer. In the experiments, this ring of high I_t was most likely present as well, but not visually captured by the applied measurement techniques; therefore, it was not visible in the contour plots.

When comparing the plots with the different turbulence models employed in Figure 5.8, the velocity contours at station $\varphi = 90°$ show the distorted velocity contours on the inside of the bend to a reasonable extent. This distortion is somewhat less pronounced in the case using the kE model than in the SST or Reynolds stress model cases. Another phenomenon that occurs predominantly in the kE and EARSM cases is the distinctively low velocity gradient at the outside of the bend. For the

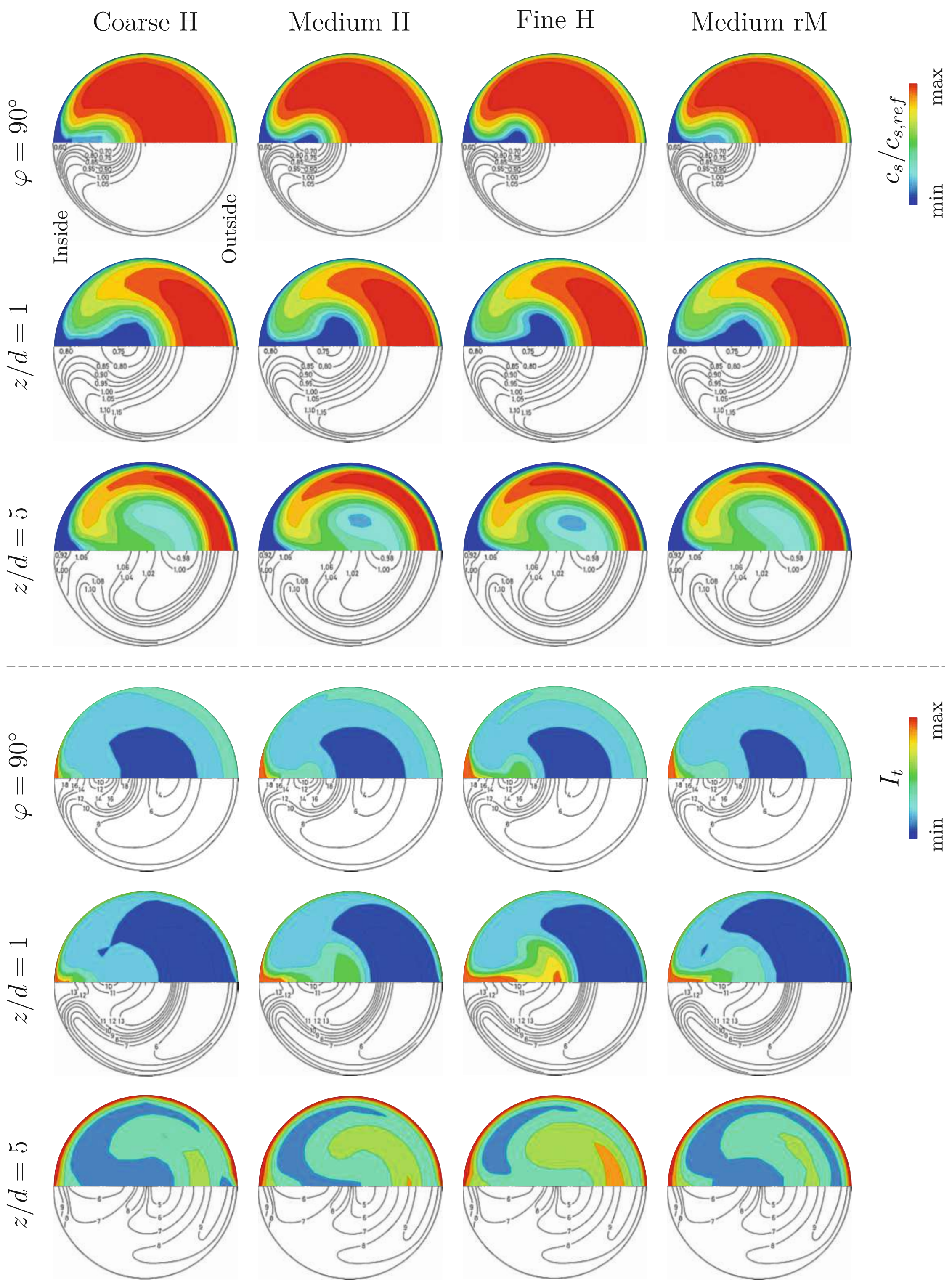

Figure 5.7: Contour plots of normalised streamwise velocity $c_s/c_{s,ref}$ (upper half) and turbulence intensity I_t (lower half) at several stations downstream the bend compared to experimental results from Sudo et al. [104].

kE model case, this gradient may be caused by the overproduction of turbulent kinetic energy at the outside of the bend, resulting in high turbulent viscosity values and increased velocity mixing.

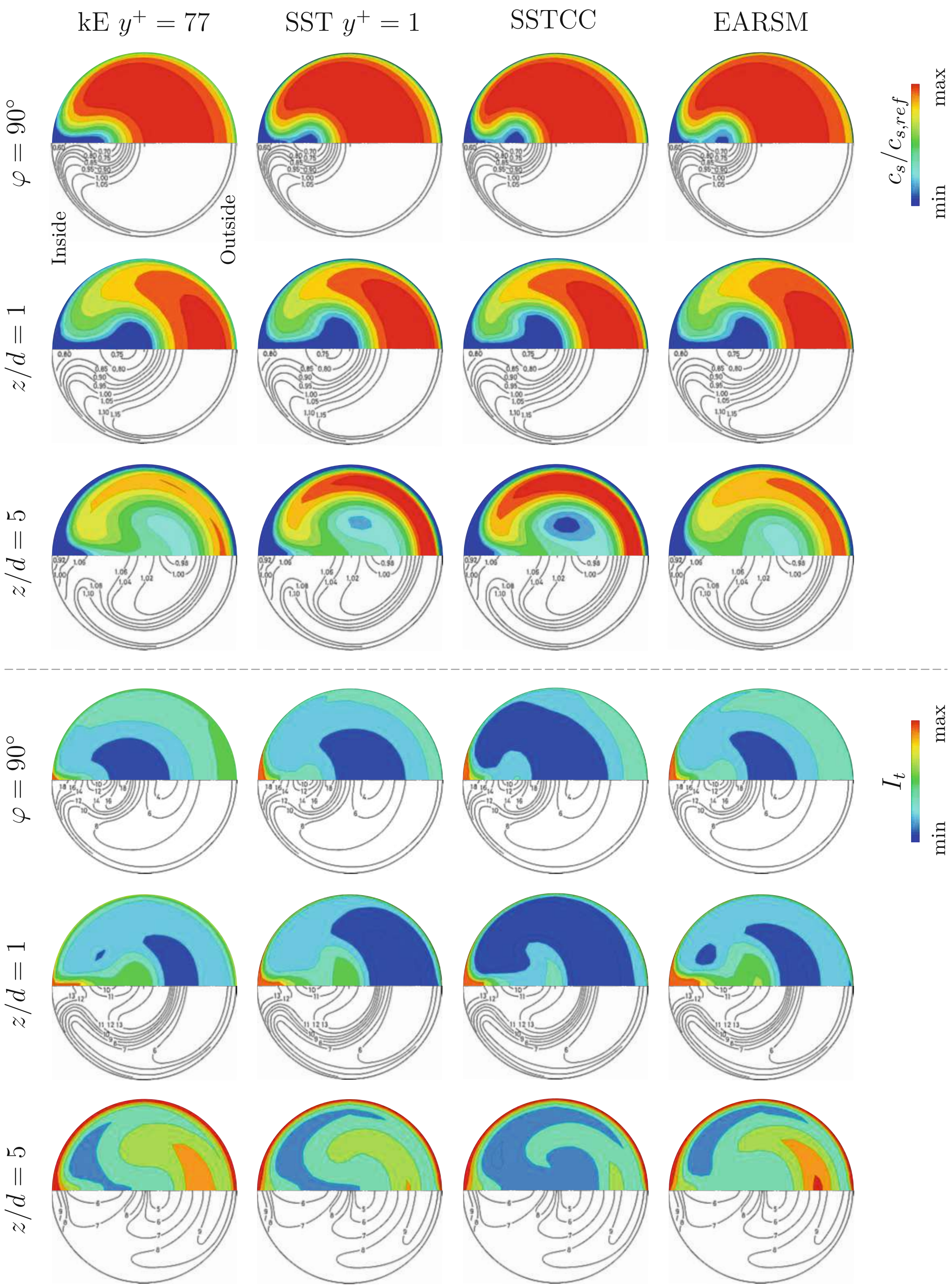

Figure 5.8: Contour plots of normalised streamwise velocity $c_s/c_{s,ref}$ (upper half) and turbulence intensity I_t (lower half) at several stations downstream the bend compared to experimental results from Sudo et al. [104].

At station $z/d = 1$, all turbulence model cases reproduce the experimental flow field reasonably well. A detailed examination of the plots of the SST models and the Reynolds stress model at this station reveals that the mushroom-shaped contour in the centre of the pipe is more prominent than in the experiments. This mushroom-shaped structure is also visible in the turbulence intensity plots of the corresponding cases. Generally, all turbulence model cases encounter issues correctly predicting all details of the turbulence intensity fields. Thus, a higher uncertainty for any turbulence-related quantity has to be considered.

At station $z/d = 5$, all turbulence models again reproduce the experimental flow field reasonably well. This time, the cases using the SST $y^+ = 1$ and SSTCC models show a small zone with a pronounced velocity deficit off the centreline. The turbulence intensity plots of all eddy viscosity models and the Reynolds stress model show a much better agreement with their experimental counterparts than at the stations upstream. Nevertheless, assessing the detailed contour bands reveals that all models still have issues closely reproducing the values of the experiment.

5.2 Configuration B - Shiraishi

While Sudo et al. [104] focused on the flow through a 90° pipe bend with large curvature radius ($R/D = 2$) at a low Reynolds number of $6.0 \cdot 10^4$, the experiments of Shiraishi et al. [92] allow for validation of pressure losses and local flow velocities in a 90° pipe bend with small curvature radius ($R/D \cong 1$) at a wide range of Reynolds numbers ($3.2 \cdot 10^5$ to $3.7 \cdot 10^6$).

5.2.1 Test configuration - B

The test rig of Shiraishi et al. [92] is sketched in Figure 5.9. From a pressurised rectifying tank (1), the flow (working fluid: water) passes the bellmouth (2) into the upstream tangent (3). This design provides a uniform velocity distribution upstream of the sharp bend (4). The bend is followed by a downstream tangent (5). Local flow velocities were evaluated by laser Doppler velocimeters upstream (I - $2.77d$) and downstream (II - $0.18d$, III - $0.62d$ and IV - $1.12d$) the bend. Pressure transducers were located at several stations upstream, in and downstream of the bend; relevant stations for this thesis are B, D and L.

5.2.2 Investigated cases - B

In the first series of simulations, different meshes (Coarse H, Medium H and Fine H with hexahedral cells and Medium rM with both hexahedral and tetrahedral cells) were tested with the k-ω Shear Stress Transport turbulence model and in a second series of simulations, the same four turbulence models (kE, SST, SSTCC and EARSM) as in Section 5.1, were investigated. If not specified explicitly, again, all of these simulations were run with the Medium H mesh[5].

A detailed description of all cases and the relevant numerical settings for modelling the flow as steady, incompressible and isothermal is presented in Appendix C.2.1.

[5] For the kE model cases, the boundary layer resolution was adjusted to meet the requirements of the wall function approach, resulting in mesh Fine H kE.

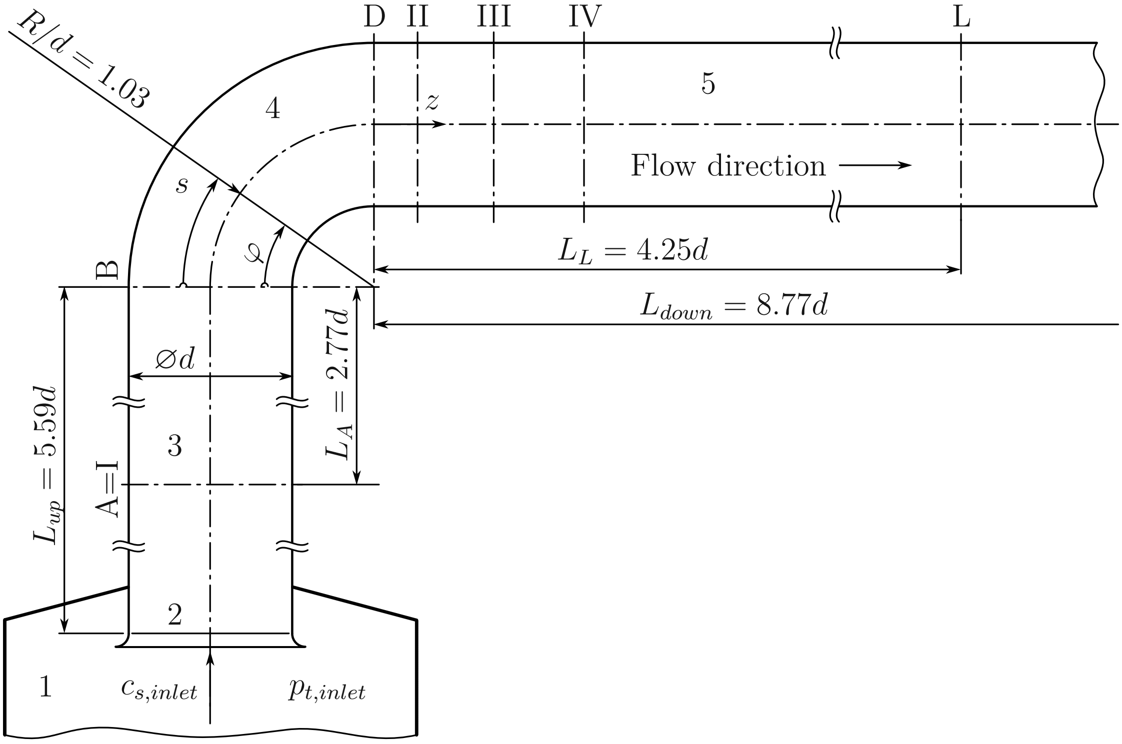

Figure 5.9: Test configuration of Shiraishi's experiment, recreated and modified from [92]. 1 Rectifying tank, 2 Bellmouth, 3 Upstream tangent, 4 90° bend, 5 Downstream tangent

5.2.3 Losses

Total pressure losses

The flow in a 90° pipe bend can be classified into three regimes according to their Reynolds number [38]:

a) Subcritical regime for $\mathrm{Re} < 1 \cdot 10^5$

b) Transition regime for $1 \cdot 10^5 < \mathrm{Re} < 2 \cdot 10^5$

c) Postcritical regime for $\mathrm{Re} > 2 \cdot 10^5$

This classification is connected with a strong dependency of the total pressure loss coefficient on the Reynolds number, exemplarily shown in Figure 5.10.

In the subcritical regime, the boundary layer is laminar. Thus, the flow separates early after the entrance in the bend (low values of the separation angle α_{sep}) and forms the large separation zone (biggest height h_{sep}). Moreover, the flow takes a long distance l_{sep} to reattach[6]. Consequently, the total pressure loss coefficient is significantly higher than in the other regimes.

In the transition regime, the boundary layer becomes turbulent; thereby, its thickness is reduced, and the effective flow channel becomes less restricted. This results

[6]The length of the separation zone l_{sep} can thus also be interpreted as a reattachment length.

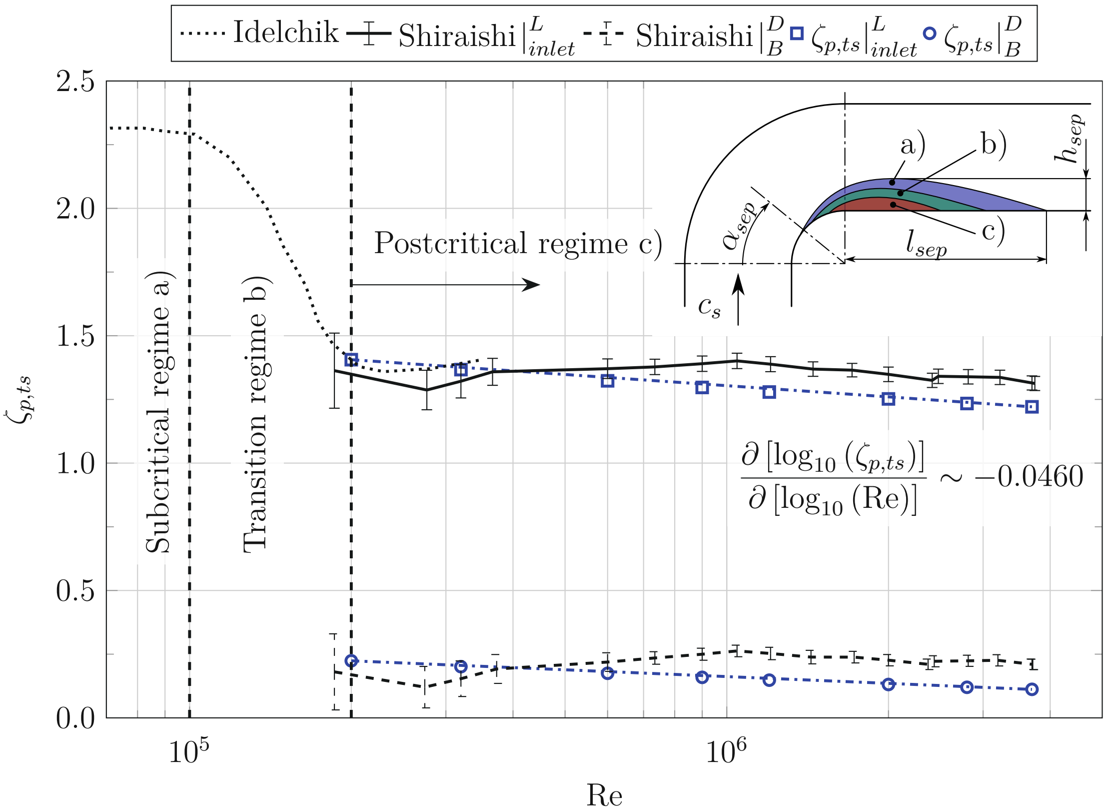

Figure 5.10: Total pressure loss coefficients against the Reynolds number evaluated for the case with mesh Medium H and SST $y^+ = 1$ turbulence model compared to the experimental values of Shiraishi et al. in [92] and Idelchik in [38].

in a sharp decline of the total pressure losses[7] that, in pipe flows, occurs typically between $1 \cdot 10^5 < \mathrm{Re} < 2 \cdot 10^5$. The Reynolds number, at which this sudden drop of the losses starts, is defined as the critical Reynolds number Re_{crit} and the Reynolds number at which the losses level off is defined as the turbulent Reynolds number Re_{turb} [38]. In the case of a 90° pipe bend, assuming a critical Reynolds number of around $1 \cdot 10^5$ and a turbulent Reynolds number of around $2 \cdot 10^5$ is plausible.

In the postcritical regime, the boundary layer has become fully turbulent. The separation starts at the highest values of the separation angle α_{sep}, and the separation zone is the smallest. The loss coefficient stays roughly constant for a wide range of Reynolds numbers, with a tendency to decrease slightly at higher Reynolds numbers $\mathrm{Re} > 1 \cdot 10^6$. Shiraishi et al. [92] explain this as a direct result of two simultaneous effects: the declining friction in the boundary layer of a hydraulically smooth pipe and the effect of separation in the elbow.

Idelchik [38] points out that the phenomena described above are similar to those of a flow around a cylinder or a sphere, where a sudden drop of the drag coefficient is observed at similar Reynolds numbers [6]. The selected simulation methods

[7]Idelchik [38] calls this decline "resistance crisis".

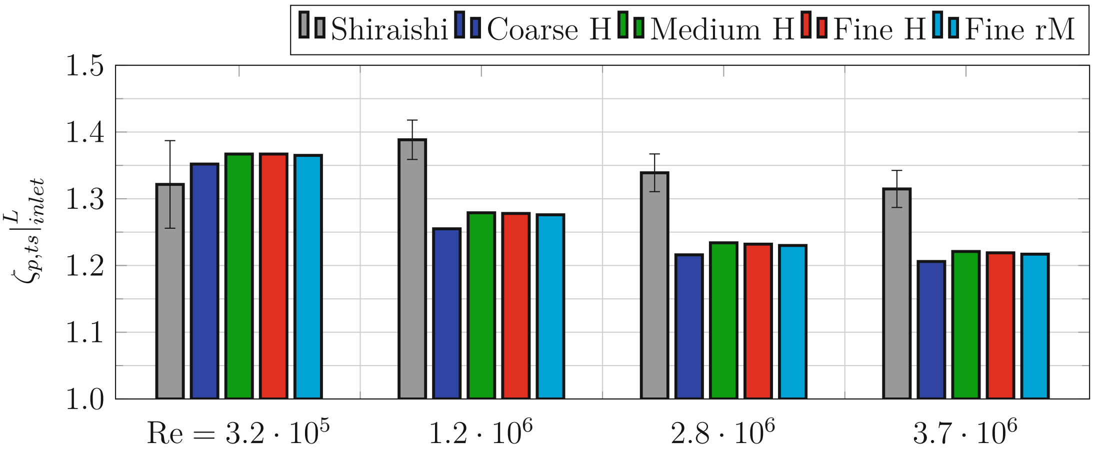

a) Losses from inlet to station L

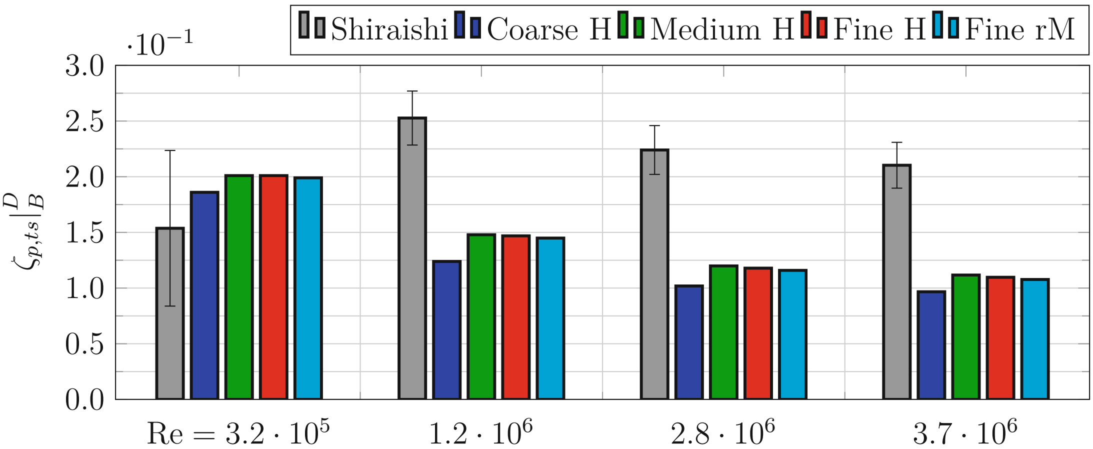

b) Losses from station B to D (bend only)

Figure 5.11: Total pressure loss coefficients for four Reynolds numbers and four meshes compared to the experimental of Shiraishi et al. [92].

Appendix C.2.1 are most suited for computing flow in the postcritical regime.

In Figure 5.10, experimental data from Idelchik [38] and Shiraishi et al. [92] is compared to simulation results for cases with mesh Medium H and the SST turbulence model. In this figure, the total pressure loss coefficient in the form of Equation (3.11) is evaluated between the inlet and station L ($\zeta_{p,ts}|_{inlet}^{L}$) and stations B and D ($\zeta_{p,ts}|_{B}^{D}$). As described by Shiraishi et al. [92], the values of

$$\zeta_{p,ts}|_{B}^{D} = \zeta_{p,ts}|_{inlet}^{L} - 1 - \lambda \cdot \left(\frac{L_{up} + 0.5R\pi + L_{down}}{d} \right) \tag{5.2}$$

were achieved by subtracting the exit and friction losses from $\zeta_{p,ts}|_{inlet}^{L}$.

The comparison of the total pressure loss curves evaluated from the inlet to station L in Figure 5.10 shows that the CFD simulations can capture the friction effect in the boundary layer very well. As the absolute differences between the simulated values of $\zeta_{p,ts}|_{inlet}^{L}$ and the corresponding experimental values are almost the same as the

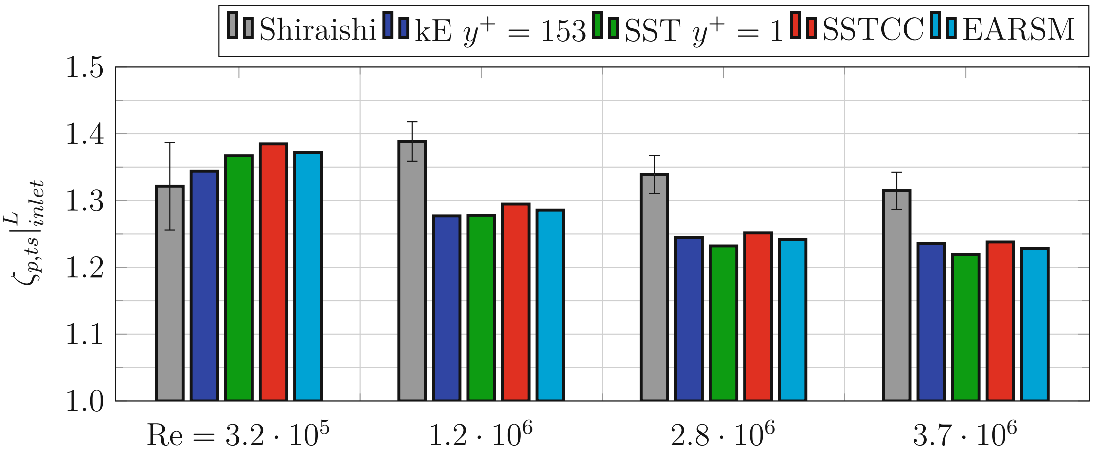

a) Losses from inlet to station L

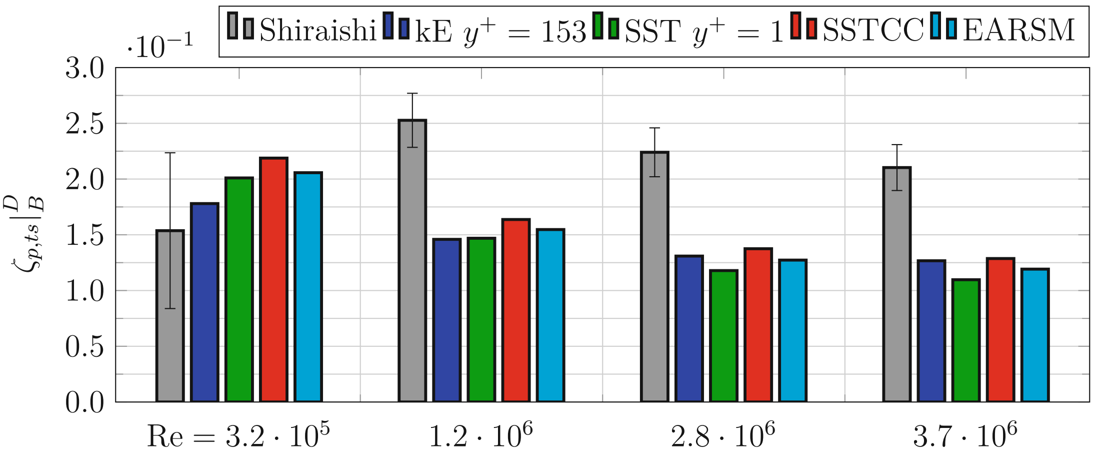

b) Losses from station B to D (bend only)

Figure 5.12: Total pressure loss coefficients for four Reynolds numbers and four turbulence models compared to the experimental values of Shiraishi et al. [92].

differences between the simulated values of $\zeta_{p,ts}|^{D}_{B}$ and the respective experimental values, the deviation between the simulation results and the experimental data can be entirely attributed to the uncertainty in the prediction of the flow separation in the elbow.

A direct comparison of the loss coefficients predicted in cases with four different meshes is plotted in Figure 5.11 for the Reynolds numbers[8] $3.2 \cdot 10^5$, $1.2 \cdot 10^6$, $2.8 \cdot 10^6$ and $3.7 \cdot 10^6$. While all meshes except Coarse H deliver similar results, only for the lowest Reynolds number $3.2 \cdot 10^5$, the values predicted by simulation lie within the margin of error of the experimental values. Again, this discrepancy arises from uncertainty in predicting the flow separation in the elbow at high Reynolds numbers.

The impact of a variation of the turbulence model on the loss coefficients is evaluated

[8]These four Reynolds numbers were selected because experimental data of the velocity plots is given for these exact Reynolds numbers.

Parameter	Meshes	a)	Turb. models	b)
a_0	-0.0075	0.0000	-0.0016	-0.0039
a_1	0.8829	0.8734	0.7849	0.8522
R^2	0.9734	0.9994	0.6856	0.9732

Table 5.1: Offset a_0, gradient a_1, and coefficient of determination R^2 of the linear trend lines. a) = Data points with mesh Fine rM only; b) = Turbulence models without kE.

in Figure 5.12. All four turbulence models deliver very similar results for the cases with high Reynolds numbers. Only in the case of the lowest Reynolds number are all turbulence models able to match the experiment within the margin of error. However, the variation in the predicted loss coefficients is also the highest for the low Reynolds number. At this Reynolds number, the kE model using wall functions[9] shows the lowest deviation from the experiments and the SSTCC model with activated curvature correction the highest.

Dissipation

In this subsection, the different techniques for loss accounting are compared, and the second law analysis method introduced in Section 3.3.2 is verified against the classical approach presented in Section 3.3.1. Therefore, the resulting values for the dissipation power coefficient $\zeta_\Phi|_A^L$, computed by the second law analysis method using Equation (3.23) are benchmarked against the values of the power loss coefficient $\zeta_{PmTE}|_A^L$, computed by the classical approach using Equation (3.14).

Part a) of Figure 5.13 compares the results of four different meshes and part b) compares the results of four different turbulence models. When evaluated between stations A and L, the dissipation power coefficient is lower than the corresponding power loss coefficient. Thus, all data points lie below the 45° line, indicating equality between the coefficients $\zeta_\Phi|_A^L$ and $\zeta_{PmTE}|_A^L$. The cases with the Coarse H mesh and the kE turbulence model especially underpredict the dissipation and thus achieve lower dissipation power coefficients. The linear trend lines[10] $y = a_0 + a_1 x$ calculated from the numerical data points show an offset to the 45° line that declines with increasing Reynolds number (towards the lower left corner of the diagrams). The red trend lines were calculated using all data points. Because of the outliers from the kE model case, this results in a low coefficient of determination R^2 for the cases with varying turbulence models. Therefore, a second trend line (green) was computed, where the data points from the kE model were excluded. This trend line fits the presented data very well. The coefficient a_0, which symbolises the offset from the vertical axis, is almost zero, which matches the expectation. If only data points from the cases with the Fine rM mesh (for which the SST turbulence model with $y^+ = 1$ was employed) are considered for the trend line

[9]The area average of y^+ is about 153 in this case.
[10]The procedure to calculate trend lines is explained in Appendix A.2.

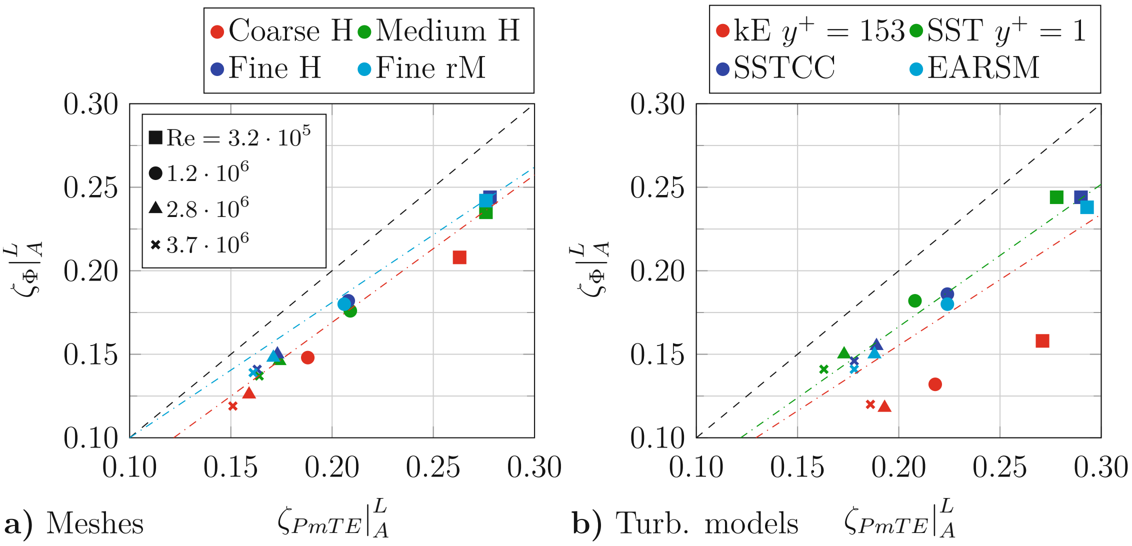

Figure 5.13: Comparison of power loss coefficients and dissipation power coefficients evaluated between stations A and L. Linear trend lines (dashdotted) are plotted for all cases (red), for the case with mesh Fine rM (cyan) and for all cases with the kE data excluded (green). Data points for high Reynolds numbers lie towards the lower left.

and a zero offset from the vertical axis is enforced, the slope coefficient a_1 becomes 0.8734. This configuration would be the closest match to the eventually chosen setup of the *AxFeeder*. All trend line coefficients are summarised in Table 5.1.

To quantify the differences between the dissipation power coefficient $\zeta_\Phi|_A^L$ and the power loss coefficient $\zeta_{PmTE}|_A^L$, in Figure 5.14, the deviations of each case averaged over all tested Reynolds numbers is plotted. The corresponding standard deviations indicate the measure of uncertainty. For most models, the ratio $\zeta_\Phi|_A^L \,/\, \zeta_{PmTE}|_A^L$ lies between 0.8 and 0.9, whereas for cases with refined mesh, the deviation becomes smaller, thus the ratio becomes closer to unity. The case with mesh Coarse H is slightly below the previously stated range, but the case with the kE model falls off drastically. This fall-off can be explained by the observation of Kock and Herwig [48, 49], that both the viscous and turbulent entropy production peak close to the wall. Melzer et al. [60] emphasise that the peak in entropy production is underestimated, especially when wall functions are used or the wall layers are not sufficiently resolved. This is the case with the kE model and when the mesh is not refined sufficiently. The low uncertainty indicates that the ratio of power coefficients is changing marginally with the Reynolds number. To further elaborate on this observation, both coefficients were plotted together with their ratio $\zeta_\Phi|_A^L \,/\, \zeta_{PmTE}|_A^L$ against the Reynolds number in Figure 5.15. Analogously to the total pressure loss coefficients in Figure 5.10, there is a steep decline at low Reynolds numbers, which levels off when the boundary layer has become fully turbulent. Then, there is a moderate decline of $\zeta_{PmTE}|_A^L$ and $\zeta_\Phi|_A^L$, whereas the ratio $\zeta_\Phi|_A^L \,/\, \zeta_{PmTE}|_A^L$ stays almost constant at around 0.84. It decreases only marginally with increasing Reynolds number.

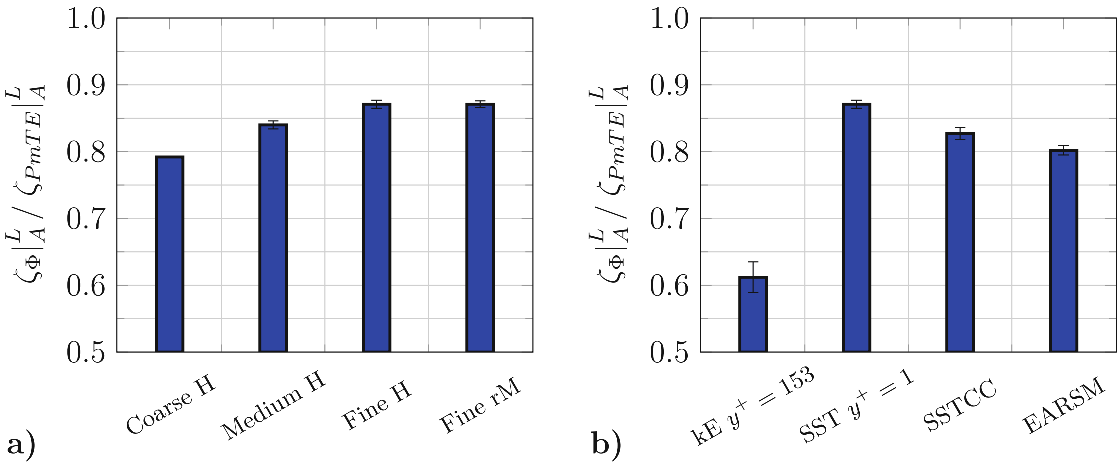

Figure 5.14: Averages and uncertainties of the ratios of the dissipation power coefficient to the power loss coefficient $\zeta_{\Phi}|_A^L \,/\, \zeta_{PmTE}|_A^L$.

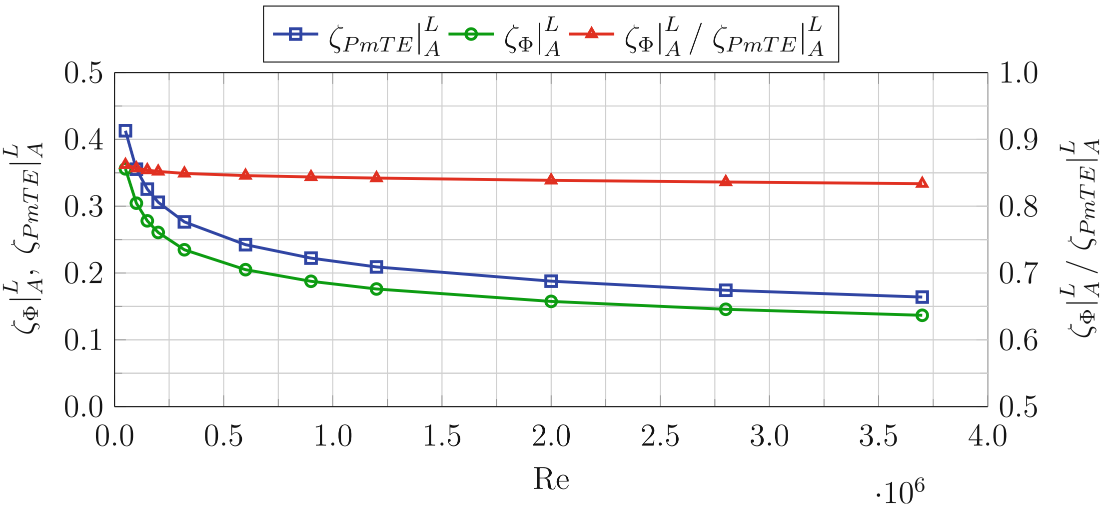

Figure 5.15: Power loss coefficient, dissipation power coefficient and their ratio against the Reynolds number evaluated for cases with Medium H mesh and SST turbulence model.

The main discrepancy between the two methods of loss accounting in pipe flows shall be explained exemplary by the case of $\mathrm{Re} = 1.2 \cdot 10^6$, mesh Fine H and SST turbulence model[11].

At first, in part a) of Figure 5.16, the longitudinal distribution of the mass average total pressure is plotted against the streamwise coordinate. The total pressure is normalised by the total pressure in station A, which is the beginning of the domain of interest for this comparison. In section AB and far downstream the bend[12], the pressure curve approaches a tangent with gradient $-\lambda$, the pipe friction

[11] To allow for precise evaluation of the effects in the downstream tangent, the domain was extended to well over $50d$ downstream the bend. To comply with the configuration of Shiraishi et al. [92], the upstream tangent was not altered.

[12] In both zones, the wall friction is the dominating effect.

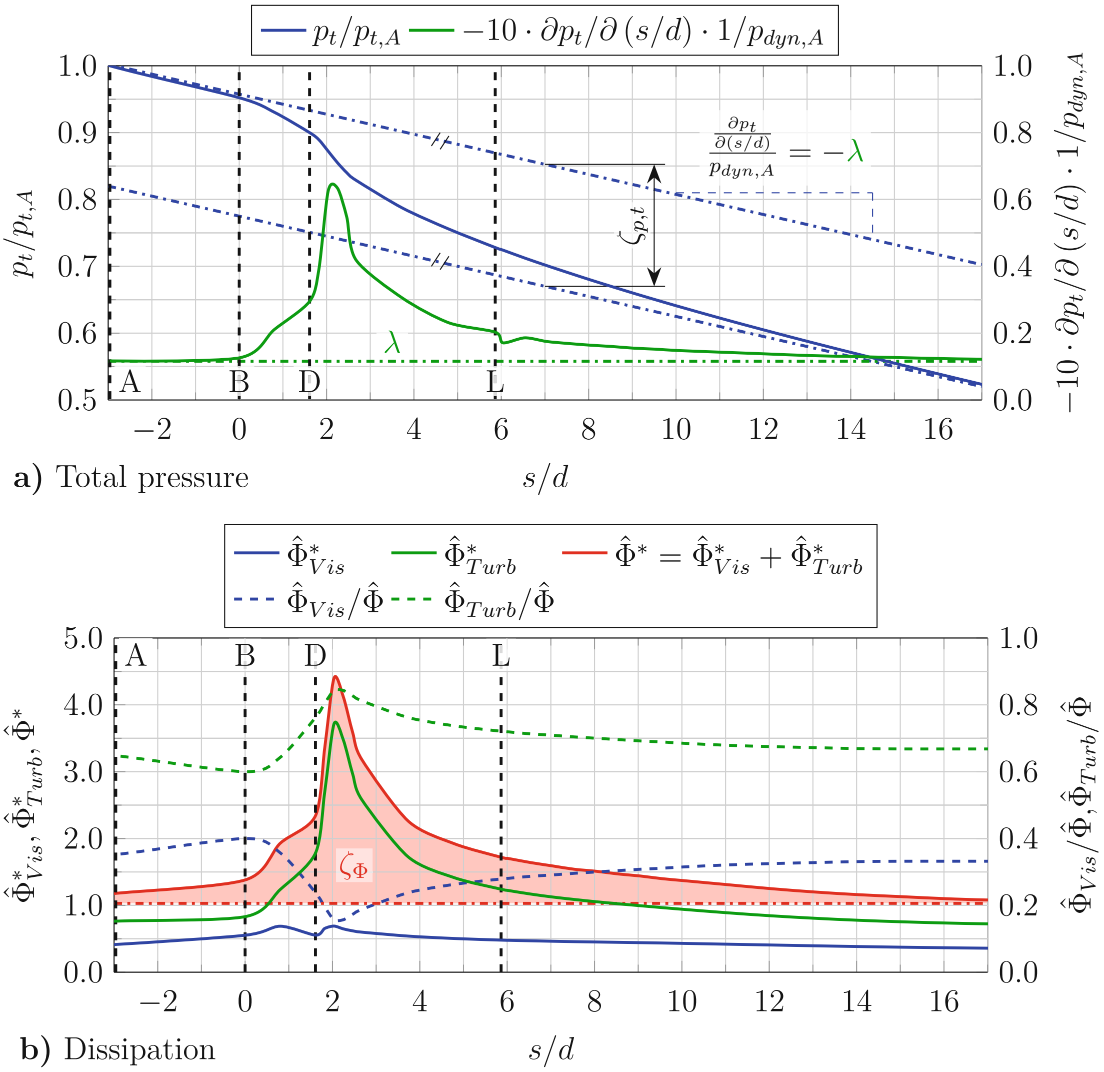

Figure 5.16: Longitudinal distribution of mass average total pressure and area-integrated dissipation for a case with $\mathrm{Re} = 1.2 \cdot 10^6$, mesh Fine H and SST turbulence model. $^* = \hat{\Phi}_i/\hat{\Phi}_{fr}$

coefficient. The effect of the change of flow direction in the bend between stations B and D can be seen in the sharp decline of the pressure curve downstream the bend, approximately in section DL. Most of the pressure losses induced by the bend, around 80 %, occur in this section. In contrast, the majority of other losses occur between stations B and D. Upstream station B, the entrance to the bend, the effect of the bend is hardly recognisable in the pressure distribution. These observations are underlined by the longitudinal evolution of the total pressure derivative, $\partial p_t/\partial(s/d)$. It is normalised by the dynamic pressure at station A, $p_{dyn,A}$, such that far upstream and downstream the bend, where all effects from the change of flow direction dissipated, the derivative becomes equal to the pipe friction coefficient λ of a straight pipe at this Reynolds number. The losses $\zeta_{p,t}$ induced by the 90° pipe bend can, therefore, be interpreted as the vertical distance between the two blue dash-dotted tangents with gradient $-\lambda$.

In part b) of the same figure, the longitudinal distribution of the cross-section integrated dissipation $\hat{\Phi}$ (defined in Equations (3.27) and (3.28)) is shown. Additionally, the individual contributions from the turbulent dissipation $\hat{\Phi}_{Turb}$ and the viscous dissipation $\hat{\Phi}_{Vis}$ are plotted. All of them were normalised by the background dissipation

$$\hat{\Phi}_{fr} = \dot{m} \cdot \frac{p_{dyn}}{\rho} \cdot \frac{\lambda}{d} = \frac{\rho d^2 \pi c_{s,ref}}{4} \cdot \frac{c_{s,ref}^2}{2} \cdot \lambda \cdot \frac{1}{d} = \frac{\rho d \pi \lambda c_{s,ref}^3}{8} \tag{5.3}$$

that arises from the friction in a straight pipe flow [50]. As for the pressure losses, most of the kinetic energy is dissipated in section DL downstream of the bend. However, significant dissipation occurs in the bend between stations B and D, upstream of the bend, and, most importantly, downstream of station L. Therefore, the lengths of influence, where $\hat{\Phi}/\hat{\Phi}_{fr} > 1$, are much longer than the distances from A to B (upstream tangent) and from D to L (downstream tangent). Schmandt and Herwig point out [84] that due to the asymptotic decay of the additional entropy generation, the upstream and downstream lengths of influence would be infinitely large. In a real-world scenario, this is not possible. Due to the constraint of the configuration of Shiraishi et al. [92], the upstream length was set from A to B, but the downstream length was increased from D up to station Z[13]. The integration of the dissipation was therefore executed from A to Z, and the area under the $\hat{\Phi}^*$ - curve (shaded in red) can be interpreted as the losses ζ_Φ.

In Table 5.2, the procedure to calculate the loss coefficients from the relations shown in the diagrams of Figure 5.16 is illustrated. To arrive at the dissipation power coefficients ζ_Φ, first, the turbulent and viscous dissipations Φ_{Turb} and Φ_{Vis} are integrated within each section, AB, BD, and DZ. This gives the powers of turbulent and viscous dissipation P_{Turb} and P_{Vis}, which, added together, form the power of dissipation P_Φ. The power from the background dissipation $P_{fr} = \hat{\Phi}_{fr} \cdot L_i$ has to be subtracted from P_Φ to achieve only that part of the power losses P_{cd}, which were induced by the change of direction. These powers are finally normalised by the power of kinetic energy $\dot{m}c_{s,ref}^2/2$ of the flow.
The procedure to calculate the total pressure loss coefficients[14] $\zeta_{p,t}$ is similar. From the total pressure losses Δp_t in every section, the friction losses $\Delta p_{t,fr}$ need to be subtracted to achieve the pressure losses $\Delta p_{t,cd}$ from the change of direction. These are normalised by the dynamic pressure $\rho c_{s,ref}^2/2$ at the reference location to achieve $\zeta_{p,t}$.

A detailed comparison of the techniques for loss accounting reveals that both loss coefficients are almost equal when evaluated between stations A to B and A to Z. Significant differences occur in section BD, where the losses from dissipation are less than half of the pressure losses. This deficit is compensated in section DZ, where the losses from dissipation are about 10 % higher than the pressure losses. This

[13]Station Z is located $50d$ downstream station A, the beginning of the domain of interest. For reasons of space, station Z is not shown in Figure 5.9 nor Figure 5.16.

[14]For ease of comparison, the total pressure loss coefficient $\zeta_{p,t}$ was picked here instead of the power loss coefficient ζ_{PmTE}. For the case of a single pipe without branches and junctions, it was shown in Equation (3.15) that ζ_{PmTE} can be reduced to $\zeta_{p,t}$.

Variable		AB	BD	DZ	AZ	Explanation
L_i	m	1.22	0.67	18.75	20.64	
P_{Turb}	W	28.54	21.64	523.34	573.52	$\int_V \Phi_{Turb}\,\mathrm{d}V$
P_{Vis}	W	15.12	10.39	225.82	251.34	$\int_V \Phi_{Vis}\,\mathrm{d}V$
P_Φ	W	43.66	32.04	749.17	824.86	$P_{Turb} + P_{Vis}$
P_{fr}	W	39.19	21.32	601.23	661.75	$\lambda{\cdot}L_i/d{\cdot}\dot{m}{\cdot}c_{s,ref}^2/2$
P_{cd}	W	4.46	10.71	147.94	163.11	$P_\Phi - P_{fr}$
ζ_Φ	1	0.004	0.009	0.125	**0.138**	$2P_{cd}/(\dot{m}c_{s,ref}^2)$
Δp_t	Pa	126	138	2190	2454	
$\Delta p_{t,fr}$	Pa	118	64	1803	1984	$\lambda \cdot l/d \cdot \rho c_{s,ref}^2/2$
$\Delta p_{t,cd}$	Pa	9	74	387	470	$\Delta p_t - \Delta p_{t,fr}$
$\zeta_{p,t}$	1	0.003	0.022	0.114	**0.139**	$2\Delta p_{t,cd}/(\rho c_{s,ref}^2)$

Table 5.2: Exemplary calculation of the loss coefficients for Re $=1.2 \cdot 10^6$.

finding underlines the observations in Figure 5.16 that additional entropy generated due to the change of flow direction in the bend has a much longer-lasting effect in the downstream tangent. If, e.g. the evaluation was conducted from A to L, as shown in Figure 5.14, then not all of the additionally generated entropy would have been considered. Thus, the discrepancies between $\zeta_{p,t}$ and ζ_Φ that appear in this section and the diagrams of the parametric study of the *AxFeeder* can be explained.

A further finding is that for the undisturbed flow, the ratio of turbulent dissipation Φ_{Turb} to viscous dissipation Φ_{Vis} is approximately 2:1. At the peak of the dissipation curve just downstream station D, this ratio becomes around 7:1.

5.2.4 Velocity distributions

The distributions of the normalised local streamwise velocity[15] $c_s/c_{s,ref}$ from the inside wall ($2r/d = -1$) to the outside wall ($2r/d = 1$) of the bend were evaluated at stations I to IV for four different Reynolds numbers, $3.2 \cdot 10^5$, $1.2 \cdot 10^6$, $2.8 \cdot 10^6$ and $3.7 \cdot 10^6$ and compared against experimental data from Shiraishi et al. [92]. The influence of grid size is discussed with the mesh study in Appendices C.2.2 and C.2.3. The influence of turbulence modelling is assessed from Figure 5.17.

All turbulence models where the wall layer was fully resolved, SST $y^+ = 1$, SSTCC and EARSM, replicate the measured velocity distributions reasonably well. There are only minor differences between simulations and experiments for the cases with the lowest Reynolds number, particularly in the flow separation region in station II

[15] The reference velocities correspond to the mean velocities calculated from the Reynolds numbers of the related cases.

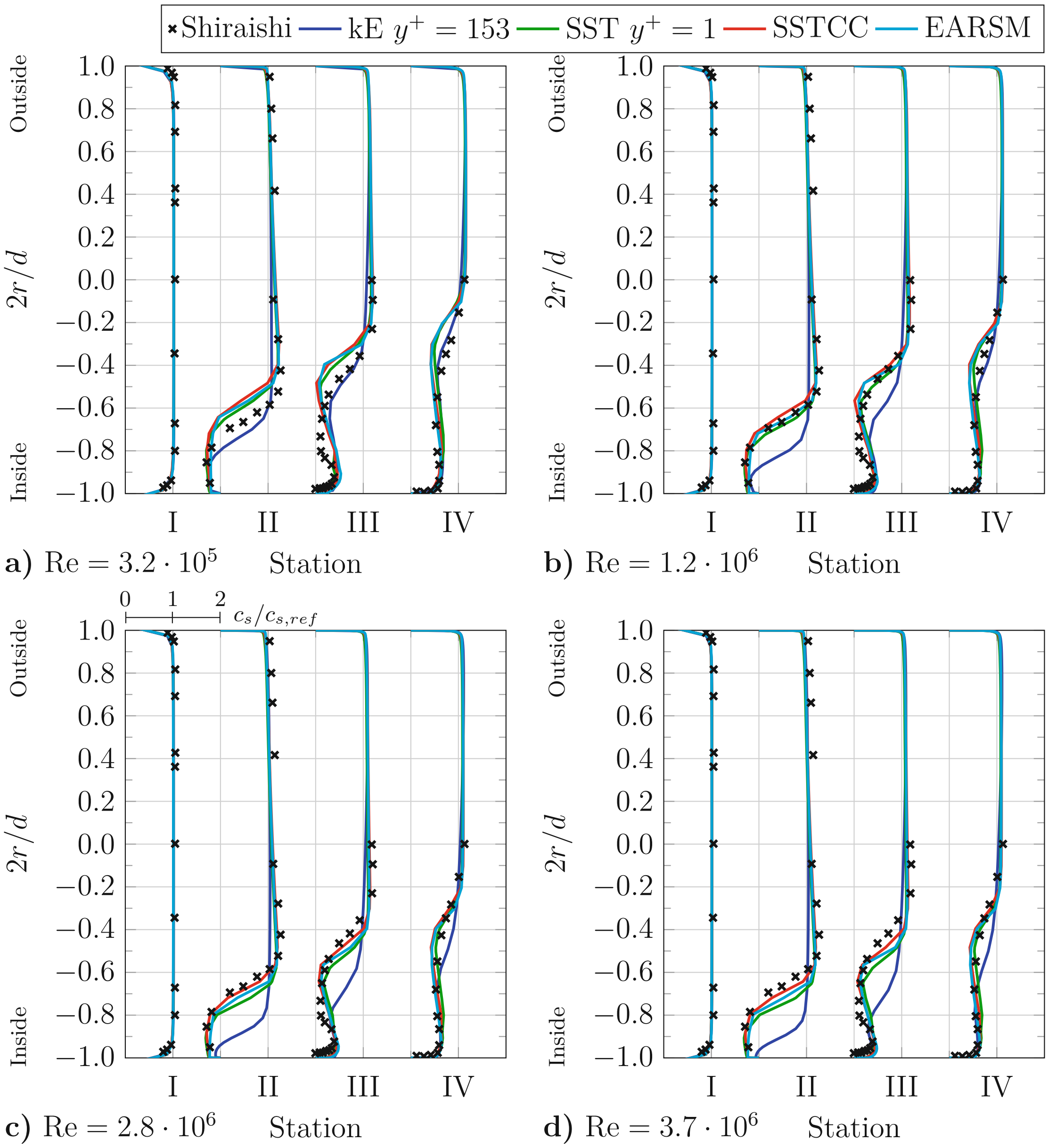

Figure 5.17: Streamwise velocity distribution at four stations for four Reynolds numbers using different turbulence models.

and the low-velocity region in station III close to the inside wall. A significant discrepancy between the CFD results and the experimental data is shown in the kE model case, where the velocity deficit caused by the flow separation at the inside of the bend cannot be captured precisely. A closer look at the profiles in this zone reveals that especially for $\mathrm{Re} \geqslant 1.2 \cdot 10^6$, the predictions of the SSTCC and the EARSM model match the experimental data better than those of the SST model. It is expected that for the parametric study of the *AxFeeder*[16], the benefits of the SSTCC or the EARSM model at high Reynolds numbers do not outweigh the extra computation effort (Table C.7) and the SST model will perform reliably.

[16]The *AxFeeder* was projected for a Reynolds number range from $2.0 \cdot 10^5$ to $2.0 \cdot 10^6$, with a focus on the design point equivalent to $\mathrm{Re} = 1 \cdot 10^6$

5.3 Analysis of the secondary flow in configurations A and B

In Chapter 2, the secondary velocity ratio ϕ_{II} was determined as a variable of the highest significance to quantify the flow disturbances in Pelton turbine distributor systems. Therefore, ϕ_{II} was chosen as one of the quantities evaluating the designs in the parametric study of the *AxFeeder* in Chapter 6. In this section, for the 90° pipe bends of Sudo et al. [104] and Shiraishi et al. [92], the sensitivity of the secondary velocity ratio to mesh refinement and the choice of turbulence model was evaluated at three stations, $\varphi = 90°$, $z/d = 1$, and $z/d = 5$. Tables C.4, C.5, C.11 and C.12 give an overview of the computed values for all cases with different meshes and different turbulence models for the two 90° pipe bend configurations.

For both configurations, the structure of the secondary velocity, a pair of counter-rotating Dean vortices [13], is correctly predicted in all combinations of meshes and turbulence models (see Figure 5.19). The choice of the turbulence model and the wall layer resolution significantly affect the secondary velocity ratios downstream of the bend. Typically, cases with the kE turbulence model under-predict the secondary flow velocity magnitudes, especially in regions close to the inside wall of the bend. This effect, which is exemplarily shown for $\mathrm{Re} = 1.2 \cdot 10^6$ in Figure 5.19 is more pronounced at stations closer to the bend at and at high Reynolds number. Generally, the SST model tends to estimate higher values of the secondary velocity ratio than the EARSM or kE model cases.

The effect of the Reynolds number on the secondary velocity ratio ϕ_{II} is presented in Figure 5.18. The three curves by Shiraishi et al. [92] show a gradual decline of ϕ_{II} with increasing Reynolds number[17]. With an increasing Reynolds number, the turbulent structures in the flow increase. Thus, the turbulent kinetic energy and the turbulent viscosity increase, and the secondary flow structures become less dominant. Because of the smaller curvature radius in the bend of Shiraishi et al. [92], ϕ_{II} at station $\varphi = 90°$ is about a third higher than in the bend of Sudo et al. [104]. For stations further downstream, the secondary flow structures in the configuration of Sudo et al. [104] appear to be longer lasting. Thus, in station $z/d = 1$, ϕ_{II} is about the same for both bends. In station $z/d = 5$ of Sudo et al. [104], ϕ_{II} is even higher than ϕ_{II} by Shiraishi et al. [92]. The contour plots in Figure 5.19 underline this observation. In the case of Shiraishi et al. [92], due to the small curvature radius, the secondary flow at $\varphi = 90°$ is primarily determined by the change of flow direction in the bend, resulting in secondary velocity vectors pointing to the outer wall of the bend. It takes several stations downstream the bend exit until the characteristic Dean vortices become visible. At the station $z/d = 1$, ϕ_{II} has its maxima close to the inside wall and at the core of the separation zone, where both vortices meet. As the flow moves to station $z/d = 5$, this region of high secondary velocity becomes more prominent and moves towards the bend centre. In turn, the magnitude of the secondary velocity dissipates.

[17] Thereby, the patterns of the secondary flow do not change. They stay the same as depicted in Figure 5.18. Only the magnitude of the secondary flow decreases.

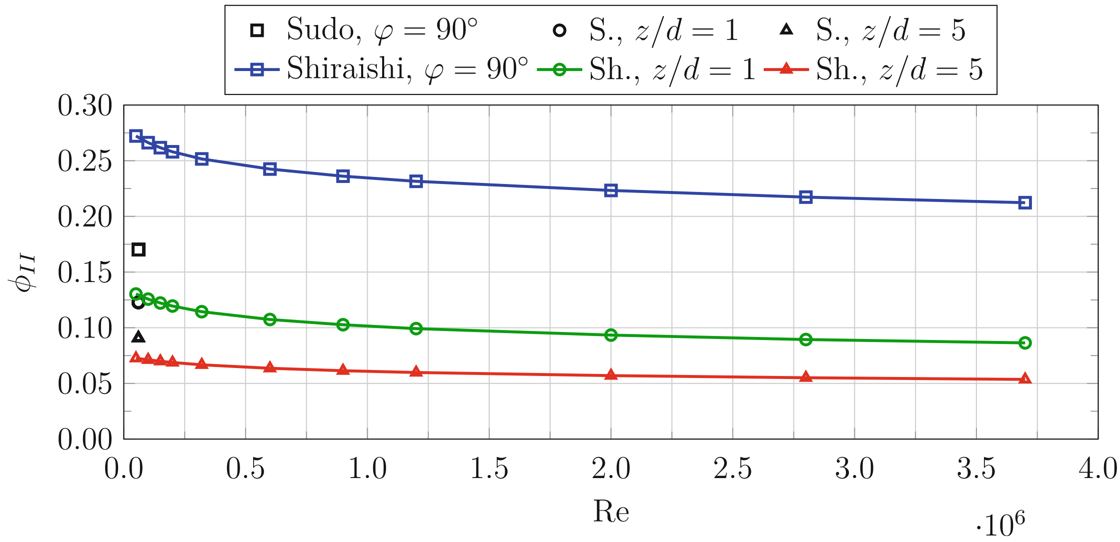

Figure 5.18: Secondary flow velocity ratio evaluated at three stations downstream the bend for the cases of Sudo et al. [104] and Shiraishi et al. [92]. All with mesh Medium H and the SST turbulence model.

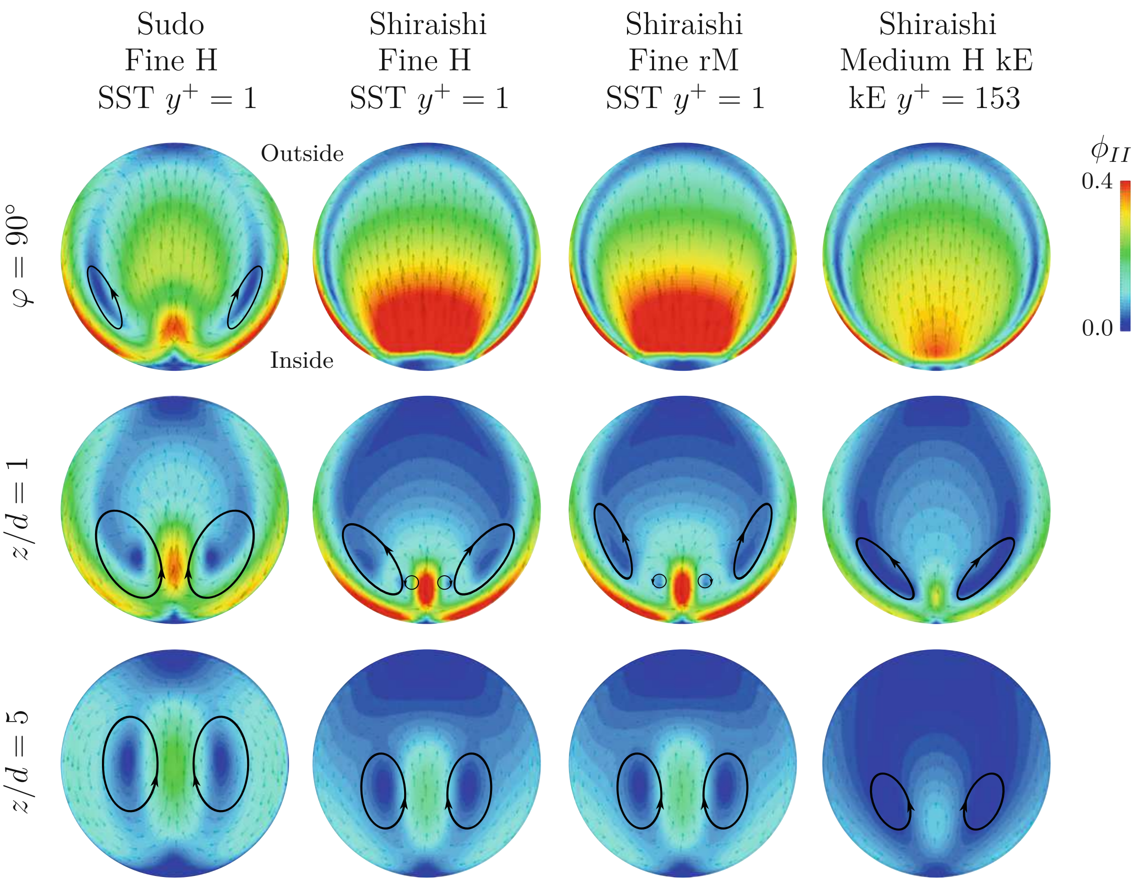

Figure 5.19: Contours of the secondary velocity ratio ϕ_{II} and vectors of secondary velocity at several stations downstream the bend for the cases of Sudo et al. [104] ($\mathrm{Re} = 6 \cdot 10^4$) and Shiraishi et al. [92] ($\mathrm{Re} = 1.2 \cdot 10^6$).

CHAPTER 6

Distributor systems with axial inflow

This chapter thoroughly investigates design concepts for a Pelton turbine distributor system with axial inflow and discusses the results of an extensive parametric study. The content of this chapter represents a comprehensive supplement and a significant expansion of a prior publication of mine, *Numerical Investigation of Pelton Turbine Distributors Systems with Axial Inflow* [30].

6.1 Introduction to the concept

6.1.1 The *AxFeeder*

In contrast to conventional Pelton turbine distributor systems, this new approach of a Pelton turbine distributor system with axial inflow[1], deemed *AxFeeder*, shows some significant differences that shall be explained by the universal sketch depicted in Figure 6.1. In flow direction, the penstock line with diameter D_1 is directly connected to the manifold element, where the incoming flow is divided into n equal streams. Thereby, as few losses and secondary flows as possible shall be induced. Station 1 is located three diameters upstream of the beginning of the manifold, and station 2 is located at the beginning of the manifold element.

Unlike in conventional distributor systems, where one branch line at a time separates from the main line, in the case of the *AxFeeder*, all branch lines[2] separate from the manifold from the same streamwise location. The n branch lines, ranging from station 51 ($5i$) to station 101 ($10i$), are connected to the manifold head at the deviation hole circle diameter D_{hc} and the deviation angle δ. The last branch line component is the injector bend, ranging from stations 81 ($8i$) to 101 ($10i$). It is pivoted relative to the branch line by the angle γ. The exact value of γ can be adjusted according to the runner's pitch cycle diameter D_p. In theory, the number

[1]Such a system was first described in the patent of Erlach and Staubli from 2008 [21].
[2]The index $i = 1 : n$ indicates the branch line number.

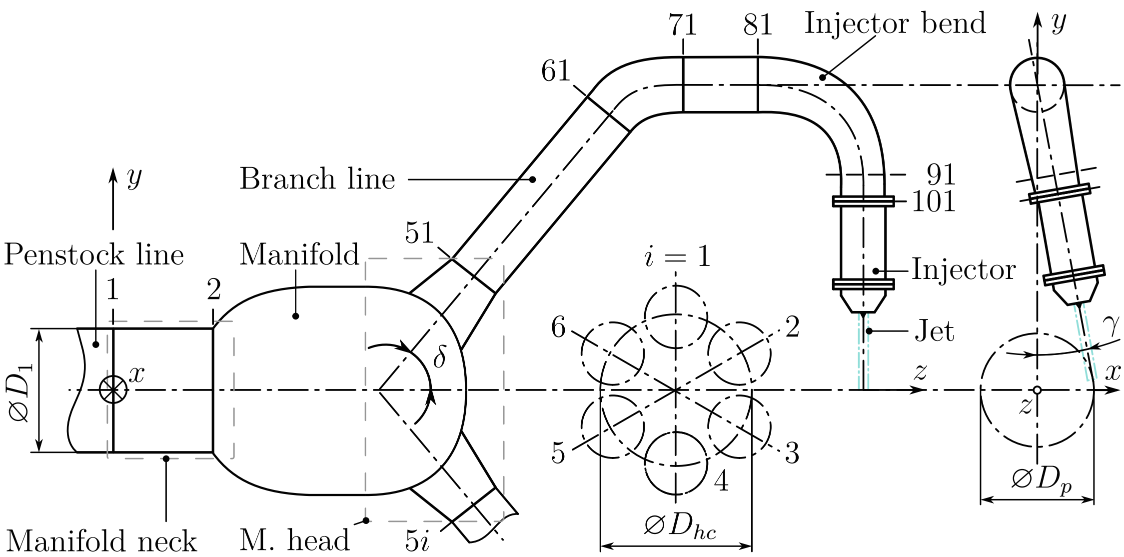

Figure 6.1: Generic sketch of the *AxFeeder* with the individual components and evaluation stations 1 to 101.

of branch lines is limited only by the space at the manifold head[3]. With Pelton turbines, for practical reasons and due to symmetry constraints, the number of branch lines lies between three and six. The branch lines are labelled such that the last digit is defined by the branch line index i, and the digits before the last denote the station in ascending order. For example, station 83 is the station at the beginning of the injector bend of branch line $i = 3$.

6.1.2 Four core designs

By its configuration, the *AxFeeder* should be compact and deliver excellent jet quality [30]. Indeed, a compact design contributes directly to the distributor's materials and manufacturing costs and the turbine hall's construction costs (see also Sections 2.3 and 2.4). Excellent jet quality is necessary as the jets affect not only the turbine efficiency (see Section 2.1) but also the distribution of mechanical loads on the runner and the turbine shaft assembly [14]. The literature in Section 2.2 emphasised a direct correlation[4] between the flow quality at the stations upstream of the injector and the jet quality. This allows the omission of the injectors and the jets from the simulations, making studying many hundreds of design variations possible in the first place[5]. Thus, one main goal of the parameter study was to evaluate the effects of different designs on the flow quality at the interface to the injector (stations $10i$). Another primary goal was to evaluate the effects of different design modifications on the power losses of the *AxFeeder*. The quantities of interest for the parameter study (= flow quality criteria) are thus: the power loss coefficient ζ_{PmTE}, the dissipation power coefficient ζ_{Φ}, and the secondary velocity ratio ϕ_{II}.

[3]The space at the manifold head is determined as a combination of the deviation hole circle diameter D_{hc} and the deviation angle δ.

[4]Semlitsch [89] found this correlation to hold for conventional Pelton turbine distributor systems.

[5]For a topologically similar case of a conventional distributor with two injectors, omitting the injectors allowed for a reduction of computation time of almost 80 %.

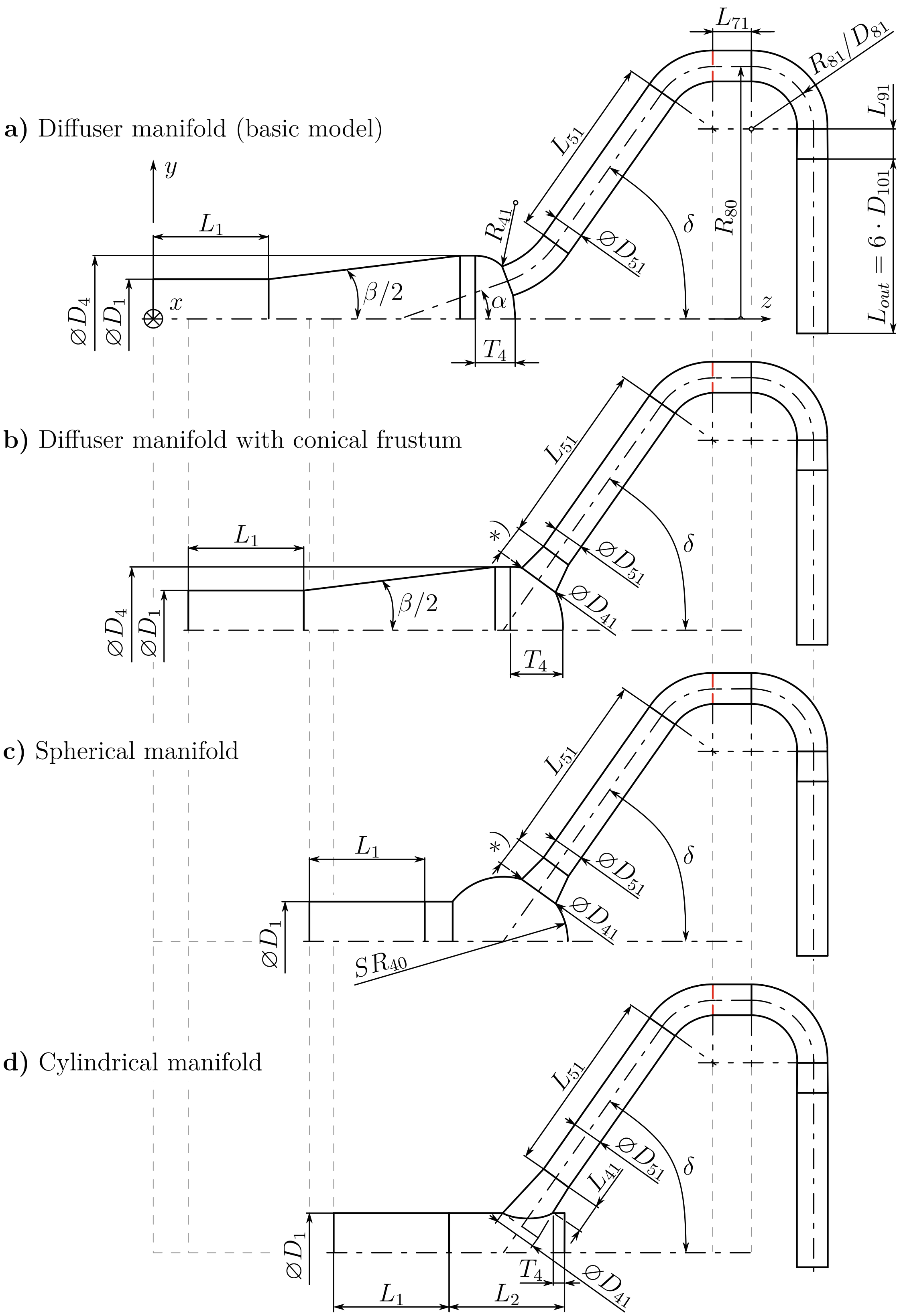

Figure 6.2: Comparison of four core manifold designs with dimensions relevant to the parametric study. Downstream station 71 (dashed red line) the dimensions are the same for all four designs (deviation of the injector bend by the pivot angle γ not shown). $*) = L_{41}$.

Therefore, four different core designs of the distributor system with axial inflow were investigated. Mid-section cuts are shown in Figure 6.2. Starting from the basic model of Figure 6.2 a) that was inspired by the patent of Erlach and Staubli [21], these four designs can be mainly distinguished by the shape of the manifold and the connection of the manifold to the branch lines. While the designs in Figure 6.2 a) and b) have a diffuser-shaped manifold, designs c) and d) have spherical and cylindrical manifold bodies. Except for the basic model a), which does not provide enough space to place a frustum, the first branch line section in variants b) to d) between diameters D_{41} and D_{51} is shaped as a conical frustum. The frustum allows for a smoother and more even transition between the manifold and the branch lines. While the diffuser-shaped manifold in designs a) and b) decelerates the flow continuously before dividing it into $n = 6$ equal streams, the diffuser increases the overall lengths of these designs drastically. For a more compact overall size of the *AxFeeder*, the diffuser is replaced by a spherical manifold, Figure 6.2 c), or completely excluded, leading to the cylindrical manifold variant, Figure 6.2 d). The manifold becomes significantly shorter in these cases than in designs a) and b). However, the *AxFeeder* is typically larger than a conventional Pelton turbine distributor system. This fact is discussed in detail in Appendix D.1.

6.2 Verification

6.2.1 Computational domain and simulation setup

The parametric study of the *AxFeeder* examines the effects of geometric changes on the flow quality in the manifold and the branch lines. Thus, the injectors were not considered in the domain. Instead of the injectors, an outlet body was fitted at the downstream end of each branch line. The length of the outlet body was determined by investigating its effect on the power loss coefficient, the dissipation power coefficient and the secondary flow ratio. To ensure a developed inflow, the inlet pipe was extended ten times its diameter upstream of station 1. The complete model with six branch lines was tested in the grid refinement and iteration number studies. A possible use of geometric symmetry was tested in the symmetry study. The effects of wall resolution and domain length downstream of the outlet were also investigated in their respective studies. The basic model with the diffuser-shaped manifold as presented in Figure 6.2 a) was employed for all these studies. The computational domain is sketched fully in Figure 6.3.

The flow is assumed to be single-phase, steady, incompressible and isothermal. The density and dynamic viscosity of water at 25 °C were set to $\rho = 997\,\mathrm{kg/m^3}$ and $\mu = 8.899 \cdot 10^{-4}\,\mathrm{Pa\,s}$. A top hat velocity profile corresponding to a Reynolds number of 10^6 was specified at the inlet of all cases presented in this section. The Reynolds number was changed only for the cases presented in Section 6.3.2. The pressure boundary condition was set to 1 bar at the outlet. A turbulence intensity of $I_t = 5\%$ together with a turbulent length scale corresponding to the hydraulic diameter of station 1 was set as turbulence boundary conditions at the inlet. A no-slip boundary condition was employed at all walls. They were set to be hydraulically smooth.

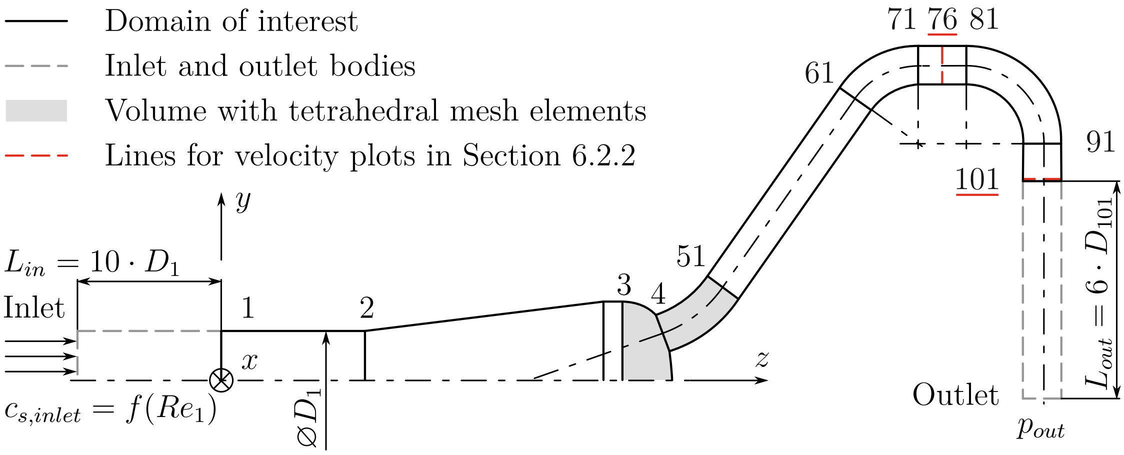

Figure 6.3: Section view of the computational domain of the verification studies.

Following the results of the comparison of different modelling approaches for the 90° bends of Sudo et al. [104], Section 5.1, and Shiraishi et al. [92], Section 5.2, the k-ω SST model [61] was employed as turbulence closure. The advection terms were solved using the high-resolution scheme, a second-order scheme that automatically blends to a first-order formulation if stability issues arise [3]. The advection of turbulence was discretised by a first-order upwind scheme. These settings were kept the same for all cases within Chapter 6 except for the change of the inflow Reynolds number in Section 6.3.2. Identical setups were determined to be trustworthy by Hahn et al. [30, 31].

6.2.2 Estimation of individual errors

Error from spatial discretisation

To estimate the discretisation error, a grid resolution study was performed following the procedure of Celik et al. [11], introduced in Section 4.4. In the studies of the 90° bends of Sudo et al. [104], Section 5.1, and Shiraishi et al. [92], Section 5.2, a mixed element type meshing approach proved to be a viable compromise between reliable, trustworthy simulation results and meshing effort. Therefore, for the grid study of the *AxFeeder*, three meshes were created that were composed of hexahedral elements for all pipe segments (including the diffuser) and tetrahedral elements in the manifold head (grey shaded area between stations 3 and 51 in Figure 6.3). This mixed element type meshing approach was maintained for all subsequent simulations of the *AxFeeder*. The three meshes consisted of $3.2 \cdot 10^6$, $7.7 \cdot 10^6$ and $18.7 \cdot 10^6$ elements. The maximum y^+ value at the walls was below 1 for all investigated cases. The uncertainties caused by spatial discretisation were computed for the power loss coefficients ζ_{PmTE} and the dissipation power coefficients ζ_Φ between stations 1 to 50, 50 to 100 and 1 to 100, and the secondary velocity ratios ϕ_{II} at stations 50, 80 and 100. The uncertainties were also computed for the normalised magnitudes of the local flow velocities $||\vec{c}||$ at stations 76 and 101.

A comprehensive list of data of the meshes is given in Table D.1.

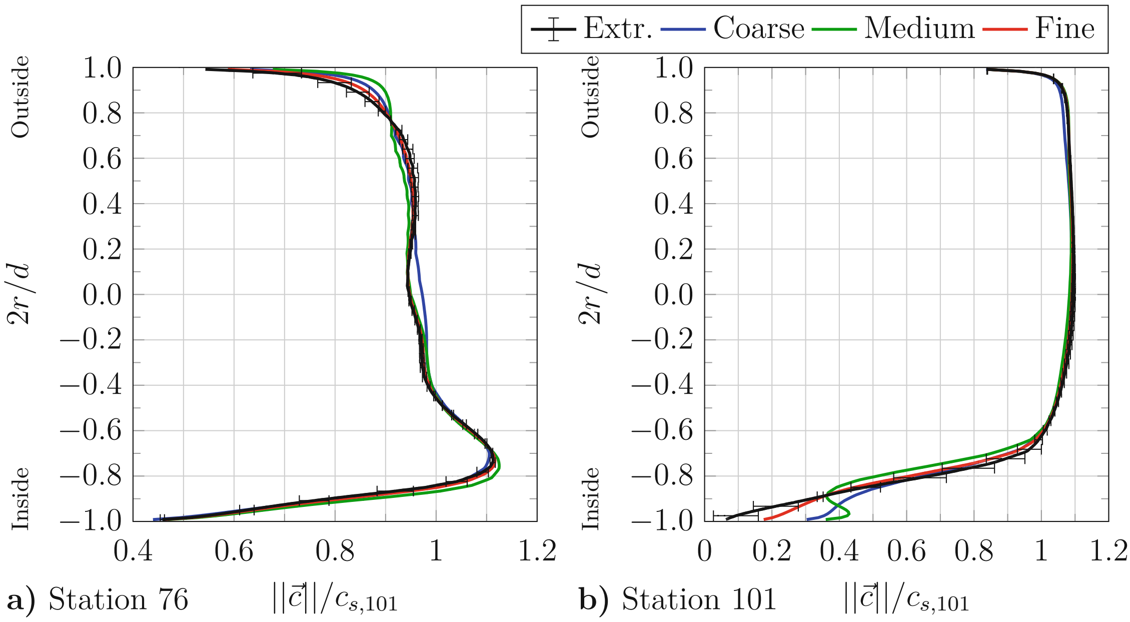

Figure 6.4: Velocity profiles including the extrapolated curves (Extr.) and the discretisation errors at stations 76 and 101.

The fine-grid convergence indices for the power loss coefficients are in the low single-digit percentage range, and the apparent order of the method lies between 1.5 and 3.7. Although the grid convergence is satisfactorily low, the value of R_{oc} indicates the divergence of the method. A possible explanation for this behaviour is that the numerical values of ζ_{PmTE} for the three grids lie very close together. Hence, their differences are marginally small. Celik et al. [11] point out that the procedure outlined in Section 4.4 does not work in such a situation. This might be the case in the present study.

The dissipation power coefficients react much more sensitively to mesh refinements, thus yielding a fine-grid convergence index of 14.6% when evaluated between stations 1 and 100. A closer look at the data reveals that this high value can be traced back to the part of the domain between stations 1 and 50, where GCI^{21}_{fine} is over 44 %. Generally, the convergence for the loss coefficients is significantly better in the domain between stations 50 and 100 than between stations 1 and 50. This is most likely caused by the local flow separations when the flow leaves the manifold and enters the branch lines[6].

The grid convergence procedure yields low, single-digit percentage values for the secondary velocity ratio ϕ_{II} at stations 50 and 80 with apparent orders of around 4.7 and 1.5, respectively. The secondary velocity ratio ϕ_{II} at station 100 reacts much more sensitively to a change of the mesh size resulting in a fine-grid convergence index of almost 14 %. One reason for the higher value of GCI^{21}_{fine} of the secondary flow ratio at station 100 can be seen in part b) of Figure 6.4, in which the normalised

[6]The transition from the manifold to the branch lines was identified as a weakness of core design a).

velocity magnitude[7] at a horizontal line (z-direction) in station 101 is plotted for the three meshes. At this station directly downstream of the injector bend, there is a velocity deficit at the inside wall of the bend. The exact prediction of this deficit poses an inherent challenge for RANS modelling. Therefore, the local GCI_{fine}^{21} values close to this velocity deficit, indicated by the error bars in Figure 6.4, are significantly larger than at the rest of the profile. While the mean value of the fine-grid convergence index is just over 3 %, the corresponding maximum reaches almost 80 %. When evaluated at station 76, the local maximum of the grid convergence index is less than 10 % and the mean value less than 1 %. The velocity curves of that respective station are plotted in Figure 6.4 a). The mean value of the apparent order of the method p_{oa} lies above three for both velocity curves. The rate of oscillatory convergence is around 75 % for both velocity curves.

The settings of the medium mesh were chosen for all subsequent simulations to maintain an adequate balance between computational times (listed in Table D.1) and numerical accuracy. The relative number and average size of the mesh elements of the *AxFeeder* medium mesh correspond to that of the fine meshes of the Sudo et al. [104] and Shiraishi et al. [92] validation cases presented in Chapter 5.

Further results of the grid study are listed in Table D.2 for the loss coefficients, in Table D.3 for the velocity magnitudes at stations 76 and 101 and in Table D.4 for the secondary velocity ratios.

Iteration number study

As raised earlier in this study, to handle the vast number of computations needed for the parametric study, the focus after the mesh study was to find additional potential for time savings in each simulation run. Therefore, it was investigated how the quantities of interest, the loss coefficients and the secondary flow velocity ratio are affected by a reduction of iteration steps. Table 6.1 lists the differences of these quantities when calculated with a reduced iteration number to their respective values at 1000 iterations. For all quantities, the differences are well below 1 %, meaning the error induced by halving the iteration number is less than the error induced by the spatial resolution of the domain. From residuals, the turbulent kinetic energy equation did not completely converge after 250 iterations. Hence, for the parametric study, the iteration count was set to 500, which implies a slightly more considerable uncertainty for the secondary velocity ratio but ensures a fully converged solution.

Symmetry study

All core designs of the *AxFeeder* are n-fold rotational symmetric by the z-axis, in the most typical case with six branch lines, $n = 6$. The simulations were chosen such that the boundary conditions allow for a symmetric flow as well. Thus, in

[7] The reference velocities correspond to the mean velocities calculated from the Reynolds numbers at the specified station. Since the diameters and therefore the mean velocities are equal for stations 76 and 101, $c_{s,101}$ is employed as a reference for both stations.

Iterations	$\zeta_{PmTE}\|_1^{100}$	$\zeta_{\Phi}\|_1^{100}$	$\phi_{II,100}$
250	0.05	0.15	0.13
500	0.00	0.09	0.27
750	0.00	-0.02	-0.02

Table 6.1: Differences in % of loss coefficients and the secondary velocity ratio to their respective values after 1000 iterations, for cases with reduced iteration number.

this subsection, it is tested if the domain can be reduced to a $360°/n = 60°$ sector model of the manifold part and only one branch line. The differences in the loss coefficients evaluated between stations 1 and 101 were 0.4 % for $\zeta_{PmTE}|_1^{101}$, and -0.5 % for $\zeta_{Phi}|_1^{101}$. With the symmetric model, the secondary velocity ratio at station 101 is slightly under-predicted compared to the full model. The difference is 5.3 %, which is still only a third of the uncertainty from the spatial discretisation. However, using symmetry allowed for the computation time to be greatly reduced (see also Table D.1). Thus, rotational symmetry was employed in all simulations of Sections 6.3.2, 6.4 and 6.5 as well as for the wall resolution study and the outlet length study.

Wall resolution study

A potential to further reduce the computational costs of each case is offered by adjusting the mesh close to the walls to enforce the use of wall functions. Consequently, on the symmetric model, it was investigated how much the flow quality criteria were affected by a reduced mesh resolution at the walls. While the power loss coefficient almost stayed constant and the secondary velocity ratio only changed by around 0.7 %, even if the wall resolution was changed such that $y^+ > 30$, the dissipation power coefficient reacted much more sensitively. A change of over 36 % was observed for this quantity. Such a sensitive reaction of the dissipation power coefficient was already witnessed in the validation of the method against the experiments from Sudo et al. [104] and Shiraishi et al. [92] and encourages keeping a satisfactory mesh resolution such that a maximum value of $y^+ < 1$ is ensured at all walls.

Outlet length study

As previously addressed, the injectors were not included in the parametric study of the *AxFeeder*. Instead, to provide sufficient distance from the evaluation stations to the boundary of the fluid domain, a cylindrical outlet body was attached to the branch line downstream of the injector bend. Table 6.2 shows the deviation of the loss coefficients and the secondary flow ratio from the mean value for four different lengths L_{out} of the outlet body. The outlet body's length has a negligible effect on the power loss and dissipation power coefficients. Again, the ratio of secondary velocity responds more sensitively, with a maximum deviation of around 1.5 % and no clear trend of whether a longer or shorter outlet body is favourable. As the

L_{out}/D_{101}	$\zeta_{PmTE}\vert_1^{100}$	$\zeta_\Phi\vert_1^{100}$	$\phi_{II,100}$
3	0.00	0.05	0.24
6	-0.12	-0.28	0.29
9	-0.02	0.01	-1.54
12	0.14	0.23	1.01

Table 6.2: Deviations of the loss coefficients and the secondary velocity ratios to their mean value in % for four different outlet body lengths.

impact of the outlet body length is still relatively small compared to the influence of the mesh on the flow quality indicators, a value of $L_{out} = 6 \cdot D_{101}$ was selected for all simulations unless specified otherwise. This choice allowed the outlet boundary conditions to be sufficiently far downstream of the last evaluation station 101 and allowed for no overlap of the outlet bodies in simulations of the entire model with six branch lines.

The length of the inlet body L_{in} may also have a non-negligible effect on the flow in the manifold. However, a fixed value of ten diameters was set for L_{in} to achieve comparable inflow conditions for all cases of the parameter study, to be identical with the inflow length of the projected test rig.

6.2.3 Compound simulation error

For the three main quantities of interest, the power loss coefficient between stations 1 and 100 (101 respectively), $\zeta_{PmTE,1011}$, the dissipation power coefficient ζ_Φ, and the secondary velocity ratio at stations 100 (101 respectively), $\phi_{II,101}$, a compound simulation error composed of the five main modelling assumptions (spatial discretisation, iteration number, symmetry, wall resolution and length of the outlet body) was computed. The procedure to calculate the compound simulation errors as a root-sum-square U_{RSS}, and the mean value of the individual errors as a root-mean-squares U_{RMS} of each quantity of interest from the individual errors u_R is thoroughly explained in Appendix A.3.3. The results of the computations are summarised in Table 6.3.

The primary source of error for all three quantities of interest is the spatial discretisation, i.e. the grid size. In fact, for both loss coefficients, $\zeta_{PmTE,1011}$ and ζ_Φ, the root-sum-square is almost entirely contributed by the spatial discretisation and the other sources of error are negligible. It could be expected that the uncertainty U_{RSS} of the power loss coefficient is the lowest as this quantity is driven mainly by the pressures within the system and, as shown in Chapter 5, pressure-related quantities were the least sensitive to the modelling assumptions made within this thesis. It was also shown in Chapter 5 and in Section 6.2.2 that both the dissipation power coefficient and the secondary velocity ratio react much more sensitively to a change in grid size. In the case of ζ_Φ, the increased uncertainty is attributed to the local flow separations at the sharp transition of the manifold to the branch lines. In the case

Source of error	u_R		
	$\zeta_{PmTE,1011}$	ζ_Φ	$\phi_{II,101}$
Spatial discretisation	2.41	14.64	13.65
Iteration number	0.00	0.09	0.27
Symmetry	0.40	0.50	5.3
Wall resolution	0.00	0.00	0.00
Outlet length	0.12	0.28	0.29
U_{RSS}	2.45	14.65	14.65
U_{RMS}	1.22	7.33	7.32

Table 6.3: Compound errors of the CFD simulation for loss coefficients and secondary velocity ratio in %.

of $\phi_{II,101}$, it was shown for the 90° pipe bends in Appendices C.1.2 and C.2.2, and for the *AxFeeder*, especially in Figure 6.4, that there is an adverse pressure gradient decelerating the flow at the inside of the bends. This gradient and the change in the flow direction induce swirling flow with an increased secondary velocity ratio and distorted velocity contours. These phenomena can only be captured in all preciseness by scale-resolving simulations.

Only for the secondary velocity ratio, with the influence of symmetry, does a different source of error than spatial discretisation play a role. The errors to due wall resolution were set to zero because, to resolve the flow close to the walls sufficiently and thus accurately compute dissipation in the boundary layer, a very fine mesh resolution with maximum values of $y^+ < 1$ for all walls was needed in any case.

The values of U_{RSS} were taken as the widths of the error bands in the operating charts of Figure 6.6.

The primary sources of error not accounted for in this study were the temporal discretisation, as a steady-state flow was assumed for all cases and the impact of turbulence modelling, as the k-ω SST model was employed for all cases. These two choices were justifiable, following the extensive comparison of CFD results achieved by setups relying on the steady-state flow assumption and the k-ω SST model against the experimental data of the 90° pipe bends of Sudo et al. [104] and Shiraishi et al. [92] that was presented in Sections 5.1 and 5.2.

6.3 Designated operating regime

The operating regime chosen for the *AxFeeder* was derived from a) the planned application of the *AxFeeder* in small hydropower plant projects and b) typical flow velocities in pressure pipelines, penstocks and turbine lines found in technical literature.

6.3.1 Selection of design parameters

With a typical maximum rated power output $P = 10\,\mathrm{MW}$ in small hydropower plants, combinations of the volumetric flow rate Q and the geodetic head[8] H can be calculated by

$$P = \rho g Q H\,. \tag{6.1}$$

A schematic overview of computed flow rates Q for several fixed values of the head H and the power output P is listed in Table 6.4. The colour code indicates sets of H, P and Q that appear to be a suitable parameter combination for employing a Pelton turbine in general, and the *AxFeeder* in particular, by a green background. The areas of application for water turbines shown by Giesecke, Mosonyi and Heimerl [25] suggest that volumetric flow rates of less than 50 L/s are outside the range of classical water turbine types. Therefore, these data points were given a grey background. If either the head becomes too low or the flow rate too high to use a Pelton turbine, then the data point was given a red background. The set of $P = 10\,000\,\mathrm{kW}$ and $H = 500\,\mathrm{m}$ requires the use of a gear unit to match the speeds of turbine and generator to be sensible for the application of a Pelton turbine. However, a gear unit is not always a preferred option with hydraulic turbines; therefore, this set is marked by a yellow background.

Q in L/s	H in m				
P in kW	50	100	250	500	1000
50	102	51	20	10	5
100	204	102	41	20	10
250	511	256	102	51	26
500	1022	511	204	102	51
1000	2045	1022	409	204	102
2500	5112	2556	1022	511	256
5000	10224	5112	2045	1022	511
10000	20449	10224	4090	2045	1022

Table 6.4: Volumetric flow rates Q of small hydropower plants suitable for the installation of a Pelton turbine.

Reference values for typical mean flow velocities in pressure pipelines, penstocks and turbine lines taken from literature lie between 1 m/s and 7 m/s. For short pipes with a diameter D_1 between 0.6 m and 4 m, a length less than 300 m, and low heads of less than 90 m, Nechleba [66] suggests the empiric correlation

$$\bar{c}_{s,max} = 4.3 - 0.5 \cdot D_1 \tag{6.2}$$

to estimate the upper limit for the mean flow velocity in a pipe with diameter D_1. The evaluation of this equation results in recommended mean flow velocities of

[8] For simplicity, the difference between geodetic head and net head shall not be considered here, as it is irrelevant for the generality of the statement made.

around 2 m/s to 4 m/s. A summary of recommended flow velocities from different authors is listed in Table 6.5. The authors seem to focus their recommendations of $\bar{c}_s$ around 3 m/s to 4 m/s. Because for a fully developed, turbulent pipe flow, a lower velocity is generally associated with lower friction losses and less dissipation, within this thesis, the projected velocity at the inlet of the *AxFeeder* was set to 3 m/s for the reference design point.

Combining these two approaches, where sensible flow rates are derived from the desired small hydro installations and sensible flow velocities are taken from literature recommendations, it is possible to estimate the size of the *AxFeeder*, expressed by the diameter of the penstock line D_1, through

$$D_1 = \sqrt{\frac{4Q}{\pi \bar{c}_s}} \,. \tag{6.3}$$

For a range of flow velocities from 3 m/s to 5 m/s, and flow rates Q_1 of 50 L/s to 1000 L/s (shaded green area in part a) of Figure 6.5), a diameter range D_1 of 150 mm to 650 mm follows.
Equally, the Reynolds number of this flow is evaluated by

$$\mathrm{Re}_1 = \frac{4Q}{D_1 \pi \nu} \,, \tag{6.4}$$

which, for the same range of flow rates as before and diameters as calculated by Equation (6.3), gives Reynolds numbers from around $5 \cdot 10^5$ to $2 \cdot 10^6$.

Following this derivation, the limits of Reynolds numbers to be investigated in Section 6.3.2 were set to $2 \cdot 10^5$ and $2 \cdot 10^6$(shaded green area in part b) of Figure 6.5). The lower limit of the Reynolds number range was chosen less than the estimated $5 \cdot 10^5$ because when the turbine is operated at part-load, the flow rate and, thus, the Reynolds number in the pipe is significantly lower. Therefore, it is of interest if, in any part of the relevant operating range of the *AxFeeder*, any of the applied flow quality criteria, especially the power losses, show a similar transition regime with a sudden fall or rise (of the losses), like it was observed in Figure 5.10. A range of penstock line diameters D_1 from 100 mm to 500 mm was chosen to accommodate a wide variety of small hydro Pelton turbine designs. With a target value as

Author	$\bar{c}_{s,min}$	$\bar{c}_{s,max}$	**Application**
Giesecke, Mosonyi and Heimerl [25]	1	7	Penstock
Horlacher [37]	1	6	General hydropower, turbine lines
Nechleba [66]	3	4	Penstock
Mosonyi [64]	3	5	Penstock, properly settled water

Table 6.5: Recommended mean flow velocities in m/s for pressure pipelines, penstocks and turbine lines.

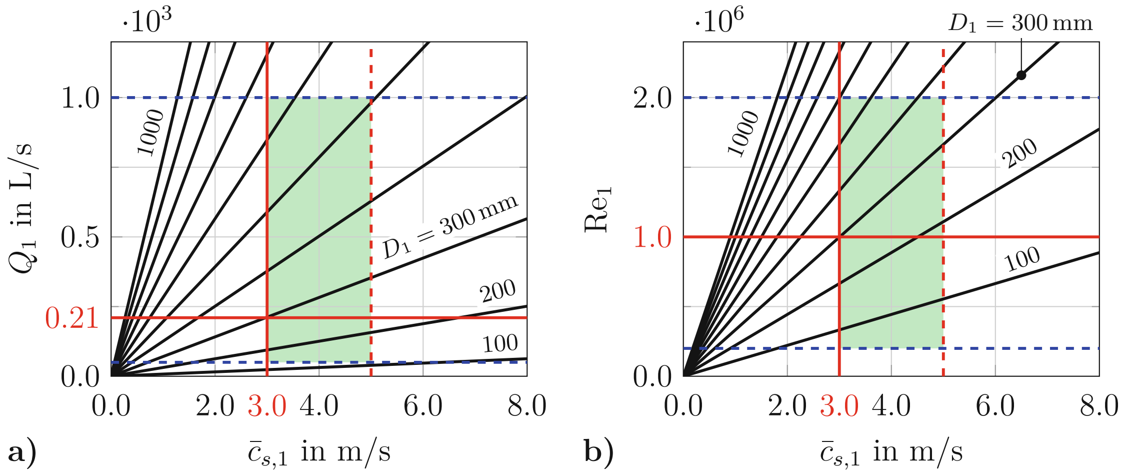

Figure 6.5: Charts of a) volumetric flow rate Q_1 and b) Reynolds number Re_1 plotted against the mean flow velocity $\bar{c}_{s,1}$ for pipes with diameter D_1.

mentioned above of 3 m/s for the inlet velocity at the reference design point and a choice of 300 mm for the diameter of the pipe, the corresponding Reynolds number becomes $1 \cdot 10^6$ and the corresponding volumetric flow rate becomes 210 L/s. This choice of $D_1 = 300$ mm and $\mathrm{Re}_1 = 1 \cdot 10^6$ was made with respect to suitable test rig sizes for the experimental testing planned within the scope of the project *AxFeeder* (FO999888084) and a possible use of the test rig design in a future small hydro field application. In combination with an assumed head of 125 m, the turbine could be rated at a power of around 250 kW. For reference, a suitable runner diameter D_p for such a turbine size would lie at around 340 mm.

So far, all the numbers given relate to reference station 1. With the split of the flow path into n branch lines, the flow quantities can be expressed with respect to the diameter of a station within the branch line, e.g. station 51 with D_{51}. The volumetric flow rate Q_{51} is thus

$$Q_{51} = \frac{D_{51}^2 \pi}{4} \cdot \bar{c}_{s,51} = \frac{Q_1}{n} = \frac{D_1^2 \pi \cdot \bar{c}_{s,1}}{4 \cdot n}, \tag{6.5}$$

and the mean flow velocity $\bar{c}_{s,51}$ becomes

$$\bar{c}_{s,51} = \frac{4Q_{51}}{D_{51}^2 \pi} = \frac{4Q_1}{D_{51}^2 \pi \cdot n} = \left(\frac{D_1}{D_{51}}\right)^2 \cdot \frac{\bar{c}_{s,1}}{n}. \tag{6.6}$$

Finally, the Reynolds number in station 51 is achieved with

$$\mathrm{Re}_{51} = \frac{\bar{c}_{s,51} \cdot D_{51}}{\nu} = \left(\frac{D_1}{D_{51}}\right)^2 \cdot \frac{\bar{c}_{s,1}}{n} \cdot \frac{D_{51}}{\nu} = \frac{D_1}{D_{51}} \cdot \frac{\mathrm{Re}_1}{n}. \tag{6.7}$$

With the *AxFeeder*, the diameter ratio D_1/D_{51} ranges from 2.07 to 3.50 and with $n = 6$ branch lines, Re_{51} lies between 0.34 and $0.58 \cdot \mathrm{Re}_1$. For the commonly used diameter ratio $D_1/D_{51} = 2.5$, $\mathrm{Re}_{51}/\mathrm{Re}_1$ amounts to around 0.42.

6.3.2 Operating regime of the diffuser manifold design

The designated operating regime covers a wide range of pipe diameters D_1, from 100 mm to 500 mm, and Reynolds numbers Re_1, from $2 \cdot 10^5$ to $2 \cdot 10^6$, which are suitable for many possible Pelton turbine layouts in small hydro applications. The diffuser manifold design (basic model) as sketched in part a) of Figure 6.2 was selected for the investigation of the operating regime because the verification of the CFD process was conducted on this design. Thus, possible uncertainties of the CFD simulations were the most well-known for this model. Altogether, 50 simulations were executed in diameter steps of 100 mm and in Reynolds number steps of $2 \cdot 10^5$. To automatise the simulation process, the diffuser manifold design model was fully parameterised such that all geometric quantities scale with the diameter D_1 of the penstock line. Therefore, the design and the operating point were entirely determined by one geometric parameter, the diameter D_1, and one flow parameter, the Reynolds number Re_1. All other quantities, e.g. dimensions and flow velocities, were derived from these two parameters.

The resulting operating charts for the loss coefficients and the secondary velocity ratio at station 101 are presented in Figure 6.6, where each set of data points for one diameter is given a unique symbol and color. In addition to the data points, for each quantity of interest, a fit function in the form $y(\mathrm{Re}_1) = k \cdot \mathrm{Re}_1^a$ with $y \in (\zeta_{PmTE,1011}, \zeta_\Phi, \phi_{II,101})$ and $k, a = \text{const.}$ was computed. The exponents of the fit function can be nicely expressed when substituting $a = -1/b$, such that b, when rounded to the nearest integer, becomes 9 for the power loss coefficient, 8 for the dissipation power coefficient and 16 for the secondary velocity ratio. All coefficients k and a of the fit functions are listed in Table 6.6.

In part a) of Figure 6.6, the loss coefficients, $\zeta_{PmTE,1011}$ and ζ_Φ, show a gradual decline with increasing Reynolds number. The decline levels off for very high Reynolds numbers. Both loss coefficients are very insensitive to a change of the diameter D_1 and thus the size of the *AxFeeder*. The variation due to different D_1 is significantly smaller than the calculated compound simulation error. This compound simulation error is indicated by the area shaded in grey. The width of this area is defined such that the distances between the fit curve and its offset curves equal the root-sum-square U_{RSS} of the individual errors.

Parameter	$\zeta_{PmTE,1011}$	ζ_Φ	$\phi_{II,101}$
k	2.938	2.962	0.101
a	-0.111	-0.129	-0.063
$b = -1/a$	9.0	7.8	15.9
R^2	0.993	0.991	0.558

Table 6.6: Parameters k, a and b and coefficient of determination R^2 of the power function fit curves.

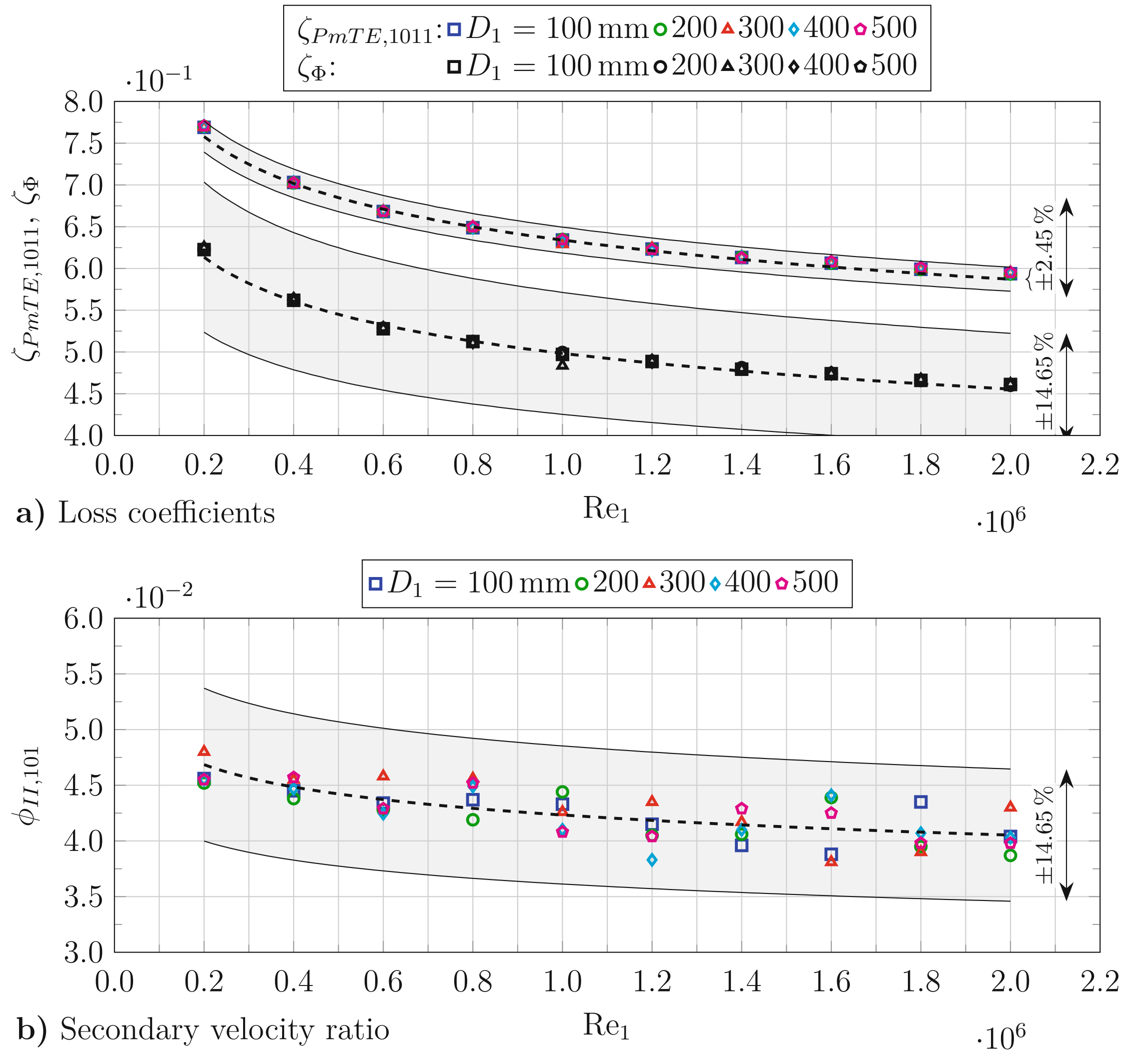

Figure 6.6: Operating charts of the *AxFeeder* with diffuser manifold (basic model) showing the loss coefficients and the secondary velocity ratio at station 101 (including their error bands) against the Reynolds number Re_1 for penstock line diameters D_1 ranging from 100 mm to 500 mm.

The secondary velocity ratio at station 101, depicted in part b) of Figure 6.6 also declines gradually towards higher Reynolds numbers and levels off for high Reynolds numbers at a value of $\phi_{II,101}$ around 0.4. The secondary velocity ratio's decline rate is less steep than the loss coefficients. The difference between $\phi_{II,101}$ at $Re_1 = 2 \cdot 10^5$ and $Re_1 = 2 \cdot 10^6$ is less than 14 % compared to about 25 % for the loss coefficients[9]. However, the scatter of the data points of different diameters D_1 is much more prominent. Thus the coefficient of determination, R^2, of the fit curve for $\phi_{II,101}$ is over 40 % lower than that of $\zeta_{PmTE,1011}$ and ζ_{Φ}. This observation again underlines that the secondary velocity and its underlying swirl phenomena are

[9]The pipe friction factor λ calculated with the correlation of Nikuradse [67], which is specified in Equation (6.10) (taken from Bohl and Elmendorf [6]), decreases by roughly a third in the very same Reynolds number range. For the *AxFeeder*, this hints that if the friction losses decrease steeper than the power losses, the local resistance of the individual components (e.g. bends, diffusers and confusers), the shape resistance, must increase slightly with the Reynolds number.

much more sensitive to any changes within the simulation (e.g. design size) and less sensitive to Reynolds number effects (e.g. boundary layer thickness)[10]. It indicates the limits of the selected steady-state simulation approach as well. However, the resulting variation in the data of the secondary velocity ratio is still clearly within the root-sum-square error band (values listed in Table 6.3); therefore, the observed trend of $\phi_{II,101}$ was deemed plausible.

As stated in Section 6.3.1, the reference design point, for which all subsequent parametric investigations presented in this chapter were executed, was chosen as $D_1 = 300\,\mathrm{mm}$ and $\mathrm{Re}_1 = 1 \cdot 10^6$ with $Q_1 = 210\,\mathrm{L/s}$. The reference velocities calculated from the Reynolds number were $c_{s,1} = 2.975\,\mathrm{m/s}$ for the penstock line and $c_{s,101} = 3.099\,\mathrm{m/s}$ for a typical branch line at station 101 with $D_{101} = 120\,\mathrm{mm}$. Reference velocities different from these values are explained if relevant. These choices were deemed reasonable for the targeted application of the *AxFeeder* as a laboratory test rig and in a small hydropower plant because none of the three main quantities of interest, $\zeta_{PmTE,1011}$, ζ_Φ and $\phi_{II,101}$ showed rapid changes, but a smooth and steady trend within the wide range of investigated Reynolds numbers.

Further, similar to the approach presented by Hahn et al. [30], the values of the loss coefficients $\zeta_{PmTE,1011} = 0.6291$ and $\zeta_\Phi = 0.4837$ as well as the secondary velocity ratio $\phi_{II,101} = 0.0426$ at this operating point were used as reference values for normalising the variables whenever appropriate, e.g. Equations (6.21) and (6.22) and Figure 6.42.

6.4 Parametric investigation

In this section, the effect of variations of relevant geometric parameters on the quantities of interest, the power loss coefficient ζ_{PmTE}, the dissipation power coefficient ζ_Φ, and the secondary velocity ratio ϕ_{II}, is studied for each of the four core manifold designs.

Table 6.7 provides an overview of the parameters varied for the four core design concepts and in which figures the corresponding results are presented. These results are shown in the form of 2-D line plots that are grouped such that the upper plot shows the loss coefficients $\zeta_{PmTE,1011}$ and ζ_Φ and the lower plot shows the secondary velocity ratio $\phi_{II,101}$ against the selected design parameter. In each of these plots, dark-grey lines (full stroke for $\zeta_{PmTE,1011}$ and $\phi_{II,101}$, dashed for ζ_Φ) indicate the corresponding reference values acquired by the investigation of the operating regime (Section 6.3.2). Small vertical bars to either the right or left of these reference lines shall provide a benchmark for a change of $\pm 5\,\%$ of the reference value.

If not stated otherwise, all simulations in this section were conducted using the symmetric models.

[10]A detailed analysis of the cause of this behaviour will have to be subject to future studies.

ID	Manifold type	Design parameters	Shown in
a)	Diffuser manifold (basic model)	diameter ratio D_{51}/D_1, throat radius R_{41}/D_{51}, diffuser angle β	Figures 6.7 to 6.14
b)	Diffuser m. with conical frustum	frustum diameter ratio D_{41}/D_{51}, deviation angle δ, horizontal pivot angle φ	Figures 6.15 to 6.22
c)	Spherical m.	sphere radius SR_{40}/D_1, deviation angle δ, frustum diameter ratio D_{41}/D_{51}	Figures 6.23 to 6.27
d)	Cylindrical m.	axial position T_4/D_{51}, deviation angle δ, throat radius R_{41}/D_{51}	Figures 6.28 to 6.32

Table 6.7: Overview of core designs and varied design parameters.

6.4.1 Diffuser manifold (basic model)

While in Figure 6.2, a comparison of all four core designs of the *AxFeeder* is shown, the parameters varied for the study of the diffuser manifold design presented in this subsection are highlighted in Figure 6.7. Here, it was chosen to investigate the effects of a change of the branch line diameter D_{51}, the throat radius R_{41} and the diffuser angle β on the flow in the manifold and the branch lines.

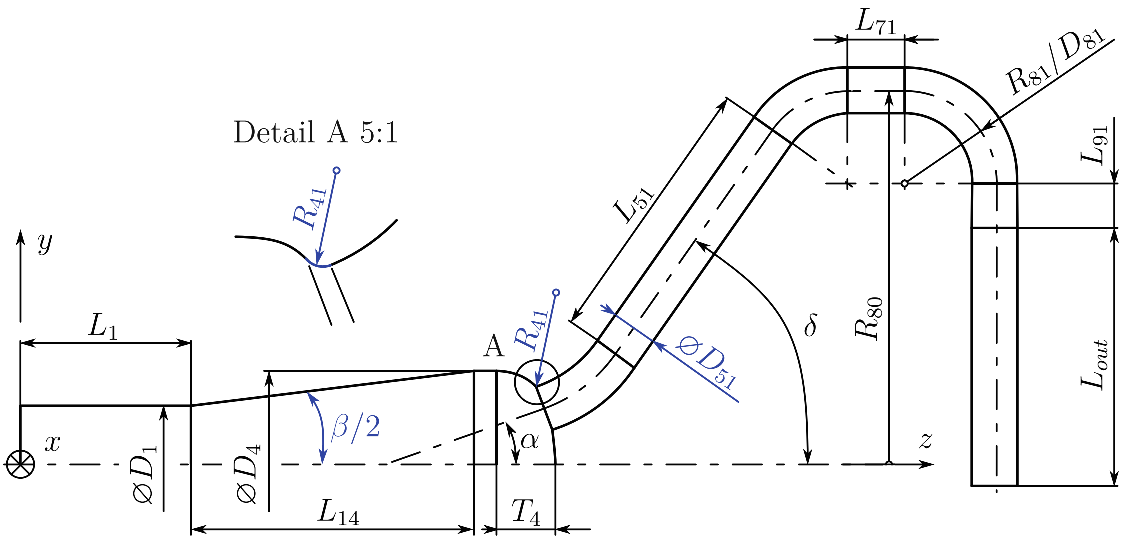

Figure 6.7: Sketch of the diffuser manifold design with dimensions relevant to the parametric study highlighted in blue.

Diameter ratio

An appropriate selection of the branch line diameters depends on several considerations: 1) From a manufacturing point of view, choosing the diameters so standard pipes can be used is desired; 2) From a design point of view, a smooth connection from the manifold to the branch lines is required; 3) From a hydraulic machinery point of view, minimal losses and limited secondary flow are needed for high efficiencies. Due to the early research stage on Pelton turbine distributor systems with axial inflow, demand 1) was given the least priority in this thesis. Instead, the diameter ratio D_{51}/D_1, within constraints of the restricted space at the manifold head, was varied from very small to very large diameters D_{51} until demand 3) was not fulfilled anymore. Demand 2) is addressed in subsequent paragraphs elaborating on the throat radius.

The results of the variation of the branch line diameter are depicted in Figure 6.8, where the loss coefficients $\zeta_{PmTE,1011}$ and ζ_Φ are plotted in part a) and the secondary velocity ratio $\phi_{II,101}$ is plotted in part b) of this figure. The loss curves and the secondary velocity ratio curve show opposing trends. A smaller branch line diameter causes a larger restriction as the flow transits through the head of the manifold into the branch line. Also, the resulting transport velocity in the principal flow direction and the Reynolds number (computed by Equation (6.7)) in the branch line increase. The plots reveal that between $0.36 < D_{51}/D_1 < 0.4$, there is an optimum, where the losses are relatively low, but the secondary velocity ratio has not yet risen steeply. Therefore, if not stated otherwise, a diameter ratio of $D_{51}/D_1 = 0.4$ was selected for further investigation within this subsection.

The reaction of the loss coefficients to a change in the branch line diameter can be explained by the following analytical model: Assuming a fully turbulent flow of a fluid with density ρ and a mean velocity c_s in a hydraulically smooth, straight, circular pipe with diameter d, the total pressure loss[11] Δp_t occurring along the length l is defined as

$$\Delta p_t = \lambda \cdot \frac{l}{d} \cdot \rho \frac{c_s^2}{2} \,. \tag{6.8}$$

If the velocity is expressed by the constant volumetric flow rate $Q = c_s \cdot d^2\pi/4$, Equation (6.8) can be rewritten as

$$\Delta p_t = \lambda \cdot \frac{l}{d} \cdot \frac{\rho}{2} \cdot \left(\frac{4Q}{d^2\pi}\right)^2 = \frac{\lambda}{d^5} \cdot \underbrace{\left(8 \cdot l \cdot Q^2 \frac{\rho}{\pi^2}\right)}_{const.} \sim const. \cdot \lambda \cdot \frac{1}{d^5} \,. \tag{6.9}$$

The total pressure loss Δp_t depends only on the pipe friction factor $\lambda = f(\mathrm{Re})$ and the inverse of the fifth power of the pipe diameter. The pipe friction factor for a hydraulically smooth pipe depends only on the Reynolds number of the flow and can be estimated by the correlation of Nikuradse [67] (taken from Bohl and Elmendorf [6]),

$$\lambda(\mathrm{Re}) = 0.0032 + 0.221 \cdot \mathrm{Re}^{-0.237} \,, \tag{6.10}$$

which is valid in the range of $1 \cdot 10^5 < \mathrm{Re} < 5 \cdot 10^6$. Given that

$$\mathrm{Re} = \frac{c_s d}{\nu} = \frac{4Q}{d\pi\nu} \sim const. \cdot d^{-1} \,, \tag{6.11}$$

thus $\lambda \sim d^{0.237}$ and finally $\Delta p_t \sim 1/d^{4.763}$, it was proved that the total pressure loss, being inversely proportional to the pipe diameter risen by a constant value greater than 4, is dominated by the pipe diameter.

[11] A detailed derivation of this equation is given in [6, 36, 38].

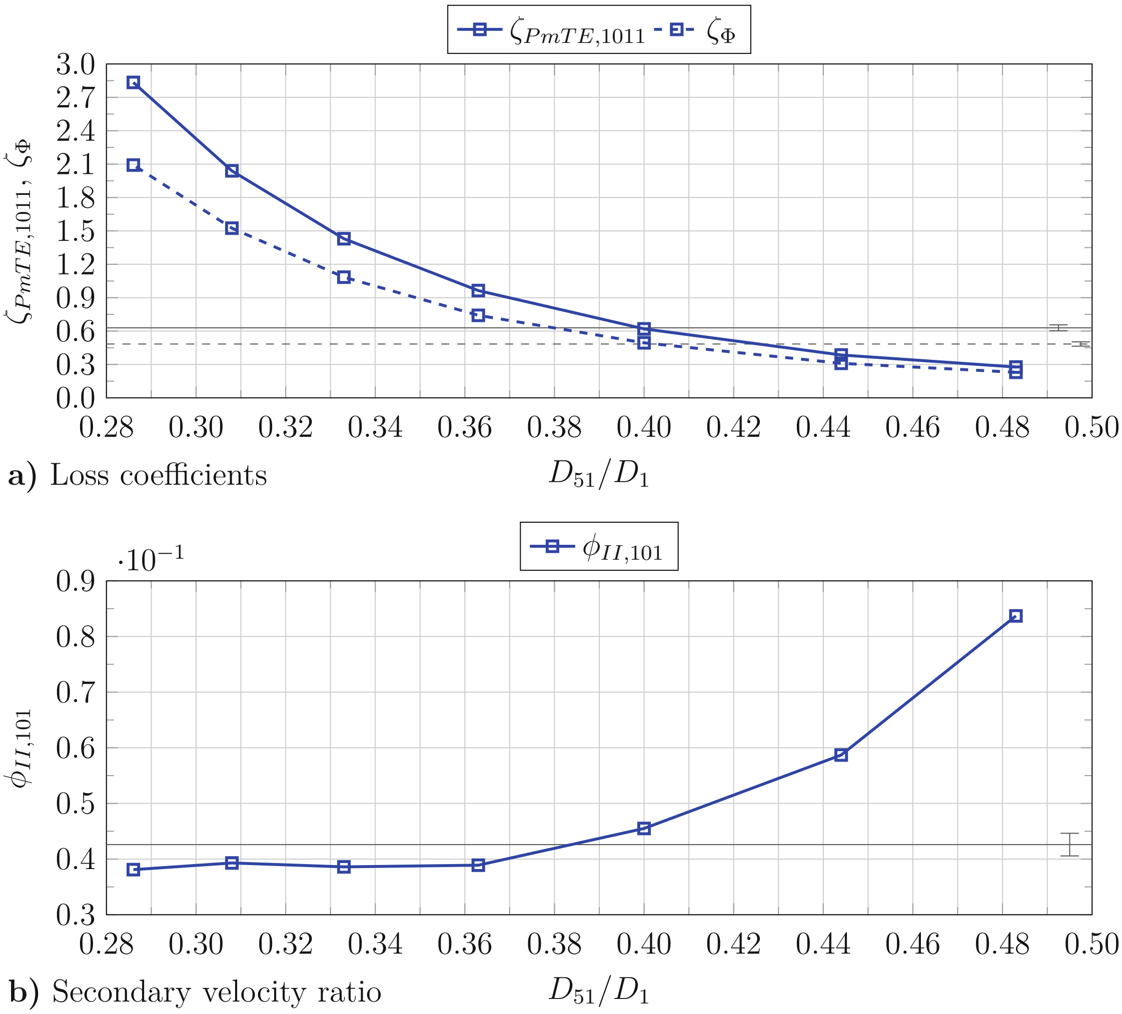

Figure 6.8: Line plots of the loss coefficients and secondary velocity ratios of the diffuser manifold design (basic model) against the diameter ratio D_{51}/D_1.

So, for two pipes A and B with same length and flow rate, the constants cancel out, and the total pressure losses relate to each other as follows

$$K_{ana} := \frac{\Delta p_{t,A}}{\Delta p_{t,B}} = \frac{\lambda_A}{\lambda_B} \cdot \left(\frac{d_B}{d_A}\right)^5 \sim \left(\frac{d_B}{d_A}\right)^{4.763} . \tag{6.12}$$

Similarly, the power losses and dissipation power of the *AxFeeder* evaluated for different diameter ratios D_{51}/D_1 can be compared,

$$K_{PmTE} := \frac{\zeta_{PmTE,1011}(D_{51}/D_1)}{\zeta_{PmTE,1011}(D_{51}/D_1 = 0.4)} \quad \text{and} \quad K_\Phi := \frac{\zeta_\Phi(D_{51}/D_1)}{\zeta_\Phi(D_{51}/D_1 = 0.4)} , \tag{6.13}$$

where $\zeta_{PmTE,1011}(D_{51}/D_1 = 0.4)$ and $\zeta_\Phi(D_{51}/D_1 = 0.4)$ were taken as the reference points. This comparison is plotted in Figure 6.9 together with the relative differences

$$\Delta K_{PmTE} := \frac{K_{PmTE} - K_{ana}}{K_{ana}} \qquad \text{and} \qquad \Delta K_\Phi := \frac{K_\Phi - K_{ana}}{K_{ana}} \tag{6.14}$$

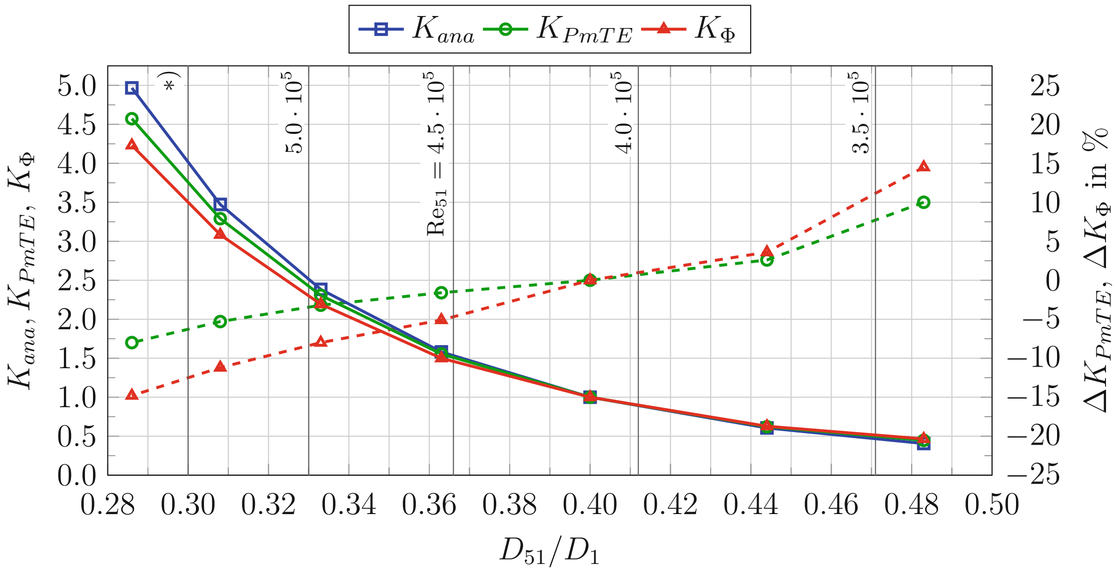

Figure 6.9: Comparison of the normalised loss coefficients against the analytical correlation. $*) = 5.5 \cdot 10^5$

between the analytical relation of Equation (6.12) and the CFD results acquired by Equation (6.13).

The relative differences between K_{PmTE} and K_{ana} are less than 5 % for all data points except for the smallest and the largest diameter ratio. The relative differences between K_Φ and K_{ana} are slightly bigger. This observation proves a satisfactory agreement between the analytical correlation of Equation (6.12) and the simulation data of both loss coefficients. Further, it is proved that the choice of the size of the branch line has a major influence on the losses of the *AxFeeder*.

Throat radius

Rounding of the transition from the manifold head to the branch line offers great potential to reduce the flow losses. However, as Figure 6.10 reveals, the loss curves and the secondary velocity ratio again show opposing trends. With the configuration with sharp transition ($R_{41}/D_{51} = 0$) as a reference, a rounded throat allows for a possible loss reduction of over a third. In turn, unfortunately, the secondary flow ratio at station 101 rises by almost 50 %. The sharp decline of the losses can be compared to the correlation of the loss coefficient for a rounded contraction. To model this, Idelchik [38] recommends

$$\zeta = \underbrace{\zeta' \cdot \overbrace{\left(\frac{A_{small}}{A_{big}}\right)^{(3/4)}}^{:=a}}_{Contraction} + \underbrace{\zeta_{fr}}_{Straight\,pipe} = \zeta' \cdot a + \zeta_{fr} \tag{6.15}$$

with the factor a accounting for the cross-section change. In the case of the *AxFeeder*, it is assumed that A_{small} corresponds to the cross-section of a single branch line and A_{big} corresponds to the $n = 6^{th}$ part of the manifold cross-section. This gives

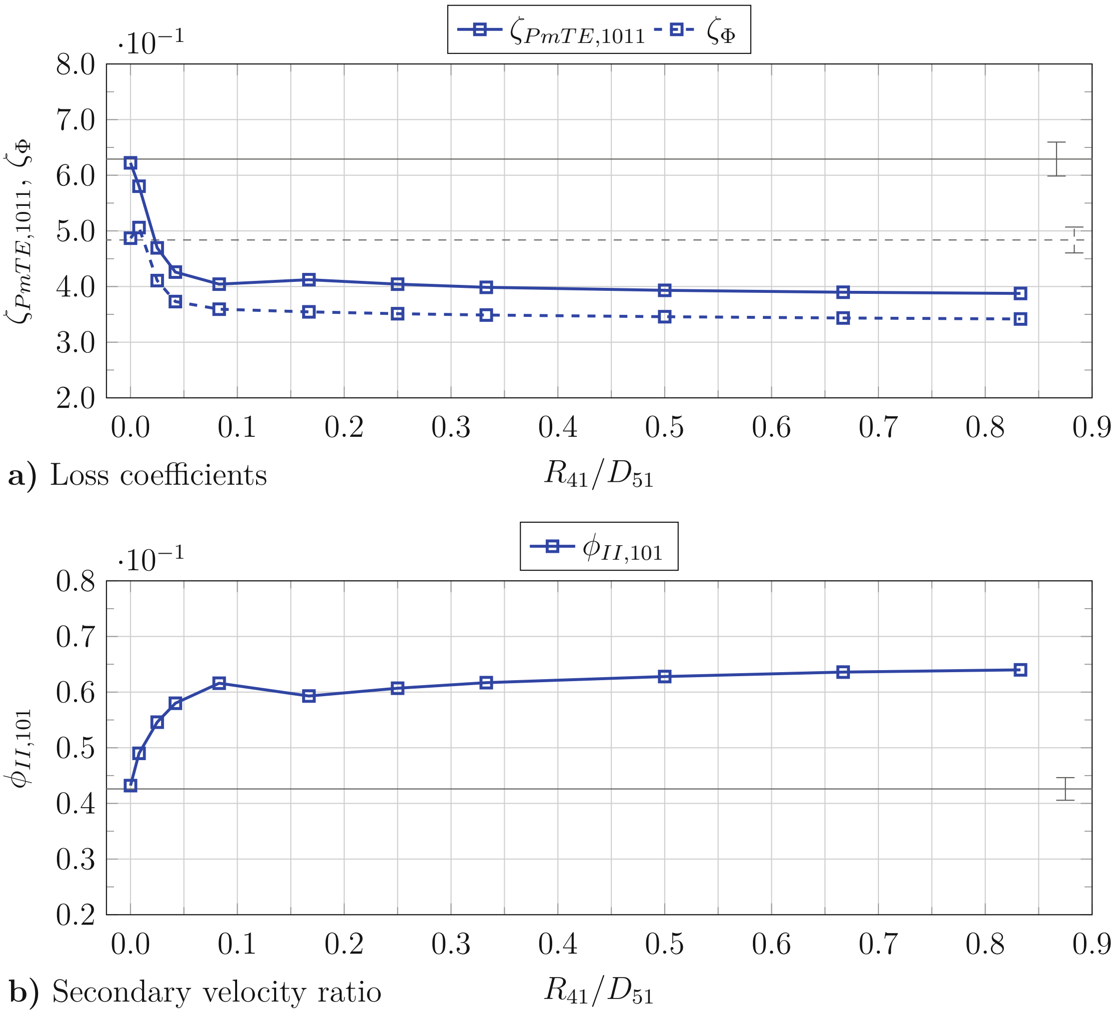

a) Loss coefficients

b) Secondary velocity ratio

Figure 6.10: Line plots of the loss coefficients and secondary velocity ratios of the diffuser manifold design (basic model) against the throat radius R_{41}/D_{51}.

a value of almost exactly 0.7 for the factor a. The resistance coefficient ζ' can be modelled as a special case of a circular bellmouth inlet. For this case, Idelchik [38] gives a correlation depending of the relative throat radius r/D

$$\zeta' = 0.03 + 0.47 \cdot 10^{-7.7 \cdot \frac{r}{D}} \tag{6.16}$$

which can be plugged into Equation (6.15), so that the correlation for the loss coefficient of a rounded contraction becomes

$$\zeta = 0.7 \cdot \left(0.03 + 0.47 \cdot 10^{-7.7 \cdot \frac{r}{D}}\right) + \zeta_{fr} \,. \tag{6.17}$$

To compare Equation (6.17) to the decline of the power loss coefficient $\frac{\partial \zeta_{PmTE,1011}}{\partial\left(\frac{R_{41}}{D_{51}}\right)}$ and the decline of the dissipation power coefficient $\frac{\partial \zeta_\Phi}{\partial\left(\frac{R_{41}}{D_{51}}\right)}$, the first derivative

$$\frac{\partial \zeta}{\partial\left(\frac{r}{D}\right)} = 0.7 \cdot \frac{\partial \zeta'}{\partial\left(\frac{r}{D}\right)} = -5.858 \cdot 10^{-7.7 \cdot \frac{r}{D}} \tag{6.18}$$

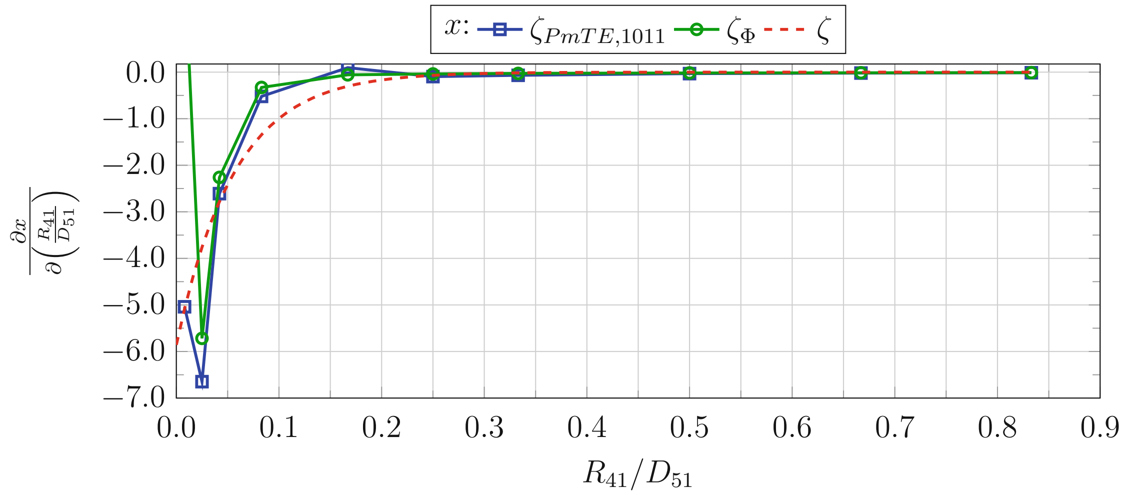

Figure 6.11: Rate of change of the loss coefficients $\zeta_{PmTE,1011}$ and ζ_{Φ} compared to the analytical correlation.

of ζ is used and plotted against the relative throat radius R_{41}/D_{51} in Figure 6.11. This figure shows that the rates of change of the loss coefficients largely agree with the analytical correlation, barring the outlier for very small throat radii. These outliers result from the fact that at very small throat radii, an even more refined mesh would be needed to capture the flow in all detail. The computational effort for this is unreasonable with the presented parametric study, as the general trend holds regardless of the outliers. Further, both Figures 6.10 and 6.11 display that the loss coefficients and the secondary velocity ratio level off at a relative throat radius of around 0.1 to 0.2, where the effect of rounding the throat diminishes.

Diffuser angle

In core design a) of the *AxFeeder*, a conical diffuser allows for the increase in pipe diameter from the manifold neck (D_1) to the manifold head (D_4). In the case of the *AxFeeder*, the area ratio

$$AR = \frac{A_2}{A_1} = \left(\frac{D_2}{D_1}\right)^2 \xRightarrow{AxFeeder} AR = \left(\frac{D_4}{D_1}\right)^2 = 2.56 \tag{6.19}$$

is fixed at 2.56, because D_1 and D_4 were fixed to allow for sufficient space at the manifold head for the connection to the branch lines. This situation resembles one of the optimum problems of Kline et al. [47], where the task was to find a suitable length and opening angle for a diffuser of fixed area ratio to achieve maximum pressure recovery. Prechter [73] advises that for such a problem, under steady flow conditions, any length is suitable as long as the opening angle stays below the limiting line a-a of the diffuser chart, Figure 6.12. So, for the parameter study of the *AxFeeder*, to keep the design as compact as possible (see [30] and Section 6.1.2), it is of particular interest to find a minimum length (in other words, a maximum diffuser angle β), for which a steady flow without separation and stall, yet at the same time with the least amount of losses and secondary flows, can be achieved.

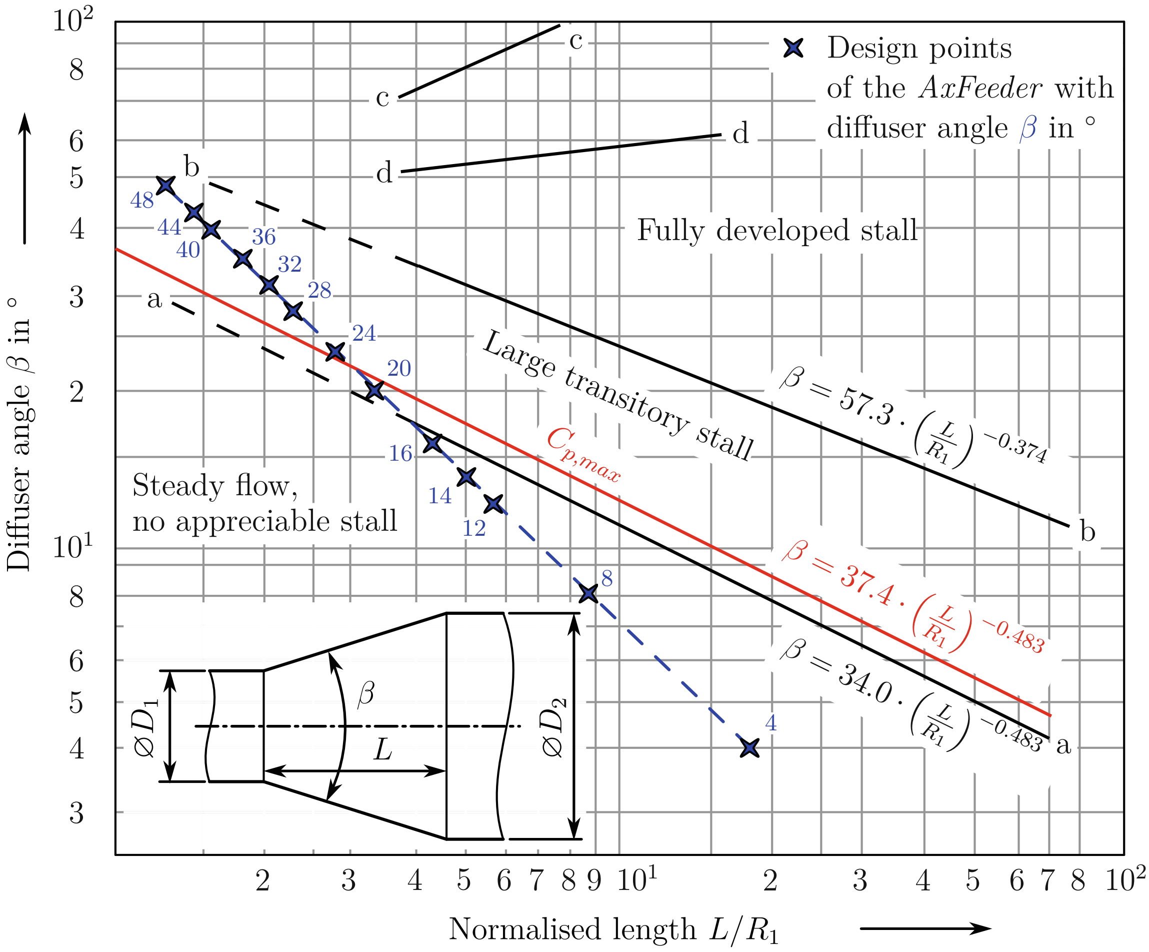

Figure 6.12: Flow regimes of conical diffusers recreated and modified from Prechter [73] as cited in Bohl and Elmendorf [6]. Strictly valid for $L/R_1 > 4$.

As stated by Sovran and Klomp [96], two parameters completely define the geometries of straight-walled and conical diffusers. These parameters are the area ratio AR and the non-dimensional lengths L/W_1 or L/R_1, respectively[12]. Therefore, because the area ratio was already set, the only independent parameter left is the diffuser half angle $\beta/2$ and, related to it, the axial length L_{14}. The diffuser half-angle was varied in steps of 2° from 2° to 24°. Thus, the range of tested diffuser angles β was from 4° to 48° with corresponding non-dimensional lengths L_{14}/R_1 from 17.18 to 1.35. All design points tested are indicated by the blue cross markers in Figure 6.12. Because of the fixed area ratio, these points lie on a straight line in the double-logarithmic plot of the flow regions. In this plot, which was recreated and modified from Prechter [73] as cited in Bohl and Elmendorf [6], the flow regimes of a conical diffuser with straight walls are shown[13]. A steady flow

[12]While in many publications, e.g. [59, 74, 96], the axial length of the diffuser (equivalent to the height of the frustum) is labelled by the letter N and the slant height is labelled by the letter L, for compliance with the nomenclature of the *AxFeeder*, in this thesis, the axial length is denoted by the letter L, e.g. L_{14}.

[13]A similar version of this plot was already shown by Kline et al. [47]. Kline [47] and Prechter [73] point out that this plot was created for plane-wall two-dimensional subsonic diffusers but can

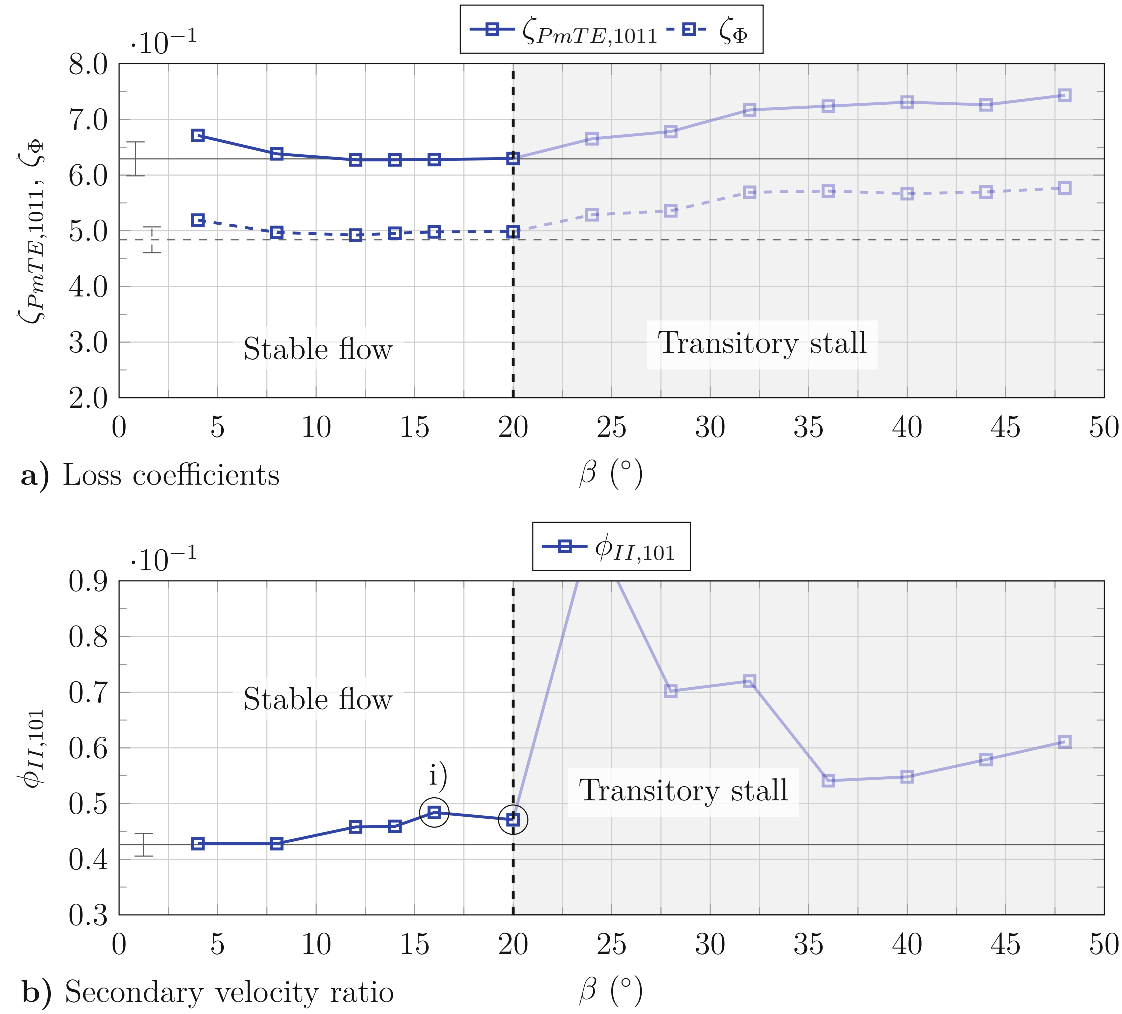

Figure 6.13: Line plots of the loss coefficients and secondary velocity ratios of the diffuser manifold design (basic model) against the diffuser angle β. i) - Data points with ○ are discussed in Figure 6.14.

without appreciable stall can be expected for short diffusers with small angles β. If a certain threshold is passed (indicated by line a-a), a large transitory stall occurs. According to Reneau et al. [74], this regime is characterised by stall regions that constantly form in, and are then washed out of the diffuser. Following McDonald and Fox [59], the curve of maximum pressure recovery $C_{p,max} = (p_2 - p_1)/p_{dyn,1}$ for conical diffusers at constant length ratio lies in the steady flow regime. However, Kline et al. [47], Prechter [73] and Reneau et al. [74] show the $C_{p,max}$ curve, depicted in red in Figure 6.12, just above line a-a, already in the transitory stall regime.

In the case of the *AxFeeder*, where minimal losses[14] and secondary flows are desired, design points with signs of stall are not favourable. Coming from line a-a and

also be applied to conical diffusers.

[14]Reneau et al. [74] showed for plane diffusers that the minimum pressure loss occurs at lower opening angles than the maximum effectiveness and the maximum of the pressure recovery, $C_{p,max}$.

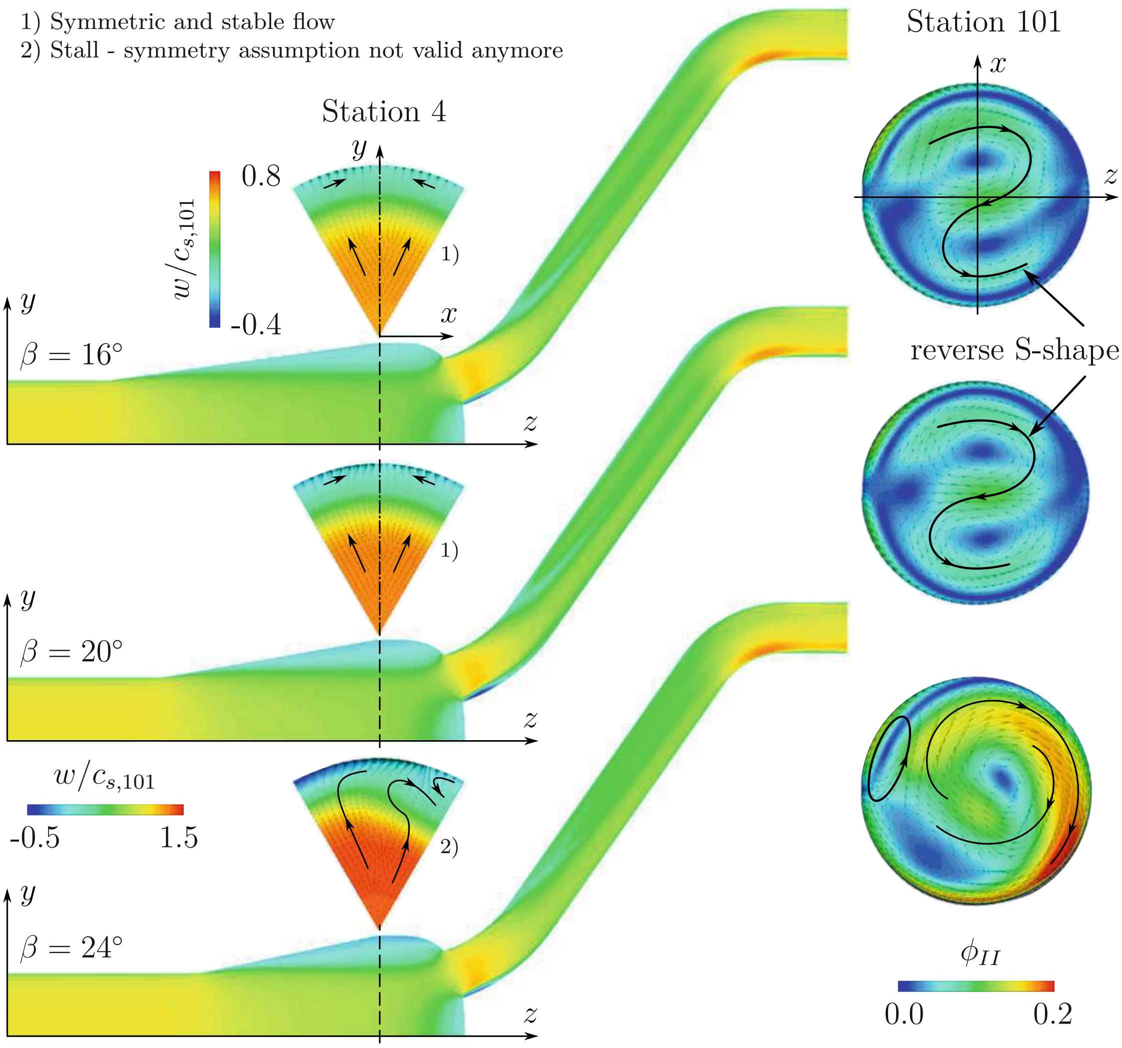

Figure 6.14: Plots of the normalised velocity component w in z-direction in the y-z plane and in station 4 as well as the secondary velocity ratio ϕ_{II} in station 101 for three different diffuser angles β.

the corresponding equation $\beta = 34.0 \cdot \left(\frac{L}{R_1}\right)^{-0.483}$, such a critical angle would be between 16° and 20° for the area ratio of the *AxFeeder* of $AR = 2.56$. The plots in Figure 6.13 indicate that the onset of stall occurs at probably around 20°, as the loss coefficients show a gradual increase from this angle to the right and the secondary velocity ratio rises sharply as well.

An even more precise picture of the flow is given in Figure 6.14, where contour plots of the cases with $\beta = 16°$, 20° and 24° are analysed. The plots in the y-z plane show the velocity component w in the z-direction normalised by the mean streamwise velocity $c_{s,101}$ in station 101. While the plots generally appear very similar to each other, a closer look reveals that the zone with low or even negative velocity w at the outer wall of the diffuser has become more prominent for the case with the biggest diffuser angle $\beta = 24°$. The contour plots of station 4 show that the flow is symmetric for the cases with $\beta = 16°$ and $\beta = 20°$, but shifted to the negative x-direction for $\beta = 24°$. In this case, the secondary flow becomes asymmetric, which indicates stall in the diffuser. Further, the asymmetric secondary flow contour indicates that the symmetry modelling assumption is no longer valid. Thus, all values for the loss coefficients and the secondary velocity ratio in the transitory stall region must be treated cautiously and consequently are greyed out in Figure 6.13. The contours of the secondary velocity ratio ϕ_{II} in station 101 are plotted on the right of Figure 6.14. While for all cases with $\beta \leqslant 20°$, the distinctive reverse S-shape pattern appears, the apparent stall in the diffuser when $\beta > 20°$ leads to a distorted spiral-like pattern of the secondary flow at this station and consequently to an unmistakable rise in $\phi_{II,101}$ (part b) of Figure 6.13. Thus, diffuser opening angles of $\beta \geqslant 20°$ must be avoided strictly. In order to avoid flow separation and stall securely, the angle β should not exceed 16° [30].

6.4.2 Diffuser manifold with conical frustum

The diffuser manifold (basic model) a) had little flexibility in the position of the first branch line segment. The tight space at the manifold head prohibited a significant variation of the deviation angle α. To overcome this, core design b), the diffuser manifold with conical frustum was established. Here, the first upward-curved segment of the branch line was removed. Instead, a straight conical frustum with base diameter D_{41}, top diameter D_{51} and constant length $L_{41} = 5/3 \cdot D_{101}$ was applied as the connecting segment between the manifold head and the branch lines. This measure made it possible to reduce the double deflection of the diffuser manifold (basic model), first by the angle α and then by the angle δ to a single deflection by the angle δ only. Further, increasing the base diameter D_{41} of the frustum allowed to lessen the restriction when the flow enters the branch line.

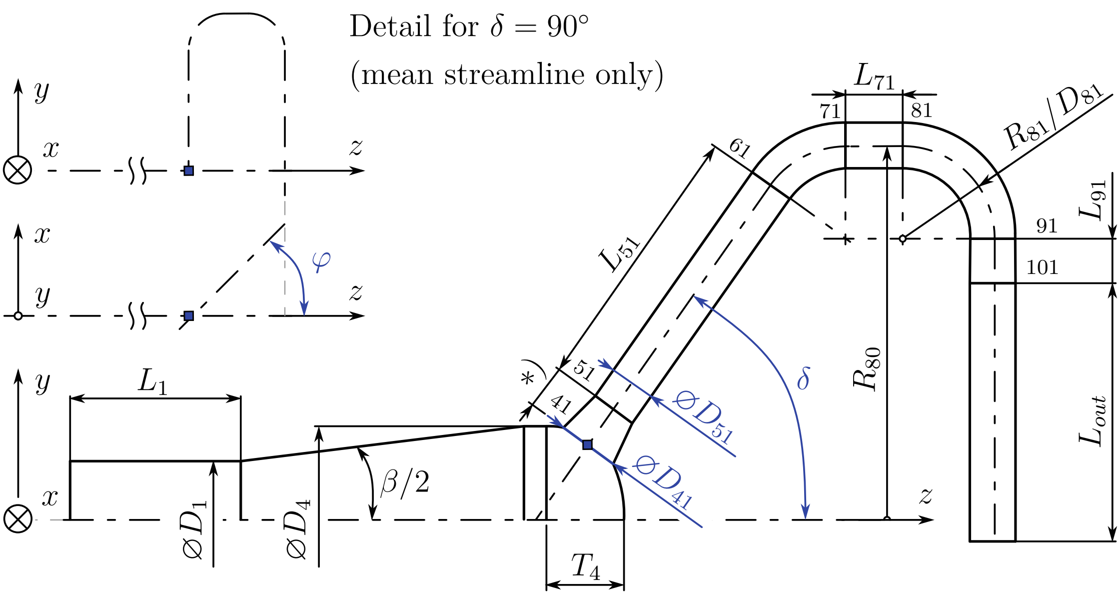

Figure 6.15: Sketch of the diffuser manifold design with conical frustum. Dimensions relevant to the parametric study are highlighted in blue. $*) = L_{41}$.

An interesting design option arises if the deviation angle δ is set to 90°. Then, the pivot angle γ of the injector bend can be set to zero, and instead, the branch line is rotated at the connecting flange (station 51) to the manifold by an angle φ to provide sufficient room for the runner. This is sketched in the detail of Figure 6.15 as well as in Figure 6.20 and intensively discussed in conjunction with Figures 6.21 and 6.22. If not stated explicitly, however, the standard branch line angles[15] were $\gamma = 9.3°$ and $\varphi = 0°$.

Following the findings of Section 6.4.1 on the selection of the diffuser angle, if not stated otherwise, for all configurations with the diffuser manifold design with conical frustum, a diffuser angle β of 14° was chosen.

Frustum diameter and deviation angle

The effect of a variation of the frustum diameter ratio D_{41}/D_{51} on the loss coefficients $\zeta_{PmTE,1011}$ and ζ_{Φ} is plotted in part a) of Figure 6.16 for five deviation angles of the branch line ranging from 50° to 90°. For all investigated combinations of the frustum diameter ratio and the deviation angle, the clear trend of rapidly decreasing losses with increasing diameter ratio becomes evident. The minimum values of the losses for diameter ratios between $D_{41}/D_{51} = 1.6$ to 1.8 (depending on the deviation angle) are almost 50 % lower than the corresponding maximum value for the configuration without a frustum ($D_{41}/D_{51} = 1.0$). If the diameter ratio becomes too large, then a slight increase in the loss coefficients is observed. This global increase can be attributed to the increase in local losses when the flow exits the frustum and enters the cylindrical part of the branch line at station 51. A minor rise in the loss coefficients was also observed if the deviation angle was increased. This increase can be explained by the general trend that the losses in a pipe correlate with the deflection of the flow (e.g. [38]).

The contour plots of the viscous dissipation Φ_{Vis} (upper row) and turbulent dissipation Φ_{Turb} (lower row) in Figure 6.17 allow for more in-depth analysis of the change of losses in cases where a conical frustum is applied. In this figure, two distinct cases with a branch line deviation angle of 90°, one without a frustum, $D_{41}/D_{51} = 1.0$, and one with a frustum of $D_{41}/D_{51} = 1.6$, are compared.
On average, the viscous dissipation is almost an order of magnitude lower than the turbulent dissipation. Roughly, four-fifths of the global dissipation losses are caused by turbulent dissipation Φ_{Turb} and only one-fifth is caused by viscous dissipation Φ_{Vis}. Irrespective of this, both viscous and turbulent dissipation have their maximum values in the wall boundary layer as well as at the sharp transition edge from the manifold neck to the frustum[16]. This transition from the manifold neck to the frustum is paramount, as most losses originate from that location. In the case without a frustum, the flow is restricted too much and forms a considerable separation zone that blocks the flow and affects the entire first part branch line

[15] These values were chosen in accordance with the designated design parameters and planned operating regime. For details, refer to Section 6.3.

[16] Great care is therefore required when selecting the turbulence model and the mesh resolution close to the walls. This issue was addressed in detail in Section 5.2.

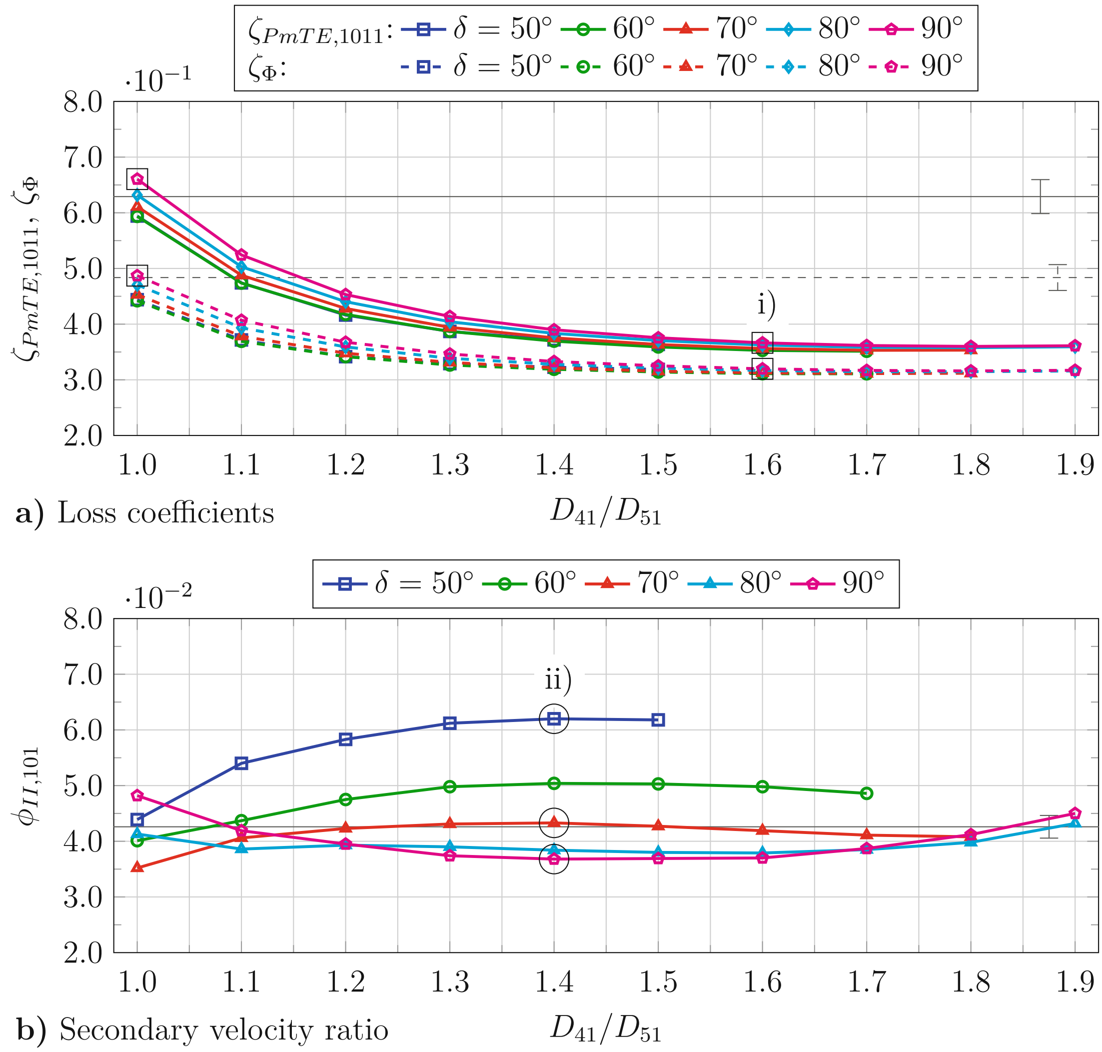

Figure 6.16: Line plots of the loss coefficients and secondary velocity ratios of the diffuser manifold design with conical frustum against the frustum diameter ratio D_{41}/D_{51} for different deviation angles δ. i) - Data points with $\square$ are shown in Figure 6.17. ii) - Data points with $\bigcirc$ are shown in Figure 6.18 and in Figure 6.19 (only $D_{41}/D_{51} = 1.4$ and $\delta = 90°$).

up to around the horizontal part between stations 71 and 81. A high amount of turbulent kinetic energy is produced in that process and, due to the direct correlation between the turbulent kinetic energy k and the turbulent dissipation Φ_{Turb} (see Equation (3.26)), the dissipation at that location is high. The larger opening of the frustum (see plots on the right of Figure 6.17) allows the flow to more evenly change its direction and enter the branch line, so that the local acceleration and deceleration of the flow is lower. Also, less turbulence is produced, and, overall, the dissipation in that zone is significantly lower.

The effect of the separation zone is even better illustrated by the contour plots of the normalised velocity in station 51, Figure 6.17, where, for the case without a frustum,

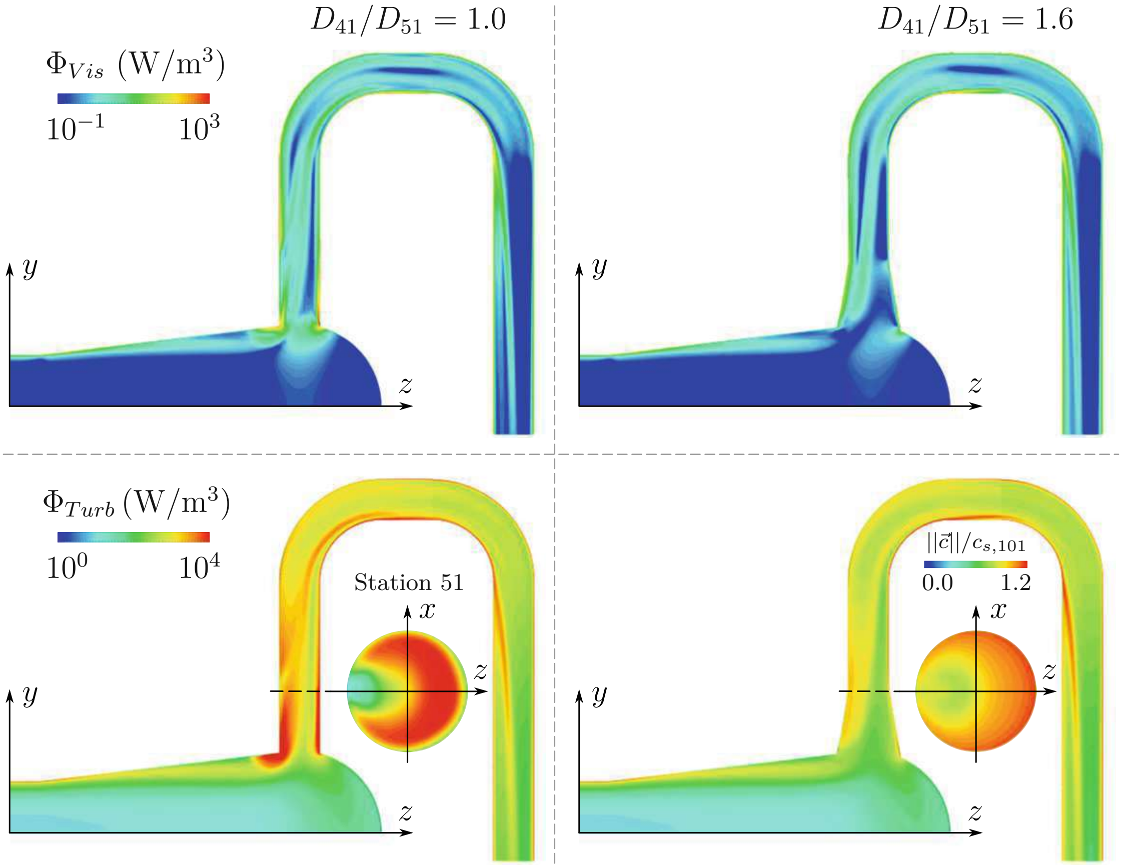

Figure 6.17: Comparison of the local losses by means of the viscous dissipation Φ_{Vis} and turbulent dissipation Φ_{Turb} in the y-z plane of a case without frustum and a case with a frustum diameter ratio $D_{41}/D_{51} = 1.6$. Contours of the normalised velocity magnitude in station 51.

a massive difference between the low velocity area at the inside (low z coordinate) of the station and the high velocity area at the outside (high z coordinate) is observed. This difference in velocity is mixed out downstream and causes additional mixing losses. In the case with the frustum, the differences between the velocity maxima and minima are around 50 % lower than in the configuration without frustum and thus also the mixing losses and the turbulent dissipation downstream are much less.

In contrast to the clear trends shown by both loss coefficients, the picture of the secondary velocity ratio appears more complex. For a wide range of frustum diameter ratios, namely $1.2 < D_{41}/D_{51} < 1.7$, the secondary velocity ratio at station 101, $\phi_{II,101}$, is largely unaffected by the diameter ratio, but decreases with an increase of the deviation angle δ (see part b) of Figure 6.16). This results in a minimum of the secondary velocity ratio for a steep deviation angle of 90° and a medium frustum diameter ratio of 1.4. Compared to the case with $\delta = 70°$ and $D_{41}/D_{51} = 1.0$, which has a similarly low secondary velocity ratio, this configuration with $\delta = 90°$ and $D_{41}/D_{51} = 1.4$ exhibits better overall performance, because it excels at both quality criteria, showing low losses and little secondary flows at the same time. A more

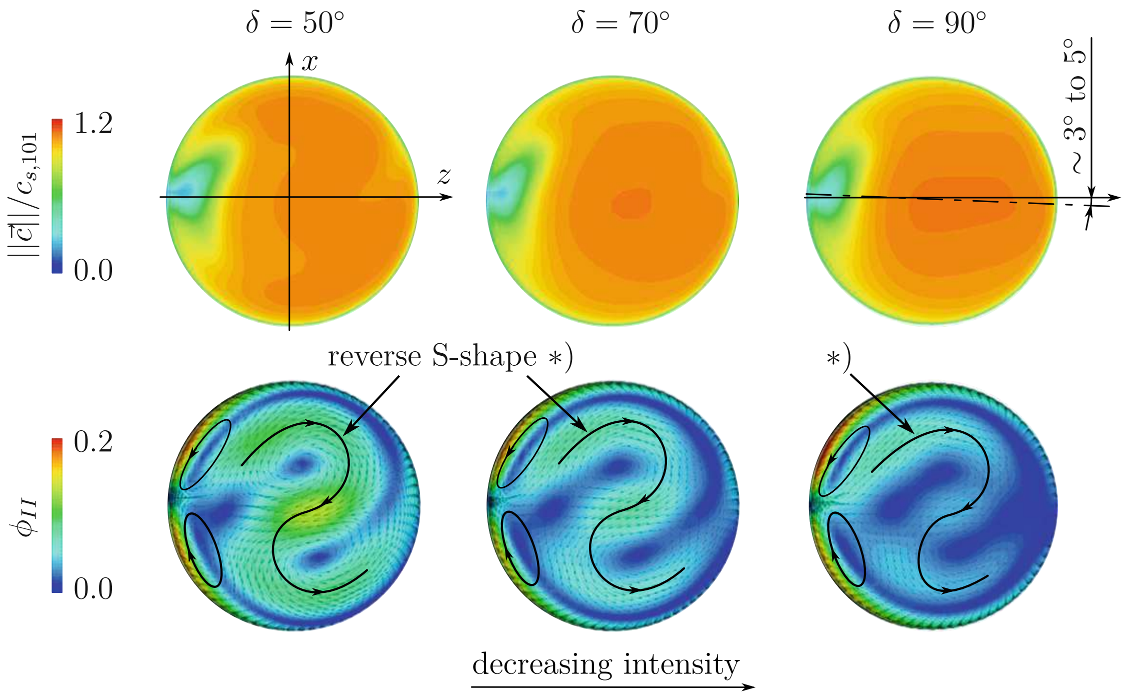

Figure 6.18: Comparison of the velocity magnitude $||\vec{c}||/c_{s,101}$ and the secondary velocity ratio ϕ_{II} in station 101 for deviation angles $\delta = 50°$, $70°$ and $90°$ of a case with a frustum diameter ratio of $D_{41}/D_{51} = 1.4$.

in-depth picture of the secondary flow in station 101 is presented in Figure 6.18, where, for a constant frustum diameter ratio of $D_{41}/D_{51} = 1.4$, the contours of the normalised velocity magnitude $||\vec{c}||/c_{s,101}$ and the secondary velocity ratio ϕ_{II} for three deviation angles $\delta = 50°$, $70°$ and $90°$ are compared. All three contour plots of the normalised velocity magnitude show a distinct velocity deficit close to the inside of the bend (low z-axis position), with the velocity core shifting towards the outside (high z-axis position). The velocity deficit is the most pronounced for the case with the obtuse branch line angle $\delta = 50°$ and gradually smaller if δ increases. Also, if δ increases, the velocity deficit becomes more (axi-)symmetric, but still with the core shifted towards the high z-axis position. Because of the pivot of the injector bend by the angle γ, the symmetry line is rotated away from the z-axis by 3° to 5°, which amounts to roughly one-third to one-half of the value of the pivot angle γ. When comparing the plots of the velocity magnitude and the plots of the secondary velocity ratio, there is a clear correlation between even and (axi-)symmetric velocity contours and low magnitudes of the secondary velocity. In contrast, the general reverse S-shape pattern with two smaller vortices and the inside of the bend does not change if the deviation angle is increased.

The distinct reverse S-shape pattern forms from a combination of superposed effects in the manifold and the branch lines. In general, the flow is subjected to a series of turns in multiple directions, and each time, there is a short straight section between the turns. At first, when the branch line is connected to the manifold head, the flow has to turn by an angle δ towards the y-axis (away from the manifold

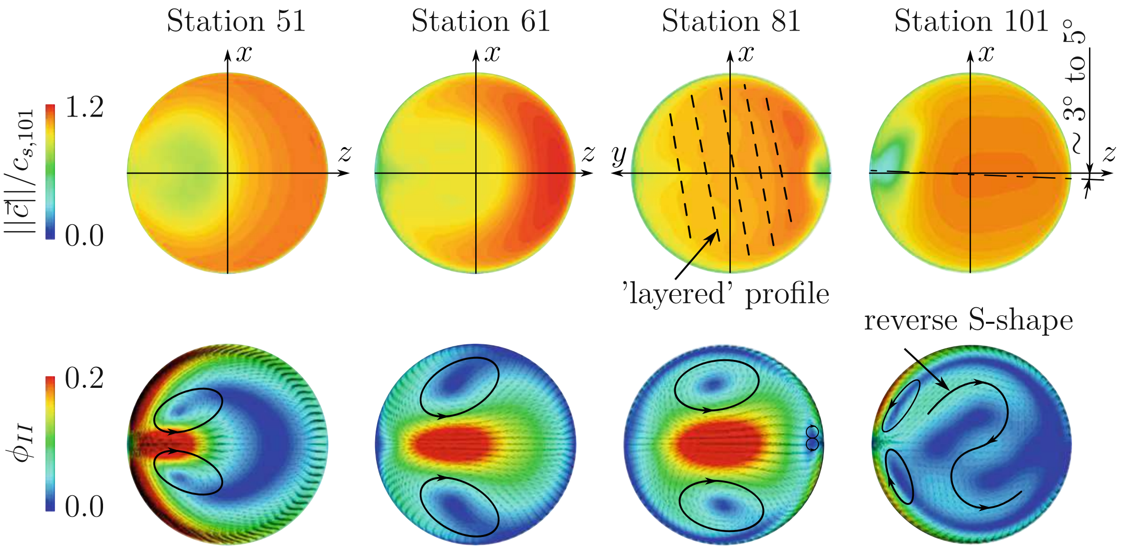

Figure 6.19: Evolution of the contours of velocity magnitude $||\vec{c}||/c_{s,101}$ and the contours of the secondary velocity ratio ϕ_{II} in stations 51 to 101 for a design with a deviation angle $\delta = 90°$ and a frustum diameter ratio of $D_{41}/D_{51} = 1.4$.

centreline). This turn is followed by a straight section (insert) of varying length[17] between stations 51 and 61 and another turn by the angle δ, this time in the opposite direction[18] (stations 61 to 71). After a short straight insert (stations 71 to 81) of length $L_{71}/D_{101} = 1.25$, the injector bend turns the flow by 90° towards the negative y-direction and, at the same time, by the pivot angle γ in the positive x-direction.

The first turn from the manifold head until the top of the frustum at station 51 induces a pair of strong counter-rotating vortices. This vortex pair is called Dean vortex[19] [13] and is very well visible in Figure 6.19. These vortices are advected with the flow along the entire branch line, and their effect also contributes to the reverse S-shape pattern in station 101. The sense of rotation of the vortices in station 51 is such that along the centerline (z-axis), the secondary flow moves in positive z-direction towards the outside of the branch line. To preserve continuity, the fluid is transported in negative z-direction along the outer wall back to the inside of the branch line. This movement contributes to the distinct shift of the core of the flow towards the positive z-direction seen in the velocity magnitude plot of station 51. As the flow is convected in the vertical tangent from station 51 to 61, the movement mentioned above shifts the centre of the velocity magnitude (= the core of the flow) even more towards the outside wall in positive z-direction. Likewise, the core of high secondary velocity magnitude has moved closer to the centre of the pipe. For the next bend, between stations 61 to 71, the maximum velocity is close to what has now become the inside of the bend. Following Idelchik [38], this situation

[17]For a deviation angle δ of 50°, the length of the insert is around $L_{51}/D_{51} = 6.2$. This value reduces gradually to $L_{51}/D_{51} = 2.6$ for $\delta = 90°$.
[18]Such a configuration is called 'gooseneck' [38].
[19]For further discussion, see also Section 6.5.3.

has positive effects on the resistance coefficient as the losses associated with the secondary excitation of transverse circulation are smaller than in the case of uniform velocity distribution[20]. The flow leaves this 'gooseneck' type configuration, and when it reaches station 81, the velocity profile appears as several layers, stacked and rotated by a certain angle. The same angle is visible in the next station, 101, after the injector bend. It is about a third to a half of the pivot angle γ. The impact of the last bend can also be seen on the right (inside with respect to the injector bend, here the negative y position) of both contours in station 81, wherein the plot of the velocity magnitude, a small beak appears. This beak can be associated with two small vortices seen in the plot of the secondary velocity ratio. Again, the vortices are of Dean-type and form in station 81 because of the upstream effect of the subsequent injector bend between stations 81 and 91. A unique feature of the injector bend is the simultaneous deflection in two directions. The rather conventional deflection turns in the negative y-direction by an angle of 90°, and the second deflection comes from the rotation by the pivot angle $\gamma = 9.3°$. While the major deflection is associated with the two aforementioned small Dean vortices, the minor deflection causes the rotation of the velocity profile and the twist in the vortices such that in station 101, the distinct reverse S-shape pattern appears.

Further investigations on the flow structures in the manifold and the branch lines of multifurcations were conducted by Semlitsch [29, 88]. There, it was shown by LES simulations that the temporal evolution of the vortical structures in the *AxFeeder* is highly chaotic and dependent on the exact operation conditions, especially the number of active branch lines. However, the time-averaged velocities, secondary velocities, and primary flow structures correlate well with the RANS modelling approach chosen in this thesis. This issue is further addressed in Appendix D.3.

Finally, two general statements can be made: First, a steeper deviation angle of the branch line (δ closer towards 90°) results in up to 10 % higher loss coefficients compared to configurations with less steep deviation angles. However, this adverse effect of steep deviation angles is outweighed by the reduction of the secondary flow ratio and can be more than compensated by increasing the frustum diameter ratio. Second, compared to the effects of other design parameters, the frustum, as a connecting part between the manifold and the branch lines, has the most significant potential to reduce the losses [30].

Pivot angle

Pivoting the entire branch line was investigated for two designs with a deviation angle δ of 90° and frustum diameter ratios D_{41}/D_{51} from 1.0 to 1.9. Figure 6.20 highlights the major geometric differences between these two configurations. In the rather 'conventional' diffuser manifold design with the standard branch line, only the last part of the branch line, the injector bend, is rotated by an angle γ, with the rotation taking place at station 81. Contrary, in the variant with $\gamma = 0°$,

[20]Idelchik [38] also comments extensively on the effect of the length of the insert between the two bends of the 'gooseneck', where a length of $L/D \sim 11$ allows for a resistance coefficient of the 'gooseneck' being approximately equal to that of one isolated bend.

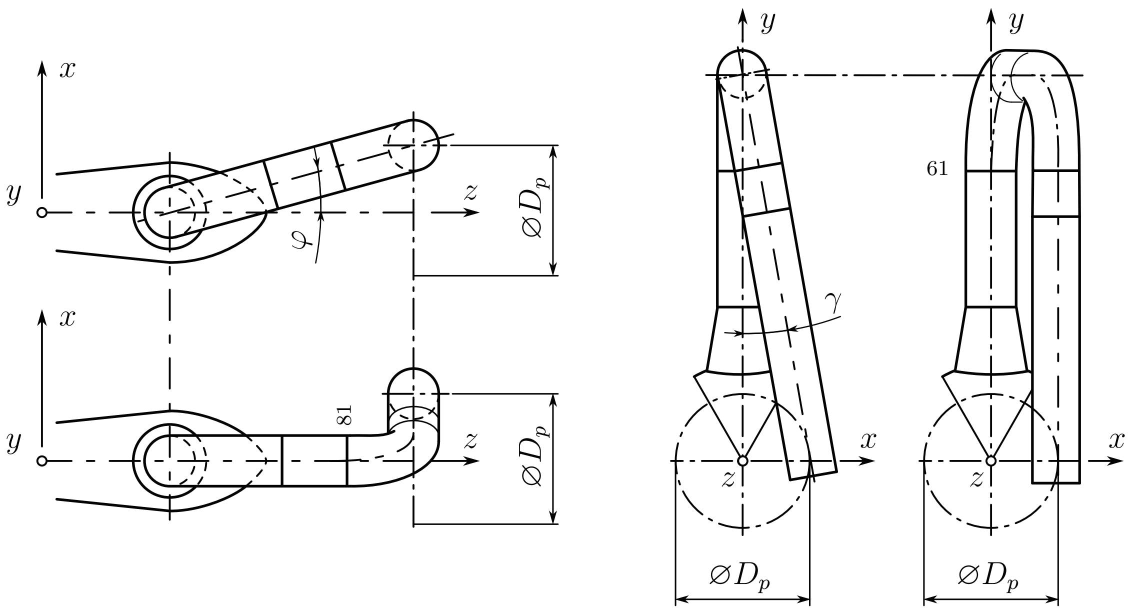

Figure 6.20: Comparative sketch of a diffuser manifold with pivoted branch line against a diffuser manifold with standard branch line.

the rotation of the branch line occurs much earlier in flow direction, at station 61, where the pivot angle φ is applied. To allow for a fair comparison of these two concepts (= using a runner with the same pitch cycle diameter $\varnothing D_p$), the angle pair (γ, φ) was either set to $(9.3°, 0°)$ or $(0°, 15°)$[21].

Apart from the differences highlighted above, all parts of the manifold and the branch lines were the same. Also, the change in the length of the mean streamline was marginal. Consequently, the power loss coefficient $\zeta_{PmTE,1011}$ and the dissipation power coefficient ζ_Φ, which are plotted in part a) of Figure 6.21, were virtually unaffected by the variation of the pivot angles.

The secondary velocity ratio $\phi_{II,101}$ at station 101, which is plotted against the frustum diameter ratio D_{41}/D_{51} in part b) of Figure 6.21, is significantly impacted by the different pivot angles. The general trend is that when the branch line is already rotated at station 61 by the pivot angle $\varphi = 15°$, the secondary velocity ratio at station 101 is around 25 % to 30 % higher than for the designs with $\varphi = 0°$. Interestingly, the data points with $D_{41}/D_{51} = 1.0$ (no frustum) are the only exceptions of that trend. Additionally, the data points almost coincide in the cases without frustum. Moreover, these two data points also have a very similar value for $\phi_{II,101}$ as the case with $D_{41}/D_{51} = 1.4$ and $\varphi = 15°$.

Putting this finding under a lens, the flow features of these four cases (highlighted by the ○ in Figure 6.21) are plotted in Figure 6.22. This figure displays the contours of the normalised velocity magnitude $||\vec{c}||/c_{s,101}$ and the secondary velocity ratio ϕ_{II} at stations 51 (after the frustum), 61 (before the first bend of the branch line),

[21]The exact value of φ would be 15.116°. However, for the sake of better readability, in the rest of this thesis, the integer value of $\varphi = 15°$ will be used.

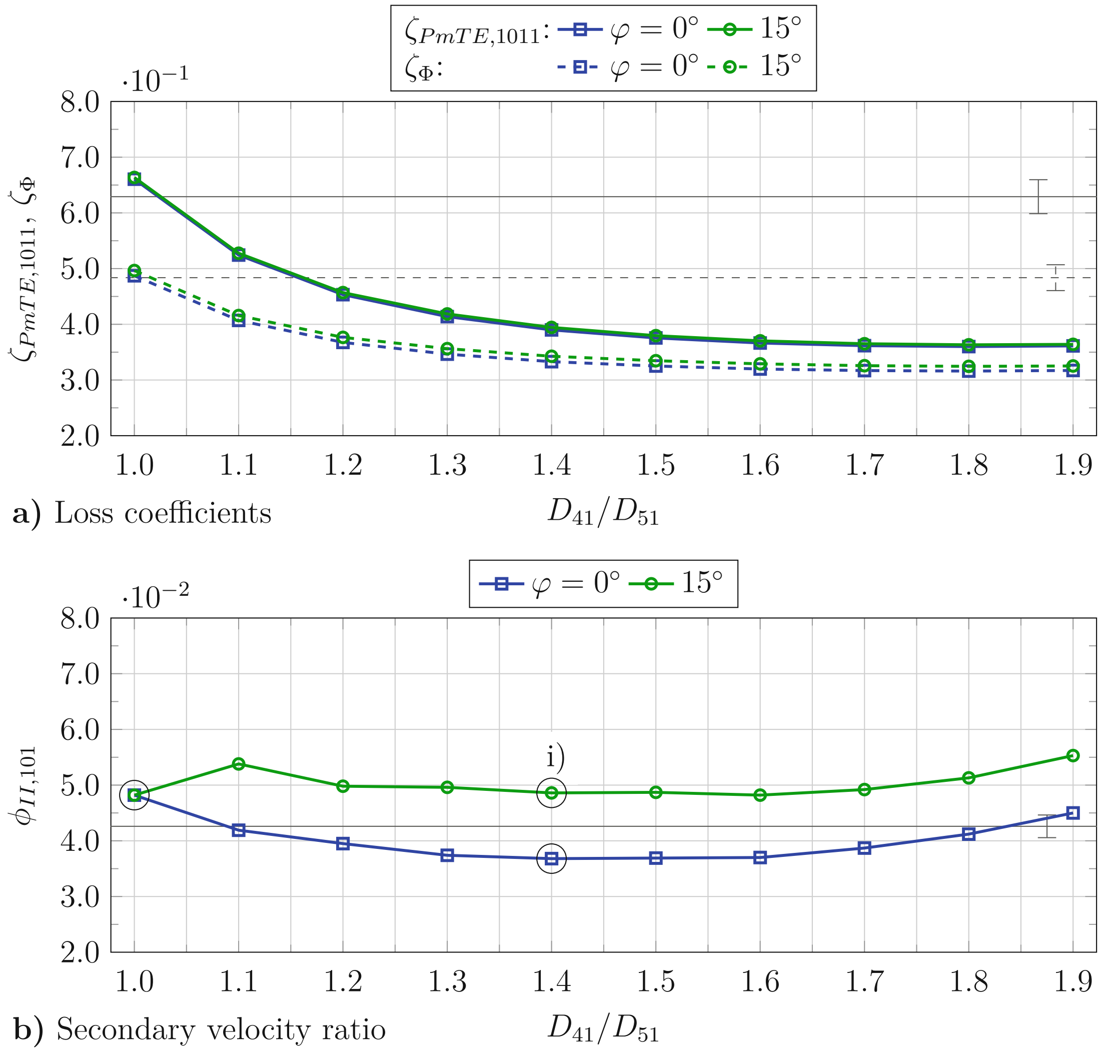

Figure 6.21: Line plots of the loss coefficients and secondary velocity ratios of the diffuser manifold design with conical frustum against the frustum diameter ratio D_{41}/D_{51} for two horizontal pivot angles φ. The deviation angle for both configurations was $\delta = 90°$. i) - Data points with ○ are compared in Figure 6.22.

81 (before the injector bend) and 101 (after the injector bend).
Thereby, the following observations were made and explanations derived:

<u>Station 51</u>: Both the velocity magnitude $||\vec{c}||/c_{s,101}$ and the secondary velocity ratio ϕ_{II} are not affected significantly by the change of the pivot angles. In cases with the frustum, the velocity is more evenly distributed across the station, and a beak located at the inside of the bend (towards the negative z-coordinate) becomes visible in the secondary flow plots.

<u>Station 61</u>: Again, the velocity is mostly unaffected by the variation of the pivot angles but becomes more evenly distributed for the cases with the frustum[22]. The

[22]The reason for this is that the frustum acts as a nozzle and nozzles equalise the flow, whereas

plots of the secondary velocity ratio look almost identical, with the only difference being that in cases with $\varphi = 15°$, the vortex pair is already slightly rotated by around $\varphi/2$ in the direction of the pivoted branch line.

Station 81: At this station, the flow-equalising effect of the frustum (nozzle) becomes prominent. The more even distribution of the velocity in station 61 for the cases with the frustum results in less distortion of the flow in the bend between station 61 and 71 and ultimately delivers the 'layered' velocity profile (indicated by the dashed lines in Figure 6.22 with its core shifted towards the inside (negative y-coordinate) of the following injector bend. The secondary velocity contours are again affected mainly by the pivot of the branch line. The two primary vortices appear to be rotated by approximately the same angle φ as the branch line itself. For the cases with the frustum, two small vortices rotating against the direction of rotation of the primary vortex pair emerge at the inside of the injector bend (negative y-coordinate).

Station 101: Direct effects of the frustum can no longer be observed at this station. Instead, for the cases with the pivoted branch line, as a direct result of the pivot angle $\varphi = 15°$, the vortical structures have become distorted and twisted by roughly two to three times the pivot angle φ. Also, the distinct reverse S-shape cannot be identified.

To ultimately explain why the configuration with $D_{41}/D_{51} = 1.4$ and $\varphi = 0°$ delivers a 25 % lower secondary velocity ratio at station 101, and the other configurations do not, it is helpful to look at the individual shortcomings of the three designs with high ϕ_{II}. In the cases without frustum, the 'layered' velocity profile with its maximum values close to the inside of the injector bend does not appear in station 81 upstream of the injector bend. However, Idelchik [38] stated that in such a situation, where the velocity has its maximum near the inner corner of the turn, the losses in a curved channel can become smaller than in the case with uniform velocity distribution. The extent of losses in curved channels is usually associated with the amount of transverse circulation (e.g. secondary flow) and mixing in the flow. Thus, minimal secondary flows downstream of the injector bend can only be achieved when the 'layered' velocity profile with its maximum values close to the inside of a bend is present upstream of the bend. This is not the case with the configurations without frustum, and thus, these configurations show a higher secondary velocity ratio in station 101. While the case with $D_{41}/D_{51} = 1.4$ and $\varphi = 15°$ also exhibits the 'layered' velocity profile in station 81, the main shortcoming of this configuration is the twisted vortices caused by the pivot of the branch line in station 61 and the consequently higher secondary velocities in station 101.

The presented illustrations can only qualitatively explain the differences in the flow structures that lead to the observed results for the secondary velocity ratio. Further research is needed to thoroughly understand how the observed effects interfere, amplify or cancel each other in the *AxFeeder*.

diffusers increase a velocity non-uniformity [26].

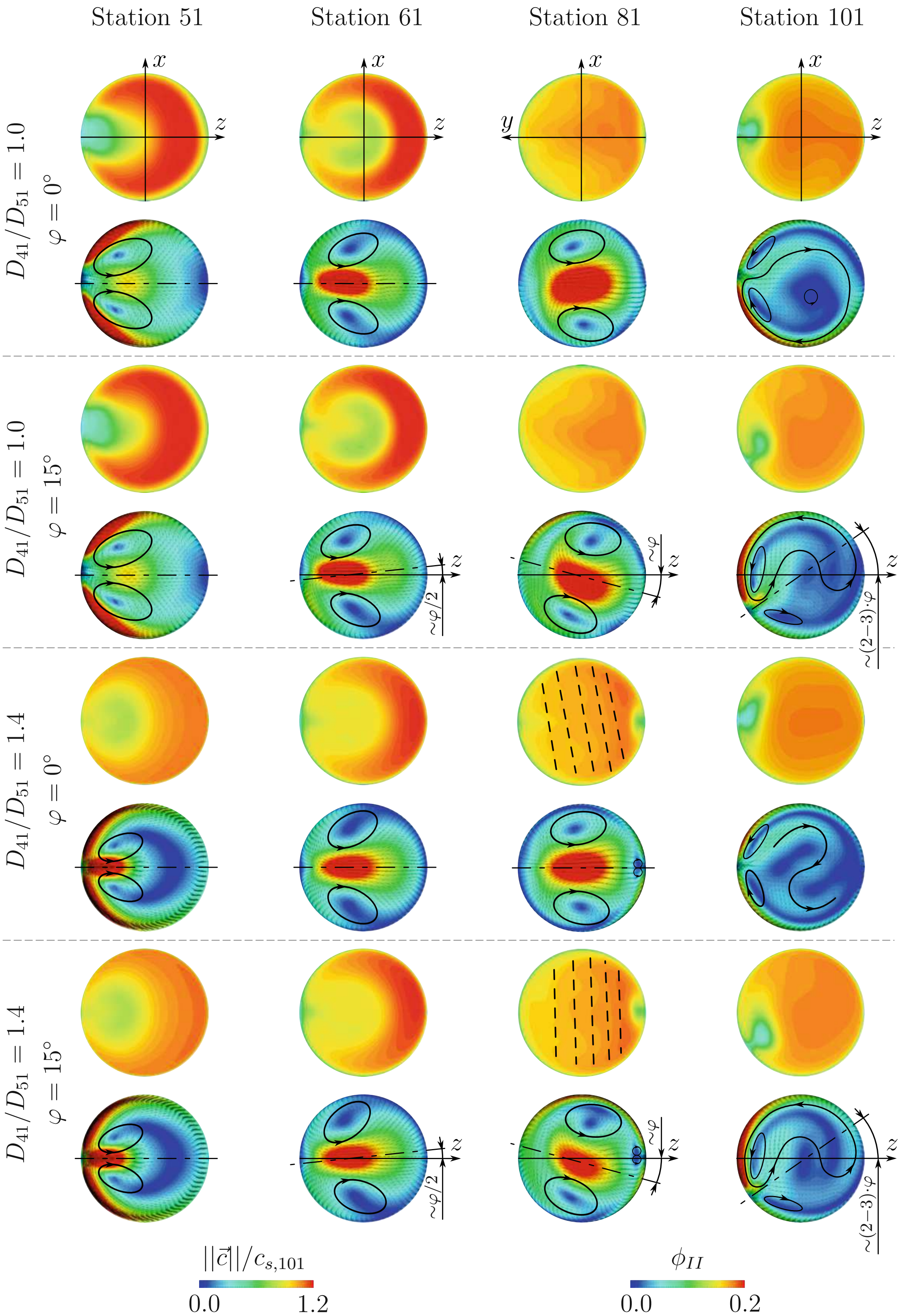

Figure 6.22: Comparison of the contours of velocity magnitude $||\vec{c}||/c_{s,101}$ (odd rows) and the contours of the secondary velocity ratio ϕ_{II} (even rows) in stations 51 to 101 for four cases with a deviation angle $\delta = 90°$.

6.4.3 Spherical manifold

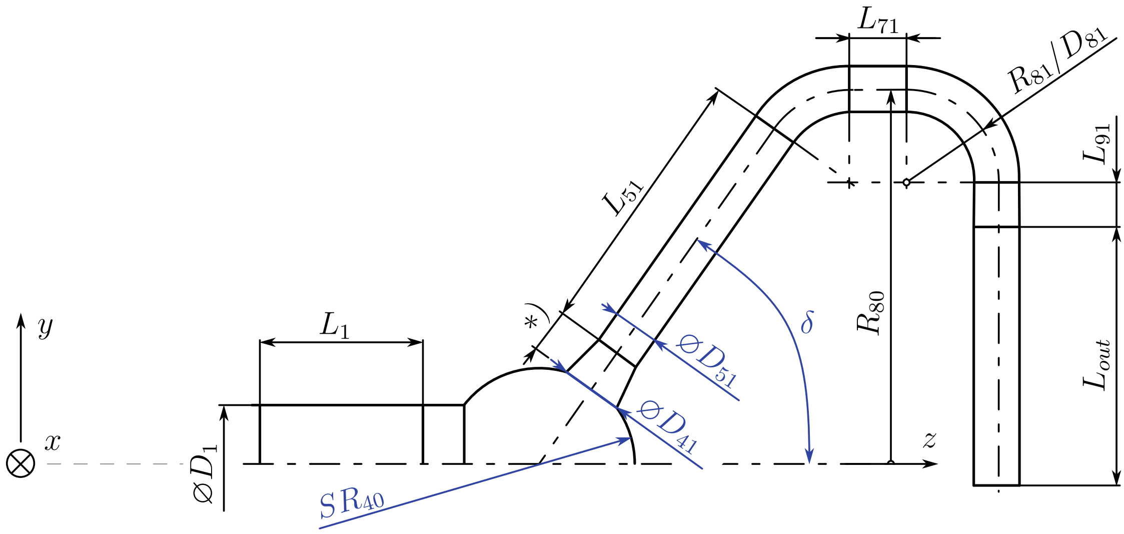

Figure 6.23: Sketch of the spherical manifold design. Dimensions relevant to the parametric study are highlighted in blue. $*) = L_{41}$.

The demand for a more compact manifold requires the replacement of the lengthy diffuser section with a shorter component. Given the demand for sufficient space at the manifold head for the connections to the branch lines, it becomes evident that a spherical shape fulfils both demands, that of a short component and that of sufficient space for the connections. Moreover, in guidelines and books for pressure vessel design, it was proved analytically that a spherical shape allows for the best utilisation of the material[23] [99]. This is especially true for the head of a pressure vessel and thus, to some extent, applies to the head of the *AxFeeder* manifold as well. In hydraulic engineering and hydropower plant construction, spherical shapes are used in junctions of the penstock lines [25, 64]. Often, the spherical parts act as a self-supporting shell that supports the pressure forces from the hydraulic head and in the inside of this shell, a thinner interior shell acting as a flow guiding device is embedded [25].

These arguments make an application of a spherical manifold with the *AxFeeder* appear plausible as long as the spherical shape of the manifold does not adversely affect the flow quality [30]. The implementation of the sphere is sketched in Figure 6.23. There, also all varied parameters, namely the radius SR_{40} of the sphere, the deviation angle δ and the frustum diameter ratio D_{51}/D_{41}, are highlighted in blue. Internal secondary shells for better flow guidance were not used because this study concentrated on finding parameter combinations that do not need additional measures to function appropriately (assuming such parameter combinations exist).

As a consequence, at first, combinations of the sphere radius SR_{40} and the deviation angle δ were investigated (see Figure 6.24). The sphere radius was increased from

[23] Roloff/Matek [99] states that under the same conditions, the necessary thickness of a spherical wall is only half of the thickness of an equivalent cylindrical wall.

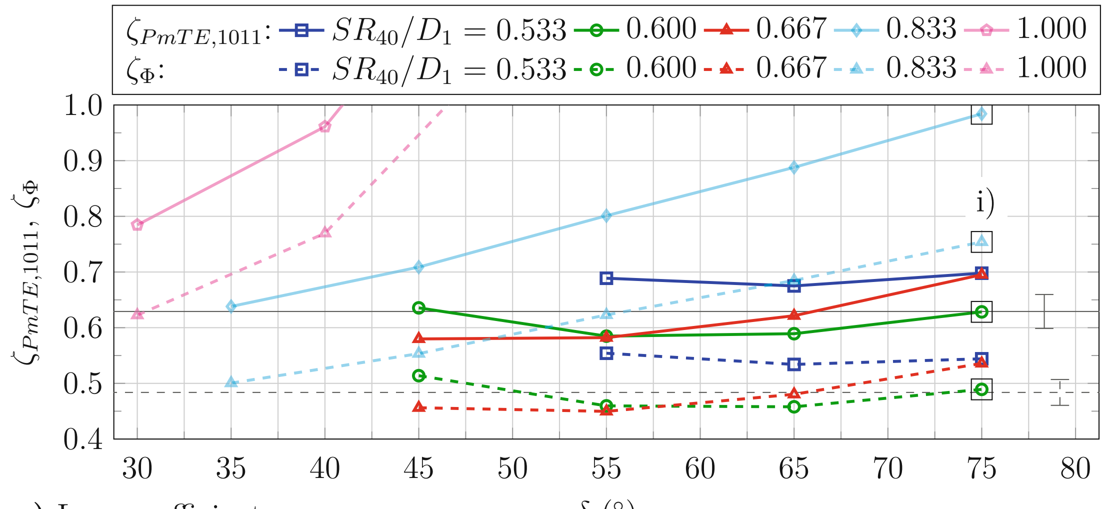

a) Loss coefficients

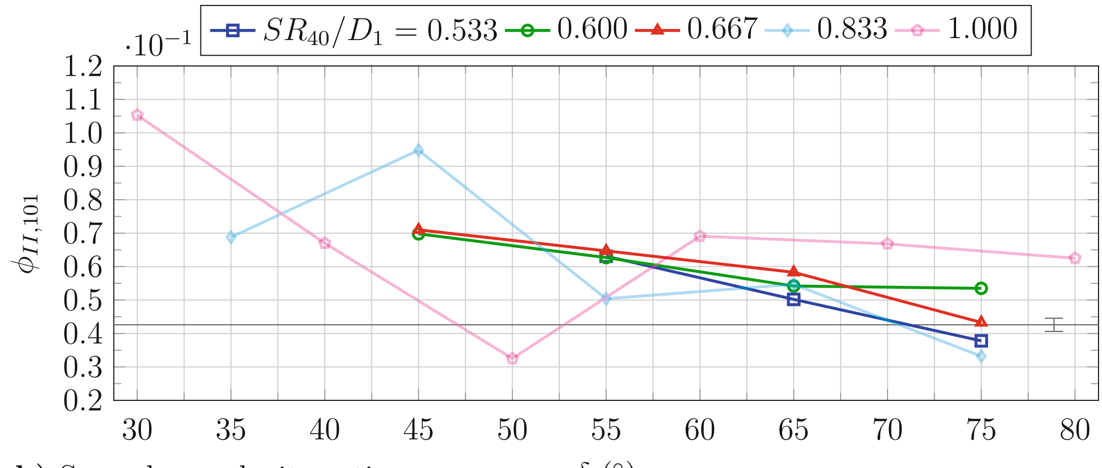

b) Secondary velocity ratio

Figure 6.24: Line plots of the loss coefficients and secondary velocity ratios of the spherical manifold design (no frustum) against the deviation angle δ for different sphere radii SR_{40}/D_1. i) - Data points with □ are compared in Figure 6.25.

the geometrically smallest possible value of 0.533 up to very large spheres with radii of $SR_{40}/D_1 = 1.000$. The deviation angle was varied from 30° to 75°. In a second series depicted in Figure 6.26, for spherical manifolds all with radius $SR_{40}/D_1 = 0.600$, the effect of applying a conical frustum as the first part of the branch line was studied as well. The frustum ratio was varied from $D_{41}/D_{51} = 1.1$ to the maximum possible frustum base diameter of $D_{41}/D_{51} = 1.4$.

The plot of the loss coefficients, part a) in Figure 6.24, reveals that for large sphere radii, especially $SR_{40}/D_1 = 0.833$ and 1.000, the losses are already disproportionately high when compared to the other cases, but do increase even further when the deviation angle of the branch line becomes steeper. When only sphere radii equal to or less than 0.667 are considered, then there is the trend that with steeper deviation angles $\delta \geqslant 55°$ a moderate sphere radius of $SR_{40}/D_1 = 0.600$ allows for the lowest losses. This trend can be explained by two facts: First, the smaller sphere with $SR_{40}/D_1 = 0.533$ has higher average flow velocities in the manifold and thus higher losses. Second, the bigger sphere with $SR_{40}/D_1 = 0.667$ is almost too big, so flow separations appear in the plenum. These are not dramatic and still allow the assumption of steady flow to hold, but the tendency of the flow to become unstable is already present. The reason why this is less problematic with the lowest deviation angle $\delta = 45°$ is that this separation does not affect the flow in the branch lines as much when the branch lines are attached more towards the axial direction (z-coordinate), rather than the radial direction (x-coordinate).

The plot of the loss coefficients in part a) of Figure 6.24 also shows that for suitable sphere radii (here, especially 0.533 and 0.600), the losses are largely independent of the deviation angle δ. On the contrary, it is precisely the opposite for the secondary velocity ratio $\phi_{II,101}$ in station 101. There is a relatively clear linear trend that a steeper deviation angle leads to lower $\phi_{II,101}$, but the sphere radii have only little effect. The main exception is the cases with the large sphere radii, $SR_{40}/D_1 = 0.833$ and 1.000. Here, a massive flow separation occurs in the sphere, leading to an inherently unsteady generation of vortices. The vortices get transported through the branch lines to station 101 and further. Semlitsch [88] showed that in multifurcations, these phenomena are highly unsteady, as these vortices are created in the manifold, then transported through the branch lines, but also tend to collapse after some time and later form again. With the steady-state simulation approach chosen in this thesis, capturing such phenomena in all detail is impossible. Only a rough approximation can be gained then. Such an approximation, though, is sufficient for the parametric study because, as pointed out in the opening paragraph of this section, only properly functioning parameter combinations are relevant for an eventual field application of the *AxFeeder*. The results of the cases with $SR_{40}/D_1 = 0.833$ and 1.000 are displayed in slightly greyed out colours in Figure 6.24 to avoid confusion with the results of the cases without significant separation in the spherical part.

A more in-depth understanding of the phenomena in the sphere that lead to the behaviour of the flow quality criteria plots can be gained from Figure 6.25, where a case with an appropriately big sphere radius of $SR_{40}/D_1 = 0.600$ and a case with extensive separation in the sphere with $SR_{40}/D_1 = 0.833$ are compared. These cases illustrate the flow behaviour for all similar cases where the plenum of the manifold is either sized appropriately (plots in the left column) or when the plenum is way too large (plots in the right column). The plots in the right column with $SR_{40}/D_1 = 0.833$ prove that in the case of an oversized sphere, the flow starts to separate at the connecting edge of the penstock and the spherical manifold. This massive separation zone, illustrated by the velocity contours in the first row of the plots, is associated with a strong vortex that effectively blocks the core flow from entering the branch line smoothly. Instead, the core flow deviates to the right and enters the branch line from the opposite side compared to the configuration with $SR_{40}/D_1 = 0.600$. Therefore, for the case with the oversized plenum and the massive separation zone, in the first part of the branch line, the separation zone occurs on the outside (towards higher values of the z-coordinate) and shifts the core of the flow more towards the centre of the branch line. This shift, unfortunately,

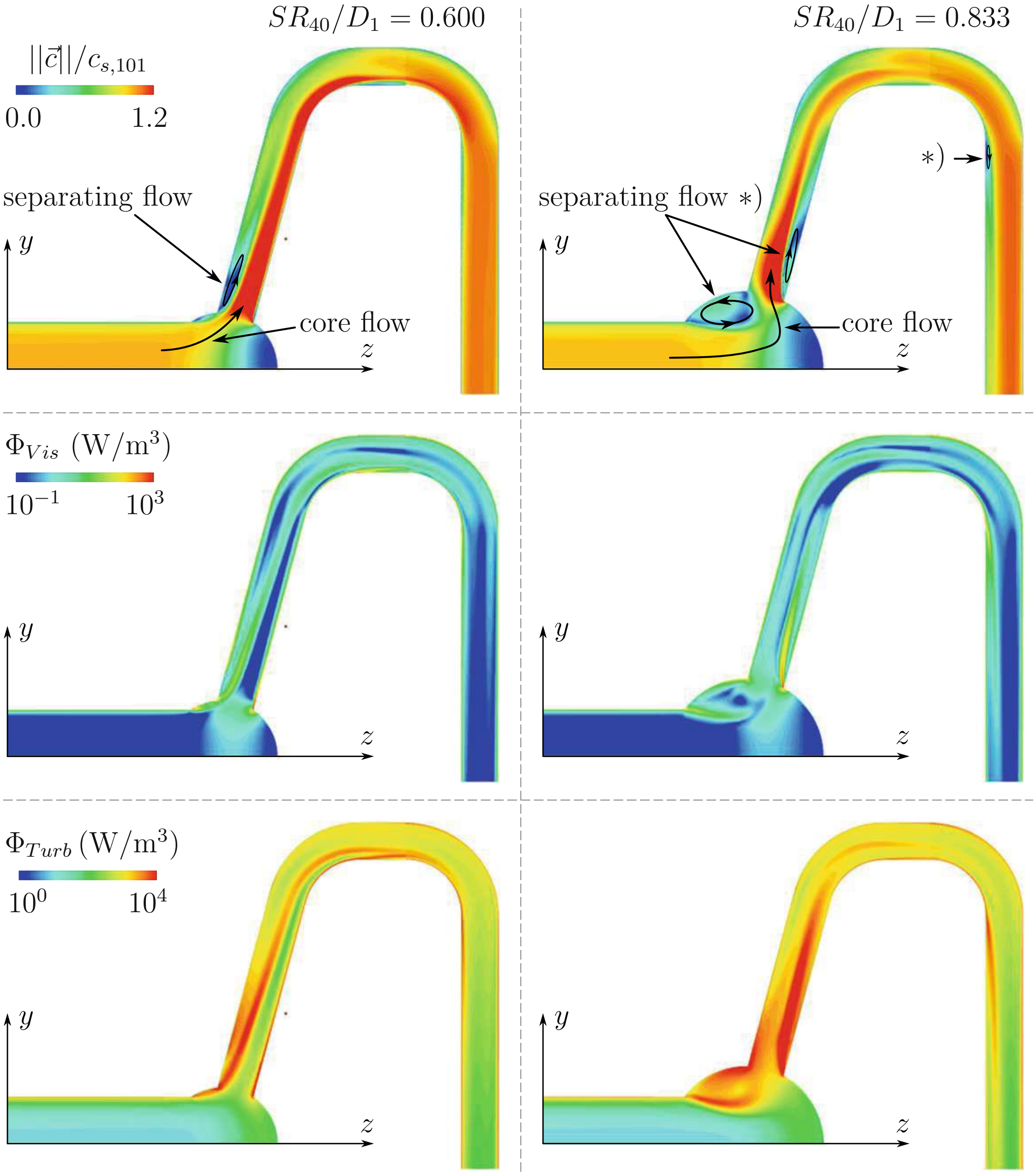

Figure 6.25: Impact of the sphere diameter on the velocity magnitude $||\vec{c}||/c_{s,101}$, and the local losses expressed by the viscous dissipation Φ_{Vis} and the turbulent dissipation Φ_{Turb} in the y-z plane. Both variants have a deviation angle δ of 75°.

adversely affects the flow when going through the bends, and after the last bend in the branch line, the separation of the flow on the inside is thus more prominent. The contour plots with the viscous dissipation Φ_{Vis} and the turbulent dissipation Φ_{Turb} in the second and third row of the plots allow to explicitly identify these separation zones as the sources for the increased losses.

Unsteady behaviour associated with flow separations in spherical-shaped penstock junctions was also observed by Ruprecht et al. [78] and Kirschner et al. [46]. Both

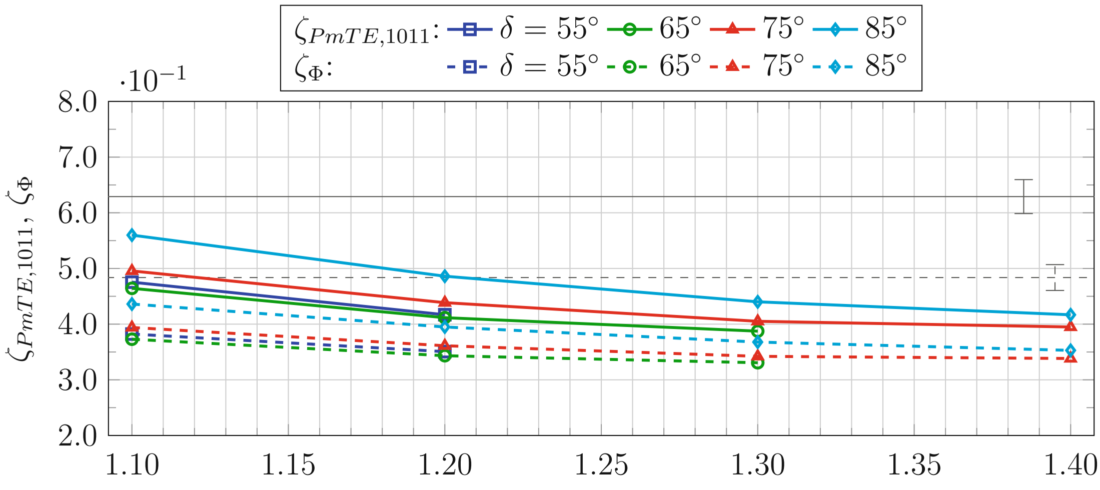

a) Loss coefficients

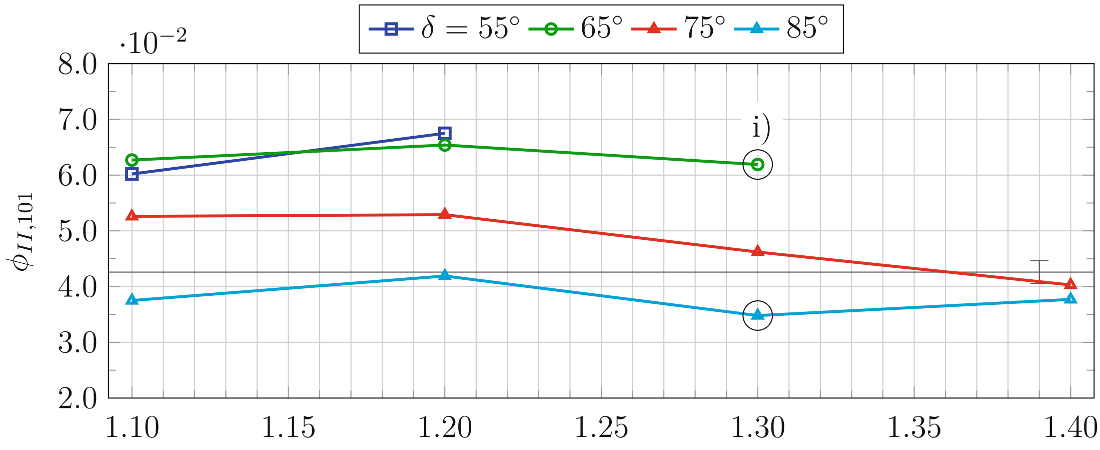

b) Secondary velocity ratio

Figure 6.26: Line plots of the loss coefficients and secondary velocity ratios of the spherical manifold design ($SR_{40}/D_1 = 0.600$) against the frustum diameter D_{41}/D_{51} for different deviation angles δ. i) - Data points with ○ are compared in Figure 6.27.

analysed a trifurcation and found that the flow separates in the sphere, vortices are created and tend to block the flow in the branches, which causes mass flow and pressure fluctuations. They came to the same conclusion as presented in this section. Reducing the volume of the sphere, and thus the space in which the flow might separate, and vortices could form is the most effective way to allow for evenly distributed, smooth flow in the branch lines.

For such a smaller sphere, with $SR_{40}/D_1 = 0.600$, the effect of applying a frustum as the first part of the branch line was investigated for several deviation angles δ. The loss coefficients are plotted in part a) of Figure 6.26, and the secondary velocity ratio is given in part b) of this figure. Similar to the experiences from the diffuser manifold, the following observations were made: First, using a frustum allows for a reduction of the losses but has only a minor effect on the secondary velocity ratio

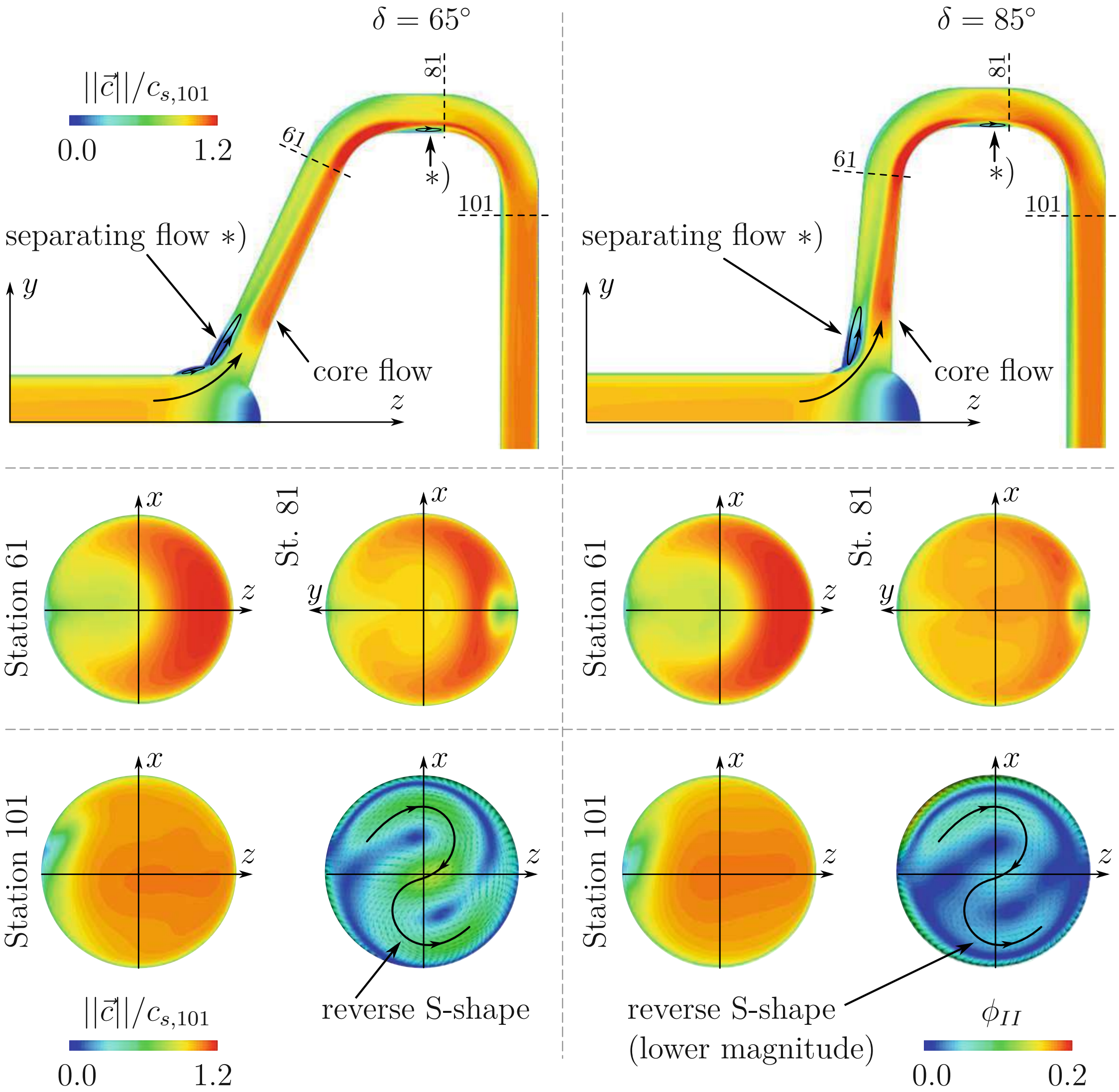

Figure 6.27: Velocity contours in the y-z plane and for several stations in the branch line for a design with a medium deviation angle $\delta = 65°$ and a design with steep deviation angle $\delta = 85°$. Both variants have a sphere radius of $SR_{40}/D_1 = 0.600$.

in station 101. Second, a steeper deviation angle causes a minor increase in the loss coefficients but a much more prominent decrease of the secondary velocity ratio $\phi_{II,101}$ in station 101.

The effects caused by the variation of the deviation angle δ are discussed under consideration of Figure 6.27, where the velocity fields of two cases, one with $\delta = 65°$ and one with $\delta = 85°$ are analysed. The top plots show the normalised velocity magnitude $||\vec{c}||/c_{s,101}$ in the y-z plane. At the transition from the penstock line to the sphere, the flow separates and forms a region with a low velocity that blocks the main flow. The core flow is thus shifted to the right of the branch line and stays there until after the first bend. Both cases deliver very similar flow in the first part until station 61, whereas the core shift towards the right side of the first tangent of the branch line is more pronounced for the case with the steeper deviation angle. This effect, however, which becomes apparent in the velocity contour plots of station 81, positively affects the flow through the two bends. In station 81, the velocity contours of the case with $\delta = 65°$ still have a very pronounced horseshoe shape. Such a horseshoe can hardly be identified in the same plots of the case with $\delta = 85°$. However, instead, the contours appear to look more similar to the layered profile witnessed already for configurations of the diffuser manifold with $\delta = 90°$ (e.g. in Figure 6.19). This layered profile type is much more favourable for the flow in the injector bend. Thus, the contours of the velocity magnitude in station 101 are much more symmetric for the case with the steeper deviation angle of 85°. The concomitant effect is seen in the plots of the secondary velocity ratio ϕ_{II} in station 101, where the flow structure is the same for both deviation angles. However, the magnitude of the secondary velocity, and thus ϕ_{II}, is much lower when the deviation angle is closer to 90°.

These observations solidify the findings of the previous studies with the diffuser manifold. They underline that a combination of the manifold shape and size, a frustum and a steep deviation angle close to 90° are essential for the flow in the branch line leaning towards the outer side of the first straight section of the branch line as this appears to be the most favourable condition for the successive bends in terms of limited secondary flow in station 101.

6.4.4 Cylindrical manifold

The studies of the previous core manifold designs proved that the shape of the manifold itself serves two primary purposes. One is to provide sufficient space for all branch lines to connect smoothly, and the other is to allow for a flow transition into the branch line such that the core of the flow is leaning towards the inner side of the subsequent bends.

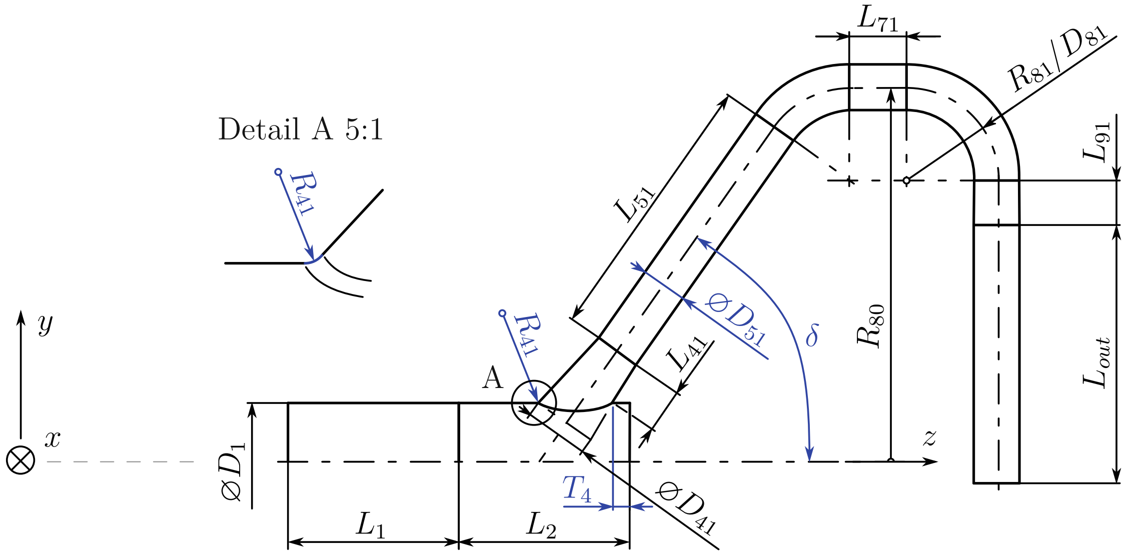

Figure 6.28: Sketch of the cylindrical manifold design. Dimensions relevant to the parametric study are highlighted in blue.

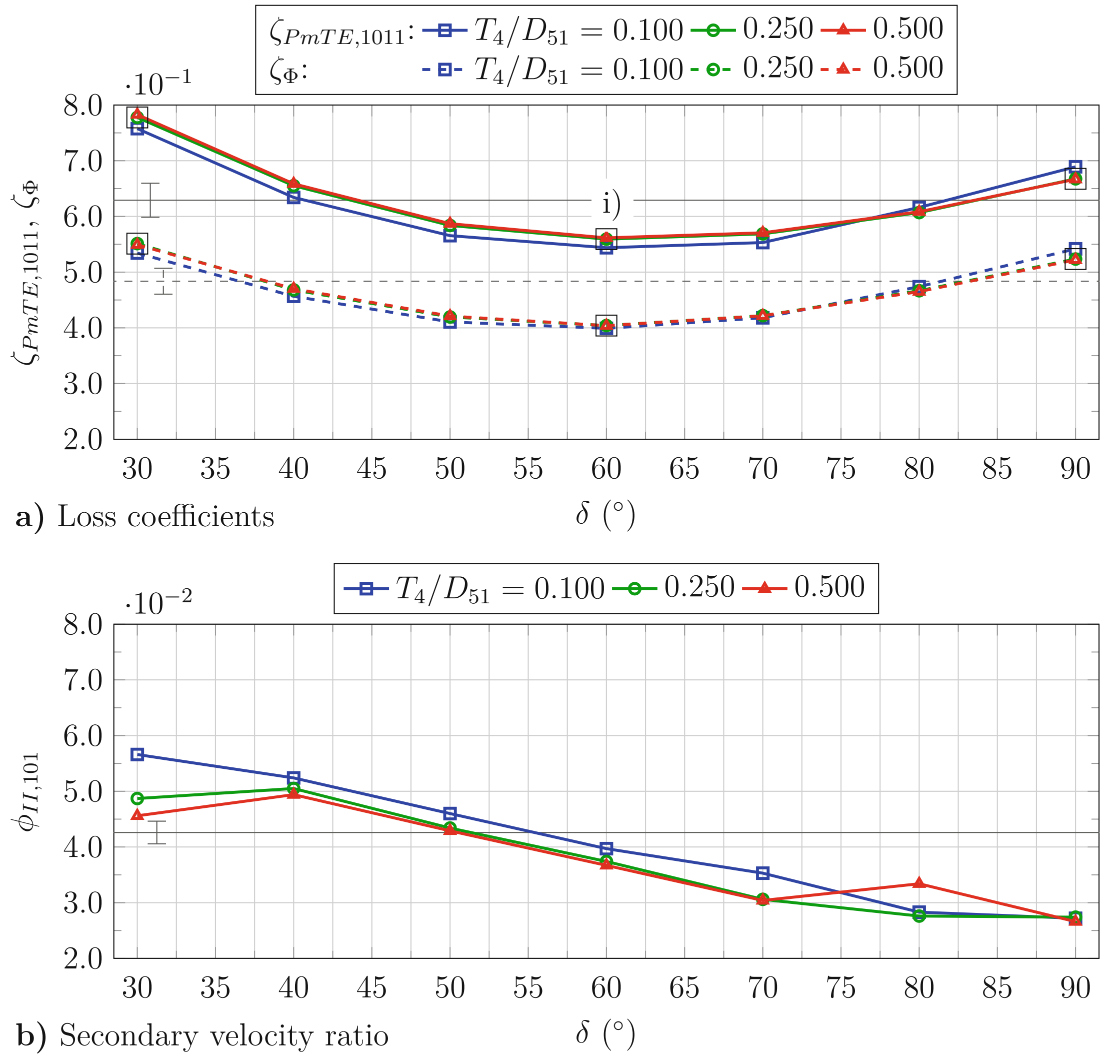

Figure 6.29: Line plots of the loss coefficients and secondary velocity ratios of the cylindrical manifold design against the deviation angle δ for different axial position T_4/D_{51} of the flat cap. i) - Data points with □ are compared in Figure 6.30.

Given the demand for simple designs and thus a possibility for cost-effective manufacturing, understanding the effects of using a plain cylindrical pipe as the manifold was highly interesting. Such a cylindrical manifold is sketched in Figure 6.28 with the parameters discussed in this section highlighted in blue. These parameters were the axial position T_4/D_{51} of the manifold head, the deviation angle δ and the throat radius R_{41}/D_{51}. The cylindrical manifold design is the shortest of the four core designs, consisting of mainly simple cylindrical components.

Using a conical frustum as the first part of the branch line proved beneficial for reducing the losses once again. However, due to the tight space of the lateral surface of the cylinder, the maximum frustum diameter was limited to $D_{41}/D_{51} = 1.2$. This frustum diameter was, therefore, selected for all cases discussed in this section.

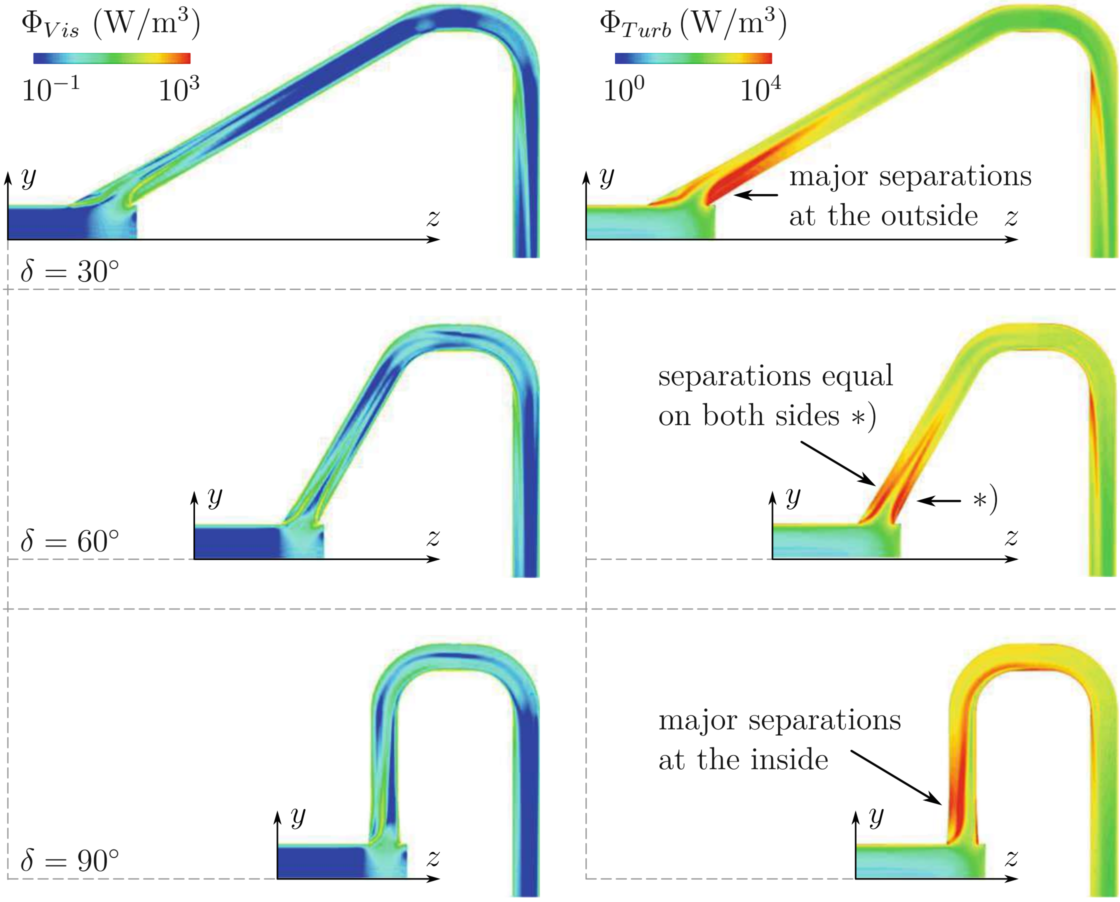

Figure 6.30: Viscous dissipation Φ_{Vis} and turbulent dissipation Φ_{Turb} in the y-z plane for three deviation angles. All variants have the same axial position of the manifold head, $T_4/D_{51} = 0.250$.

In the first series of simulations, the effects of a change of the deviation angle δ and the axial position of the manifold head T_4/D_{51} were tested. The impact of a variation of these two parameters on the flow quality criteria is plotted in Figure 6.29. Two trends can be identified: First, the axial position of the manifold head has minimal impact on both loss coefficients and the secondary velocity ratio at station 101. Second, however, increasing the deviation angle δ towards its maximum of 90° causes a roughly linear decline of the secondary velocity ratio, which levels off at $\delta \approx 80°$. On the contrary, the curves of the loss coefficients are of parabolic shape. They decrease between $\delta = 30°$ and $\delta = 60°$, where they achieve their minima. Then, from $\delta = 60°$ to $\delta = 90°$, an increase in the losses can be observed. This behaviour is investigated in detail with the help of the contour plots of the viscous dissipation Φ_{Vis} and the turbulent dissipation Φ_{Turb} depicted in Figure 6.30. This figure compares three configurations with $T_4/D_{51} = 0.250$. The overall length and the branch line length decrease with an increase of the deviation angle δ. Therefore, the maximum of the losses at $\delta = 30°$ can be explained by considering two aspects: the significantly longer branch line and the major separation resulting from the sharp edge at the outside (high z-position) of the branch line. At the inside of the branch line, the flow benefits from the flat deviation angle of only 30°, and thus, the

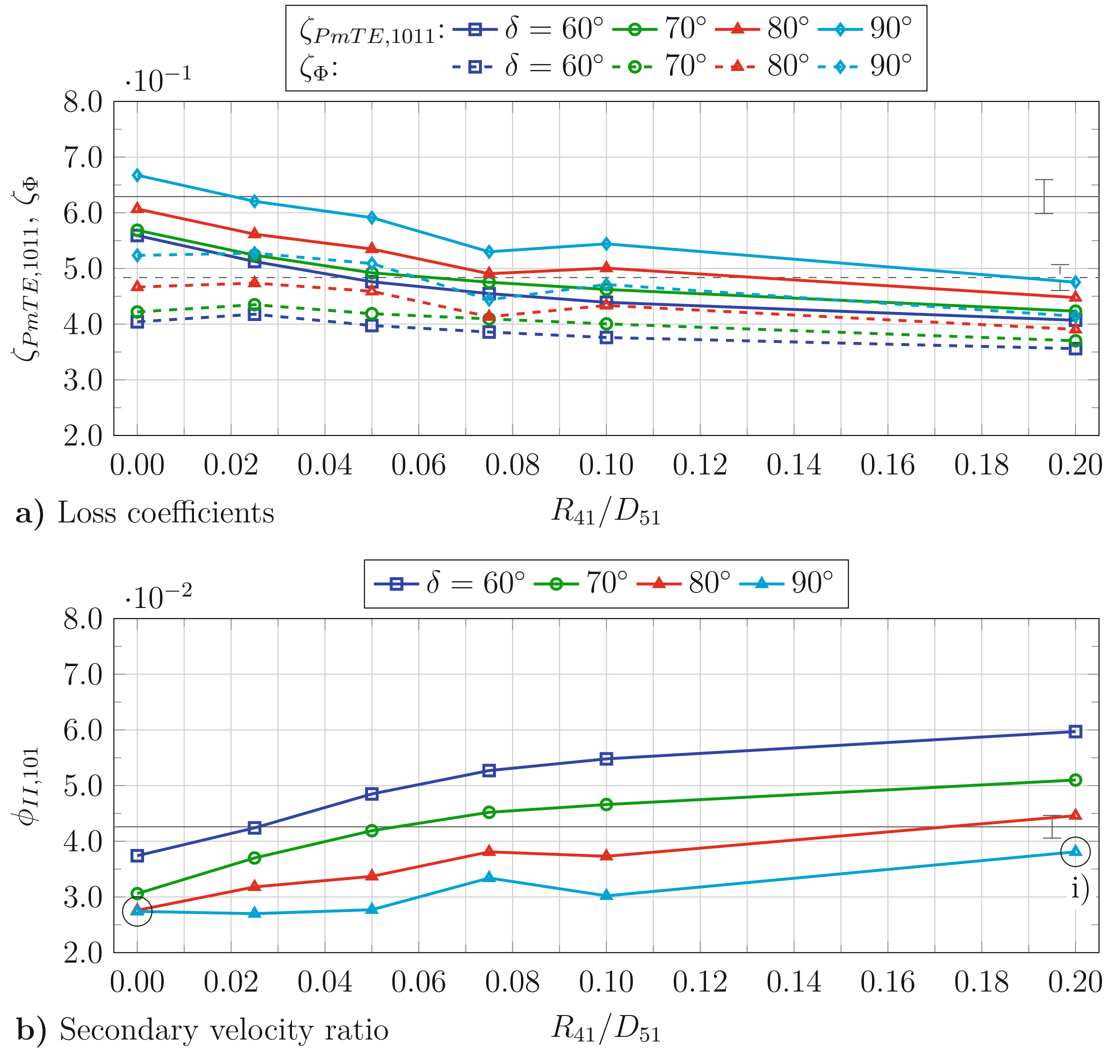

Figure 6.31: Line plots of the loss coefficients and secondary velocity ratios of the cylindrical manifold design against the throat radius R_{41}/D_{51} for different deviation angles δ. Same axial position $T_4/D_{51} = 0.250$ for all cases. i) - Data points with ○ are compared in Figure 6.32.

separation is less pronounced. The other extreme is given by the case with $\delta = 90°$, where major separations occur at the inside (low z-position) of the first part of the branch line that in the case of the cylindrical manifold can only be mitigated to a minor extent by the conical frustum, because of the limited size of the frustum. The case in the middle, with $\delta = 60°$, shows approximately equally sized separation zones at both the inside and the outside of the first branch line tangent. While this is not ideal, it is the best combination for the cylindrical manifold when considering losses.

The contour plots of Figure 6.30 highlighted the weak spot of the cylindrical manifold design, namely the transition from the cylindrical manifold into the conical frustum. To compensate for this weakness and given the significant potential of reducing flow losses by rounding the transition from the manifold to the branch line,

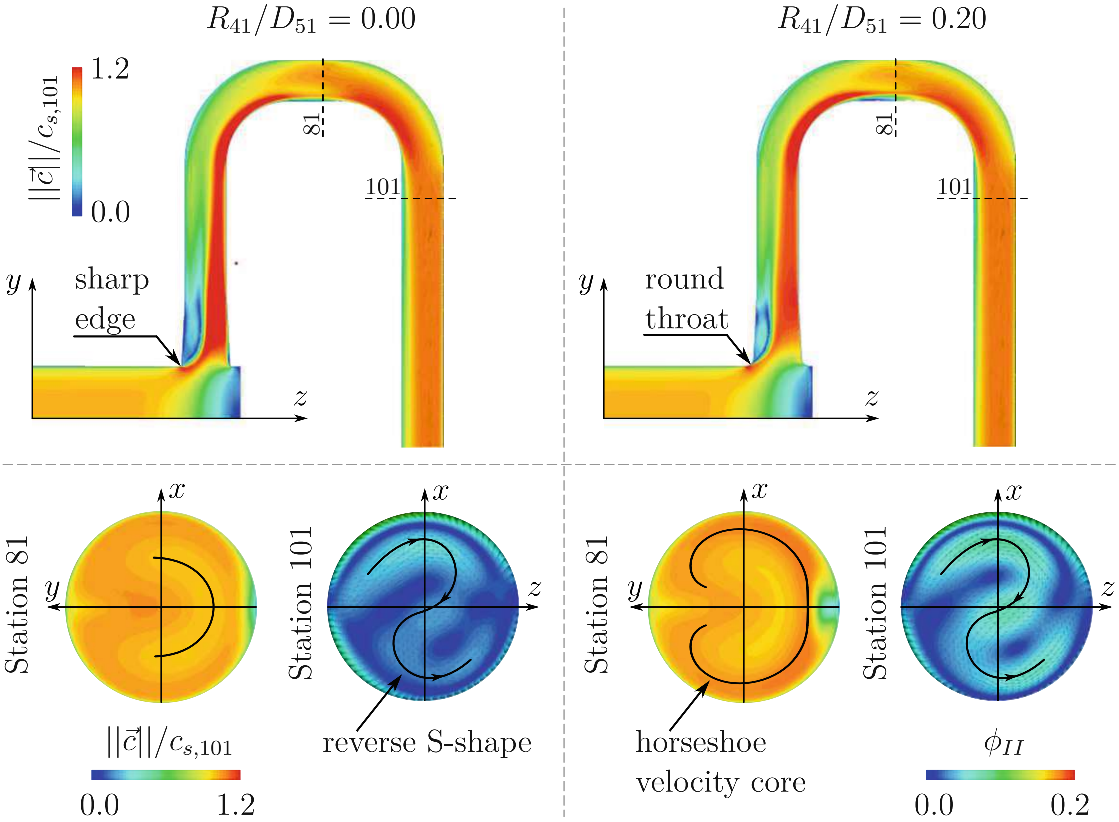

Figure 6.32: Velocity contours in the y-z plane and for several stations in the branch line for two designs with a deviation angle δ of 90° and an axial position $T_4/D_{51} = 0.250$, one with a sharp edge, $R_{41}/D_{51} = 0.00$, and one with a large throat radius $R_{41}/D_{51} = 0.20$.

a rounded throat was also investigated for the cylindrical manifold. However, with the knowledge from Section 6.4.1, this time, the throat radius R_{41}/D_{51} was only varied between 0.0 to 0.2, as the plots of Figure 6.10 demonstrated, that an increase of the throat radius beyond those values would not lead to further improvements of the flow quality criteria.

A quick analysis of Figure 6.31 underlines what was already found in [30] and in Section 6.4.1, namely that the losses are reduced by rounding the throat at the cost of increased secondary velocity ratios. The reason why applying a radius worsens the secondary velocity ratio at a station far downstream of the throat section is explained by the contour plots of Figure 6.32. It was already discussed with the diffuser manifold in Figures 6.19 and 6.22 and the spherical manifold in Figure 6.27 that the shape of the velocity profile in station 81 upstream the injector bend has a significant impact on the contours and strength of the secondary velocities in station 101. The velocity profile in station 81 is heavily influenced by how the flow transitions from the manifold to the branch line. With the sharp edge at the throat, the flow separates at a distinct position when it enters the frustum section of the branch line. At the inside of the frustum, a spacious separation zone forms that pushes the core of the flow to the right side of the branch line (high z-position). This shift of the velocity core positively affects the flow through both bends of the branch line. Ultimately, the magnitude of the secondary velocity in station 101 is low, and the reverse S-shape flow pattern appears. With the configuration using a round throat, the effects and processes in the flow are similar to those in the configuration with the sharp edge. However, when the flow enters the frustum part, due to the rounded throat, the separation zone becomes less pronounced, and the flow aligns more to the centre of the branch line. Therefore, the flow enters and exits the first bend before station 81 in a less favourable condition. The velocity profile takes the shape of a horseshoe, and the differences between contours with higher velocities and contours with lower velocities become more prominent. Consequently, in station 101, after the flow has moved through the injector bend, the magnitude of the secondary velocity has increased significantly compared to the case with a sharp-edged throat, and the reverse S-shape is more easily recognisable.

6.5 Influence studies

This section focused on three critical areas of piping systems design. The first focused on how a steady reduction of the branch line diameter at different positions in the branch line affects the flow. A second aspect considered was the possible flow changes when installing segmented bends instead of smooth bends. Third, internal structures acting as flow-guiding devices were investigated.

The following influence studies were all conducted on the diffuser manifold design with conical frustum (design b) in Figure 6.2). The most important common dimensions were: the diffuser angle $\beta = 14°$, the deviation angle $\delta = 90°$, the base diameter of the frustum $D_{41}/D_{101} = 1.6$[24] and its length $L_{41}/D_{101} = 5/3$. A throat radius was not applied to either of the designs in this section.

6.5.1 Influence of converging branch lines

The driving factor behind this study was that a continuous (confuser-type) reduction of the branch line diameter at a suitable position would simultaneously reduce flow losses and velocity non-uniformities.

Regarding losses, Section 6.4.1 showcased an analytical correlation linking the total pressure loss Δp_t and the diameter d for a straight pipe flow. Specifically, this derivation, culminating in Equation (6.9), highlighted that the losses are inversely proportional to the fifth power of the diameter. It was also proved that this conclusion holds if the Reynolds number dependency of the pipe friction factor is included in the model. For the study of the converging branch line, it has to be considered that the increase of the pipe diameter will only be effective for parts of the branch line, and, depending on the design variant A, B or C sketched in Figure 6.33, a change of the relative curvature radii of the bends might obstruct the benefits of the increased diameter.

[24] In the cases without a convergent branch line, this dimension would be equal to frustum diameter ratio $D_{41}/D_{51} = 1.6$.

Regarding velocity non-uniformities, Greitzer et al. [26] and Sigloch [94] explain that in channels with decreasing width (e.g. nozzles and confusers), the non-uniformity of the streamwise velocity component decreases. Greitzer et al. [26] showed by the example of linear shear flow in a two-dimensional channel (with station 1 upstream and station 2 downstream a diffuser or nozzle) that the velocity gradient in station 2 is the same as in station 1. However, the velocity differences at station 2 are greater than at station 1 for a diffuser ($AR > 1$) and less than station 1 for a nozzle ($AR < 1$) [26]. Employing vortex theory, Greitzer et al. [26] also proved that nozzles tend to increase the uniformity of the flow concerning swirl angularity[25], while diffusers tend to worsen it [26]. The previous statements can be summarised by

$$\frac{(c_{s,max} - c_{s,min})_2}{(c_{s,max} - c_{s,min})_1} = AR \begin{cases} > 1 \ldots \text{Diffuser} \\ = 1 \ldots \text{Straight pipe} \\ < 1 \ldots \text{Nozzle} \end{cases}, \tag{6.20}$$

where $AR = A_2/A_1$ is the area ratio of the diffuser or the nozzle.

In order to determine what type of convergent branch line has the most significant effect on the losses and the secondary flow of the *AxFeeder*, three variants were tested. In the first two variants, A and B, the injector bend between stations 81 and 91 was the convergent bend. In the third variant, C, the first bend between stations 61 and 71 was the convergent bend. A branch line equipped with a convergent bend is sketched in Figure 6.33, displaying all dimensions and stations relevant to the current study.

For all cases of variant A, the absolute values of the curvature radii R_{61} and R_{81}, as well as the distance between the two bends, L_{71}, were fixed. That means, by increasing the pipe diameter between stations 51 and 81, upstream of the converging bend, the relative curvature radii of the two bends, R_{61}/D_{61} and R_{81}/D_{81} as well as the relative length L_{71}/D_{71} decrease. With this approach, the overall size of the *AxFeeder* stays the same because the radius R_{80} and the axial length z_A do not change. For the cases with variant B, the relative curvature radii of the two bends, R_{61}/D_{61} and R_{81}/D_{81} and the relative length L_{71}/D_{71} was fixed such that the absolute values of the curvature radii R_{61} and R_{81}, and the length L_{71} increases with the pipe diameter at these stations. The relative curvature radii being fixed effectively leads to a slight scaling of the *AxFeeder* such that the external dimensions, here expressed by the radius R_{80} and the axial length z_B, increase fractionally[26]. To keep the runner pitch cycle diameter D_p the same, the pivot angle γ of the injector bend needs to be adjusted by a few tenths of a degree according to the change of R_{80}. The same approach as for variant B was chosen for the cases with variant C, except for the diameter reduction in the first bend instead of the second.

[25]The swirl angle is defined as the ratio of the circumferential velocity (swirl velocity) $\omega \cdot r$ to the streamwise velocity. A detailed explanation is presented in Section 3.4.3.

[26]The increase of R_{80} is approximately proportional to $(D_{51}/D_{101})^{\frac{1}{4}}$.

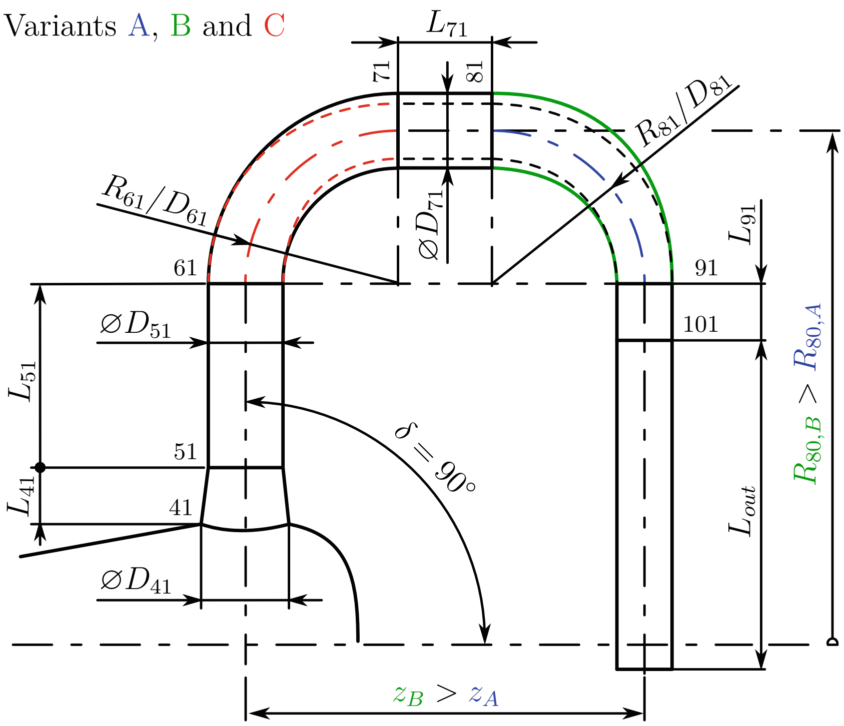

Figure 6.33: Sketch of the branch line with the convergent bend coloured in blue and green for variants A and B, and red for variant C.

As presented in [30], the diameter ratios D_{51}/D_{101} (for variants A and B) and D_{51}/D_{71} (for variant C) were varied between 1.0 (no converging bend) and 1.6 (no frustum). In cases where the diameter ratio of the converging bend is smaller than 1.6, there is a first reduction of the branch line diameter in the frustum from D_{41} to D_{51}, and a second diameter reduction in the converging bend from D_{51} to D_{101} (variants A and B) or D_{71} (variants C).

The resulting values of the loss coefficients and the secondary velocity ratio in station 101 are plotted in Figure 6.34. All three variants have markedly low loss coefficients, which are sufficiently low that the reference line is no longer included. The losses for variants A and B decrease from $1.0 \leqslant D_{51}/D_{101} \leqslant 1.4$. For $D_{51}/D_{101} > 1.4$, a minor increase is observed. Variant C shows a similar behaviour, with two exceptions. One is the roughly 10 % to 30 % higher losses and the other one is that the minimum of the loss coefficients appears at a lower diameter ratio $D_{51}/D_{71} = 1.3$. The higher losses are attributed to a smaller portion of the branch line being subjected to the larger diameters before the converging bend in variant C. The increase of the loss coefficients for large values of the converging bend diameter ratio can be explained by the corresponding change of the frustum diameter ratio D_{41}/D_{51}. If the diameter ratio of the converging bend increases, the diameter ratio of the frustum becomes smaller until there is only a straight pipe section left, when $D_{51}/D_{101} = 1.6$. However, as plot a) of Figure 6.16 illustrates for the diffuser manifold design with conical frustum, reducing the frustum diameter increases the losses. This is the case here as well. The absence of the frustum results in a much

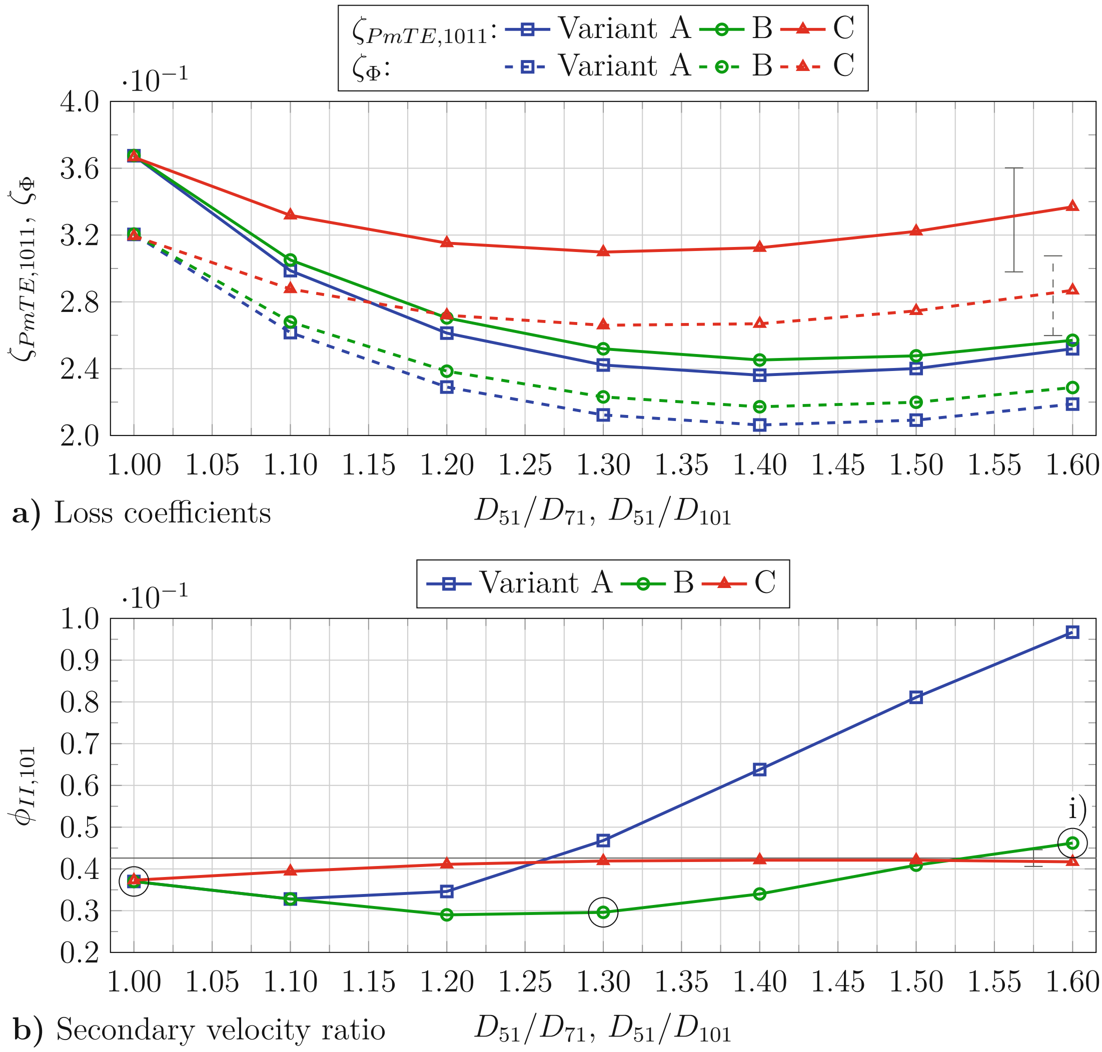

Figure 6.34: Line plots of the loss coefficients and secondary velocity ratios of the diffuser manifold design with conical frustum against the taper ratios D_{51}/D_{71} (Variant C) and D_{51}/D_{101} (Variants A and B). i) - Data points with ○ are compared in Figure 6.35.

larger separation zone in the pipe section between stations 51 and 61 and, in turn, negatively affects the flow through the first bend. However, the increase in the losses is much less pronounced here and the positive effect due to the increased branch line diameter still dominates. The ratio between the dissipation power coefficient and the power loss coefficient $\zeta_\Phi/\zeta_{PmTE,1011}$ lies between 0.85 to 0.89, with an average value of 0.8721. This value is almost the same as the value of 0.8734 achieved by the mixed-element type mesh Fine rM in combination with the SST turbulence model with $y^+ = 1$ for the same ratio when analysing the 90° pipe bend of Shiraishi et al. [92] (which is discussed in Section 5.2.3, especially Figures 5.13 and 5.14 and Table 5.1).

The plot of the secondary velocity ratio $\phi_{II,101}$ in part b) of Figure 6.34 reveals that implementing a convergent part in the branch line is treacherous. In Variant A,

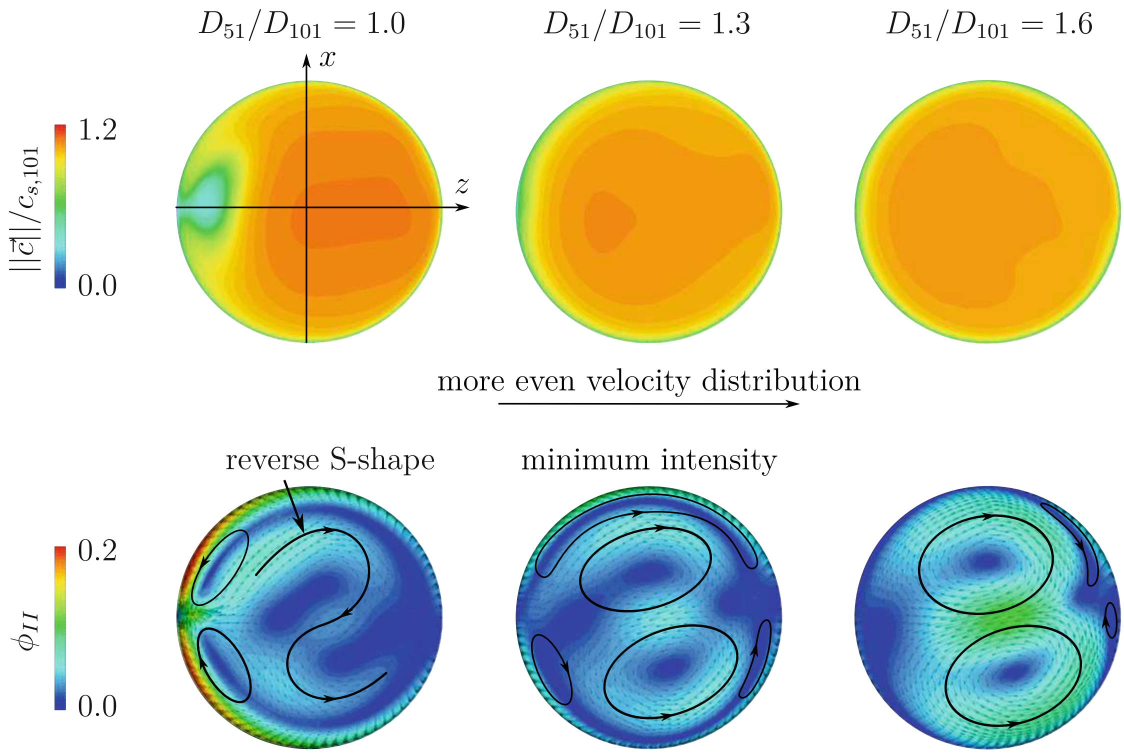

Figure 6.35: Contour plots of the velocity magnitude $||\vec{c}||/c_{s,101}$ and the secondary velocity ratio $\phi_{II,101}$ in station 101 for three bend diameter ratios of variant B.

$\phi_{II,101}$ shows a slight decline for bend diameter ratios less than 1.2. As the diameter ratio becomes larger and thus the relative curvature radii become smaller, a significant increase of the secondary flow in station 101 is observed. This increase is associated with the decrease of the relative curvature radius of both bends as the flow is subjected to sharper turns and becomes more prone to flow separations. In variant C, there is a minor but steady increase of the secondary velocity ratio when the diameter ratio D_{51}/D_{71} of the convergent bend rises. Here, the effect of the changes in flow directions in the injector bend dominates over the effects resulting from the reduction of the channel diameter in the bend before.

The most remarkable observation is delivered by variant B, where the secondary velocity ratio goes down for small diameter ratios D_{51}/D_{101}, then levels off around $D_{51}/D_{101} = 1.2$ to 1.3 before it rises again with increasing values of D_{51}/D_{101}. As proved by the contour plots of the velocity magnitude $||\vec{c}||/c_{s,101}$ in station 101, provided in Figure 6.35, the velocity becomes more uniform, if the contraction of the injector bend is larger. Interestingly, though, the secondary velocity ratio at the same station does not only change in magnitude, but also, the vortex pattern becomes different. The reverse S-shape structure, which was commonly seen in many designs presented in Sections 6.4.2 to 6.4.4 as well as in this figure in the case $D_{51}/D_{101} = 1.0$, vanishes for the other two cases, $D_{51}/D_{101} = 1.3$ and $D_{51}/D_{101} = 1.6$ respectively. Instead, for these two cases, two counter-rotating vortices become dominant. This vortex-pair grows when the contraction in the converging bend increases and eventually pushes the smaller vortices, which are seen in case $D_{51}/D_{101} = 1.3$, to the right (high z-position) until some are eliminated. This behaviour is a highly complex superposition of the effects induced by the frustum that heavily impacts how the flow enters the branch line and goes through all parts upstream of the converging injector bend and the effects of the contraction in the injector bend. Additionally, the 'gooseneck' type of the first part of the branch line between stations 51 and 81 and the double deflection in the injector bend play an important role here too. Moreover, if the diameter of the branch line upstream the injector bend is higher, the Reynolds number becomes smaller and, as explained in Figure 5.18, the secondary flow ratio increases as well.

Therefore, at the current state of this research, parameter combinations exist where the effects mentioned above are combined very favourably, and both quality criteria, the loss coefficients and the secondary velocity ratio reach unmatched minima. Unfortunately, due to the highly complex nature of all effects, it is impossible to isolate the individual effects and their impact on the flow.

6.5.2 Influence of segmented bends

For pipe sections in hydraulic turbines (e.g. pressure lines, distributor systems, spiral casings, draft tubes), it is common practice that changes in the flow direction are made in segmented elbow bends of rectangular or circular cross-sections. This technique allows for greater flexibility and simpler manufacturing of the individual components of the pipe sections compared to being made of one piece. Still, it may be too costly for small hydropower projects, where using standardised parts as often as possible is desired to keep investment costs low. With that in mind, the parametric investigations presented in Section 6.4 were conducted on branch line designs equipped with smooth bends. However, with converging branch lines appearing beneficial to the flow quality but difficult to manufacture, segmented bends have become an option for the *AxFeeder*. These segmented bends allow for simpler manufacturing of the branch line, particularly the convergent injector bend. Therefore, this section compares the flow in a branch line with smooth bends to that in a branch line with segmented bends.

All configurations in this subsection were designed with a convergent injector bend (diameter reduction from station 81 to 91 as in variant B) of Section 6.5.1. Four cases were compared altogether, where the first case (oo) was equipped with smooth bends entirely, the second case (xo) had a segmented bend in the first part and a smooth bend in the second part of the line, the third case had a smooth bend in the first part and a segmented bend in the second part of the line and the fourth case (xx) had two segmented bends. A comparison of these two approaches is sketched in Figure 6.36, where the segmented bend design (dashed blue lines) was overlayed to the smooth bend design (solid black lines). The segmented bends were composed of six elements, where the first and last elements showed a direction change of 9° and the four mid elements a direction change of 18°. The relatively high number of six elements was chosen following suggestions from Bohl and Elmendorf [6] and Idelchik [38] that the flow resistance of segmented bends decreases and the flow turns smoother if the number of segments is increased.

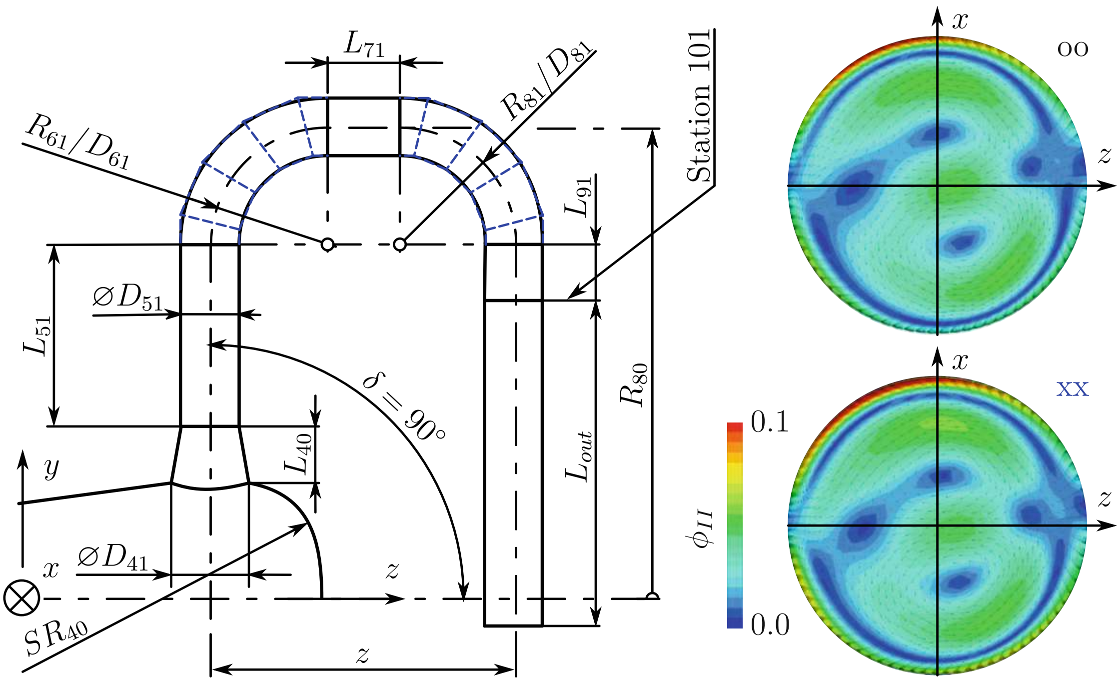

Figure 6.36: Comparison the geometry and the secondary velocity ratio ϕ_{II} at station 101 of a branch line with convergent injector bend. Smooth bends are sketched by black lines and the symbol oo and segmented bends were drawn in dashed blue lines and show the symbol xx.

Figure 6.37 compares the flow quality criteria of these four bend configurations in part a) and highlights the differences between these configurations in part b). All three quality criteria showed a continuous increase if segmented bends were used. However, the increase of both, the power losses $\zeta_{PmTE,1011}$ and the secondary velocity ratio $\phi_{II,101}$ amount to only slightly more than 5 % compared to the configuration with smooth bends. Moreover, the flow structure stays the same. This observation is underlined by the plots of the secondary velocity ratio in station 101 as depicted in Figure 6.36, where the pattern of the contours does not change. Only the magnitude of the secondary velocity ratio appears to be higher with the configuration xx with segmented bends. Interestingly, the dissipation power coefficient ζ_Φ does only change marginally by less than 0.5 %. The effect of segmented bends on the turbulent flow structures seems negligible. Thus, the change of the turbulent dissipation and the associated losses might have only been captured partially in this simulation.

Therefore, it is concluded that both variants, smooth bends and segmented bends, show a similar flow behaviour and are both viable design options for the *AxFeeder*.

6.5.3 Influence of simple internals

The task to reduce flow losses and secondary flows eventually leads to a point where changes in the outer contour of the manifold and branch lines are no longer worth the effort. Idelchik [38] points out the potential of installing turning vanes in pipe

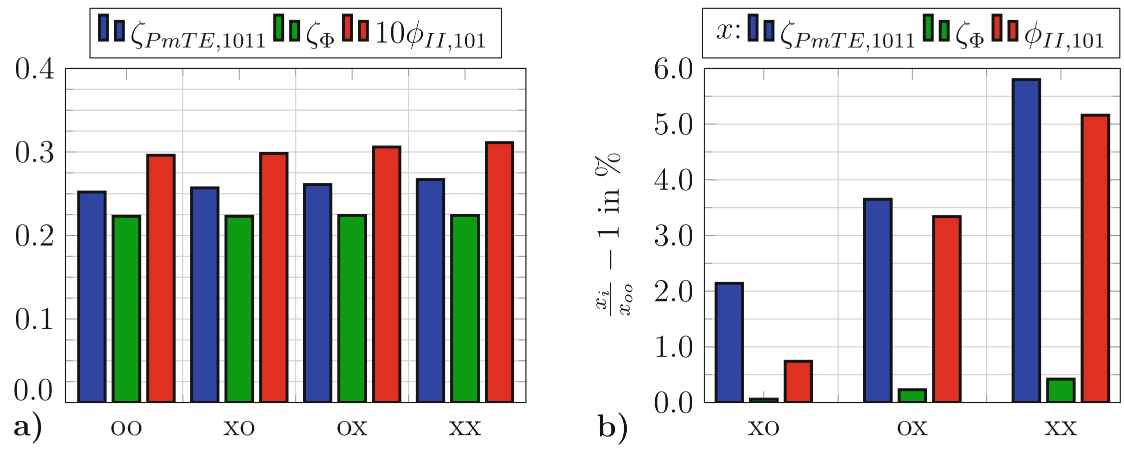

Figure 6.37: Flow quality criteria of cases with branch lines with and without segmented bends. a) absolute values of the quality criteria; b) change relative to smooth bend branch line. oo - both bends smooth, xo - first bend segmented, second one smooth, ox - first bend smooth, second one segmented, xx - both bends segmented

elbows and bends by elaborating on the beneficial effects on pressure losses and uniformity of the velocity distribution of several types of guide vane configurations. While the common goal of all types of flow guiding devices is to eliminate the eddy zone at the inner wall of the channel [38], guide vanes prove to be especially helpful for tight elbows with a curvature radius R/D less than 0.9 to 1.0 [38].

In all configurations that are not stated otherwise, the branch lines of the *AxFeeder* have a curvature radius of $R_{61}/D_{61} = R_{81}/D_{81} = 2$. This decision was inspired by the investigation of Ito [39] on pressure losses in various types of smooth pipe bends. Ito [39] stated that minimal pressure losses would occur at $R/D = 2.5$ for 90° bends at $\mathrm{Re} = 2 \cdot 10^5$ and emphasised this by a diagram indicating minimal losses between $2 < R/D < 3$. Given the importance of a compact design of the *AxFeeder*, the value of $R/D = 2$ was selected for the branch lines. This number is greater than the limit of the curvature radius of around 0.9 to 1.0 below which the installation of guide vanes is usually recommended. Therefore, unlike stated by Idelchik [38], for the *AxFeeder*, guide vanes in the branch lines might not only show positive effects but instead, an increase in losses is expected.

With that in mind, guide vanes were tested at two positions in the *AxFeeder*[27]. In one case, the "vanes" were installed as an annular guide ring between stations 3 and 4 (GR34). In the second case, one thin guide vane follows a 90° arc between stations 81 and 91 (GV89). The guide ring and the guide vane have an elliptical leading and trailing edge with length $D_{51}/10$. In addition to the traditional guide vanes, the effect of a conical intrusion body (CIB) located at the bottom of the manifold (similar to the "Verdrängungskörper" envisioned by Erlach [20, 21]) was tested as well. Details of the shape and the position of these simple internals are sketched in Figure 6.38.

[27] Convergent bends were not used in this study.

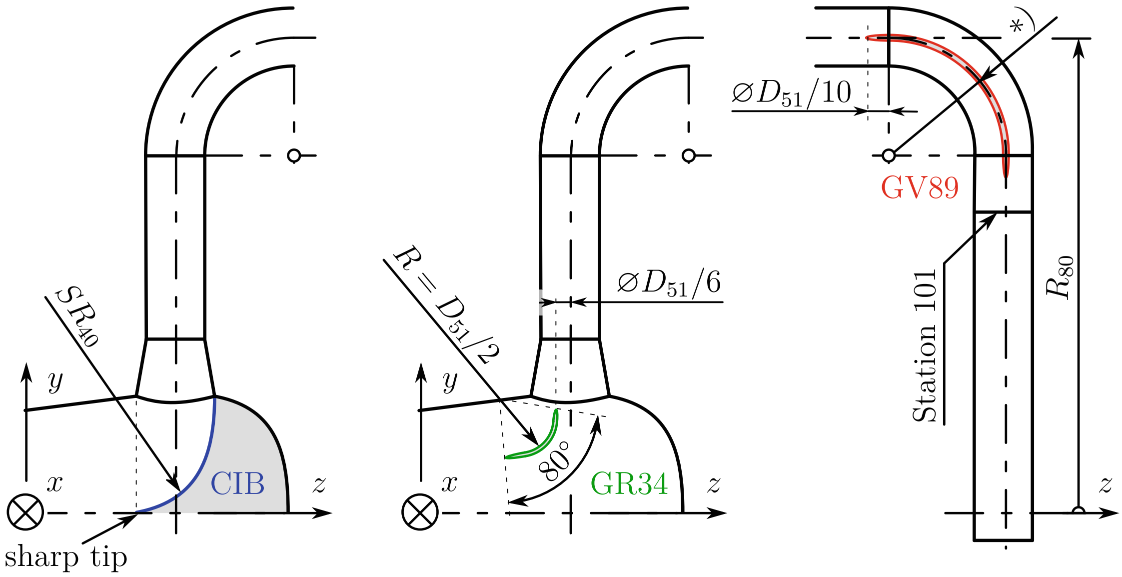

Figure 6.38: Comparison of the shape and the position of three simple internals. Lengths of leading and trailing edges greatly exaggerated for visual purposes. $*) = R_{81}/D_{81}$

In Figure 6.39, part a) compares the absolute values of the flow quality criteria, $\zeta_{PmTE,1011}$, ζ_{Φ} and $\phi_{II,101}$ whereas part b) highlights the relative changes compared to a configuration without any additional internal flow guiding device. The conical intrusion body positioned at the bottom of the manifold does not alter the quality criteria by much. While the CIB helps to reduce the losses slightly, it has almost no noticeable effect on the secondary velocity ratio in station 101. This observation is underlined by Figure 6.40, which shows that the flow structure in the branch lines of the design with the CIB is very similar to the flow structure of the configuration without internals. Both cases have a dominant reverse S-shaped secondary velocity pattern and two minor counter-rotating vortices towards the inner side of the bend (in negative z-direction).

The two guide vane configurations have a much more pronounced effect on the manifold and branch line flow. As Figure 6.40 shows, GR34 suppresses the creation of the vortical structures in the branch line that lead to the characteristic S-shaped secondary flow pattern in station 101. Instead, the two counter-rotating vortices form a secondary flow pattern in this station similar to a deformed Dean circulation[28]. Furthermore, the patterns of the magnitude of velocity $||\vec{c}||$ and of the secondary velocity ratio $\phi_{II,101}$ look identical to the patterns of the 90° pipe bend cases of Sudo et al. [104] and Shirashi et al. [92] discussed in Sections 5.1 and 5.2, in particular Figures 5.8 and 5.19. However, the removal of the reverse S-shape comes at the cost of drastically increased losses of around 20 % and swirl strength,

[28]Dean vortices are a pair of counter-rotating vortices that appear in a curved pipe. Dean [13] was the first to find a solution to the corresponding equations. Sudo et al. [105] studied the secondary flow in curved circular pipes and found five characteristic patterns of secondary flows. The deformed Dean circulation in the branch line of the *AxFeeder* can be classified as type II of the five types of Sudo et al. [105].

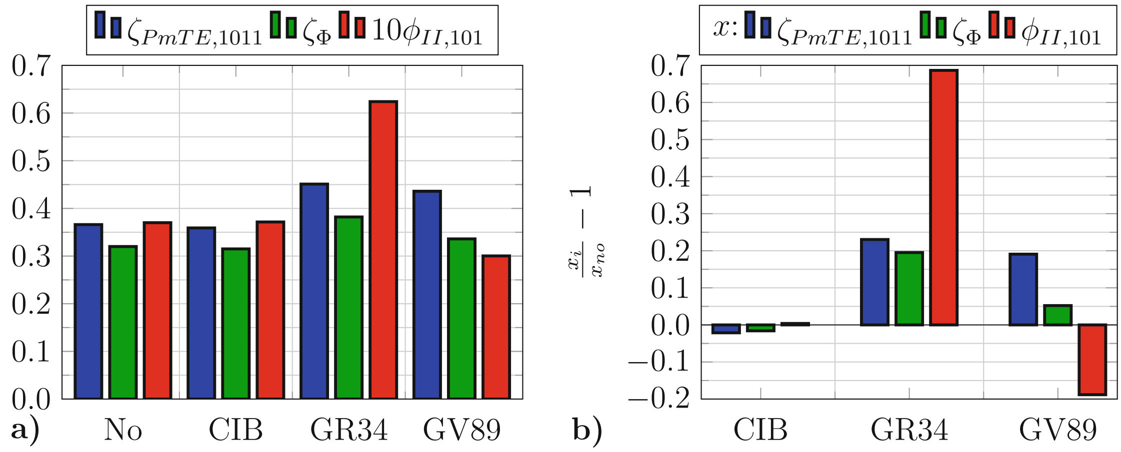

Figure 6.39: Flow quality criteria of *AxFeeder* designs with simple internals. a) absolute values of the quality criterita; b) change relative to an *AxFeeder* without internals.

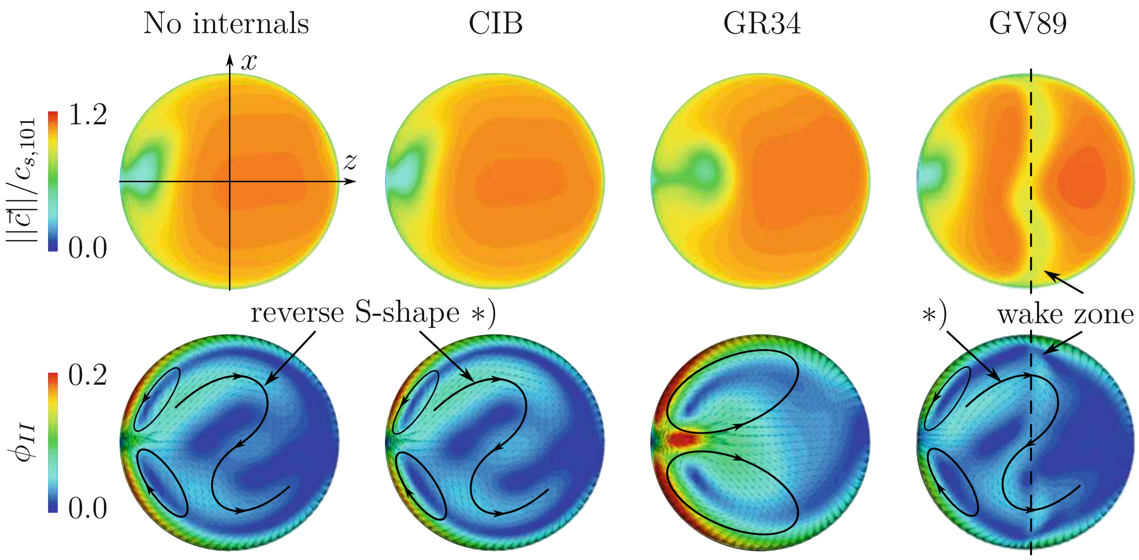

Figure 6.40: Plots of normalised velocity magnitude $\|\vec{c}\|/c_{s,101}$ and secondary velocity ratio ϕ_{II} at station 101 for the four cases with different internals. The same coordinates account for all plots.

hence the almost 70 % higher secondary velocity ratio $\phi_{II,101}$. Therefore, installing a guiding device in the manifold is not recommended, as the effort to make such a device work exceeds the potential gains.

On the contrary, a guide vane installed in the injector bend (GV89) showed rather promising results. While the power losses increased by just over 19 %, the secondary velocity ratio decreased by the same amount. Also, the secondary flow pattern stays similar to that of the case without internals (see plots on the right of Figure 6.40). The reverse S-shape and the two minor vortices can be recognised, albeit the magnitude of the secondary velocity is much weaker. Also, the contours of the velocity magnitude allow for identifying the wake of the guide vane.

Thus, regarding the application of guide vanes in a Pelton turbine distributor system, two design philosophies can be pursued: a) minimising the losses (when no guide vanes are used) at the expense of higher secondary flow velocities or b) if guide vanes were installed, minimising the amount of secondary flow at the cost of higher losses. The research of Semlitsch [89] emphasises the effect of secondary flow structures upstream of the injectors on the formation of the water jet. Further, the practical examples of [56, 70] prove that for conventional distributor systems, in cases where minimising the secondary flow was given priority, flow calming devices like guide vanes upstream the injectors were a go-to solution in past Pelton power plant (refurbishment) projects. Therefore, it is safe to conclude that using guide vanes will also be viable for the *AxFeeder*.

6.6 Comparison of design concepts

Finally, the interesting question is: Which design has the lowest losses and the least amount of secondary flow and is thus the most favourable for hydropower plant applications?

To answer this question, the individual core designs of the *AxFeeder* are compared in this section. As defined in Section 6.3.2, the loss coefficients and the secondary flow ratio of the diffuser manifold design (basic model) computed for an inlet diameter of $D_1 = 300\,\text{mm}$ and an inflow Reynolds number of $\text{Re}_1 = 1 \cdot 10^6$ were chosen as the reference. These values were: power loss coefficient $\zeta_{PmTE,1011,ref} = 0.6291$, dissipation power coefficient $\zeta_{\Phi,ref} = 0.4837$, and secondary velocity ratio $\phi_{II,101,ref} = 0.0426$.

The normalised loss coefficients are then defined as

$$\zeta_{PmTE,norm} = \frac{\zeta_{PmTE,1011}}{\zeta_{PmTE,1011,ref}} \qquad \text{and} \qquad \zeta_{\Phi,norm} = \frac{\zeta_{\Phi}}{\zeta_{\Phi,ref}}\,, \tag{6.21}$$

and the normalised secondary velocity ratio as

$$\phi_{II,norm} = \frac{\phi_{II,101}}{\phi_{II,101,ref}}\,. \tag{6.22}$$

With these normalised coefficients, it is possible to compare the best variants for every varied parameter of the four core designs. However, before that, it has to be decided how to merge both quality criteria into a compound quantity suitable to rank the individual configurations. As raised by Hahn et al. [30], in the design of Pelton turbine distributor systems, one target is to achieve minimal flow losses, and another is to have a low level of secondary flow. The results from the parametric investigation (Section 6.4) showed that these two targets are often contrary, see for example Figure 6.31. Hence, in this thesis, as in [30], it is assumed that both criteria are equally important. Then, the normalised quantities can be added geometrically

$$r_{\zeta\phi} = \sqrt{(\zeta_{PmTE,norm})^2 + (\phi_{II,norm})^2} = \sqrt{\left(\frac{\zeta_{PmTE,1011}}{\zeta_{PmTE,1011,ref}}\right)^2 + \left(\frac{\phi_{II,101}}{\phi_{II,101,ref}}\right)^2} \tag{6.23}$$

ID	Manifold type	Design parameters
a1	Diffuser manifold (basic model)	$\underline{D_{51}/D_1 = 0.40}$, $R_{41}/D_{51} = 0.000$, $\beta = 14°$
a2		$D_{51}/D_1 = 0.40$, $\underline{R_{41}/D_{51} = 0.025}$, $\beta = 14°$
a3		$D_{51}/D_1 = 0.40$, $R_{41}/D_{51} = 0.000$, $\underline{\beta = 8°}$
b1	Diffuser manifold with conical frustum	$\underline{D_{41}/D_{51} = 1.6}$, $\underline{\delta = 90°}$, $\varphi = 0°$
b2		$D_{41}/D_{51} = 1.6$, $\delta = 90°$, $\underline{\varphi = 15°}$
b3	Convergent branch line	Variant B, $D_{41}/D_{51} = 1.3$
b4	Segmented bend	xx
b5	Simple internals	GV89
c1	Spherical manifold	$\underline{SR_{40}/D_1 = 0.533}$, $\underline{\delta = 75°}$, $D_{41}/D_{51} = 1.00$
c2		$SR_{40}/D_1 = 0.600$, $\delta = 85°$, $\underline{D_{41}/D_{51} = 1.30}$
d1	Cylindrical manifold	$\underline{T_4/D_{51} = 0.500}$, $\underline{\delta = 70°}$, $R_{41}/D_{51} = 0.00$
d2		$T_4/D_{51} = 0.250$, $\delta = 90°$, $\underline{R_{41}/D_{51} = 0.10}$

Table 6.8: Explanation of abbreviations used in Figure 6.41. Parameters, which were varied in the relevant study series, are underlined.

to achieve a single value $r_{\zeta\phi}$, the compound quality coefficient for each case to quantify the overall quality. The value of $r_{\zeta\phi}$ can be interpreted as the distance of a data point plotted in a $\phi_{II,norm}$ - $\zeta_{PmTE,norm}$ coordinate system to the centre point $(0,0)$. Then, $r_{\zeta\phi}$ corresponds to the radius of a circle, for which all data points of a variant lie either outside or on the circle, and no data point of this variant lies inside. The approach above was used to determine the best variants presented in Figure 6.41 and Table 6.8. The $r_{\zeta\phi}$-concept is utilised in the scatter plot of all variants, Figure 6.42, and the summary of the best configuration of the four manifold types, Table 6.9.

In Figure 6.41, bar charts of the normalised loss coefficients $\zeta_{PmTE,norm}$ and $\zeta_{\Phi,norm}$ as well as the normalised secondary velocity ratio $\phi_{II,norm}$ are plotted for all manifold types and the most relevant parameter combinations. An overview of the parameter combinations and an explanation of the abbreviations used in this figure is presented in Table 6.8. The analysis of Figure 6.41 reveals that for all core designs, except for the cylindrical manifold[29], the normalised loss coefficients are lower than the normalised secondary velocity ratio. Further, the minimum value of the normalised losses is at around 0.4, whereas the minimum of the normalised secondary velocity ratio lies just below 0.7. These observations indicate that for complex piping systems such as the *AxFeeder*, reducing pressure losses and dissipation is more straightforward than improving the secondary flow. It was proved in Sections 6.4.2 and 6.4.3 that using a conical frustum is especially beneficial for

[29]And except for case c1 with a spherical manifold.

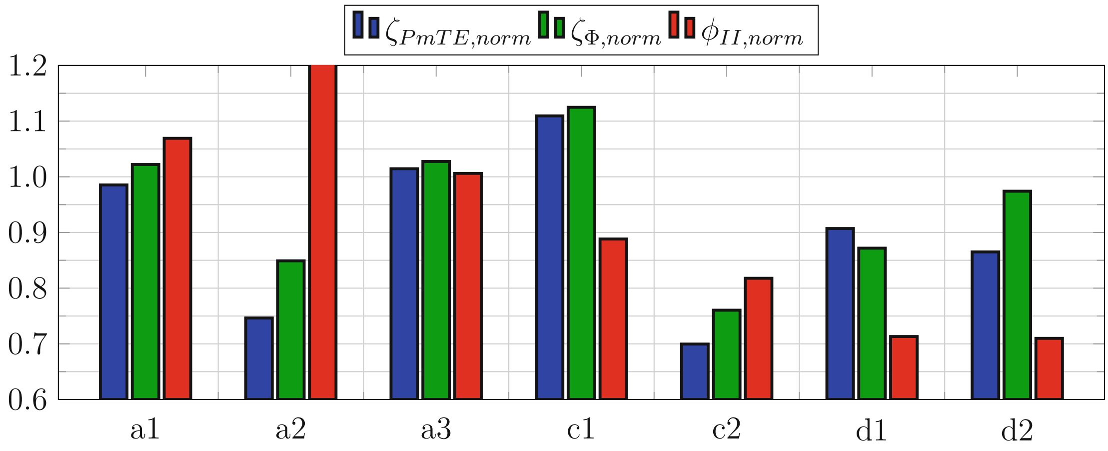

a) Core designs a) - Diff. man. (basic mod.), c) - Sph. man. and d) - Cyl. man.

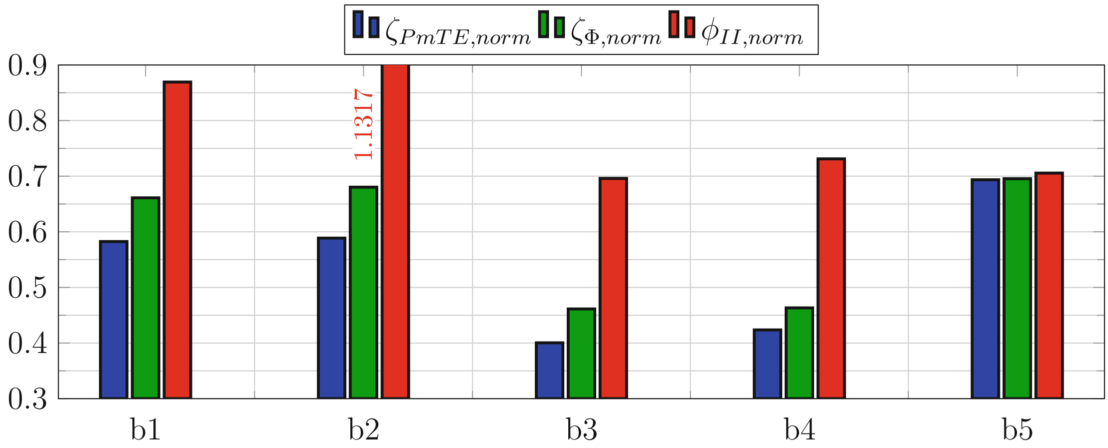

b) Core design b) - Diffuser manifold with conical frustum

Figure 6.41: Normalised quality criteria for the best case of every varied parameter of the four core designs. Abbreviations are explained in Table 6.8.

reducing the flow losses, as cases b1 to b5 and c2 underline. In these six cases, where the frustum was installed, the power and dissipation losses, with normalised power loss coefficients of less than 0.7 and normalised dissipation power coefficients of less than 0.75 for all of the six, were consistently lower than for designs without the frustum.

Another takeaway from Figure 6.41 is that all configurations of core design b) with the diffuser manifold and the conical frustum, except for case b2 with the branch line pivoted by the angle $\varphi = 15°$, have comparably low normalised quality criteria. Their normalised power loss coefficients and the normalised dissipation power coefficients are lower than those of any other design. Comparing cases b1 and b2 (both without the convergent bend) to cases b3 and b4 (both with converging injector bend), it becomes evident what an efficient measure a convergent injector bend is to reduce both quality criteria simultaneously. A closer look at cases b3, b4 (both with the converging injector bend but no guide vanes) and b5 (no convergent branch line but guide vane in the injector bend) shows that all three cases achieve a similar value of the secondary velocity ratio. However, the two cases with the convergent branch lines, b3 and b4, have drastically lower losses. From a fluidic point of view, employing a convergent bend is thus favourable over installing a guide vane.

The scatter plot in Figure 6.42 intends to give a more detailed view of where the individual configurations rank amongst each other in terms of power losses and secondary flows. Therefore, the resulting quality criteria of around 180 cases are plotted in the $\phi_{II,norm}$ - $\zeta_{PmTE,norm}$ plane. All cases with the diffuser manifold (basic model), a1 to a3, are given blue markers; the cases with the diffuser manifold with conical frustum, b1 to b5, have green markers; those with the spherical manifold, c1 and c2, use red markers and those with the cylindrical manifold, d1 and d2 are shown by cyan coloured markers. For each manifold type, data points with the same marker type belong to the same study series, explained in Table 6.8, e.g. red circles indicate the study series c2 with the spherical manifold, where the frustum diameter was varied. The configurations with the best (= lowest) compound quality coefficient $r_{\zeta\phi}$ of each core design are denoted by enlarged, filled markers. The quality criteria of these four cases are summarised in Table 6.9, which also shows the relative distances

$$\Delta r_{\zeta\phi} = 1 - \frac{r_{\zeta\phi}(b,c,d)}{r_{\zeta\phi}(a)} \tag{6.24}$$

between these four cases. This quantity can also be read as a measure of how much the compound quality coefficient of a design was improved over the reference case.

Notably, the blue and red markers are widespread, mainly towards the plane's upper and right half, thus showing unfavourably high secondary velocity ratios and power losses [30]. The cyan data points are centred around the middle of the $\phi_{II,norm}$ - $\zeta_{PmTE,norm}$ plane with a minor concentration of points at very low secondary velocity ratios of $\phi_{II,norm}$ between 0.6 to 0.7. These values are even lower than the best configuration of the cylindrical manifold type and the overall best configuration of the diffuser manifold type with a conical frustum and a converging injector bend[30]. Unfortunately, the corresponding power losses and, thus, the compound quality coefficients are high.

The data points of core design b) are clustered towards the left side of the plane. This clustering, again, is a direct consequence of the conical frustum employed for most cases of this design type, which leads to lower losses and the shift to the left. The losses of most cases of type b) are lower than those of the other three types[31]. However, the data points of type b) are spread along a considerable segment of the vertical axis, emphasising that only a few carefully selected geometry combinations serve both purposes, reducing losses and secondary flows simultaneously. The most

[30]Therefore, these cases are called non-dominated configurations.

[31]These cases are also non-dominated configurations. In an optimisation context, all these non-dominated configurations form the Pareto front [44, 107], which is also drawn in Figure 6.42. The 'horizontal leg' of the Pareto front consists of cases with very low secondary velocity ratios, and the 'vertical leg' consists of cases with very low power loss coefficients.

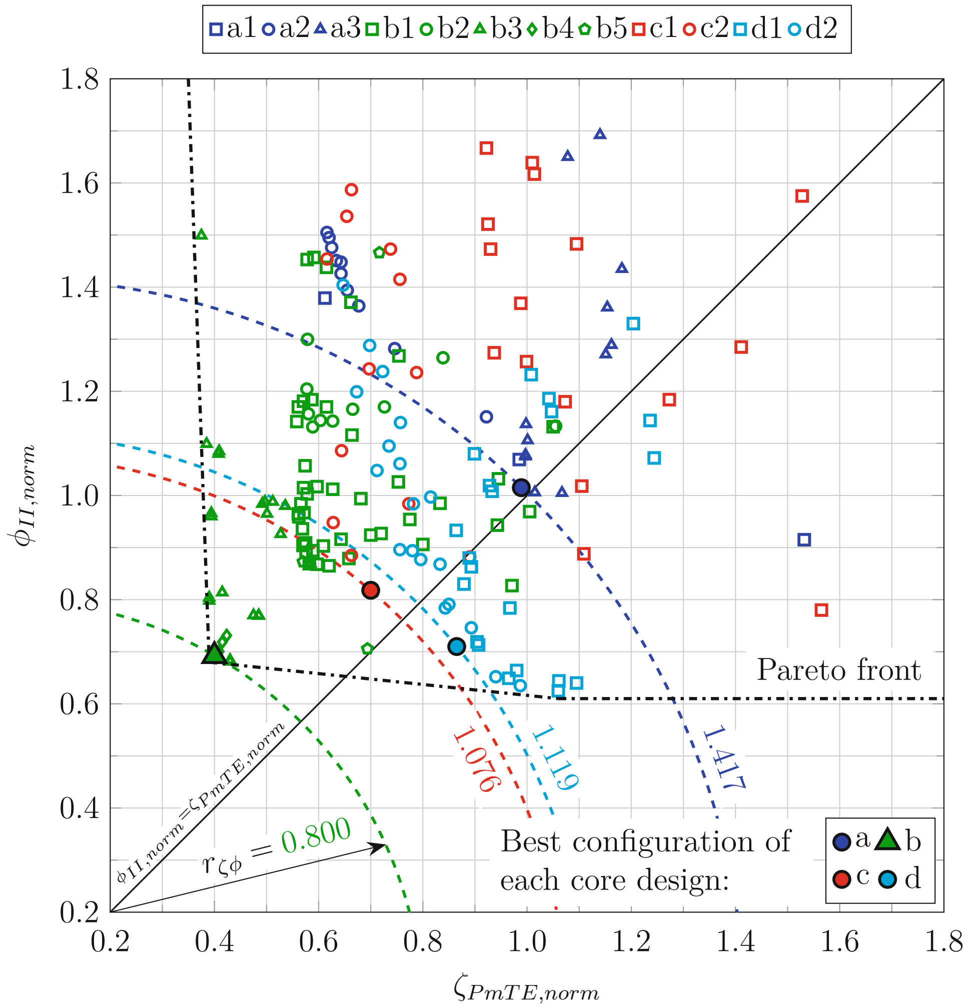

Figure 6.42: Scatter plot of normalised quality criteria for all cases presented in Sections 6.4 and 6.5. Abbreviations are explained in Table 6.8. Data of the best configurations are summarised in Table 6.9.

suitable design of the *AxFeeder* with the lowest compound quality coefficient of $r_{\zeta\phi} = 0.8$ is of type b3, with a diffuser with a conical frustum and converging injector bend. This case is indicated by a large, green-filled triangular marker in Figure 6.42.

When comparing the four manifold types, it stands out that most configurations of types b) and d) are better in terms of $r_{\zeta\phi}$ than the diffuser manifold (basic model) of type a). Interestingly, most configurations of type c), the spherical manifold, are worse than the best of type a). Only a few selected cases of type c) have a lower compound quality coefficient. Especially the cases with a conical frustum and the branch line deviation angles close to 90° perform better than the other designs with a spherical manifold. The best configuration of the spherical manifold performs even better than the best configuration of the cylindrical manifold. Here, it is worth reminding that the cylindrical manifolds lack space for an adequately sized conical frustum and, thus, are subject to higher losses during the transition of the flow from the manifold to the branch lines.

ID	Manifold type	a)	$\phi_{II,101}$	b)	c)	$r_{\zeta\phi}$	$\Delta r_{\zeta\phi}$ (%)
a2	Diffuser man. (basic model)	0.6223	0.0432	0.989	1.015	1.417	0
b3	$*$)	0.2519	0.0295	0.400	0.692	0.800	43.5
c2	Spherical man.	0.4401	0.0348	0.700	0.818	1.076	23.9
d2	Cylindrical man.	0.5442	0.0302	0.865	0.710	1.119	20.9

Table 6.9: Summary of the quality criteria of the best configuration of each manifold type shown in Figure 6.42. $*$) - Diffuser manifold with the conical frustum and convergent branch line variant B. a) - $\zeta_{PmTE,1011}$, b) - $\zeta_{PmTE,norm}$, c) - $\phi_{II,norm}$.

The list of the four best cases, given in Table 6.9, strengthens these observations by translating the improvement of the best cases of the four manifold types into numerical values. For type a), the diffuser manifold (basic model), finding a design that performs better than the reference was impossible. On the contrary, the overall best of type b), the diffuser with conical frustum, a deviation angle $\delta = 90°$ and converging injector bend, achieves an improvement of almost 44 %.

CHAPTER 7

Conclusion

This thesis investigated the flow in a novel Pelton turbine distributor system with axial inflow, the *AxFeeder*, using incompressible, steady-state CFD simulations. The most relevant findings, discoveries and recommendations for future research are presented in this final chapter.

7.1 Summary

Four core designs of Pelton turbine distributor systems with axial inflow were conceptualised to evaluate the effects of different configurations on the flow quality criteria, the power loss coefficient ζ_{PmTE}, the dissipation power coefficient ζ_{Φ}, and the secondary velocity ratio ϕ_{II}. The study included around 180 geometric variations of the core designs, the diffuser manifold (basic model), the diffuser manifold with conical frustum, the spherical manifold and the cylindrical manifold. Additionally, the effects of converging branch lines, segmented bends and simple internals were explored.

Variations of the diffuser angle and the sphere radius proved it is of the highest importance to avoid stall and any form of distinct flow separation in the manifold. Also, the transition from the manifold head to the branch line must be designed carefully. All flow quality criteria were significantly improved by applying an appropriately sized conical frustum as the first element of the branch line. Combined with a steep deviation angle close to 90°, a separation zone at the inside of the first turn shifted the core of the flow towards the outside of the first straight segment of the branch lines. This shift positively affected the flow through the first bend. It facilitated a layered velocity profile upstream of the injector bend, where the highest velocities were located towards the inner side of the injector bend. The layered velocity profile positively affected the flow through the injector bend. The velocity profiles upstream of the injector position at station 101 appeared to be much more symmetric, and the magnitude of the secondary flow was much less. The reverse S-shape pattern of the secondary velocity ratio in that station was commonly seen with all designs where the phenomena described above occurred.

All flow quality criteria were improved simultaneously by using a convergent injector bend. A guide vane in the injector bend increased the losses but reduced the secondary velocity ratio at about the same rate. Segmented bends were found to have slightly higher losses and secondary flow ratios than smooth bends.

The comparison of all cases in Section 6.6 revealed that the overall best configuration in terms of flow quality criteria was the *AxFeeder* equipped with a diffuser-shaped manifold, conical frustum and a converging branch line of a deviation angle of 90°.

7.2 Answers to research questions

In the course of this dissertation, several answers to the initial research questions emerged:

1. What potential Pelton turbine distributor system designs allow axial inflow and outflow tangential to the runner?
   Four core designs were introduced where the flow enters the manifold in the axial direction and is turned towards the radial direction at the transition of the manifold and the branch lines. The branch lines are routed such that the flow leaves the branch lines in a direction tangential to the runner.

2. Is a steady-state simulation approach feasible to accurately predict the flow in such a Pelton turbine distributor system?
   The comparison to 90° pipe bend cases proved that a steady-state simulation approach is feasible to predict power losses, dissipation and secondary flows accurately and reproducibly, providing for an adequately sized mesh with sufficient wall resolution in combination with the k-ω SST turbulence model. At the benefit of low computational costs for each case, this approach has the acceptable drawback of slightly increased uncertainty for predicting vortical structures and, thus, secondary flow.

3. How does the operating regime of such a Pelton turbine distributor system in the context of small hydropower plants look like, and what is a realistic design case?
   In the Reynolds number range typical for a Pelton turbine distributor system, the operating charts showed continuously declining curves for the power losses, the dissipation power and the secondary velocity ratio with increasing Reynolds number. Thus, a realistic design case of a small hydropower plant projected a Pelton turbine with a rated power of around 250 kW, at an assumed head of 125 m. The corresponding volumetric flow rate became 210 L/s, which, with a suitable penstock diameter of 300 mm, resulted in a corresponding Reynolds number of $1 \cdot 10^6$.

4. How does the flow behave in a Pelton turbine distributor system with axial inflow, and what components significantly influence the flow quality?
   The four areas found to be most important for achieving high-quality flow were the rate of expansion of the manifold, i.e. the diffuser angle and the

sphere diameter, the transition from the manifold to the branch line by a conical frustum, a steep deviation angle of the branch line close to 90° and a converging injector bend. When all components of the distributor system were well harmonised, the secondary flow showed a distinct reverse S-shape pattern in station 101 with an average magnitude of less than the 90° pipe bend cases. The explanation found was that in such a manifold-branch line combination, when entering the branch line through the conical frustum, the core of the flow was shifted favourably towards the inside of the two bends in the branch line.

5. Which combination of geometric parameters is favourable?
   The most favourable configuration of the *AxFeeder* was equipped with a diffuser-shaped manifold with an opening angle $\beta = 14°$, a conical frustum with base diameter $D_{41}/D_{101} = 1.6$, a branch line with a deviation angle $\delta = 90°$ and a converging injector bend with a diameter ratio of $D_{51}/D_{101} = 1.30$. The compound quality coefficient $r_{\zeta\phi}$ of this configuration was almost 44 % less than that of the reference.

7.3 Future research

This thesis contributed to understanding the flow in Pelton turbine distributor systems with axial inflow, the *AxFeeder*. Building on this contribution, further research effort would benefit the future potential contributions of this dissertation.

One of the most pressing questions outside the scope of this thesis is how the *AxFeeder* performs under different operation conditions. Here, it is of special interest if the flow structures stay the same when only one, two or three of the six branch lines are active and the others are shut down. Recently, Semlitsch [88] has conducted numerical studies on that matter. Parallel to these numerical studies, as part of the project *AxFeeder*[1], in the hydraulic laboratory of the Institute of Energy Systems and Thermodynamics at TU Wien a test rig is under construction. When fully commissioned, measurements of the flow in the manifold, the branch lines, and the jets will allow for deeper insight into the flow phenomena of the *AxFeeder* and possible correlations between the flow in the distributor system and the jets.

The reverse S-shape secondary flow pattern of the *AxFeeder* was not seen before with conventional distributor systems. Therefore, it is recommended that the flow structure upstream of the injector be investigated to determine how this type of flow structure affects the formation of the jet in the nozzle and, thus, the jet shape and orientation. After-effects on the jet bucket interactions need to be considered as well.

With potential small hydro applications of the *AxFeeder*, close attention will be paid to manufacturing complexity, costs and scalability. Once the flow in the *AxFeeder* is fully understood, a study of the economics of the Pelton turbine distributor with axial inflow is of high practical relevance and, thus, warmly recommended.

[1]FFG project number: FO999888084

Bibliography

[1] AIAA G-077-1998: Guide for the Verification and Validation of Computational Fluid Dynamics Simulations, 2002.

[2] Anderson, J. D., *Fundamentals of aerodynamics*, 6th ed.; McGraw-Hill series in aeronautical and aerospace engineering; McGraw Hill Education: New York, 2017.

[3] ANSYS CFX 19.2: CFX-Solver Theory Guide, 2023.

[4] ASME PTC 19.1-2005: Test Uncertainty, 2005.

[5] Benzon, D. S., *The Turgo impulse turbine; a CFD based approach to the design improvement with experimental validation*; Department of Engineering, Faculty of Science and Technology, Lancaster University: Phd thesis, 2016.

[6] Bohl, W., and Elmendorf, W., *Technische Strömungslehre*; Vogel Buchverlag: Würzburg, 2014.

[7] Böhle, M., Fleder, A., and Mohr, M., *Study of the losses in fluid machinery with the help of entropy* In 16^{th} International Symposium on Transport Phenomena and Dynamics of Rotating Machinery, Honolulu, Hawaii, USA, 2016.

[8] Boussinesq, J., *Essai sur la théorie des eaux courantes / par J. Boussinesq*; Impr. nationale (Paris): 1877.

[9] Brauch, W., Dreyer, H.-J., and Haacke, W., *Mathematik für Ingenieure*, 9th ed.; Vieweg+Teubner Verlag Wiesbaden: Stuttgart, 1995.

[10] Casey, M., and Wintergerste, T. Best Practice Guidelines, Version 1.0, European Research Community On Flow, Turbulence and Combustion - ERCOFTAC: 2000.

[11] Celik, I. B., Ghia, U., Roache, P. J., and Freitas, C. J. (2008). Procedure for estimation and reporting of uncertainty due to discretization in CFD applications. *Journal of Fluids Engineering 130*, 078001.

[12] Chongji, Z., Yexiang, X., Wei, X., Tao, W., Jin, Z., Zhengwei, W., and Yongyao, L. (2016). Numerical Analysis of Pelton Nozzle Jet Flow Behavior Considering Elbow Pipe. *IOP Conference Series: Earth and Environmental Science 49*, 022005.

[13] Dean, W. (1927). XVI. Note on the motion of fluid in a curved pipe. *The London, Edinburgh, and Dublin Philosophical Magazine and Journal of Science 4*, 208–223.

[14] Deng, H., Song, K., Deng, F., Huang, Y., Luo, T., Zhou, Y., Qin, B., Zeng, Y., Yu, Z., Pang, J., and Liu, X. (2023). Nozzle Jet Deviation from Bucket Pitch Circle's Effect on the Stability and Efficiency of Pelton Turbine. *Processes 11*, 1342.

[15] DIN 1319-4: Grundlagen der Meßtechnik, Teil 4: Auswertung von Messungen, Meßunsicherheit, 1999.

[16] Dixon, S. L., and Hall, C., *Fluid mechanics and thermodynamics of turbomachinery*; Butterworth-Heinemann: 2013.

[17] Durbin, P., A Perspective On Recent Developments In RANS Modeling In *Engineering Turbulence Modelling and Experiments 5*, Rodi, W., and Fueyo, N., Eds.; Elsevier Science Ltd: Oxford, 2002, pp 3–16.

[18] Erlach, J., and Erlach, P., *We proudly present the first up to Six Jets Horizontal Pelton Turbine.* In Hidroenergia 2014, European Small Hydropower Association (ESHA) Congress, Istanbul, Turkey, 2014.

[19] Erlach, J., and Erlach, P. (2016). Neues Pelton-Konzept - bis zu sechs Düsen in horizontaler Anordnung. *WasserWirtschaft 106*, 18–24.

[20] Erlach, J., *"New Pelton concept" up to six nozzles horizontal* In 17th International Seminar on Hydropower Plants, Laxenburg, Austria, 2012.

[21] Erlach, J., and Staubli, T. Pelton turbine with a supply system, WO 2008/003390 A1, 2007.

[22] Fan, W., Sun, L., and Guo, P. (2024). Investigation on unstable flow characteristics and energy dissipation in Pelton turbine. *Engineering Applications of Computational Fluid Mechanics 18*, 2304643.

[23] Ferziger, J. H., Perić, M., and Street, R. L., *Computational Methods for Fluid Dynamics*, 4th ed.; Springer Cham: 2020.

[24] Fiereder, R., Riemann, S., and Schilling, R. (2010). Numerical and experimental investigation of the 3D free surface flow in a model Pelton turbine. *IOP Conference Series: Earth and Environmental Science 12*, 012072.

[25] Giesecke, J., Heimerl, S., and Mosonyi, E., *Wasserkraftanlagen: Planung, Bau und Betrieb*, 6th ed.; Springer Vieweg Berlin, Heidelberg: 2014.

[26] Greitzer, E. M., Tan, C. S., and Graf, M. B., *Internal Flow: Concepts and Applications*; Cambridge Engine Technology Series; Cambridge University Press: 2004.

[27] Gupta, V., Prasad, V., and Khare, R., *Numerical Simulation for Visualising Effect of Jet Shape on Various Parameters of Multi Jet Pelton Turbine Model* In Thirty-first National Convention of Electrical Engineers on 'Renewable Energy and Green Technology for Sustainable Development', India, 2015.

[28] Hahn, F. J. J., Maly, A., Semlitsch, B., and Bauer, C., *Numerical investigation of the secondary flow pattern in a Pelton turbine jet* In *Proceedings of the* 3rd*IAHR Young Professionals Congress*, 2022, pp 121–122.

[29] Hahn, F. J. J., Maly, A., and Semlitsch, B. Zwischenbericht: FO999888084 - AxFeeder, 2024.

[30] Hahn, F. J. J., Maly, A., Semlitsch, B., and Bauer, C. (2023). Numerical Investigation of Pelton Turbine Distributor Systems with Axial Inflow. *Energies 16*, 2737.

[31] Hahn, F. J. J., Semlitsch, B., and Bauer, C. (2022). On the numerical assessment of flow losses and secondary flows in Pelton turbine manifolds. *IOP Conference Series: Earth and Environmental Science 1079*, 012082.

[32] Han, L., Duan, X., Gong, R., Zhang, G., Wang, H., and Wei, X. (2019). Physic of secondary flow phenomenon in distributor and bifurcation pipe of Pelton turbine. *Renewable energy 131*, 159–167.

[33] Hankeln, F., and Riedelbauch, S. (2019). Investigation of hydraulic losses in a centrifugal pump with low specific speed. *Wasserwirtschaft 109*, 37–41.

[34] Herwig, H., Gloss, D., and Wenterodt, T. (2008). A new approach to understanding and modelling the influence of wall roughness on friction factors for pipe and channel flows. *Journal of Fluid Mechanics 613*, 35–53.

[35] Herwig, H., and Schmandt, B. (2014). How to determine losses in a flow field: A paradigm shift towards the second law analysis. *Entropy 16*, 2959–2989.

[36] Herwig, H., and Schmandt, B., *Strömungsmechanik: Physikalisch-mathemat. Grundlagen und Anleitung zum Lösen von Aufgaben*, 4th ed.; Springer Vieweg Berlin, Heidelberg: 2018.

[37] Horlacher, H.-B., and Helbig, U., *Rohrleitungen 2: Einsatz, Verlegung, Berechnung, Rehabilitation*, 3rd ed.; Springer Vieweg Berlin, Heidelberg: 2023.

[38] Idelchik, I. E., *Handbook of hydraulic resistance*, 3rd ed.; Jaico Publishing House: 2005.

[39] Ito, H. (1960). Pressure Losses in Smooth Pipe Bends. *Journal of Basic Engineering 82*, 131–140.

[40] Jošt, D., Škerlavaj, A., Pirnat, V., Morgut, M., and Nobile, E. (2019). Detailed analysis of flow in two Pelton turbines with efficiency and cavitation prediction. *International Journal of Fluid Machinery and Systems 12*, 388–399.

[41] Jošt, D., Škerlavaj, A., Pirnat, V., Morgut, M., and Nobile, E. (2019). Numerical prediction of efficiency and cavitation for a Pelton turbine. *IOP Conference Series: Earth and Environmental Science 240*, 062033.

[42] Kato, M., and Launder, B. E., *The modeling of turbulent flow around stationary and vibrating square cylinders* In *Proceedings of the* 9th *Symposium on Turbulent Shear Flows*, 1993, pp 1041–1046.

[43] Khan, F., and Kumar, A. (2023). Pelton turbine jet flow investigations using laser Doppler velocimetry. *Physics of Fluids 35*, 125138.

[44] Kim, K.-Y., Samad, A., and Benini, E., *Design Optimization of Fluid Machinery, Applying Computational Fluid Dynamics and Numerical Optimization*, 1st ed.; John Wiley & Sons Singapore Pte. Ltd: Singapore, 2019.

[45] Kirkup, L., and Frenkel, R. B., Some statistical concepts In *An Introduction to Uncertainty in Measurement: Using the GUM (Guide to the Expression of Uncertainty in Measurement)*; Cambridge University Press: 2006, pp 53–82.

[46] Kirschner, O., Wack, J., Junginger, B., Junginger, J., Ruprecht, A., and Riedelbauch, S. (2019). Experimentelle und numerische Strömungsanalyse einer Trifurkation eines 150-MW-Kraftwerkes. *Wasserwirtschaft 109*, 44–47.

[47] Kline, S. J., Abbott, D. E., and Fox, R. W. (1959). Optimum Design of Straight-Walled Diffusers. *Journal of Basic Engineering 81*, 321–329.

[48] Kock, F., and Herwig, H. (2004). Local entropy production in turbulent shear flows: a high-Reynolds number model with wall functions. *International journal of heat and mass transfer 47*, 2205–2215.

[49] Kock, F., and Herwig, H. (2005). Entropy production calculation for turbulent shear flows and their implementation in CFD codes. *International Journal of Heat and Fluid Flow 26*, 672–680.

[50] Kock, F., *Bestimmung der lokalen Entropieproduktion in turbulenten Strömungen und deren Nutzung zur Bewertung konvektiver Transportprozesse*; Berichte aus der Strömungstechnik; Shaker Verlag: Aachen, 2003.

[51] Kuhlmann, H., *Strömungsmechanik: Eine kompakte Einführung für Physiker und Ingenieure*; Pearson Deutschland: 2014.

[52] Launder, B. E., and Sandham, N. D., *Closure Strategies for Turbulent and Transitional Flows*; Cambridge University Press: 2002.

[53] Launder, B., and Spalding, D. (1974). The numerical computation of turbulent flows. *Computer Methods in Applied Mechanics and Engineering 3*, 269–289.

[54] Laurien, E., and Oertel, H. J., *Numerische Strömungsmechanik: Grundgleichungen und Modelle – Lösungsmethoden – Qualität und Genauigkeit*, 6th ed.; Springer Vieweg Wiesbaden: 2018.

[55] Lei, H., Gaofu, Z., Ruzhi, G., Hongda, W., and Wei, L. (2019). Physics of bad-behaved flow in 6-Nozzle Pelton turbine through dynamic simulation. *IOP Conference Series: Earth and Environmental Science 240*, 022018.

[56] Mack, R., Gola, B., Smertnig, M., Wittwer, B., and Meusburger, P. (2014). Modernization of vertical Pelton turbines with the help of CFD and model testing. *IOP Conference Series: Earth and Environmental Science 22*, 012002.

[57] Mack, R., and List, B., *Multijet Horizontal Pelton Turbine Concept, Development and Prototype* In 21^{st} International Seminar on Hydropower Plants, Laxenburg, Austria, 2022.

[58] Mack, R., Mössinger, P., and Necker, J. (2022). Gerlos I ist die weltweit erste horizontale sechsdüsige Pelton-Turbine. *Wasserwirtschaft 113*, 60–61.

[59] McDonald, A., and Fox, R. (1966). An experimental investigation of incompressible flow in conical diffusers. *International Journal of Mechanical Sciences 8*, 125–139.

[60] Melzer, S., Pesch, A., Schepeler, S., Kalkkuhl, T., and Skoda, R. (2020). Three-Dimensional Simulation of Highly Unsteady and Isothermal Flow in Centrifugal Pumps for the Local Loss Analysis Including a Wall Function for Entropy Production. *Journal of Fluids Engineering 142*, 111209.

[61] Menter, F. R. (1994). Two-equation eddy-viscosity turbulence models for engineering applications. *AIAA Journal 32*, 1598–1605.

[62] Menter, F. R., Garbaruk, A., and Egorov, Y. (2012). Explicit algebraic Reynolds stress models for anisotropic wall-bounded flows. *Progress in flight physics 3*, 89–104.

[63] Menter, F. R., Kuntz, M., and Langtry, R. (2003). Ten years of industrial experience with the SST turbulence model. *Turbulence, Heat and Mass Transfer 4*.

[64] Mosonyi, E., *Water Power Development: High-head power plants, Volume Two/A*; Water Power Development; Akadémiai Kiadó, Budapest: 1965.

[65] NASA Langley Research Center, Turbulence Modeling Resource: The Explicit Algebraic Stress k-omega Turbulence Model. https://turbmodels.larc.nasa.gov/easmko.html (accessed Aug. 8, 2024).

[66] Nechleba, M., *Hydraulic Turbines: Their Design and Equipment*; ARTIA, Prague: 1957.

[67] Nikuradse, J., *Gesetzmäßigkeiten der turbulenten Strömung in glatten Rohren*; Forschungsheft 356; VDI-Verl.: Berlin, 1932.

[68] Parkinson, E., Lestriez, R., and Chapuis, L., *Flow Calculations in Pelton Turbines - Part 1: Repartitor and Injector Numerical Analysis.* In 19th *IAHR Symposium on Hydraulic Machinery and Systems*, 1998, pp 285–293.

[69] Patel, K., Patel, B., Yadav, M., and Foggia, T. (2010). Development of Pelton turbine using numerical simulation. *IOP conference series: Earth and environmental science 12*, 012048.

[70] Peron, M., Parkinson, E., Geppert, L., and Staubli, T., *Importance of Jet Quality on Pelton Efficiency and Cavitation* In IGHEM 2008 - International Conference on Hydraulic Efficiency Measurements, Milan, Italy, 2008.

[71] Petley, S. M., Židonis, A., Panagiotopoulos, A., Benzon, D. S., Aggidis, G. A., Anagnostopoulos, J. S., and Papantonis, D. E. (2019). Out With the Old, in With the New: Pelton Hydro Turbine Performance Influence Utilizing Three Different Injector Geometries. *Journal of Fluids Engineering 141*, 081103.

[72] Petley, S. M., *Numerical and Experimental Investigation of Flow in Horizontal Axis Pelton Turbines*; Department of Engineering, Faculty of Science and Technology, Lancaster University: Phd thesis, 2018.

[73] Prechter, H. (1961). Gesichtspunkte zur Auslegung von Diffusoren unter Berücksichtigung neuerer Forschungsergebnisse. *Der Maschinenmarkt (13a), Würzburg–Nr. 182*, 19–26.

[74] Reneau, L. R., Johnston, J. P., and Kline, S. J. (1967). Performance and Design of Straight, Two-Dimensional Diffusers. *Journal of Basic Engineering 89*, 141–150.

[75] Riemann, S., *Untersuchung der instationären Strömung in einer Peltonturbine*; Institut für Energietechnik MW7, Lehrstuhl für Fluidmechanik, Technische Universität München: Phd thesis, 2009.

[76] Roache, P. J. (1997). Quantification of Uncertainty in Computational Fluid Dynamics. *Annual Review of Fluid Mechanics 29*, 123–160.

[77] Rocks, A., *Generalerneuerung Vermuntwerk* In 9. Praktikerkonferenz, Graz, Austria, 2021.

[78] Ruprecht, A., Bauer, C., Göde, E., Janetzky, B., Llosa, P., Maihöfer, M., and Welzel, B., *Strömungseffekte in einem Dreifach-Abzweiger (Trifurkation) - Numerische Analyse und deren Grenzen* In 10. Internationales Seminar Wasserkraft - Energienutzung an der Wende zum 3. Jahrtausend, Laxenburg, Austria, 1998.

[79] Russo, F., and Basse, N. T. (2016). Scaling of turbulence intensity for low-speed flow in smooth pipes. *Flow Measurement and Instrumentation 52*, 101–114.

[80] Sandmaier, L., Meusburger, P., and Benigni, H. (2023). Transient 3D CFD Simulation of a Pelton Turbine - A State-of-the-Art Approach for Pelton Development and Optimisation. *International Journal of Turbomachinery, Propulsion and Power 8*, 10.

[81] Santolin, A., Cavazzini, G., Ardizzon, G., and Pavesi, G. (2009). Numerical investigation of the interaction between jet and bucket in a Pelton turbine. *Proceedings of the Institution of Mechanical Engineers, Part A: Journal of Power and Energy 223*, 721–728.

[82] Schlichting, H., and Gersten, K., *Grenzschicht-Theorie*, 10th ed.; Springer Berlin, Heidelberg: 2006.

[83] Schmandt, B., and Herwig, H. (2011). Diffuser and nozzle design optimization by entropy generation minimization. *Entropy 13*, 1380–1402.

[84] Schmandt, B., and Herwig, H. (2011). Internal Flow Losses: A Fresh Look at Old Concepts. *Journal of Fluids Engineering 133*, 051201.

[85] Schmandt, B., and Herwig, H. (2015). Losses Due to Conduit Components: An Optimization Strategy and Its Application. *Journal of Fluids Engineering 138*, 031204.

[86] Schwarze, R., *CFD-Modellierung: Grundlagen und Anwendungen bei Strömungsprozessen*, 6th ed.; Springer Berlin, Heidelberg: 2013.

[87] Seetharam, H. C., Rodgers, E. J., and Wentz Jr., W. H. Experimental Studies of Flow Separation of the NACA 2412 Airfoil at Low Speeds, NASA-CR-197497, 1977.

[88] Semlitsch, B., *On the Generation of Large-Scale Vortical Flow Structures in Pipe Multifurcations* In 32nd Symposium on Hydraulic Machinery and Systems, Roorkee, India, 2024.

[89] Semlitsch, B. (2024). Effect of inflow disturbances in Pelton turbine distributor lines on the water jet quality. *International Journal of Multiphase Flow 174*, 104786.

[90] Semlitsch, B. (2024). On the Water Jet Quality at Part-Load Operation of Pelton turbines. *Journal of Physics: Conference Series 2752*, 012164.

[91] Shih, T.-H., Liou, W. W., Shabbir, A., Yang, Z., and Zhu, J. (1995). A new k-ε eddy viscosity model for high reynolds number turbulent flows. *Computers & Fluids 24*, 227–238.

[92] Shiraishi, T., Watakabe, H., Sago, H., Konomura, M., Yamaguchi, A., and Fujii, T. (2006). Resistance and fluctuating pressures of a large elbow in high Reynolds numbers. *Journal of Fluids Engineering 128*, 1063–1073.

[93] Sick, M., Schindler, M., Drtina, P., Schärer, C., and Keck, H., *Numerical and experimental analyses of Pelton Turbine Flow Part 1: Distributor and Injector.* In 20th IAHR Symposium on Hydraulic Machinery and Systems, Charlotte, North Carolina, USA, 2000.

[94] Sigloch, H., *Technische Fluidmechanik*, 9th ed.; Springer Vieweg Berlin, Heidelberg: 2014.

[95] Smirnov, P. E., and Menter, F. R. (2009). Sensitization of the SST Turbulence Model to Rotation and Curvature by Applying the Spalart–Shur Correction Term. *Journal of Turbomachinery 131*, 041010.

[96] Sovran, G., and Klomp, E. D. (1967). Experimentally Determined Geometries for Rectilinear Diffusers with Rectangular, Conical, or Annular Cross Section. *Fluid Mechanics of Internal Flow*, 270–307.

[97] Spalart, P., and Shur, M. (1997). On the sensitization of turbulence models to rotation and curvature. *Aerospace Science and Technology 1*, 297–302.

[98] Spalart, P., and Allmaras, S., *A one-equation turbulence model for aerodynamic flows* In 30th Aerospace Sciences Meeting and Exhibition, Reno, Nevada, USA, 1992.

[99] Spura, C., Fleischer, B., Wittel, H., and Dieter, J., *Roloff/Matek Maschinenelemente: Normung, Berechnung, Gestaltung*, 26th ed.; Springer Vieweg Wiesbaden: 2023.

[100] Spurk, J., and Aksel, N., *Strömungslehre: Einführung in die Theorie der Strömungen*, 9th ed.; Springer Vieweg Berlin, Heidelberg: 2019.

[101] Staubli, T., Abgottspon, A., Weibel, P., Bissel, C., Parkinson, E., Leduc, J., and Leboeuf, F., *Jet quality and Pelton efficiency* In *Proceedings of Hydro-2009*, Lyon, France, 2009.

[102] Staubli, T., and Bissel, C. Jet Improvement for Swiss Pelton Plants, 2009.

[103] Staubli, T., Weibel, P., Bissel, C., Karakolcu, A., and Bleiker, U., *Efficiency increase by jet quality improvement and reduction of splashing water in the casing of Pelton turbines* In 16th International Seminar on Hydropower Plants, Laxenburg, Austria, 2010.

[104] Sudo, K., Sumida, M., and Hibara, H. (1998). Experimental investigation on turbulent flow in a circular-sectioned 90-degree bend. *Experiments in Fluids 25*, 42–49.

[105] Sudo, K., Sumida, M., and Yamane, R. (1992). Secondary motion of fully developed oscillatory flow in a curved pipe. *Journal of Fluid Mechanics 237*, 189–208.

[106] Sun, L., Wang, Z., Zhou, H., Wang, Z., and Guo, P. (2024). Numerical assessment of transient flow and energy dissipation in a Pelton turbine during startup. *Physics of Fluids 36*, 094119.

[107] Thévenin, D., and Janiga, G., *Optimization and Computational Fluid Dynamics*, 1st ed.; Springer Berlin, Heidelberg: 2008.

[108] Timischl, W., *Angewandte Statistik: Eine Einführung für Biologen und Mediziner*, 3rd ed.; Springer Vienna: 2013.

[109] TIWAG - Tiroler Wasserkraft AG: Saubere Energie für Tirol - Kraftwerksgruppe Sellrain-Silz. https://www.tiwag.at/uploads/tx_bh/409/tiwag_unsere_kraftwerke_kraftwerksgruppe_sellrain-silz_kw-broschuere-ssi_webansicht_rz.pdf?mod=1643192107 (accessed July 29, 2024).

[110] Unterberger, P., Bauer, C., Gaschl, J., and Mack, R., *Studies on the free jet of Pelton nozzles* In 16th International Seminar on Hydropower Plants, Laxenburg, Austria, 2010.

[111] VDI 4675-2: Bilanzgerechte Mittelung inhomogener Strömungsfelder, Blatt 2: Anwendungen, 2019.

[112] Wallin, S., and Johansson, A. V. (2000). An explicit algebraic Reynolds stress model for incompressible and compressible turbulent flows. *Journal of Fluid Mechanics 403*, 89–132.

[113] Wilcox, D., *Turbulence Modeling for CFD*, 3rd ed.; DCW Industries, Incorporated: 2006.

[114] Yakhot, V., Orszag, S. A., Thangam, S., Gatski, T. B., and Speziale, C. G. (1992). Development of turbulence models for shear flows by a double expansion technique. *Physics of Fluids A: Fluid Dynamics 4*, 1510–1520.

[115] Yilin, Z., Jie, L., Yexiang, X., Quanwei, L., Haijun, L., Qingpin, D., and Zhaoning, W. (2024). Numerical method analysis of the multi-nozzle distributor hydraulic performance for a Pelton turbine. *Journal of Physics: Conference Series 2752*, 012043.

[116] Zeng, C., Xiao, Y., Luo, Y., Zhang, J., Wang, Z., Fan, H., and Ahn, S.-H. (2018). Hydraulic performance prediction of a prototype four-nozzle Pelton turbine by entire flow path simulation. *Renewable Energy 125*, 270–282.

[117] Zhang, Z., and Casey, M. (2007). Experimental studies of the jet of a Pelton turbine. *Proceedings of the Institution of Mechanical Engineers, Part A: Journal of Power and Energy 221*, 1181–1192.

[118] Zhang, Z., *Freistrahlturbinen: Hydromechanik und Auslegung*, 1st ed.; Springer Berlin, Heidelberg: 2009.

[119] Zhou, L., Hang, J., Bai, L., Krzemianowski, Z., El-Emam, M. A., Yasser, E., and Agarwal, R. (2022). Application of entropy production theory for energy losses and other investigation in pumps and turbines: A review. *Applied Energy 318*, 119211.

[120] Zidonis, A., *Optimisation and efficiency improvement of Pelton hydro turbine using Computational Fluid Dynamics and experimental testing*; Department of Engineering, Faculty of Science and Technology, Lancaster University: Phd thesis, 2015.

APPENDIX A

Statistical definitions

This chapter summarises the statistical terms and definitions used in this dissertation in compact form from the relevant standard literature.

A.1 Basic definitions

All definitions and explanations in this section are taken from Kirkup et al. [45]:

A.1.1 Mean

The mean value[1] $\bar{x}$ of n measurements of a quantity x is defined as

$$\bar{x} = \frac{1}{n}\sum_{i=1}^{n} x_i \,. \tag{A.1}$$

A.1.2 Standard deviation

The standard deviation (of the population) $u(x)$ is defined as

$$u(x) = \sqrt{\frac{\sum_{i=1}^{n}(x_i - \bar{x})^2}{n-1}} \,, \tag{A.2}$$

and can be interpreted as a measure of the spread of values. Kirkup et al. [45] propose *root-mean-square* or *rms residual* as alternative names[2] for $u(x)$. According to Kirkup et al. [45], in certain subjects, e.g. meteorology, the standard deviation is interpreted as a measure of the uncertainty of a quantity. Following the idea of uncertainty and in agreement with Appendix A.3, within this thesis, the standard deviation shall be treated and understood as an uncertainty in the sense of Kirkup et al. [45].

[1]The mean value is also referred to as arithmetic average.
[2]Consequently, in the context of CFD results, the symbol u_{RMS} is used when talking about root-mean-square values.

A.2 Regression analysis

The definitions and explanations of this section are summarised from Brauch et al. [9].

A.2.1 Linear regression

Given a set of data points $P_i(x_i, y_i)$, we assume these points do not fulfil the linear function

$$y = a_0 + a_1 x \tag{A.3}$$

exactly. The differences $e_i = a_0 + a_1 x_i - y_i$ are called errors. The coefficients a_0 and a_1 shall be calculated such that the sum of squares of the errors

$$f(a_0, a_1) = \sum_{i=1}^{n} e_i^2 = \sum_{i=1}^{n} (a_0 + a_1 x_i - y_i)^2 = \text{Minimum} \tag{A.4}$$

becomes a minimum (= method of least squares estimation). Therefore, the partial derivatives of f must vanish

$$\frac{\partial f(a_0, a_1)}{\partial a_j} = 2 \sum_{i=1}^{n} (a_0 + a_1 x_i - y_i) x_i^j = 0\,. \tag{A.5}$$

This gives the normal equations

$$n a_0 + a_1 \sum x_i - \sum y_i = 0 \tag{A.6}$$

$$a_0 \sum x_i + a_1 \sum x_i^2 - \sum x_i y_i = 0 \tag{A.7}$$

with the solution

$$a_0 = \frac{\sum x_i^2 \sum y_i - \sum x_i \sum x_i y_i}{n \sum x_i^2 - \left(\sum x_i\right)^2} \quad \text{and} \quad a_1 = \frac{n \sum x_i y_i \sum y_i - \sum x_i \sum y_i}{n \sum x_i^2 - \left(\sum x_i\right)^2} \tag{A.8}$$

A.2.2 Non-linear regression

In case of an exponential regression function $v = Ae^{ku}$, the natural logarithm needs to be taken, such that the resulting linear function $\ln(v) = \ln(A) + ku$ can be substituted according to $y = \ln(v)$ and $x = u$ with the coefficients $a_0 = \ln(A)$ and $a_1 = k$. Then, the procedure of Appendix A.2.1 can be employed accordingly.

A.2.3 Coefficient of determination

The coefficient of determination [108] is defined as

$$R^2 = 1 - \frac{\sum_{i=1}^{n} e_i^2}{\sum_{i=1}^{n} (y_i - \bar{y})^2} \tag{A.9}$$

and can be interpreted as an indication of how well the regression function fits the data set.

A.3 Expanded uncertainty

The combined standard uncertainty u_R of a result $R = f(X_i)$ depending on its parameters X_i, which are assumed to be mutually uncorrelated, is defined following [4, 15] as

$$u_R = \sqrt{\sum_{i=1}^{I} \left[\frac{\partial R(X_i)}{\partial X_i}\right]^2 \cdot u^2\left(X_i\right)} = \sqrt{\sum_{i=1}^{I} \left[c_i \cdot u\left(X_i\right)\right]^2}\,, \tag{A.10}$$

where $c_i \coloneqq \partial R(X_i)/\partial X_i$ is the sensitivity coefficient and $u(X_i)$ the (measurement) uncertainty of a parameter X_i. The expanded uncertainty in the result at approximately 95 % confidence is given by $U_{R,95} = 2u_R$. Thus, with 95 % confidence, the true result should lie in the interval $R \pm U_{R,95}$ [4].

A.3.1 Expanded uncertainty for the velocity ratio

The combined standard uncertainty $u_R(c/c_{s,ref})$ of the normalised velocity $c/c_{s,ref}$ is computed as

$$u_R\left(\frac{c}{c_{s,ref}}\right) = \sqrt{\left[\frac{\partial\left(\frac{c}{c_{s,ref}}\right)}{\partial c}\right]^2 \cdot u^2(c) + \left[\frac{\partial\left(\frac{c}{c_{s,ref}}\right)}{\partial c_{s,ref}}\right]^2 \cdot u^2(c_{s,ref})}\,. \tag{A.11}$$

Inserting the sensitivity coefficients

$$\frac{\partial\left(\frac{c}{c_{s,ref}}\right)}{\partial c} = \frac{1}{c_{s,ref}} \quad \text{and} \quad \frac{\partial\left(\frac{c}{c_{s,ref}}\right)}{\partial c_{s,ref}} = -\frac{c}{c_{s,ref}^2} \tag{A.12}$$

into Equation (A.11) the expanded uncertainty finally becomes

$$U_{R,95}\left(\frac{c}{c_{s,ref}}\right) = \frac{2}{c_{s,ref}} \cdot \sqrt{u^2(c) + \left(\frac{c}{c_{s,ref}}\right)^2 \cdot u^2(c_{s,ref})}\,. \tag{A.13}$$

A.3.2 Expanded uncertainty for the turbulence intensity

The combined standard uncertainty $u_R(I_t)$ of the turbulence intensity I_t is computed as

$$u_R(I_t) = \sqrt{\left(\frac{\partial I_t}{\partial k_a}\right)^2 \cdot u^2(k_a)}\,. \tag{A.14}$$

With

$$\frac{\partial I_t}{\partial k_a} = \frac{1}{3} \cdot \left(\frac{2k_a}{3}\right)^{-1/2}\,, \tag{A.15}$$

Equation (A.14) becomes

$$u_R(I_t) = \frac{1}{3} \cdot \sqrt{\frac{3}{2k_a}} \cdot u(k_a) = \frac{u(k_a)}{3\sqrt{I_t}}\,, \tag{A.16}$$

and the expanded uncertainty evaluates to

$$U_{R,95}(I_t) = \frac{2u(k_a)}{3\sqrt{I_t}} \,. \tag{A.17}$$

Table A.1 lists the calculated minimum, maximum and mean relative values of the expanded uncertainties for the normalised velocity $U_{R,95}\left(\frac{c}{c_{s,ref}}\right)$ and the turbulence intensity $U_{R,95}\,(I_t)$.

%	min	max	mean
$U_{R,95}\,(c/c_{s,ref})$	3.07	3.08	3.08
$U_{R,95}\,(I_t)$	11.9	14.0	12.8

Table A.1: Minimum, maximum and mean value of the expanded uncertainties for the normalised velocity and the turbulence intensity. Values calculated from measurement errors given by Sudo et al. [104].

A.3.3 Expanded uncertainty for CFD results

In CFD simulations, it is of general interest to assess the errors[3] made by, e.g. spatial and temporal discretisation, turbulence modelling, multiphase modelling, wall resolution, use of symmetries, and other modelling choices. Combining these individually computed errors is required to achieve an overall error (= expanded uncertainty) of the simulation [5, 72, 120] when following the concept of expanded measurement uncertainties. If we assume that the overall error of a CFD simulation is some appropriate sum of the individual errors induced by the modelling choices made by the user, we can deduce from Kirkup et al. [45]) that the uncertainty coefficients c_i become one for all i and Equation (A.10) simplifies to

$$U_{RSS} := u_R(c_{i=1,\ldots I} = 1) = \sqrt{\sum_{i=1}^{I} u^2\,(X_i)}\,, \tag{A.18}$$

where U_{RSS} is known as the root-sum-square of the individual errors. This root-sum-square can be geometrically interpreted as the radius of the hull of a volume in an I-dimensional space with the CFD result as the centre point and the hull's volume as the uncertainty space where the actual value of the result could be located anywhere within this volume. The root-mean-square of the individual uncertainties is achieved by

$$U_{RMS} := \sqrt{\frac{\sum_{i=1}^{I} u^2\,(X_i)}{I-1}}\,, \tag{A.19}$$

and, in this context, indicates some mean value of the individual errors.

[3]When discussing CFD, using the word 'error' seems more common than the use of 'uncertainty'. However, when mathematically analysing errors/uncertainties, this specific choice of words does not make a difference.

APPENDIX B

Scripts

B.1 Script for creating secondary flow variables in CFD-Post

The code snippet in Listing B.1 displays a minimum working example of an algorithm to compute secondary velocities introduced in Section 3.4 in the post-processing utility CFD-Post. The code was tested with CFD-Post 19.2 and CFD-Post 2022 R1. This snippet was also published in a prior publication of mine, [30].

Listing B.1: Minimal working example for secondary flow variables in CFD-Post

```
# Definition of Perl variables
! @Coordinates = ('X','Y','Z');
! @VelocityComponents = ('u','v','w');

# Create expressions
LIBRARY:
  CEL:
    EXPRESSIONS:
      Velocity projected to surf normal = Velocity u * Normal X +
        ↪ Velocity v * Normal Y +Velocity w * Normal Z

      # Loop through every member of @Coordinates
      ! for ($i=0; $i<@Coordinates; $i++) {
          Primary Flow Velocity $Coordinates[$i] = Velocity projected
            ↪  to surf normal* Normal $Coordinates[$i]
          Secondary Flow Velocity $Coordinates[$i] = Velocity
            ↪ $VelocityComponents[$i] - Primary Flow Velocity
            ↪ $Coordinates[$i]
      !}
    END
  END
END
```

```
# Create user vector variables
USER VECTOR VARIABLE: V Primary Flow Velocity
  Boundary Values = Conservative
  Calculate Global Range = On
  Recipe = Expression
  Variable to Copy = Pressure
  Variable to Gradient = Pressure
  X Expression = Primary Flow Velocity X
  Y Expression = Primary Flow Velocity Y
  Z Expression = Primary Flow Velocity Z
END
USER VECTOR VARIABLE: V Secondary Flow Velocity
  Boundary Values = Conservative
  Calculate Global Range = On
  Recipe = Expression
  Variable to Copy = Pressure
  Variable to Gradient = Pressure
  X Expression = Secondary Flow Velocity X
  Y Expression = Secondary Flow Velocity Y
  Z Expression = Secondary Flow Velocity Z
END
# End of script
```

APPENDIX C

Additional data of Chapter 5

C.1 Data of Section 5.1

C.1.1 Overview of cases and numerical settings - A

The flow in the 90° pipe bend is assumed steady, incompressible, and isothermal. The density and dynamic viscosity of the working fluid were set to $\rho = 997\,\mathrm{kg/m^3}$ and $\mu = 8.899 \cdot 10^{-4}\,\mathrm{Pa\,s}$. This data corresponds to the physical properties of water at 25 °C. A bulk velocity corresponding to a Reynolds number of $6.0 \cdot 10^4$ was specified at the outlet. A total pressure condition with the relative pressure set to 0 Pa was defined at the inlet. A turbulence intensity of $I_t = 5\,\%$ and a turbulent length scale corresponding to the pipe diameter were set as turbulence boundary conditions at the inlet. A no-slip boundary condition was employed at all walls. They were set to be hydraulically smooth. The advection terms were solved using the high-resolution scheme, a second-order scheme that automatically blends to a first-order formulation if stability issues arise [3]. The advection of turbulence was discretised by a first-order upwind scheme. These settings were kept the same for all cases within Section 5.1.

Four meshes were tested to understand the impact of different meshing approaches on the quantities of interest. Three were made up entirely of hexahedral cells (indi-

ID	Name	$N_m/*)$	Type	$h/h_{MediumH}$	a)	b)
1	Coarse H	0.49	H	1.27	$8.0 \cdot 10^{-6}$	0.49
2	Medium H	1.00	H	1.00	$4.0 \cdot 10^{-8}$	1.00
3	Medium rM	1.19	M	0.94	$7.0 \cdot 10^{-8}$	1.16
4	Fine H	2.54	H	0.73	$6.0 \cdot 10^{-8}$	2.68

Table C.1: Cases of the mesh study. a) - RMS Residuals of the momentum equation after 1000 iterations. b) - Relative compute time. $*) = N_{m,MediumH}$

ID	Name	a)	y^+_{ave}	y^+_{max}	b)	c)
1	kE $y^+ = 77$	kE	77	117	$1.0{\cdot}10^{-10}$	0.31
2	SST $y^+ = 1$	SST	0.22	0.43	$4.0 \cdot 10^{-8}$	1.00
3	SST CC	SSTCC	0.22	0.43	$5.3 \cdot 10^{-8}$	1.05
4	EARSM	EARSM	0.22	0.43	$3.8 \cdot 10^{-8}$	1.21

Table C.2: Cases of the turbulence model study. a) - Turbulence model (abbreviation). b) - RMS Residuals of the momentum equation after 1000 iterations. c) - Relative compute time.

cated by a trailing H), sizing from coarse to fine. One was made of a combination of hexahedral elements in the straight pipe sections and refined tetrahedral elements in the bend (indicated by the letters rM). All cases for which the meshes were varied were run with the k-ω Shear Stress Transport (SST) turbulence model. Table C.1 summarises the mesh data and the computational effort of these cases.

Four different turbulence closures were employed to test the sensitivity of the local and integral flow variables on the turbulence model: the k-ε model (kE) of Launder and Spalding [53] with the scalable wall function approach [3]; the k-ω Shear Stress Transport model of Menter [61] with automatic wall treatment for ω-based models [3]; further, the SST model activated curvature correction (SSTCC) and the Baseline-Explicit Algebraic Reynolds Stress model (EARSM) of Menter, Garbaruk and Egorov [62]. Unless explicitly stated otherwise, all cases for which the turbulence models were varied were run with mesh Medium H and a maximum value of $y^+ < 1$. For case 1 with the kE turbulence model, the wall resolution was adjusted for the use of wall functions. A summary of the cases is listed in Table C.2.

C.1.2 Estimation of discretisation error - A

The Grid Convergence Method[1] introduced by Celik et al. [11] was employed to assess the uncertainty of the presented results due to spatial discretisation. The grid study used the hexahedral element meshes: Coarse H, Medium H, and Fine H. The pressure coefficient C_p, the intensity of secondary flow I_s, the turbulence intensity I_t, as well as the local flow velocities c_s and c_θ were selected as quantities of interest.

In Figure C.1, the longitudinal distributions of C_p, I_s and I_t, as well as their respective extrapolated values, are plotted against the normalised streamwise coordinate. The discretisation error is also shown as error bars to the extrapolated curves. The variation between the results from the three meshes is almost negligible for the pressure coefficients and the intensity of secondary flow.
Accordingly, the maximum values for the grid convergence indices are less or around 2 % and the corresponding mean values are less than 0.5 % (Table C.3). The low level of dependencies of C_p and I_s on the mesh size is confirmed by the high values of the apparent order p_{oa}. Oscillatory convergence occurs at 14 % to 42 % of the

[1] The general procedure of this method is explained in Section 4.4.

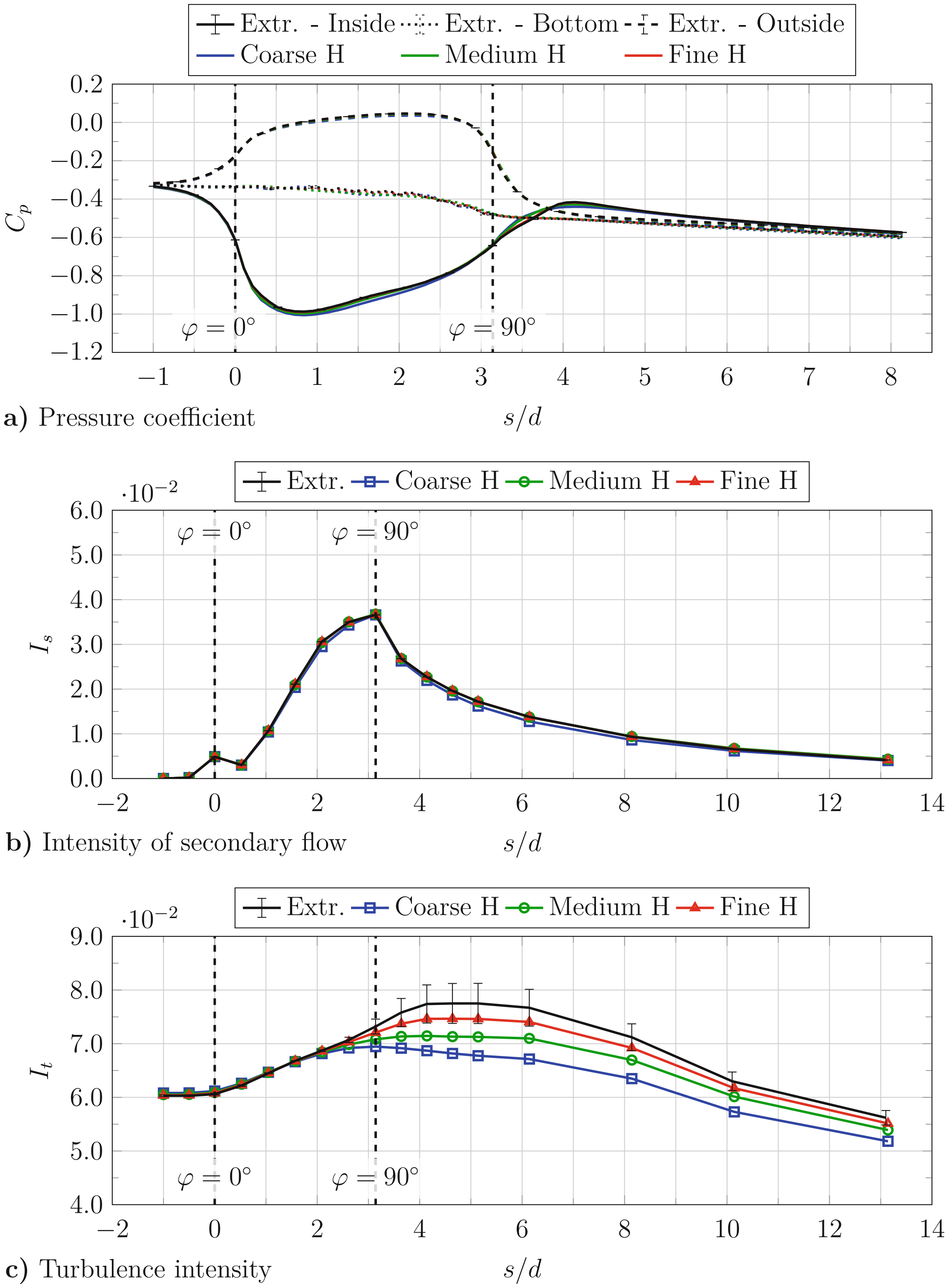

Figure C.1: Longitudinal distributions of C_p, I_s and I_t including the extrapolated curves (Extr.) and the discretisation errors.

points for C_p and almost 50 % of the points for I_s. The turbulence intensity reacts more sensitively to a change in the mesh size. The results for I_t start to vary at

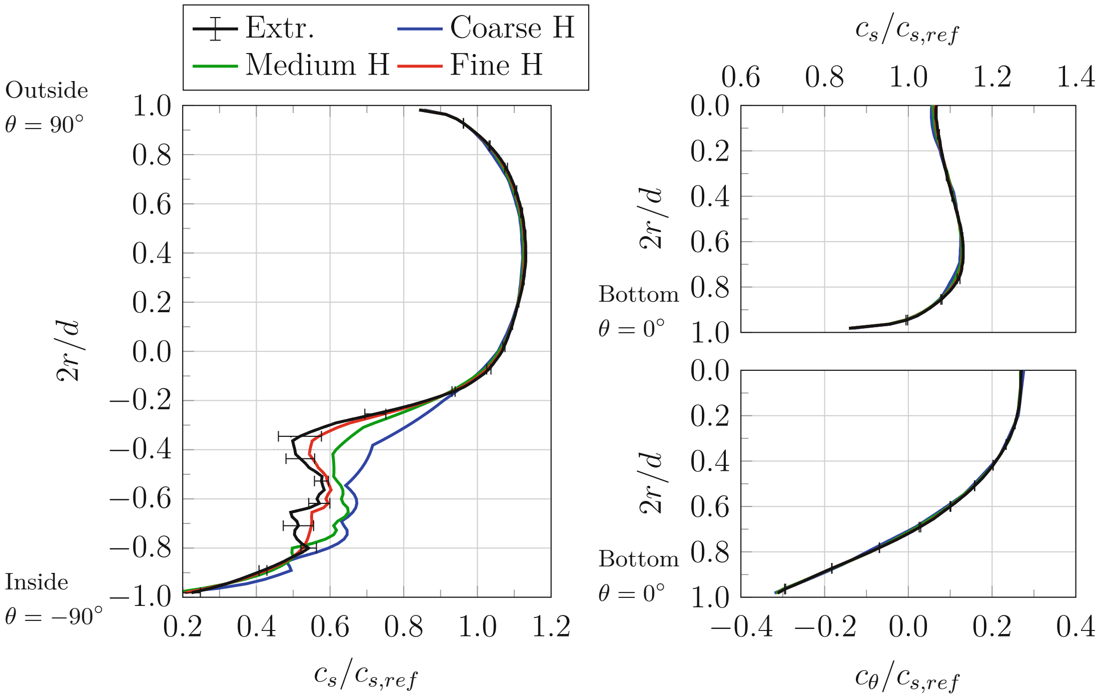

Figure C.2: Velocity profiles including the extrapolated curves (Extr.) and the discretisation errors at station $\varphi = 90°$.

about $s/d \sim 2$, which is close to station $\varphi = 60°$, where, in the velocity plots, e.g. Figures 5.5 and 5.6, the flow shows tendencies to separate from the inside wall of the bend. This higher variance results in an average grid convergence index of 2 %, with a maximum of just under 5 %. Similarly, the apparent order of 2.5 is much less than those of C_p and I_s. Oscillatory convergence does not occur for I_t.

The effect of a change of the mesh size on the local flow velocities was studied for three stations: $\varphi = 60°$ because there, the flow starts to separate; $\varphi = 90°$ because the velocity deficit is most prominent at this station; and $z/d = 1.0$, because in the *AxFeeder* application the injector will be placed approximately one diameter downstream the last bend. The velocity profiles for the three meshes and the extrapolated profiles together with the discretisation errors are exemplarily depicted at station $\varphi = 90°$ in Figure C.2, the resulting uncertainties for all three stations are summarised in Table C.3. While for most of the domain, the profiles overlap almost perfectly, close to the inside wall of the bend, between $-0.8 < r/d < -0.2$, the correct prediction of the velocity deficit poses an inherent challenge to the simulation model. Thus, the curves of the streamwise velocity in the horizontal plane vary significantly in this area. Not unexpectedly, the mean values of the grid convergence index are up to 3 %, and the maxima are well over 10 %. The mean order of accuracy lies between 3 and 7, and oscillatory convergence occurs at about a quarter of the data points.

Station	Location	Quantity	a)	b)	$p_{oa,mean}$	R_{oc} (%)
Streamlines along the wall	Inside Sl.*	C_p	1.34	0.22	5.21	20.9
	Bottom Sl.		2.18	0.42	4.05	41.8
	Outside Sl.		0.58	0.14	4.49	14.3
All stations between $-1 \leqslant s/d \leqslant 13$		I_s	0.71	0.14	7.63	47.1
		I_t	4.83	2.04	2.48	0.0
$\varphi = 60°$	horz. plane	$c_s/c_{s,ref}$	4.43	0.32	4.59	16.5
	vert. plane	$c_s/c_{s,ref}$	0.06	0.01	6.96	41.3
	vert. plane	$c_\theta/c_{s,ref}$	3.52	0.32	5.86	35.8
$\varphi = 90°$	horz. plane	$c_s/c_{s,ref}$	13.06	2.45	3.22	11.9
	vert. plane	$c_s/c_{s,ref}$	0.33	0.13	3.49	29.4
	vert. plane	$c_\theta/c_{s,ref}$	18.38	1.32	5.08	43.1
$z/d = 1.0$	horz. plane	$c_s/c_{s,ref}$	9.41	1.93	4.36	1.8
	vert. plane	$c_s/c_{s,ref}$	2.09	0.54	4.45	29.4
	vert. plane	$c_\theta/c_{s,ref}$	11.38	2.87	5.04	29.4

Table C.3: Maximum and mean values of the grid convergence indices, a) - $GCI^{21}_{fine,max}$ (%), b) - $GCI^{21}_{fine,mean}$ (%), mean value of the apparent order p_{oa} of the numerical method and ratio of data points with oscillatory convergence R_{oc} for several quantities. Sl.* = Streamline.

C.1.3 Secondary velocity ratio - A

The grid convergence indices GCI^{21}_{fine} for the secondary velocity ratio ϕ_{II} are almost zero at all stations except for those affected by the distorted velocity profiles at the inside of the bend. The distortion zone starts to take effect on the local grid convergence approximately between stations $\varphi = 90°$ and $z/d = 1$, resulting in a maximum fine-grid convergence index of over 7 %. At these locations, the apparent order p_{oa} of the method is close to or even below one, indicating difficult conditions to achieve grid convergence. At all other stations, p_{oa} is greater than two. At the stations upstream of the bend, the solutions from the three grids are almost equal. Hence, their difference is close to zero, such that the procedure of Celik et al. [11], summarised in Section 4.4, does not work in its strict sense but instead indicates that either oscillatory convergence occurs or the exact solution is already obtained.

The following tables, Tables C.4 and C.5, list the computed values for the secondary velocity ratio ϕ_{II}, the respective mean values $\bar{\phi}_{II}$, the uncertainties $u(\phi_{II})$ and the normalised uncertainties $u(\phi_{II})/\bar{\phi}_{II}$ for four meshes and four turbulence models. The cases with the different meshes were all run with the SST $y^+ = 1$ turbulence model, and the cases with the various turbulence models were run with mesh Medium H, whereby for the kE model case, the boundary layer resolution was adjusted. For the cases with different meshes, only the magnitudes of the secondary

Case	$\varphi = 90°$	$z/d = 1$	$z/d = 5$
Coarse H	17.05	12.26	8.61
Medium H	17.01	12.27	9.08
Fine H	16.94	12.19	9.08
Medium rM	16.76	12.16	8.36
$\bar{\phi}_{II}$	16.94	12.22	8.78
$u(\phi_{II})$	0.13	0.05	0.36
$u(\phi_{II})/\bar{\phi}_{II}$	0.75	0.44	4.11

Table C.4: Secondary velocity ratio ϕ_{II} in % for four meshes evaluated at three stations.

Case	$\varphi = 90°$	$z/d = 1$	$z/d = 5$
kE $y^+ = 77$	16.33	12.04	6.45
SST $y^+ = 1$	17.01	12.27	9.08
SSTCC	16.74	12.05	9.44
EARSM	15.64	10.97	7.33
$\bar{\phi}_{II}$	16.43	11.83	8.08
$u(\phi_{II})$	0.60	0.59	1.42
$u(\phi_{II})/\bar{\phi}_{II}$	3.64	4.96	17.62

Table C.5: Secondary velocity ratio ϕ_{II} in % for four turbulence models at three different stations.

velocities vary to a minor extent. Thus, the relative uncertainties $u(\phi_{II})/\bar{\phi}_{II}$ of the investigated cases are very low as well. Changing the turbulence model and the wall layer resolution has a much more significant effect on the secondary velocity ratios downstream of the bend. The uncertainties from the turbulence model cases are about an order of magnitude higher than those of the cases with different meshes. A comparison against the secondary velocity ratios computed for the 90° pipe bend of Shiraishi et al. [92] is presented in Section 5.3.

C.2 Data of Section 5.2

C.2.1 Overview of cases and numerical settings - B

The measurements of Shiraishi et al. [92] have shown flow separations at the inside wall of the bend, causing unsteady fluctuations in the pressure signals. This behaviour indicates the need for unsteady, possibly scale-resolving flow simulations. However, for the parametric study of the *AxFeeder*, presented in Section 6.4, the emphasis lies on using a reliable and efficient numerical setup. Hence, unsteady simulations are ruled out as being too costly. Consequently, the computations of

ID	Name	$N_m/*)$	Type	$h/h_{MediumH}$	a)	b)
1	Coarse H	0.46	H	1.30	$6.6 \cdot 10^{-6}$	0.45
2	Medium H kE	0.55	H	1.22	$1.0 \cdot 10^{-12}$	0.13
3	Medium H	1.00	H	1.00	$2.0 \cdot 10^{-6}$	1.00
4	Fine H	1.83	H	0.82	$8.0 \cdot 10^{-5}$	1.86
5	Fine rM	2.48	M	0.74	$2.2 \cdot 10^{-6}$	2.32

Table C.6: Cases for the mesh study. a) - RMS Residuals of the momentum equation after 1000 iterations. b) - Relative compute time. For case 2, convergence was achieved after 239 iterations. $*) = N_{m,MediumH}$

Section 5.2 were executed using steady-state RANS simulations to test the accuracy and applicability of the RANS approach for the flow in a sharply turning bend.

Like in Appendix C.1.1, the flow was further assumed incompressible and isothermal. The density and dynamic viscosity of the working fluid (water at 25 °C) were set to $\rho = 997\,\mathrm{kg/m^3}$ and $\mu = 8.899 \cdot 10^{-4}\,\mathrm{Pa\,s}$. A total pressure condition with the relative pressure set to 0 Pa was defined at the inlet. A turbulence intensity of $I_t = 5\,\%$ and a turbulent length scale corresponding to the pipe diameter were set as turbulence boundary conditions at the inlet. A no-slip boundary condition was employed at all walls, and all walls were set to be hydraulically smooth[2]. At the outlet, a bulk velocity perpendicular to the boundary region was specified to achieve the desired Reynolds number for the case. All solver settings were the same as in Appendix C.1.1.

Based on the experiences in Section 5.1, five different meshes were employed to analyse the sensitivity of the predicted losses and velocity profiles on the mesh sizes. Four meshes with different average cell sizes were made entirely from hexahedral elements (Coarse H, Medium H kE, Medium H and Fine H). In one mesh (Fine rM), the bend is discretised by tetrahedrons, and only the upstream and downstream tangents are built from hexahedrons. For all meshes except for Medium H kE, the boundary layer was fully resolved, such that the wall-adjacent node lay in the viscous sublayer region of the boundary layer. For the case with mesh Medium H kE, the grid resolution is such that the wall-adjacent mesh node lies within the log-law region of the boundary layer. All cases for which the meshes were varied were run with the k-ω Shear Stress Transport (SST) turbulence model. Table C.6 gives an overview of the mesh data and the computational effort of these cases.

The same four turbulence models as in Section 5.1 were tested to determine the sensitivity of the flow variables on the turbulence model. All of theses cases were run with mesh Fine H and a maximum value of $y^+ \sim 1$, except for the case with the k-ε model. In this case, mesh medium H kE was used, and the area average of y^+ was about 153. An overview of the resulting cases is depicted in Table C.7.

[2]This agrees with the information provided by Shiraishi et al. [92] because the simulations are compared to experimental data acquired under hydraulically smooth pipe conditions.

ID	Name	a)	y^+_{ave}	y^+_{max}	b)	c)
1	kE $y^+ = 153$	kE	153	232	$1.0 \cdot 10^{-12}$	0.07
2	SST $y^+ = 1$	SST	0.67	1.18	$8.0 \cdot 10^{-5}$	1.00
3	SST CC	SSTCC	0.67	1.18	$7.6 \cdot 10^{-5}$	1.03
4	EARSM	EARSM	0.67	1.20	$2.0 \cdot 10^{-6}$	1.18

Table C.7: Cases for the turbulence model study. a) - Turbulence model (abbreviation). b) - RMS Residuals of the momentum equation after 1000 iterations. c) - Relative compute time. For case 1, convergence was achieved after 239 iterations.

C.2.2 Estimation of discretisation error - B

As in Appendix C.1.2, a grid study was conducted with meshes Coarse H, Medium H and Fine H, for all loss coefficients, the streamwise velocity distributions and the secondary velocity ratios at three stations downstream of the bend.

Most investigated quantities show excellent convergence towards their fine-grid solutions. For the total pressure loss coefficients and the power loss coefficients, the grid convergence index is significantly less than 0.5 % for all Reynolds numbers, and the apparent order of the numerical method is well above 6 for all tested cases. The numerical uncertainty of the dissipation power coefficient is observably higher but still less than 5 % for all Reynolds numbers, and the apparent order is at least 3.5 for the worst case, but over 5 for all the other cases.

The grid convergence of the streamwise velocity was evaluated at stations II, III and IV, downstream of the bend, for all four Reynolds numbers. The mean values of the grid convergence index are in the order of 1 % for all cases, and the apparent order consequently is very high, the minimum of p_{oa} being over 7. Most cases show a significant amount of oscillatory convergence, with R_{oc} ranging from 10 % to 80 %. These quantitative observations are underlined by the plots of Figure C.3, where the solutions for the three grids and the extrapolated velocity curves are depicted. The solution of mesh Coarse H falls off, but the curves for meshes Medium H, Fine H and the extrapolated curve are very close. Therefore, the high local maxima of GCI^{21}_{fine} shown in Table C.9 at stations II and II for $\mathrm{Re} = 3.2 \cdot 10^5$ are local effects that do not deteriorate the numerical predictions overall.

The secondary velocity ratio ϕ_{II} converges well towards the fine grid solution. The exceptions are the high Reynolds number cases ($\mathrm{Re} = 2.8 \cdot 10^6$ and $3.7 \cdot 10^6$) at station $z/d = 1$. The separation in the bend affects the flow the most at this location. Thus, the high errors of the method and the apparent order at $\mathrm{Re} = 2.8 \cdot 10^6$ below one indicate divergence. The steady-state modelling approach reaches its limits in such situations, and unsteady or scale-resolving CFD methods are expected to perform better. However, the achieved contours for the secondary flows downstream of the bend in Figure 5.19 appear trustworthy. Therefore, the chosen grid resolution was sufficient to capture the effects discussed in Section 5.2.

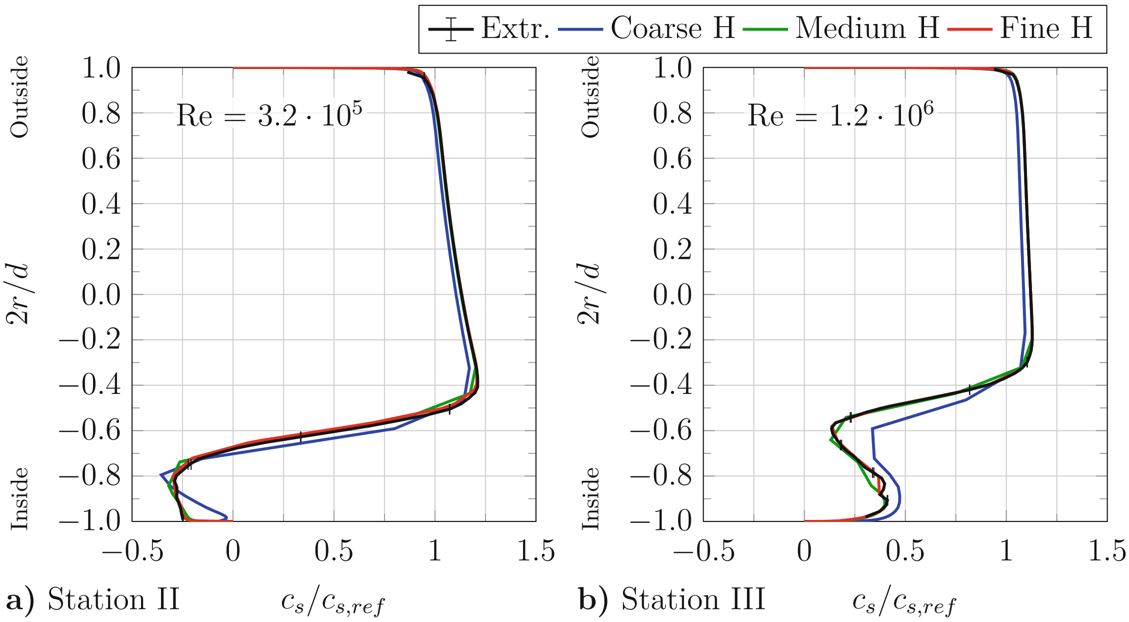

Figure C.3: Velocity profiles including the extrapolated curves (Extr.) and the discretisation errors at stations II and III.

Detailed results of the grid study are listed in Table C.8 for the loss coefficients, in Table C.9 for the streamwise velocity and in Table C.10 for the secondary velocity ratio.

Quantity	Re	GCI^{21}_{fine} (%)	p_{oa}	R_{oc}
$\zeta_{p,ts}\|^{L}_{inlet}$	$3.2 \cdot 10^5$	0.00	16.46	0
	$1.2 \cdot 10^6$	0.01	12.36	1
	$2.8 \cdot 10^6$	0.04	8.67	1
	$3.7 \cdot 10^6$	0.05	7.99	1
$\zeta_{PmTE}\|^{L}_{A}$	$3.2 \cdot 10^5$	0.31	6.77	0
	$1.2 \cdot 10^6$	0.06	11.86	1
	$2.8 \cdot 10^6$	0.10	10.59	1
	$3.7 \cdot 10^6$	0.12	10.06	1
$\zeta_{\Phi}\|^{L}_{A}$	$3.2 \cdot 10^5$	4.40	3.57	0
	$1.2 \cdot 10^6$	2.10	5.41	0
	$2.8 \cdot 10^6$	1.56	5.69	0
	$3.7 \cdot 10^6$	1.89	5.26	0

Table C.8: Grid convergence index GCI^{21}_{fine} (%), apparent order p_{oa} of the numerical method and indicator of oscillatory convergence R_{oc} for the different formulations of loss coefficients.

Station	Re	a)	b)	p_{oa}	R_{oc}
II	$3.2 \cdot 10^5$	36.39	1.17	7.14	9.8
	$1.2 \cdot 10^6$	3.32	0.16	12.90	25.6
	$2.8 \cdot 10^6$	2.22	0.17	14.67	35.4
	$3.7 \cdot 10^6$	5.79	0.33	12.07	30.5
III	$3.2 \cdot 10^5$	13.15	1.12	7.26	19.5
	$1.2 \cdot 10^6$	1.94	0.25	12.50	39.0
	$2.8 \cdot 10^6$	1.09	0.13	14.83	63.4
	$3.7 \cdot 10^6$	1.61	0.20	11.69	41.5
IV	$3.2 \cdot 10^5$	1.85	0.28	8.61	32.9
	$1.2 \cdot 10^6$	0.90	0.19	10.15	76.8
	$2.8 \cdot 10^6$	1.29	0.17	9.43	80.5
	$3.7 \cdot 10^6$	1.06	0.14	10.09	78.0

Table C.9: Maximum and mean values of the grid convergence indices, a) - $GCI^{21}_{fine,max}$ (%), b) - $GCI^{21}_{fine,mean}$ (%), mean value of the apparent order p_{oa} of the numerical method and ratio of data points with oscillatory convergence R_{oc} for the normalised streamwise velocity $c_s/c_{s,ref}$ at stations II, III and IV.

Station	Re	GCI^{21}_{fine} (%)	p_{oa}	R_{oc}
$z/d = 0$	$3.2 \cdot 10^5$	0.18	7.26	0
	$1.2 \cdot 10^6$	0.04	12.17	0
	$2.8 \cdot 10^6$	0.00	19.40	0
	$3.7 \cdot 10^6$	0.01	14.82	0
$z/d = 1$	$3.2 \cdot 10^5$	0.87	6.69	0
	$1.2 \cdot 10^6$	0.28	11.78	1
	$2.8 \cdot 10^6$	35.27	0.34	1
	$3.7 \cdot 10^6$	9.76	1.10	1
$z/d = 5$	$3.2 \cdot 10^5$	0.68	9.41	0
	$1.2 \cdot 10^6$	1.82	6.45	1
	$2.8 \cdot 10^6$	0.18	12.11	1
	$3.7 \cdot 10^6$	0.32	13.90	1

Table C.10: Grid convergence index GCI^{21}_{fine} (%), apparent order p_{oa} of the method and indicator of oscillatory convergence R_{oc} for the secondary velocity ratio ϕ_{II} at stations $z/d = 0$, $z/d = 1$, and $z/d = 5$.

C.2.3 Further velocity profiles

The velocity plots of Figure C.4 underline that all meshes except Coarse H, including mesh Fine rM with the mixed element type approach, can qualitatively replicate the measured velocity distributions. There are minor discrepancies at the inner wall of the bend at stations II and II for all Reynolds numbers due to the flow separation zone and the resulting velocity deficit. However, this deficit occurs to a similar extent in all three cases, Medium H, Fine H, and Fine rM.

In Figure C.5, the streamwise velocity distribution for the four Reynolds numbers in stations II and III is shown for the case with mesh Fine H and the SST turbulence

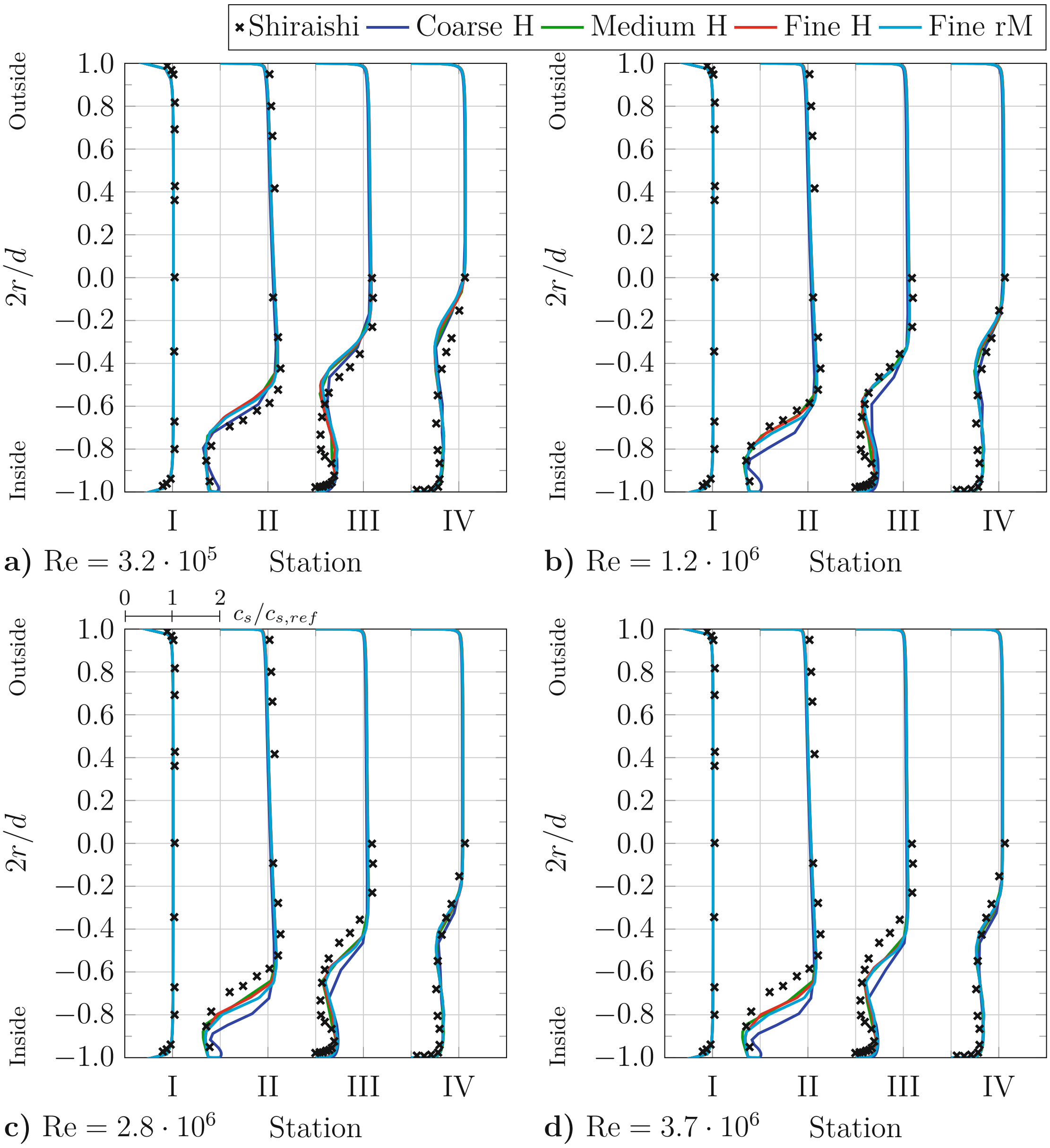

Figure C.4: Streamwise velocity distribution at four stations for four Reynolds numbers using different meshes.

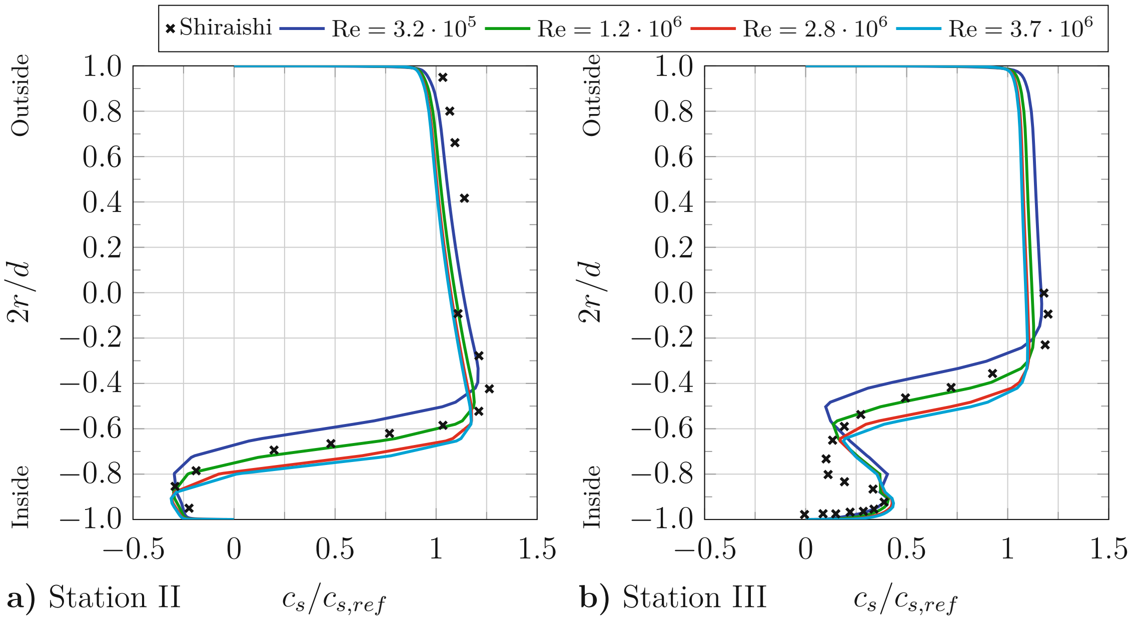

Figure C.5: Influence of the Reynolds number on the streamwise velocity distribution for a case with mesh Fine H and the SST turbulence model.

model. Shiraishi et al. [92] pointed out that, in the postcritical regime, the flow pattern in the bend was independent of the Reynolds number[92]. This Reynolds independence comes from the fact that the velocity profiles are determined mainly by the extent of the separation zone, which, as Idelchik [38] discussed, for flows in the postcritical regime does not change its size significantly. Thus, the separation zone and the flow pattern become independent of the Reynolds number. Therefore, in this thesis, the experimental velocity profiles shown in Figures 5.17, C.4 and C.5 are identical for all four Reynolds numbers[3]. The CFD results do not exhibit such independence for all Reynolds numbers. However, with increasing Reynolds number, the profiles become more and more alike, and especially for $\mathrm{Re} = 2.8 \cdot 10^6$ and $\mathrm{Re} = 3.7 \cdot 10^6$, they look almost identical.

C.2.4 Secondary velocity ratio - B

As in Appendix C.1.3, the secondary velocity ratio ϕ_{II} is evaluated at three stations downstream the bend, namely $\varphi = 90°$, $z/d = 1$ and $z/d = 5$. The computed values for the secondary velocity ratio at these stations are listed in Table C.11 for the cases with different meshes and in Table C.12 for the cases with different turbulence models, each for all of the four Reynolds numbers $3.2 \cdot 10^5$, $1.2 \cdot 10^6$, $2.8 \cdot 10^6$ and $3.7 \cdot 10^6$. Additionally, the respective mean values $\bar{\phi}_{II}$, the uncertainties $u(\phi_{II})$ and the normalised uncertainties $u(\phi_{II})/\bar{\phi}_{II}$ are plotted for each Reynolds number. The procedure for calculating the mean values and the uncertainties is explained in Appendices A.1.1 and A.1.2.

[3]Shiraishi et al. [92] showed four different curves, one for each Reynolds number. However, these curves were so closely together that a clear distinction was invisible to the naked eye.

Case	Re $= 3.2 \cdot 10^5$			Re $= 1.2 \cdot 10^6$		
	$\varphi = 90°$	$z/d = 1$	$z/d = 5$	$\varphi = 90°$	$z/d = 1$	$z/d = 5$
Coarse H	24.28	11.34	6.61	21.40	9.96	6.07
Medium H	25.16	11.44	6.67	23.15	9.92	5.98
Fine H	25.28	11.67	6.88	23.22	10.14	6.22
Fine rM	25.26	12.04	7.18	23.14	10.42	6.46
$\bar{\phi}_{II}$	24.99	11.62	6.84	22.73	10.11	6.18
$u(\phi_{II})$	0.41	0.27	0.23	0.77	0.20	0.18
$u(\phi_{II})/\bar{\phi}_{II}$	1.65	2.33	3.30	3.38	1.94	2.97

Case	Re $= 2.8 \cdot 10^6$			Re $= 3.7 \cdot 10^6$		
	$\varphi = 90°$	$z/d = 1$	$z/d = 5$	$\varphi = 90°$	$z/d = 1$	$z/d = 5$
Coarse H	20.14	9.11	5.55	19.76	8.86	5.39
Medium H	21.73	8.94	5.51	21.23	8.64	5.36
Fine H	21.74	9.12	5.74	21.26	8.81	5.58
Fine rM	21.64	9.34	5.95	21.17	8.99	5.77
$\bar{\phi}_{II}$	21.31	9.13	5.69	20.85	8.82	5.53
$u(\phi_{II})$	0.68	0.14	0.17	0.63	0.13	0.16
$u(\phi_{II})/\bar{\phi}_{II}$	3.19	1.52	3.03	3.04	1.45	2.97

Table C.11: Secondary velocity ratio ϕ_{II} in % for four meshes evaluated at three stations.

The cases with the different meshes were all run with the SST $y^+ = 1$ turbulence model, and the cases with the different turbulence models were run with mesh Medium H, whereby for the kE model case, the boundary layer resolution was adjusted. A detailed discussion of the results and a comparison against the secondary velocity ratios computed for the 90° pipe bend of Sudo et al. [104] is presented in Section 5.3.

With peak values ranging from 18 % to 25 %, the secondary velocity ratios are the highest directly at the exit of the bend at station $\varphi = 90°$. At station $z/d = 1$ one diameter downstream, the secondary velocity ratios were more than halved and naturally decreased even more as the flow moved further downstream. Tables C.11 and C.12 indicate that the uncertainties contributed by the spatial discretisation lie at around 3 % regardless of the Reynolds number. Thereby they are significantly less than the uncertainties resulting from turbulence modelling, which lie at around 4 % to 8 % at station $\varphi = 90°$ directly at the bend exit and increase to 16 % to 24 % at station $z/d = 5$. Generally, the uncertainty grows with increasing Reynolds number for the cases with different turbulence models.

Case	Re = $3.2 \cdot 10^5$			Re = $1.2 \cdot 10^6$		
	$\varphi = 90°$	$z/d = 1$	$z/d = 5$	$\varphi = 90°$	$z/d = 1$	$z/d = 5$
kE high Re	22.72	9.69	4.54	20.1	7.83	3.53
SST y+1	25.28	11.67	6.88	23.22	10.14	6.22
SSTCC	25.44	11.32	6.77	23.84	9.89	6.01
EARSM	24.66	10.42	5.59	22.89	8.8	4.77
$\bar{\phi}_{II}$	24.53	10.77	5.95	22.51	9.16	5.13
$u(\phi_{II})$	1.08	0.78	0.96	1.43	0.92	1.08
$u(\phi_{II})/\bar{\phi}_{II}$	4.42	7.21	16.08	6.37	10.02	20.99

Case	Re = $2.8 \cdot 10^6$			Re = $3.7 \cdot 10^6$		
	$\varphi = 90°$	$z/d = 1$	$z/d = 5$	$\varphi = 90°$	$z/d = 1$	$z/d = 5$
kE high Re	18.62	6.93	3.06	18.09	6.62	2.92
SST y+1	21.74	9.12	5.74	21.26	8.81	5.58
SSTCC	22.61	8.96	5.52	22.2	8.66	5.37
EARSM	21.65	7.76	4.25	21.23	7.45	4.09
$\bar{\phi}_{II}$	21.15	8.19	4.64	20.7	7.88	4.49
$u(\phi_{II})$	1.51	0.9	1.08	1.55	0.9	1.07
$u(\phi_{II})/\bar{\phi}_{II}$	7.14	11	23.15	7.51	11.41	23.86

Table C.12: Secondary velocity ratio ϕ_{II} in % for four turbulence models evaluated at three stations.

APPENDIX D

Additional data of Chapter 6

D.1 Comparison of the *AxFeeder* concept to a conventional distributor system

In hydropower projects, the space needed for the Pelton turbine and its components (including the distributor system) significantly influences the layout of the turbine hall and, thus, the scope of excavation works and overall construction costs. Hence, this influence is one of the decisive factors in the project's early layout and design phase. Therefore, comparing the new *AxFeeder* concept to a conventional distributor system is of great interest. For the *AxFeeder*, a configuration with diffuser manifold, conical frustum and a 90° deviation angle of the branch lines as introduced in part b) of Figure 6.2 was chosen for comparison. This type of *AxFeeder* was comprehensively studied in Sections 6.4.2 and 6.5 and was eventually selected for the experimental testing planned in the project *AxFeeder* (FO999888084). For the conventional distributor line, a design suitable for the same head, flow rate (and thus the same Reynolds number range) and runner size was selected. This conventional distributor was thoroughly investigated by Hahn et al. [31] and by Semlitsch [89].

The two concepts are directly compared in Figure D.1 with the *AxFeeder* in grey and the conventional distributor in blue. The external dimensions of the *AxFeeder* in radial direction (expressed by R_{80}) are roughly 10 % to 20 % larger than those of the conventional distributor (R_{KVTL}). The larger dimensions are owed to maximising the curvature radius of the bends in the branch lines of the *AxFeeder*. Naturally, this comes with additional manufacturing and material costs for the *AxFeeder* concept but minimises losses and secondary flows. Maximising the curvature radius could have been done for the conventional distributor, too, but during its design phase, the emphasis lay on finding a very compact yet well-performing distributor. The comparison of the two concepts also reveals that the conventional distributor line is much more slender in the z-direction and allows the position of the turbine shaft with the generator unit on both sides of the distributor, where for the *AxFeeder*, the generator must be positioned on the opposite side of the manifold.

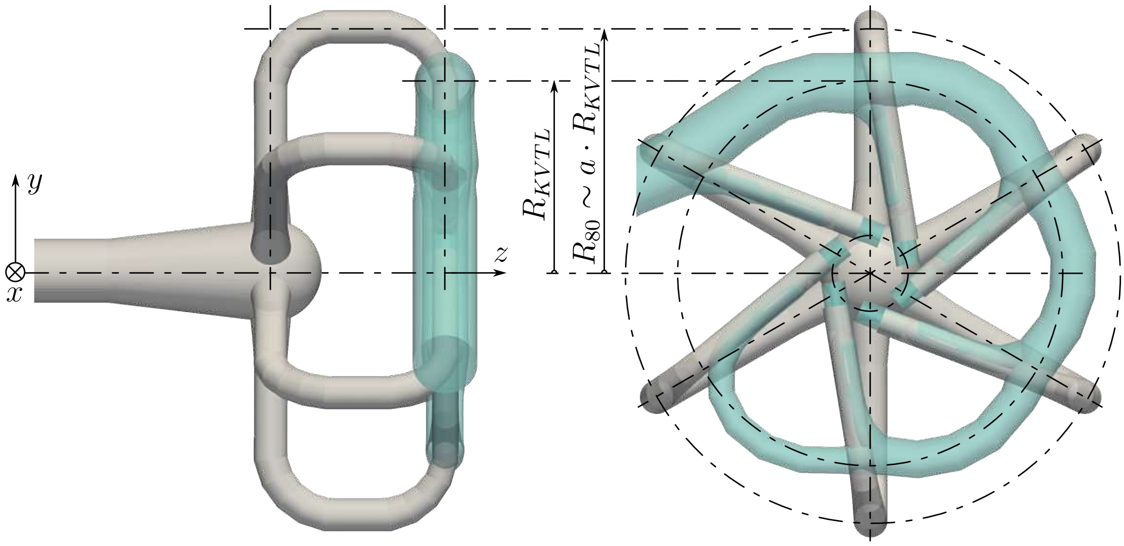

Figure D.1: Size comparison of the *AxFeeder* design with diffuser manifold and conical frustum (grey) to a conventional distributor system (blue) for the same designated operating data. $a = 1.1$ to 1.2.

In summary, this comparison of the two concepts underlines that additional focus on further reducing the overall size and complexity of the *AxFeeder* must be paid to pose a cost-effective and compact alternative to the conventional distributor system for Pelton turbines.

D.2 Data of Section 6.2

A detailed discussion of the grid resolution study for the cases of the *AxFeeder* was presented in Section 6.2.2.

D.2.1 Mesh data - *AxFeeder*

The most relevant features of the investigated meshes are listed in Table D.1.

ID	Name	$N_m/*)$	$h/h_{MediumH}$	a)	b)	c)	d)
1	Coarse	0.42	1.33	$1.8 \cdot 10^{-4}$	0.25	0.93	0.23
2	Medium	1.00	1.00	$1.6 \cdot 10^{-4}$	0.25	1.00	1.00
3	Fine	2.43	0.74	$1.2 \cdot 10^{-4}$	1.00	2.22	2.22
4	Symmetric	0.21	0.93	$1.2 \cdot 10^{-4}$	1.00	0.55	0.14

Table D.1: Meshes for the verification studies of the *AxFeeder*. a) - RMS Residuals of the momentum equation after 1000 iterations. b) - Relative number of processor cores used. c) - Relative compute time for each case. d) - Product of relative core number and relative compute time. $*) = N_{m,MediumH}$

D.2.2 Spatial discretisation error - *AxFeeder*

Tables D.2 to D.4 summarise the computed values for the fine-grid convergence GCI^{21}_{fine}, the apparent order of the numerical method p_{oa} and the ratio of oscillatory convergence R_{oc} for the power loss coefficients, the dissipation power coefficient, the local velocities and the secondary velocity ratio.

Quantity	Stations	GCI^{21}_{fine} (%)	p_{oa}	R_{oc}
$\zeta_{PmTE}\|_{1}^{50}$	1-50	2.41	1.52	-1.58
$\zeta_{PmTE}\|_{50}^{100}$	50-100	0.11	3.64	-3.00
$\zeta_{PmTE}\|_{1}^{100}$	1-100	1.05	1.79	-1.71
$\zeta_{\Phi}\|_{1}^{50}$	1-50	44.49	0.53	0.88
$\zeta_{\Phi}\|_{50}^{100}$	50-100	3.08	1.40	0.68
$\zeta_{\Phi}\|_{1}^{100}$	1-100	14.64	0.78	0.82

Table D.2: Grid convergence index GCI^{21}_{fine} (%), apparent order p_{oa} of the numerical method and indicator of oscillatory convergence R_{oc} for the loss coefficients.

Station	a)	b)	p_{oa}	R_{oc}
71	9.47	0.96	3.72	75.2
101	79.94	3.39	3.29	74.4

Table D.3: Maximum and mean values of the grid convergence indices, a) - $GCI^{21}_{fine,max}$ (%), b) - $GCI^{21}_{fine,mean}$ (%), mean value of the apparent order p_{oa} of the numerical method and ratio of data points with oscillatory convergence R_{oc} for the normalised velocity $||\vec{c}||/c_{s,ref}$ at stations 76 and 101.

Quantity	Station	GCI^{21}_{fine} (%)	p_{oa}	R_{oc}
$\phi_{II,50}$	50	1.19	4.71	-4.15
$\phi_{II,80}$	80	2.13	1.47	-0.65
$\phi_{II,100}$	100	13.65	1.38	-1.51

Table D.4: Grid convergence index GCI^{21}_{fine} (%), apparent order p_{oa} of the numerical method and indicator of oscillatory convergence R_{oc} for the secondary velocity ratio ϕ_{II} at three stations $z/d = 0$, $z/d = 1$, and $z/d = 5$.

D.3 Comparison to Large Eddy Simulation results

In [29, 88], Semlitsch investigated the generation of large-scale vortical flow structures for several operating conditions of the *AxFeeder*. Thereby, among other things, Semlitsch [29, 88] compared the time-averaged velocity magnitudes $||\vec{c}||/c_{s,1}$ from Large Eddy Simulations (LES) to those predicted by Reynolds-Averaged Navier-Stokes (RANS) simulations for an operating point with one active injector. This operating condition was of particular interest for the project *AxFeeder* (FO999888084) and thus selected for in-depth flow analysis.

The results of Semlitsch [29, 88] shall now serve as a reference to the results obtained from the parametric investigation (Section 6.4) and the influence studies (Section 6.5). Therefore, in Figure D.2, the normalised velocity contours in the y-z plane are plotted for four cases, where case a) shows the temporal average of the flow velocity of the LES approach and cases b) to d) show flow velocity from RANS computations[1]. Cases a) and b), which were executed by Semlitsch [29, 88] using OpenFOAMv2312, employed already a slightly scaled-down configuration of the *AxFeeder* as this smaller variant was deemed more suitable for comparison with eventual experiments. However, all cases were set up such that the inflow Reynolds number of $1 \cdot 10^6$ was the same. A detailed comparison of all commons and differences of these four cases is given in Table D.5.

The time-averaged velocity contours are very similar for all cases shown in Figure D.2, regardless of the solver or modelling details. The main difference between the RANS results using OpenFOAM, case b) and CFX, cases c) and d), lies in the prediction of the flow separation in the branch line. This separation is slightly more pronounced in the horizontal pipe section (between stations 71 and 81) on the inside after the first bend for the OpenFOAM cases. On the contrary, the separations on the outside of the first bend of the branch line are more prominent in the CFX cases. While all RANS cases predict an almost perfectly symmetric flow field, in case a) with the LES results, a minor asymmetry can be detected in the diffuser and the frustum parts. At the base of the frustum, where the branch lines are attached to the manifold, the flow separation zone is significantly wider than that of the RANS cases and gets smaller towards the top end.

An even more in-depth comparison between the two main CFD modelling strategies, LES and RANS, is presented in Figure D.3, where, for four cases, the secondary velocity ratio ϕ_{II} is plotted in station 101. The LES approach is shown in the top row of this figure, case a). The contour on the very left depicts the time-averaged secondary velocity ratio, whereas the three plots next to this contour illustrate the instantaneous values at three points in time. The lower row of Figure D.3 displays ϕ_{II} for three different RANS cases. Interestingly, the (time-averaged) contours of the LES and the RANS cases a) and b) (both with one active branch line)

[1] The truncated view of the branch lines in case a) is a result of a viewing error not within my area of responsibility. The geometries of cases a) and b) were identical, though.

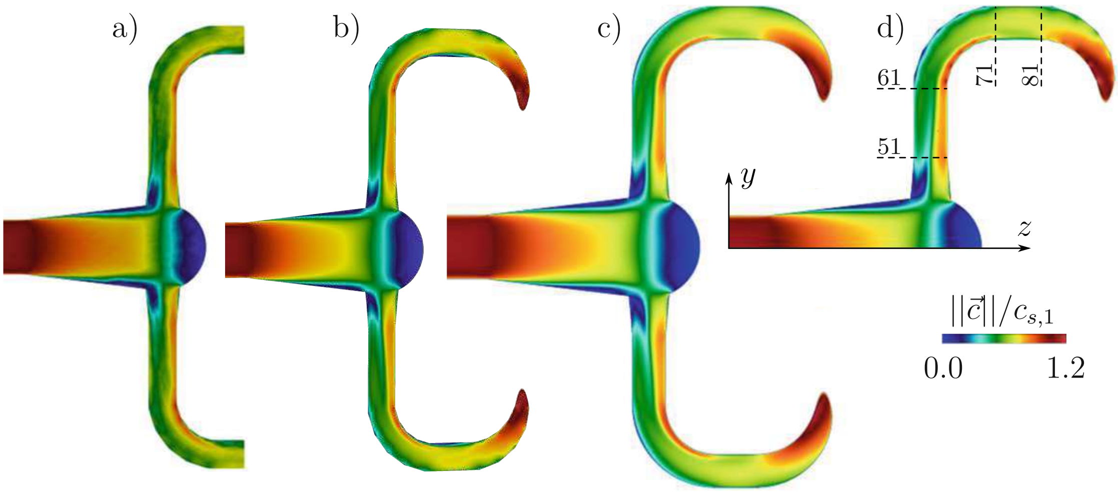

Figure D.2: Comparison of the time-averaged velocity contours $||\vec{c}||/c_{s,1}$ predicted by the LES and RANS approaches. Parts a) and b) recreated and modified with kind permission of Semlitsch [29, 88].

Case	a)	b)	c)	d)
Solver	OpenFOAM v2312		CFX 19.2	
Type	LES	RANS		
Scale	0.868		1	
Symmetry	no			yes
Bends	segmented		smooth	segmented

Table D.5: Characteristics of the four cases (all with $\mathrm{Re}_1 = 1 \cdot 10^6$, six active branch lines) compared in Figure D.2.

appear very similar. The beak at the inside (negative z-direction) from the LES flow field is more prominent and shifted to the positive x-direction. The beak of the corresponding RANS plot appears less pronounced and relatively symmetric. The lesser extent of the beak is presumably related to the fact that the RANS code cannot resolve the larger vortical scales, but the LES code can. However, the prediction of the secondary flows by the RANS method is sufficiently similar in the four discussed cases, regardless of the differences in the modelling and setup. The main characteristics of the cases are summarised in Table D.5.

One effect that has to be addressed is the difference in the Reynolds numbers between cases a) and b), where only one branch line was activated, and cases c) and d), where all six branch lines were activated. Therefore, the mass flow and the Reynolds number in the manifold are higher in these cases. The flow structures stay comparable in all four cases, except for the beak, which is hardly visible in cases c) and d). The magnitude of the secondary velocity and, hence, the secondary velocity ratio is lower in cases c) and d). This observation agrees with the trend observed in Figure 6.6, where the secondary velocity ratio in station 101 decreases with around the $-1/16^{th}$ power of the Reynolds number.

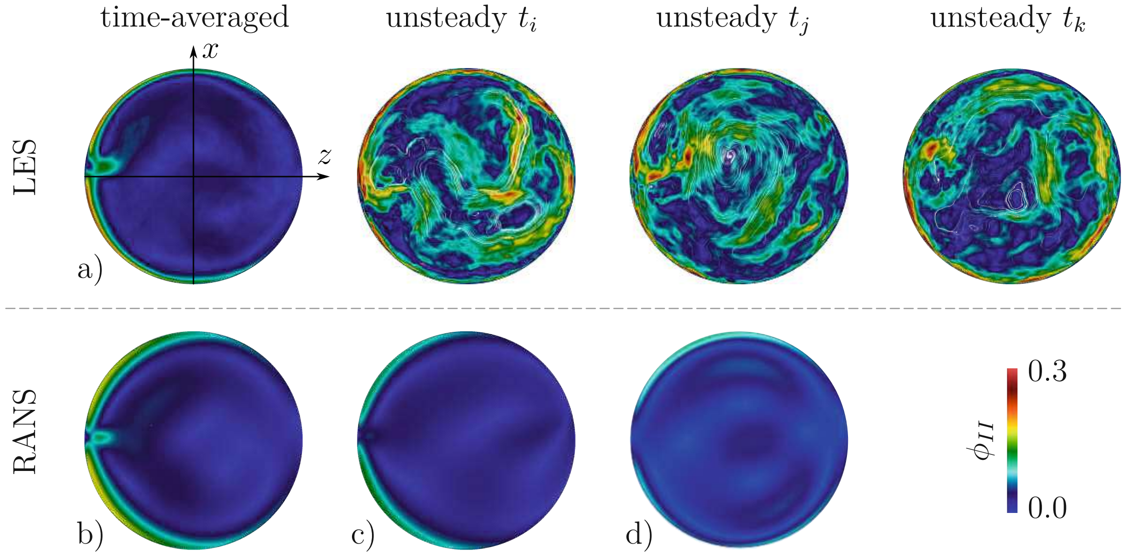

Figure D.3: Comparison of the secondary velocity ratio ϕ_{II} in station 101 predicted by the LES and RANS approaches. Parts a) to c) recreated and modified with kind permission of Semlitsch [29].

<table>
<tr><th>Case</th><th>a)</th><th>b)</th><th>c)</th><th>d)</th></tr>
<tr><td>Solver</td><td colspan="3">OpenFOAM v2312</td><td>CFX 19.2</td></tr>
<tr><td>Type</td><td>LES</td><td colspan="3">RANS</td></tr>
<tr><td>Scale</td><td colspan="3">0.868</td><td>1</td></tr>
<tr><td>$*$)</td><td colspan="2">1</td><td colspan="2">6</td></tr>
<tr><td>Re_1</td><td colspan="2">$2 \cdot 10^5$</td><td colspan="2">$1 \cdot 10^6$</td></tr>
<tr><td>Symmetry</td><td colspan="3">no</td><td>yes</td></tr>
</table>

Table D.6: Characteristics of the four cases (all with segmented bends) compared in Figure D.3. $*$) = Active branch lines

Overall, the agreement between the different modelling methodologies is quite satisfactory, and further validates the applicability of the RANS approach chosen for the simulations conducted within this thesis.

Curriculum vitae

Personal data

Name Dipl.-Ing. Franz Josef Johann Hahn, BSc
Date of birth 13^{th} November 1991 in Tulln, Austria
Nationality Austrian

Education

2019–2024 **Doctoral degree in Mechanical Engineering**, *TU Wien*, Vienna, Austria

Thesis Numerical investigation and optimisation of a new Pelton turbine distributor system

2016–2018 **Master's degree in Mechanical Engineering**, *TU Wien*, Vienna, Austria, Passed with distinction

Thesis Performance Improvement of a High Specific Speed Mixed-Flow Pump by Means of Multi-objective Optimization

2012–2016 **Bachelor's degree in Mechanical Engineering**, *TU Wien*, Vienna, Austria

Thesis Spline-gestützte Auswertung von Spritzbildern einer Peltonturbine zur Analyse des Wasserabflusses aus den Bechern

2006–2011 **College for Mechanical Engineering**, *HTBL Hollabrunn*, Hollabrunn, Austria

Honours

2021 Christiana HÖRBIGER Award - Award promoting the international mobility of young scientists

2016–2017 Scholarship for academic excellence at TU Wien, (gpa $<$ 1.2)

2012–2013 Scholarship for academic excellence at TU Wien, (gpa $<$ 1.7)

2006–2011 Five-time recipient of the "Löffler-Müller" scholarship for academic excellence at HTBL Hollabrunn (grade point average (gpa): 1.0)

Professional experience

2019–2024 **Project/University assistant**, *Research Group of Fluid-Flow Machinery, Institute of Energy Systems and Thermodynamics*, TU Wien, Austria
Conducting research on Pelton turbines and components of Pelton turbines, collaboration in the research project "AxFeeder", creating publications of research outcomes;
Teaching hydraulic machinery and CFD simulations to bachelor's and master's students;
Industrial projects in the field of Pelton turbines/components, collaboration in the research project "WakaSi", co-organisation of Viennahydro 2022

2018 **Student researcher**, *Research Group of Fluid-Flow Machinery, Institute of Energy Systems and Thermodynamics*, TU Wien, Austria
Refurbishment, design improvement and optimisation of mixed-flow pumps; Assisting the organising committee of Viennahydro 2018

2016–2018 **Tutor**, *Institute of Mechanics and Mechatronics*, TU Wien, Austria
Tutoring the exercise courses "Mechanics of solid bodies 1" and "Mechanics of solid bodies 2" for bachelor's students

2007–2017 **Student Trainee**, *multiple employers*, Austria
29 months of traineeships and summer internships with, i.e. Voith Paper GmbH, St. Pölten (20 months); Voith Hydro GmbH & Co. KG, St. Pölten (4 months); Siemens AG Österreich, Vienna; EVN AG, Dürnrohr

2011–2012 **Military service**, *Österreichisches Bundesheer*, Austria

Technical experience

Proficient with

Office	Microsoft Office, LaTeX, Citavi
Simulation	ANSYS Workbench, CFX, Fluent
CAD	SolidWorks, Pro/Engineer, AutoCAD Mechanical

Have experience with

Simulation	OpenFOAM
CAD	Solid Edge, NX, CATIA
Mathematics	Mathcad, MATLAB
Programming	Bash, Perl, Excel VBA, Python LabView, WordPress

Publications

Lead author

[1] Hahn, F. J. J., Maly, A., Semlitsch, B., and Bauer, C. (2023). Numerical Investigation of Pelton Turbine Distributor Systems with Axial Inflow. *Energies 16*, 2737.

[2] Hahn, F. J. J., Maly, A., Semlitsch, B., and Bauer, C., *Numerical investigation of the secondary flow pattern in a Pelton turbine jet* In *Proceedings of the* 3rd*IAHR Young Professionals Congress*, 2022, pp 121–122.

[3] Hahn, F. J. J., Semlitsch, B., and Bauer, C. (2022). On the numerical assessment of flow losses and secondary flows in Pelton turbine manifolds. *IOP Conference Series: Earth and Environmental Science 1079*, 012082.

[4] Hahn, F. J. J., Unterluggauer, J., and Bauer, C. (2019). Performance improvement of a mixed-flow pump by means of multi-objective optimization. *Wasserwirtschaft 109*, 31–36.

Co-author

[1] Medeiros Dalla Costa, D., Hahn, F. J. J., and Reichl, I., *Computer Aided Engineering in Augmented Reality: Flow Visualizations for Hydro Power Applications* In *Proceedings of the Austrian-Slovenian HPC Meeting 2023*, ed. by Reiter, E., EuroCC Austria: 2023, pp 40–40.